Université de Toulouse

THÈSE

En vue de l'obtention du

DOCTORAT DE L'UNIVERSITÉ DE TOULOUSE

Délivré par :

Institut Supérieur de l'Aéronautique et de l'Espace (ISAE)

Présentée et soutenue par :
Mehdi AIT IGHIL

le lundi 28 janvier 2013

Titre :

Simulateur de canal de propagation basé sur une approche physico-statistique et adapté à la modélisation des multitrajets pour les systèmes de navigation par satellite

Enhanced physical-statistical simulator of the land mobile satellite channel for multipath modelling applied to satellite navigation systems

---

École doctorale et discipline ou spécialité :

ED MITT : Réseaux, télécom, système et architecture

Unité de recherche :

Équipe d'accueil ISAE-ONERA SCANR

Directeur(s) de Thèse :

M. Fernando PEREZ-FONTAN (directeur de thèse)
M. Michel BOUSQUET (co-directeur de thèse)

Jury :

M. Claude OESTGES, Université Catholique de Louvain - Rapporteur
M. Rodolphe VAUZELLE, Université de Poitiers - Rapporteur
M. Joel LEMORTON, ONERA Toulouse
M. Roberto PRIETO CERDEIRA, ESA/ESTEC - Examinateur
M. Michel BOUSQUET, ISAE - co-directeur de thèse
M. Fernando PEREZ-FONTAN, Université de Vigo - directeur de thèse

"J'ai refait tous les calculs,
ils confirment l'opinion des spécialistes :
notre projet est irréalisable.
Il ne nous reste plus qu'une chose à faire :
le réaliser."

Pierre Georges LATÉCOÈRE (1883-1943)
Pionnier de l'Aéropostale

Acknowledgments

Over the past three years I have worked as a PhD student in the radio communication and propagation research unit at the electromagnetic and radar department at ONERA Toulouse. During these three years, I have received support and encouragement from a great number of individuals who I would like to thank.

In first place, I would like to thank all the partners of this work which have made this research project possible: ONERA (Office National d'Etudes et de Recherches Aérospatiales) through M. Florent CHRISTOPHE and Dr. Laurent CASTANET, CNES (Centre National d'Etudes Spatiales) through Mdm Géraldine ARTAUD, Thales Alenia Space through M. Christophe BOURGA and the COST action ic0802 "Propagation tools and data for integrated Telecom, Navigation and Earth Observation systems".

I would also like to thank Prof. Michel BOUSQUET from ISAE Toulouse (Institut Supérieur de l'Aéronautique et de l'Espace), France, and Prof. Fernando PEREZ-FONTAN from the University of Vigo, Spain, who treated me as a son in Vigo, for their great contributions when supervising this work and during the writing of the present manuscript.

I do not forget Dr. Guillaume CARRIE, Dr. Paul THEVENON and Dr. Frédéric LACOSTE to whom I would like to address my sincere thanks for the very special place they occupied during this journey and Dr. Joel LEMORTON who acted as a mentor, a colleague and a friend. This whole work is closely related to their guidance, assistance and advices.

In a more personal way, I would like to express my gratitude to M. Hervé LANCIEN who gave me the taste for physics in high school, Dr. Yves LOSTANLEN who was the first to make the idea of doing a PhD grew up in my mind and Prof. M'Hamed DRISSI who followed my academic career during the last eight years always providing wise thoughts.

Last but not least, I would like to thank my closest friends, my family and Lucie who always gave me unyielding support especially through the difficult times.

Contents

Introduction 1

1 Critical review of existing LMS channel models and proposed approach 5
1.1 Three different approaches for modelling the Land Mobile Satellite channel . . . 5
1.1.1 Statistical approaches . . . 6
1.1.1.1 Narrow-band fades distribution models . . . 6
1.1.1.2 Narrow-band state-oriented models . . . 10
1.1.1.3 Wide-band models . . . 11
1.1.1.4 Perez-Fontan, University of Vigo, 2001 [Pere 01] . . . 12
1.1.1.5 Carrie, ONERA, 2012 [Carr 12] . . . 13
1.1.2 Deterministic approaches . . . 15
1.1.2.1 Full-wave methods . . . 16
1.1.2.2 Asymptotic methods . . . 16
1.1.3 Hybrid physical-statistical approaches . . . 17
1.1.3.1 Oestges, UCL, 2000 [Oest 00] . . . 17
1.1.3.2 King, University of Surrey, 2007 [King 07a] . . . 19
1.1.3.3 Lehner, DLR, 2007 [Lehn 07b] . . . 19
1.1.3.4 Abele, ONERA, 2009 [Abel 09] . . . 22
1.1.3.5 Li, University of Poitiers, 2010 [Li 10] . . . 25
1.1.4 Details on the virtual city concept . . . 27
1.2 Proposed approach for designing a new LMS channel simulator . . . 29
1.2.1 Objectives and constraints of the model . . . 29
1.2.1.1 Objectives . . . 29
1.2.1.2 Constraints . . . 30
1.2.2 Presentation of a new hybrid physical-statistical LMS channel simulator: SCHUN . . . 31
1.2.2.1 Positioning of the chosen approach . . . 31
1.2.2.2 Macro architecture of the channel simulator . . . 32
1.2.2.3 Typical outputs and signal model . . . 34
1.3 Summary . . . 34

2 Simplifying the representation of complex façades in urban environments 37
2.1 Details of the experimental protocol . . . 38
2.1.1 Appropriate numerical method: Method of Moments . . . 38
2.1.2 Definition of the façades . . . 38
2.1.3 Definition of urban canyons . . . 41
2.2 Preliminary observations made on isolated canonical façades . . . 41
2.2.1 Analysis of surface currents . . . 42
2.2.2 Analysis of Radar Cross Sections . . . 43
2.2.3 Analysis of the near field scattering pattern . . . 48
2.3 Influence of small features on MP power estimation . . . 51
2.3.1 Simple narrow-band channel model . . . 51
2.3.2 Qualitative analysis of MP power time series on simple urban canyons . . . 52
2.3.3 Statistical analysis of MP power time series on simple urban canyons . . . 54
2.4 Influence of small features on navigation receivers . . . 57
2.4.1 Simple wide-band channel model . . . 57
2.4.2 Influence of resolution and speed . . . 59
2.4.3 Influence of incidence . . . 61
2.4.4 Influence of direct signal attenuation . . . 62
2.5 Summary and recommendations . . . 65

3 Simplified EM interaction model for urban building scattering 67
3.1 Observation made in the vicinity of complex façades . . . 68
3.1.1 Narrow-band observations - MoM . . . 68
3.1.2 Wide-band observations - Asymptotic tool . . . 69
3.1.3 DoA observation - Measurements campaigns . . . 70
3.2 Proposed approach for a new building scattering model based on EM theory . . . 72
3.2.1 Approach of the Three Component Model (3CM) . . . 72
3.2.2 Physical base of the specular reflection component . . . 73
3.2.3 Physical base of the backscattering component . . . 75
3.2.4 Physical base of the incoherent scattering component . . . 77
3.3 Numerical validation of the 3CM in simple cases . . . 80
3.3.1 Narrow-band validation on isolated façades . . . 80
3.3.2 Narrow-band validation on simple canyons . . . 84
3.3.3 Wide-band validation on simple canyons . . . 87
3.4 Summary . . . 89

4 Implementation and validation of the SCHUN LMS channel simulator 91
4.1 Implementation of the SCHUN simulator . . . 92
4.1.1 The SCHUN LMS channel simulator . . . 92
4.1.1.1 The macro-architecture of the simulator . . . 92
4.1.1.2 Capabilities of the channel simulator . . . 92
4.1.1.3 Basic scenario . . . 93
4.1.2 Virtual environment synthesis . . . 93
4.1.2.1 Layout of environment objects . . . 93
4.1.2.2 Building synthesis . . . 94
4.1.2.3 Façade synthesis . . . 95
4.1.3 Direct path blockage models . . . 96
4.1.3.1 Simple model for building blockage . . . 96
4.1.3.2 Building diffraction model . . . 97
4.1.4 Introduction of a new multipath reduction method . . . 98
4.2 Saint Lary experimental validation for satellite communication systems . . . 102
4.2.1 Presentation of the Saint-Lary 2012 measurement campaign . . . 102
4.2.2 Presentation of Saint-Lary virtual environment . . . 105
4.2.2.1 Modelling of the buildings . . . 105
4.2.2.2 Presentation of the façade library . . . 106
4.2.3 Comparison with experimental SISO co and cross circular polarised channels in S-band . . . 109
4.2.3.1 Narrow-band time-series . . . 109
4.2.3.2 Doppler spectrum . . . 111
4.2.3.3 Estimation of the Rice factor . . . 112
4.2.3.4 Level crossing rate and fade duration . . . 113
4.3 Toulouse Capitole experimental validation for satellite navigation systems . . . 115
4.3.1 Presentation of the Toulouse-Capitole 2011 measurement campaign . . . 115
4.3.2 Presentation of Toulouse-Capitole virtual environments . . . 117
4.3.2.1 SE-WorkBench synthetic environment . . . 117
4.3.2.2 SCHUN virtual environment . . . 118
4.3.3 Indirect experimental validation on GNSS software receivers . . . 122
4.3.3.1 Preliminary results . . . 122
4.3.3.2 Estimated C/N0 time-series . . . 125
4.3.3.3 Pseudo-range error time-series . . . 128
4.4 Discussion . . . 134

Conclusion 137

Appendices **139**

A Basics of satellite navigation systems **139**
A.1 Satellite navigation systems 139
A.2 GNSS software receivers 151

B Basics of EM numerical methods **155**
B.1 Current-based asymptotic methods 155
B.2 Ray-based asymptotic methods 158
B.3 Electromagnetic reference codes 163

C Numerical validation of the three separate EM components of the 3CM **169**
C.1 Validation of the simplified PO algorithm used for the specular component . . . 169
C.2 Validation of the double bounce reflection algorithm used for the backscattering component 174
C.3 Validation of the rough surfaces models used for the incoherent component . . . 176

D Résumé étendu **179**
D.1 Introduction 179
D.2 Etude critique et proposition d'un nouveau simulateur 183
D.3 Etude de l'influence des détails sur des façades complexes 189
D.4 Présentation d'un nouveau modèle d'interaction onde/bâtiments 194
D.5 Implémentation et validation du simulateur de canal SCHUN 198
D.6 Conclusion 206

Personnal Bibliography **209**

Bibliography **211**

List of Figures

1.1 Description of the three scale propagation mechanisms [Saun 07] 7
1.2 pdf of fading depth from real measured signal [Satn 08] 7
1.3 Typical Rayleigh and Rice configuration examples 8
1.4 Example of a two states first order Markov chain 11
1.5 Cluster approach used in Saleh Valenzuela modelling [Sale 87] 12
1.6 Tapped-delay line approach used in Jahn model [Jahn 01] 12
1.7 Example of wide-band statistical model based on Markov chains [Pere 01] 13
1.8 Block diagram of the MIMO channel model introduced by Carrie [Carr 12] . . . 14
1.9 Validation example of the narrow-band model on second order statistics [King 07a] 20
1.10 Principle of the wide-band model [King 07b] 20
1.11 Block diagram and reflector model of the Land Mobile Multipath Channel Model [Lehn 07a] 22
1.12 Principle of the Abele model 23
1.13 Example of mapping of the normalised RCS for a typical rough surface at 2.2GHz [Abel 08] 24
1.14 Measurement validation examples of the Abele model [Abel 09] 25
1.15 Principle of the Li deterministic-statistical model [Li 10] 25
1.16 DLR virtual city approach for placing trees [Krac 07] 28
1.17 Guildford building height and street width statistics [Oest 99a] 29
1.18 Positioning of the proposed approach 33
1.19 Macro architecture of the SCHUN LMS channel simulator 33

2.1 Example of canonical façades extracted from periodic architectural motives on complex urban buildings 39
2.2 Representation of the four level of details for the City centre façade in [m] . . . 40
2.3 Representation of the four levels of details for the ONERA office façade in [m] . 40
2.4 Representation of the three different urban canyons 41
2.5 Quasi-optical inter-element shadowing visible on surface currents over the city centre façade in the case of a normal incidence with ϕ polarisation 42
2.6 Dihedral reflections are visible on surface currents over the city centre façade in the case of a typical LMS incidence (elevation 40°, azimuth 40°) with ϕ polarisation 42
2.7 Edge diffraction is visible on edge currents on the city centre façade in the case of extreme incidence (elevation 80°) with ϕ polarisation 43
2.8 Edge diffraction visible on current distribution over the ONERA office façade in the case of extreme incidence (elevation 80°) with ϕ polarisation 43
2.9 Near field pseudo-RCS of the city centre façade with polarisation ϕ in configuration 40° elevation, 40° azimuth for all four resolutions 44
2.10 Far field RCS of the city centre façade with polarisation ϕ in configuration 40° elevation, 40° azimuth for all four resolutions 45
2.11 Illustration of the isolation principle of the guardrail contribution from the rest of the city centre façade. 46
2.12 Illustration of the four different classes of details. 47
2.13 Contribution of the details for different source incidences. From left to right increasing azimuth (0°, 40°, 80°) and from top to bottom increasing elevation (0°, 40°, 80°). Case of the city centre façade illuminated with θ polarisation . . 48
2.14 Near field scattering in the horizontal plane near the city centre façade with ϕ polarisation at 40° elevation, 40° azimuth 49
2.15 Near field scattering in the horizontal plane near the ONERA office façade with ϕ polarisation at 40° elevation, 40° azimuth 49

2.16 Scattering flux in the horizontal plane near the city centre façade with ϕ polarisation at 0° elevation, 40° azimuth . . . 50
2.17 Complex narrow-band time series synthesis and summing principle used for simple urban scenarios . . . 52
2.18 Multipath scattered power time series as a function of the resolution. Simulated case: urban canyon1, azimuth 40°, elevation 40°, Tx polarisation θ, speed 50 km/h 53
2.19 Multipath scattered power time series as a function of the resolution. Simulated case: urban canyon1, azimuth 40°, elevation 80°, Tx polarisation ϕ, speed 50 km/h . . . 53
2.20 Multipath scattered power time series as a function of the resolution. Simulated case: urban canyon3, azimuth 80°, elevation 80°, Tx polarisation ϕ, speed 90 km/h . . . 54
2.21 Influence of the environment resolution on the MP scattered power relative to the high resolution . . . 55
2.22 Influence of the canyon geometry on the MP scattered power relative to the high resolution . . . 55
2.23 Influence of the speed on the MP scattered power relative to the high resolution 56
2.24 Power variation of all rays as a function of the environment resolution along a linear trajectory of the mobile in Canyon 1 . . . 58
2.25 Evolution of the channel parameters along a linear trajectory of the mobile in Canyon 1 . . . 58
2.26 Example of pseudo-range estimations as a function of the environment resolution 60
2.27 Influence of the environment resolution on pseudo-range errors in the case of unblocked LOS signal (0 dB attenuation) . . . 61
2.28 Parametric representation of the influence of the resolution and the speed on {Mean,Std} error couple . . . 61
2.29 Example of pseudo-range estimations as a function of the environment resolution in the case of extreme incidence configurations . . . 62
2.30 Influence of the extreme incidences on the pseudo-range error for the null resolution in the case of unblocked LOS signal . . . 63
2.31 Example of pseudo-range estimations as a function of the environment resolution with 20 dB attenuation on the direct signal . . . 63
2.32 Influence of the environment resolution on the pseudo-range error for a 20 dB attenuated on the direct signal. Left diagram presents the cdf of the mean error. Right diagram presents the cdf of the std of the error . . . 64

3.1 Narrow-band total scattered power received when passing close to a complex façade using MoM tool . . . 68
3.2 Wide-band delay/Doppler instantaneous channel impulse response when passing in a simple urban canyon using asymptotic GO/PO tools . . . 69
3.3 Probability density function of the position of the scatterers extracted from measurements realised by DLR 2in 002 [Lehn 08] and physical interpretation of each scattering region . . . 71
3.4 Decomposition principle of the 3CM . . . 72
3.5 Validation of the simplified PO algorithm on 3D bistatic RCS of a PEC plate . . 74
3.6 Principle of the equivalent plate to reproduce the backscattering component . . 75
3.7 Illustration of the empirical correction function used to compensate the diffraction phenomenon when using the equivalent plate model to reproduce the backscattering component . . . 76
3.8 Validation of the double bounce reflection algorithm considering bistatic RCS on a PEC dihedral . . . 77
3.9 Example of bistatic RCS of a square of 5m width using the slightly rough surface models . . . 78
3.10 Example of bistatic RCS of a square of 5m width using the rough surface models 79

3.11 Three different representations of a complex city center façade . . . 80
3.12 Repartition of the three component into the total narrow-band power scattered by a complex city centre façade. . . . 81
3.13 Total narrow-band power scattered by a complex city centre façade for various incidence angles . . . 82
3.14 Three different representations of a complex ONERA office façade . . . 83
3.15 Repartition of the three component into the total narrow-band power scattered by a complex ONERA office façade. . . . 83
3.16 Total narrow-band power scattered by a complex ONERA office façade for various incidence angles . . . 84
3.17 3CM simplified representation of the simulated street canyon . . . 84
3.18 Total narrow-band scattered power in a simple urban canyon . . . 85
3.19 Spectrogram along the receiver trajectory . . . 86
3.20 Power spectral density along the receiver trajectory . . . 86
3.21 Power delay/Doppler channel impulse response . . . 87
3.22 τ_{mean} and τ_{RMS} function of the mobile position . . . 88

4.1 Macro architecture of the SCHUN LMS channel simulator . . . 92
4.2 Example of the environment decomposition used in the SCHUN formalism . . . 94
4.3 Example of statistically synthesised virtual city profile . . . 95
4.4 MIMO example using simple LOS blockage model . . . 96
4.5 Validation of the building diffraction model comparing UTD from SCHUN and PTD and ECM from SE-WorkBench . . . 97
4.6 Example of reduced channel impulse responses . . . 100
4.7 Influence of the MP reduction process on the GNSS pseudo-range error time series 100
4.8 Influence of the MP reduction process on the GNSS correlation functions and S curves . . . 101
4.9 Emulation of a GEO satellite over Saint Lary village [Laco 12] . . . 102
4.10 Terrain height profile for the Tx-Rx link and first Fresnel ellipsoid [Laco 12] . . . 103
4.11 Measurement van used during the Saint Lary measurement campaign . . . 104
4.12 Reference trajectory in Saint Lary village . . . 105
4.13 Saint Lary building footprints extracted from the official land register map . . . 105
4.14 Common brick house front (façade 1) . . . 107
4.15 Old stone house front (façade 2) . . . 107
4.16 Wooded balconies (façade 3) . . . 107
4.17 Shop window (façade 4) . . . 108
4.18 Saint Lary virtual environment in the SCHUN formalism from the transmitter point of view . . . 108
4.19 SISO narrow-band time-series for co and cross circular polarised channels . . . 109
4.20 Filtered SISO narrow-band time-series for co and cross circular polarised channels 109
4.21 Presence of a tree on the LOS signal explaining the slight shadowing . . . 110
4.22 Cumulative distribution function of the total attenuation for co-polarised channels 110
4.23 Mean Doppler spectrum along the receiver trajectory . . . 111
4.24 Spectrogram along the receiver trajectory . . . 112
4.25 Estimated Rice factor K versus co-polarised coherent power . . . 113
4.26 Level crossing rate and fade duration . . . 113
4.27 Zoom on the co-polarised narrow-band power time series (blue=experimental, green=SCHUN) . . . 114
4.28 Reference trajectory in Toulouse Capitole environment . . . 116
4.29 Measurement equipement during the Toulouse Capitole measurement campaign 116
4.30 Skyplot of the GNSS constellation at the time of the measurement . . . 117
4.31 SE-WorkBench synthetic environment . . . 118
4.32 Toulouse-Capitole building footprints extracted from the official land register map 119
4.33 Typical Toulouse Hausmanian house front (façade 1) . . . 119

4.34 Window shop (façade 2) . . . 120
4.35 Modern flat house front (façade 3) . . . 120
4.36 Old façade with metallic guardrail (façade 4) . . . 120
4.37 Toulouse-Capitole virtual environment in the SCHUN formalism from the PRN07 point of view . . . 121
4.38 Influence of the environment instability on the C/N0 parameter estimated by one reference receiver (4T) for PRN07 . . . 122
4.39 Influence of the elevation changes of PRN10 on the estimated C/N0 using Rx 4T during the three measurement loops . . . 123
4.40 Influence of the elevation changes of PRN13 on the estimated C/N0 using Rx 4T during the three measurement loops . . . 123
4.41 Comparison of narrow-band time-series using SE-WorkBench and SCHUN for PRN04. BGM is used as a reference . . . 124
4.42 Comparison of narrow-band time-series using SE-WorkBench and SCHUN for PRN07. BGM is used as a reference . . . 124
4.43 Comparison of the estimated C/N0 time-series for the PRN02 . . . 125
4.44 Comparison of the estimated C/N0 time-series for the PRN04 . . . 125
4.45 Comparison of the estimated C/N0 time-series for the PRN07 . . . 126
4.46 Comparison of the estimated C/N0 time-series for the PRN08 . . . 126
4.47 Comparison of the estimated C/N0 time-series for the PRN10 . . . 126
4.48 Comparison of the estimated C/N0 time-series for the PRN13 . . . 127
4.49 Estimation principle of the pseudo-range error due to multipath in experimental conditions . . . 129
4.50 Raw pseudo-range error time-series for the PRN04 . . . 130
4.51 Raw pseudo-range error time-series for the PRN10 . . . 130
4.52 Corrected pseudo-range error time-series for the PRN02 . . . 131
4.53 Corrected pseudo-range error time-series for the PRN07 . . . 131
4.54 Corrected pseudo-range error time-series for the PRN10 . . . 131
4.55 Distribution of the pseudo-range errors and DLL jitter versus the estimated C/N0 for the PRN02 . . . 132
4.56 Distribution of the pseudo-range errors and DLL jitter versus the estimated C/N0 for the PRN07 . . . 133
4.57 Distribution of the pseudo-range errors and DLL jitter versus the estimated C/N0 for the PRN10 . . . 133

A.1 GPS control segment [Offi 12] . . . 140
A.2 Galileo frequency plan [Euro 10] . . . 141
A.3 Galileo spectrum . . . 142
A.4 GPS Modulation scheme . . . 142
A.5 Decomposition of GPS navigation message . . . 143
A.6 Auto-correlation and inter-correlation functions between two different C/A codes [Roug 12] . . . 144
A.7 GPS Signal processing principle [NAVS 96] . . . 145
A.8 Triangulation principle [Nahi 09] . . . 146
A.9 Estimation of delay and Doppler during acquisition step [Al B 07b] . . . 147
A.10 Example of auto-correlation functions for different signals [Roug 12] . . . 148
A.11 Synchronisation principle using Early Prompt Late signal replicas [Kapl 05] . . . 148
A.12 Discriminator outputs versus of input errors (S curve) . . . 149
A.13 Principle of building blockage . . . 149
A.14 Principle of urban multipath . . . 150
A.15 Impact of the multipath on the correlation function and on synchronisation processing . . . 151
A.16 Influence of power, delay and phase of one constant multipath on the pseudo-range error estimation . . . 151

A.17 Tracking architecture of JGNSS software receiver [Arta 07] 153

B.1 Chosen convention for incident and reflected bases [Bala 89] 155
B.2 Ray lunching pseudo algorithm 158
B.3 Principle of the shooting and bouncing ray algorithm 159
B.4 Ray tracing pseudo algorithm 159
B.5 Principle of the ray tracing algorithm 160
B.6 Geometry of the stationnary diffraction point 160
B.7 Definition of the edge fixed coordinate [McNa 90] 161
B.8 Elsem3D result examples. (left) Surface currents on MACH generic plane at 1.25GHz (10^6 unknowns). (right) Surface currents on a vehicular for EMC issues 164
B.9 Multiple interaction principle of SE-Ray-EM [SE 12] 165
B.10 Principle of the tapped-delay line centering process 166
B.11 Example of typical outputs provided by Onera wide-band module 167

C.1 Validation of the simplified PO algorithm on 3D bistatic RCS of a PEC plate . . 170
C.2 Validation of the simplified PO algorithm on polarised RCS considering PEC plate 171
C.3 Validation of the simple PO algorithm considering dielectric materials of a plate 172
C.4 Validation of the simple PO algorithm considering oblique oriented PEC plate . 172
C.5 Validation of the simple PO algorithm considering 3.5GHz center frequency . . . 172
C.6 Validation of the simple PO algorithm in near field conditions of a PEC plate . 172
C.7 Validation of the 3CM PO algorithm using the super imposition principle 173
C.8 Validation of the double bounce reflection algorithm considering bistatic RCS on PEC dihedral 174
C.9 Validation of the double bounce reflection algorithm considering multiple incidences on PEC dihedral 175
C.10 Validation of the double bounce reflection algorithm on polarised RCS considering PEC dihedral 175
C.11 Validation of the double bounce reflection algorithm considering on dielectric dihedral 176
C.12 Example of bistatic RCS using the slightly rough surface models 177
C.13 Example of bistatic RCS using the very rough surface models 177
C.14 Example of tuning the very rough surface model to fit the guardrail scattering function 178

D.1 Classification des différentes approches et positionnement de l'approche retenue 184
D.2 Architecture hybride proposée pour le simulateur SCHUN 188
D.3 Représentation des quatre niveaux de détail d'une façade type centre ville de Toulouse 190
D.4 Motif de diffusion en champ proche dans le plan horizontal d'une façade complexe de type centre ville dans une configuration polarisation ϕ, 40° d'élévation, 40° d'azimut 190
D.5 Exemple de série temporelle de puissance faible bande fonction de la résolution du canal. Paramètres de simulation: canyon urbain 1, azimut 40°, élévation 80°, Tx polarisation ϕ, vitesse 50 km/h 191
D.6 Influence de la résolution de l'environnement sur la puissance totale diffusée par rapport à la résolution élevée 192
D.7 Influence de la vitesse sur la puissance totale diffusée par rapport à la résolution élevée 192
D.8 Evolution des paramètres large bande en fonction du déplacement du mobile dans le canyon urbain (Délais, réponse impulsionnelle instantanée, Doppler) 193
D.9 Etude paramétrique de l'influence de la résolution de l'environnement et de la vitesse du mobile sur le couple d'erreur {Mean,Std} 193

D.10 Puissance totale faible bande reçue lorsqu'un mobile passe à proximité d'une façade complexe (Simulation Elsem3D - MoM) . . . 194
D.11 Principe de décomposition du modèle 3CM . . . 195
D.12 Puissance totale diffusée par une façade canonique isolée de type centre ville de Toulouse pour différents couples élévation/azimut du satellite . . . 196
D.13 Représentation 3CM simplifiée du canyon concidéré . . . 197
D.14 Spectrogramme le long de la trajectoire du mobile . . . 197
D.15 Réponse impulsionnelle instantanée du canal représentée dans l'espace Puissance/Délais/Doppler . . . 198
D.16 Exemple d'environnement générique généré statistiquement à partir du concept de ville virtuelle . . . 199
D.17 Validation du modèle de diffraction par les bâtiments en comparant la méthode UTD utilisée dans SCHUN aux méthodes PTD et ECM utilisées dans SE-WorkBench . . . 200
D.18 Exemple de réduction du nombre de multitrajets dans la réponse impulsionnelle instantannée . . . 200
D.19 Trajectoire de référence dans le village de Saint Lary . . . 201
D.20 Distribution de l'atténuation sur le canal co-polarisé . . . 201
D.21 Spectrogramme le long de la trajectoire du mobile . . . 202
D.22 Estimation du facteur de Rice en fonction de la puissance cohérente sur le canal co-polarisé . . . 202
D.23 Trajectoire de référence dans le centre ville de Toulouse . . . 204
D.24 Comparaison des séries temporelles de C/N0 estimées pour le PRN07 . . . 204
D.25 Principe d'estimation de l'erreur de pseudo-distance commise par le récepteur et dû aux multitrajets en conditions expérimentales . . . 205
D.26 Série temporelle d'erreur de pseudo-distance pour le PRN07 . . . 205
D.27 Distribution de l'erreur de pseudo-distance et variance de la boucle DLL en fonction du C/N0 estimé pour le PRN07 . . . 206

List of Tables

1.1 Classification of the different approaches 6
1.2 Comparison between Rice, Loo and Corazza distributions [Saun 07] 9
1.3 Summary of the different numerical methods associated to the deterministic approaches 16
1.4 Channel parameters of interest for LMMC model 21
1.5 Measured building height parameters for log-normal distributions [COST 02] . . 28
1.6 Critical review of the existing LMS channel models depending on imposed constraints 32

2.1 Contribution of each class of details for specular and non specular zones for city centre façade in configuration 40° elevation, 0° azimuth, θ polarisation 46

4.1 Simulation parameters for MIMO example using the simple LOS blockage model 97
4.2 Influence of the MP reduction process on the computation time 99
4.3 Summary of the C/N0 comparisons for both in-situ measurements using reference GNSS receivers (Rx 4T, Rx 6H) and post-processed channels using JGNSS (BGM experimental, SCHUN simulation) for PRN02, PRN04, PRN07, PRN08, PRN10 and PRN13 127

B.1 Linear interpolation of the F function for argument x between 0.3 and 5.5 . . . 162

D.1 Synthèse des différentes méthodes numériques présentent dans les approches déterministes185
D.2 Comparaison critique des modèles de canal existant en fonction de nos objectifs 187
D.3 Résumé des comparaisons des séries temporelles de C/N0 utilisant des récepteurs embarqués durant les mesures (Rx 4T et Rx 6H) ainsi que les données post-traitées en utilisant JGNSS à partir des données BGM et du simulateur SCHUN pour les PRN02, PRN04, PRN07, PRN08, PRN10 et PRN13 203

List of Abbreviations

3CM	Three Component Model
EM	Electromagnetic
GEO	Geostationary Earth Orbit
LMS	Land Mobile Satellite
MEO	Medium Earth Orbit
MoM	Method of Moments
MP	Multipath
SCHUN	Simplified CHannel for Urban Navigation

Introduction

The present study is at the interface between the field of EM *(ElectroMagnetic)* wave propagation modelling and the field of signal processing applied to satellite navigation systems.

Although the modelling of EM wave propagation has been investigated since early nineteenth century with the emergence of wireless technologies [Kenr 30] [Lowe 16] [Stra 30], it had to wait for World War II to boost microwave applications and EM wave propagation modelling, especially for radar and communications purposes. Since then, EM wave propagation has experienced a spectacular growth and the demand for new wireless systems does not fall off. Nowadays, wireless mobile technologies are present everywhere. As an example, we can mention terrestrial mobile telecommunication systems (GSM, UMTS or LTE standards), indoor broadband systems (Wifi a,b,g,n standards) and finally satellite-to-earth links (DVB-S or SDMB multimedia broadcasting standards). However, each of the mentioned wireless system is facing specific EM wave propagation impairments. Contrary to terrestrial and indoor EM propagation channels, satellite solutions are highly impacted by the atmosphere and the distance from the satellite. Satellite-to-earth links may suffer from low received power due to the distance, troposphere attenuation or depolarisation effects due to the Faraday rotation depending on the frequency of the link.

Over the past twenty years and thanks to their huge cover area associated to reduced operating costs, satellites systems have first democratised voice and message transmission and more recently multimedia broadcasting and satellite navigation systems. From multimedia broadcasting to navigation applications, there are several main differences. The first one is their respective goal, maximum throughput for multimedia broadcasting and maximum synchronisation for navigation systems. To do so, the actual trend for multimedia broadcasting systems is to increase frequency up to Ka and Q/V bands to have access to wider bandwidth while satellite navigation systems use wider spreading codes for a more accurate synchronisation. The second main difference is the space segment where multimedia broadcasting systems mainly use unique GEO *(Geostationary Earth Orbit)* satellites while navigation systems uses MEO *(Medium Earth Orbit)* satellite constellations. It results in a different satellite motion from fixed to polar orbiting satellites with elevation and azimuth changes resulting in Doppler shifts as a side effect. One last main difference between both applications is due to the receiver motion: fixed or mobile. Fixed multimedia broadcasting systems mainly use fixed stations where almost optimal propagation conditions are always achieved. However, for recent mobile broadcasting systems such as SDMB standard or for navigation purposes, the receiver is moving in complex environments where optimal propagation conditions are rarely fulfilled leading to shadowing, blockage, multipath fading, delayed echoes, Doppler spreading or depolarization issues.

For economic reasons, satellite system evolutions are rare and operating margins are more and more reduced. This implies a strict control of many parameters impacting the whole system. To accurately design and maintain such complex systems, specific tools are to be created and integrated into system simulation chains where EM wave propagation is one among many other parameters impacting system performances.

Thus, the present study aims at modelling the LMS *(Land Mobile Satellite)* propagation channel, keeping in mind a system approach for the final application: satellite navigation systems. This work addresses the specific problematic of MP *(Multi-Paths)* in urban environments for mobile receivers where propagation conditions are severely impaired.

The underlying stakes of the present study are to have a better a priori understanding of the propagation conditions of EM waves in urban environments to guarantee a coherent evolution for the next generation systems. As an example, this work could lead to design new robust receivers based on antenna arrays, to test new signal modulations for MP robustness or to adjust satellite availability. This work could also contribute to standardise integrity concepts and error envelopes for critical applications such as autonomous transportation or aviation. Finally, this work might be an alternative to expensive measurement campaigns.

Over the last decade, several solutions have been proposed to model the LMS propagation channel for mobile satellite communications and satellite navigation systems. Among all, some of them are of high interest for the present study.

Two main approaches in the literature are sustainable for LMS channel modelling. The first approach encompasses all deterministic tools. They are based on ray-tracing techniques and use more or less rigorous EM algorithms to reproduce interactions between wave fronts and synthetic environments. Particularly adapted to model the LMS propagation channel, deterministic approaches can deliver a wide range of outputs in site-specific conditions, e.g. power, phase, polarisation, delay, DoA or Doppler. However, such approaches have several drawbacks. First, they need a precise description of the synthetic environment e.g materials, geometry of the scene or details on buildings. Second, they are hard to implement since they use complex EM numerical methods resulting in accurate but time-consuming simulations.

The second approach encompasses all hybrid physical-statistical models. Hybrid approaches are a trade-off between computation time and solution accuracy. Since this trade-off is specific for each LMS application and depends on the final parameter studied, from the level crossing rate for communication systems to the pseudo range error for satellite navigation systems, a very wide range of hybrid approaches have been proposed. One of them has been introduced by Oestges [Oest 00] in 2000. Computationally efficient, this model presents the advantage of being based on EM numerical methods computing interactions on a simplified environment. Designed for LMS telecommunication systems, it suffers from unrealistic wide-band representation of the channel. More recent work has been proposed by Lehner [Lehn 07b] in 2007. Based on measurement campaigns, this wide-band model designed for navigation purposes shows the advantage of being standardised by ITU under Recommendation ITU-R P.681-7 [ITU 09]. However, this model presents several drawbacks: it is mainly empirical, does not integrate any EM numerical method, is irrelevant for environments very different from those where measurements were made, is not suitable for satellite diversity and is restricted to L-band.

At the end, hybrid physical-statistical approaches seem to be well adapted to model the LMS propagation channel since sufficiently accurate with reasonable computation time, which is of first interest for system simulations contrary to deterministic tools. However, existing models are either not adapted to satellite navigation and wide-band issues or incomplete in terms of EM modelling impacting their overall versatility.

Thus, this study is motivated by the need to understand and rigorously model the EM wave propagation phenomena for satellite navigation systems to achieve better channel accuracy without neglecting time efficiency. This study consists in elaborating an enhanced physical-statistical simulator of the land mobile satellite channel for multipath modelling applied to satellite navigation systems.

The approach that has been followed during this study can be divided into four parts.

Chapter 1 presents a critical review of the existing LMS channel models and details our proposed modelling approach. The first section reviews the main approaches that can be found in the literature to model the LMS propagation channel. Three approaches are detailed in the first subsections, namely statistical, deterministic and hybrid physical-statistical. A particular focus is made on hybrid physical-statistical approaches. The virtual city concept is also presented in the last subsection. The second section details the followed approach to design a new wide-band real-time LMS channel simulator SCHUN *(Simplified CHannel for Urban Navigation)*. The first subsection exposes the main objectives and constraints to be fulfilled by the simulator. From the critical review of the existing LMS models, a hybrid physical-statistical approach has been chosen and is presented in the second subsection. This subsection presents the positioning of the chosen approach with respect to existing models, the chosen macro architecture and the typical outputs of the proposed LMS channel simulator.

Chapter 2 is focused on the issue of how to model complex urban environments and how to simplify façade representation. The main interrogation here is on how small features present on complex façades interact with EM wave fronts and how to remove such small features to simplify the representation of complex urban environments. The first section details the experimental protocol that has been used, where small features present on façades have been studied using MoM *(Method of Moments)* techniques. The second section presents some preliminary observations on surface currents, radar cross sections or near field scattering patterns made on isolated canonical façades. The third section presents the results of the impact of small features on narrow-band time series completed in the fourth section by wide-band results on the influence of the small features on satellite navigation software receivers. Finally, in the fifth section, the 2.5D facade approximation is presented and recommendations are made on what level of simplification is achievable and acceptable when representing the environment for narrow-band and wide-band studies.

Chapter 3 is focused on the issue of how to simply the modelling of EM interactions on buildings and introduces a new physical simplified interaction model for urban building scattering, the *(Three Component Model)* or 3CM according to the 2.5D facade approximation. The 3CM is based on a simplified physical approach where the scattering pattern of any complex façade can be divided into the contribution of three different propagation mechanisms, namely the specular reflection, the backscattering and the incoherent scattering. The first section presents some observations, made on simulation results and experimental measurements, which have been made prior to the design of this urban building scattering model. The second section presents the chosen approach and details each of the three propagation mechanisms. The third section details some EM numerical validation of the 3CM model considering simple urban scenarios and canonical configurations using a commercial software tool based on asymptotic methods as a reference.

Chapter 4 presents the integration of the results obtain from the previous chapters into an enhanced physical-statistical simulator of the land mobile satellite channel for multipath modelling applied to satellite navigation systems: SCHUN. The first section is dedicated to the overall presentation of the implementation of the SCHUN simulator. The first subsection is a reminder of the main design choices that have been made, the capabilities and the basic scenario handled by the simulator. The second subsection details how virtual environments are synthesised and the

third subsection details the direct path blockage model retained to reproduce building blockage effects. The fourth subsection presents a new method to reduce the number of multipath. Second and third sections present some experimental validations of the SCHUN simulator based on two measurement campaigns. The experimental validation made in the second section is oriented toward MIMO satellite communication systems with polarisation diversity. For this validation, several system parameters have been analysed on synthesised narrow-band power time series such as, co and cross circular polarised channels, Doppler spectrum, fade distribution, Rice factor estimation, level crossing rate or fade duration. The other experiment presented in the third section is oriented toward an indirect wide-band validation, where the channel is observed and compared through its influence on a satellite navigation software receiver. Several internal parameters of the receiver are compared such as C/N0 and pseudo-range error to a satellite using measured channels and synthesised channels using the SCHUN simulator. Finally, a short discussion is made on the fourht section on SCHUN capabilities and actual limitations.

This document is ended by the conclusion.

Chapter 1

Critical review of existing LMS channel models and proposed approach

Contents

1.1 Three different approaches for modelling the Land Mobile Satellite channel 5
1.1.1 Statistical approaches 6
1.1.2 Deterministic approaches 15
1.1.3 Hybrid physical-statistical approaches 17
1.1.4 Details on the virtual city concept 27
1.2 Proposed approach for designing a new LMS channel simulator 29
1.2.1 Objectives and constraints of the model 29
1.2.2 Presentation of a new hybrid physical-statistical LMS channel simulator: SCHUN 31
1.3 Summary 34

The objectives of Chapter 1 are to give an overview of the existing scientific literature related to this PhD work, and to introduce the logical approach yielding to propose a new LMS channel simulator. The first section presents the three main approaches commonly used to model the LMS propagation channel, namely statistical, deterministic and hybrid physical-statistical. For each approach, the main models are described, followed by a short critical review of the approach. The last subsection introduces the virtual city concept and its current limitations. The second section presents the chosen approach. This section is divided into two subsections, the first one presents the objectives and the constraints that have to be fulfilled while the second subsection presents the overall positioning of this PhD work among existing models, the proposed macro-architecture of the simulator and the typical expected outputs.

1.1 Three different approaches for modelling the Land Mobile Satellite channel

Three types of modelling approaches are commonly found in the literature to model the LMS propagation channel, namely statistical, deterministic, and hybrid physical-statistical. The modelling approach chosen by the user will reflect a trade-off between computation time and accuracy of the expected solution. Intuitively, the introduction of statistics into the approach reduces time computation to the detriment of accuracy by operating simplifications. On the contrary, the introduction of determinism into the approach increases time computation for the benefit of the accuracy by using complex EM models.

Although different in their respective design, all channel modelling approaches can be grouped considering the modelling of two critical entities: the propagation environment and the EM

interactions on the environment. From the literature, all the models presented hereafter have been grouped in Tab.1.1 depending on the modelling of each two critical entities. Statistical approaches are based on statistical environments with very simplified, or absent, statistical interactions. Deterministic approaches are based on deterministic environments on which physical interactions are computed. Hybrid physical-statistical approaches are based either on statistical environments with physical interactions or on deterministic environments with statistical interactions.

In the following, a detailed presentation of each approach is made, where the most common models are briefly described. A critical review of each approach is presented at the end of each section.

		Interactions	
		Physical	**Statistical**
Environment	**Deterministic**	Full-wave methods Asymptotic methods	[Li 10]
	Statistical	[Oest 00] [King 07a] [Lehn 07b] [Abel 09]	Markov chains [Pere 01] [Carr 12]

Table 1.1: Classification of the different approaches

1.1.1 Statistical approaches

Statistical approaches can be divided in three classes. The narrow-band approaches, based on fade distributions, state-oriented models based on Markov chains, and wide-band approaches oriented toward multipath modelling. Particular models based on Markov chains oriented toward multipath modelling and MIMO LMS channel modelling, introduced by Perez-Fontan [Pere 01] and Carrie [Carr 12] respectively, are presented at the end of this section.

1.1.1.1 Narrow-band fades distribution models

Many types of fade distribution models have been proposed over the past years to describe the narrow-band EM propagation channel. As visible in Fig.1.1, the total received power can be divided according to three propagation mechanism scales. First, very large scale attenuation, namely path loss, is due to the influence of travelled distance of EM waves from the transmitter. Second, large scale attenuation, namely shadowing, is due to blocking propagation conditions mainly encountered when objects intersect the LOS *(Line Of Sight)* . Third, small scale attenuation, namely fast fading, is due to constructive and destructive wave front recombination from multipath, depending on the environment of the receiver.

The narrow-band models presented hereafter are based on fade distribution models which are merging two propagation scales, namely shadowing and fast fading, path loss being easily modelled apart. Such merging principle makes those models macroscopic with a low versatility in terms of environment diversity. As an example, in Fig.1.2, the pdf *(Probability Density Function)* of the total receiver power of the measured signal is the combination of two distinct statistical laws, one for the LOS condition, the other one for the NLOS *(Non Line Of Sight)* condition.

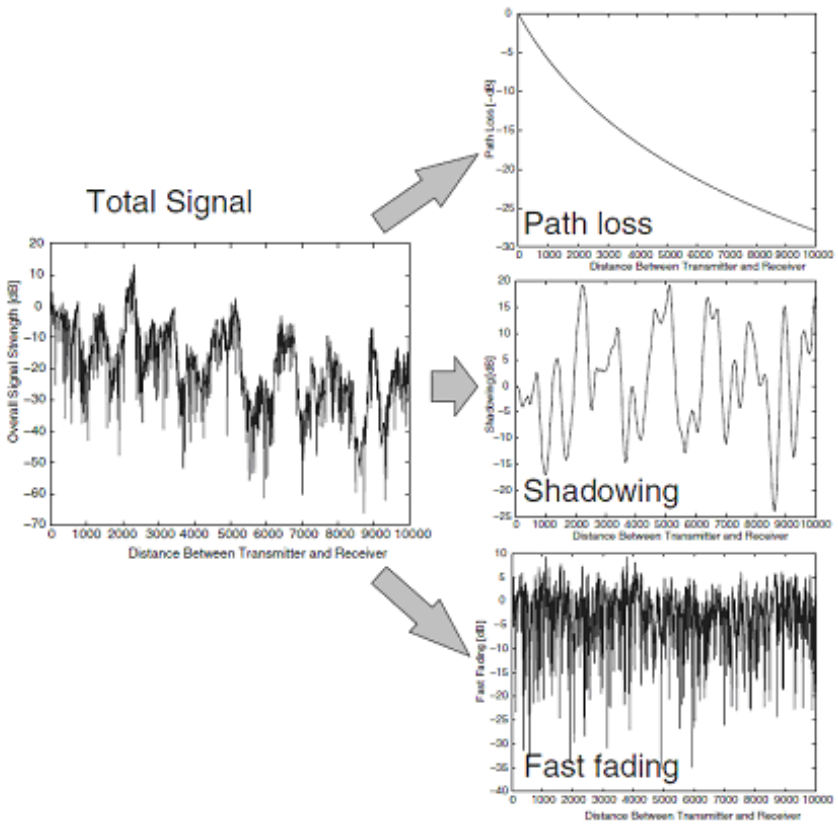

Figure 1.1: Description of the three scale propagation mechanisms [Saun 07]

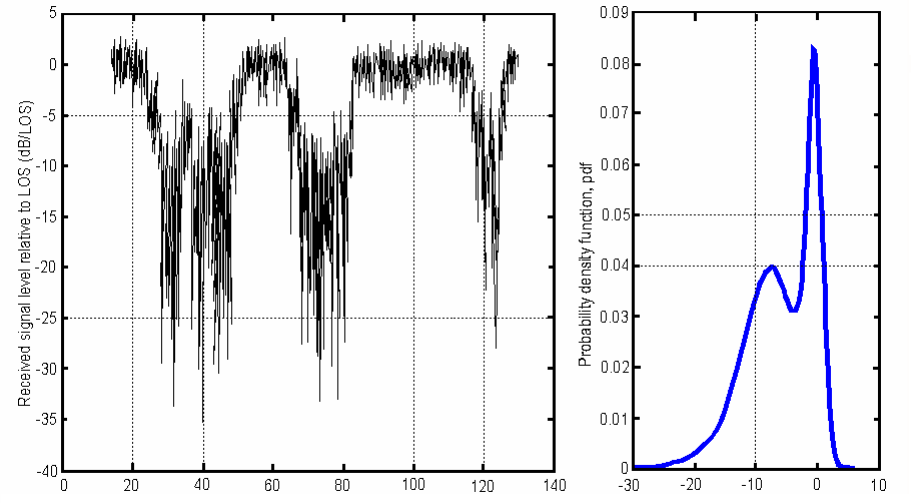

Figure 1.2: pdf of fading depth from real measured signal [Satn 08]

Because of this merging principle, narrow-band fade distribution models give rise to unrealistic fade durations or unpredictable local influence of the real environment on the system. Even more, since they are narrow-band oriented, the time spreading information, linked to multipath representation, does not exist. Due to those limitations, fade distribution models are usually used to predict system operating margin which consists in the prediction of the averaged fade depth using Eq.1.1 from [Pere 01]:

$$f_{overall}(r) = p_{LOS}\, F_{LOS}(r) + p_{NLOS}\, F_{NLOS}(r) \tag{1.1}$$

where p_{LOS} and p_{NLOS} represents respectively the probability of being in LOS or NLOS conditions and F_X the probability density function associated to the X condition. In general, F_{LOS} is

assimilated to a Rice distribution while F_{NLOS} is assimilated to a Rayleigh distribution. In the following, the main fade distribution models encountered in the literature are detailed.

1.1.1.1.1 Rayleigh

The Rayleigh model lies on the assumption that numerous incoherent components are summed at the receiver with statistically independent delays and complex amplitudes. This model is usually used when the direct signal is blocked in rich scattering environments such as urban centres or indoor environments. The Rayleigh law can be mathematically described as the norm of a complex number where real and imaginary parts are two Gaussian variables of mean 0 and standard deviation σ as presented in Eq.1.2 where r describes a Rayleigh random variable. The associated pdf and cdf are respectively given by Eq.1.3 and Eq.1.4.

$$r = |\alpha| = \sqrt{x^2 + y^2} \tag{1.2}$$

$$f(r) = \frac{r}{\sigma^2} e^{-r^2/2\sigma^2} \tag{1.3}$$

$$F(r) = \int_0^r f(u)\,du = 1 - e^{-r^2/2\sigma^2}\ ,\ r \geq 0 \tag{1.4}$$

1.1.1.1.2 Rice

Contrary to the Rayleigh distribution, the Rice distribution is representative of one main and constant component, e.g. LOS, plus incoherent smaller contributions randomly distributed following a Rayleigh process, e.g. multipath. This model is usually used in rich scattering semi-opened environments where the LOS is present.

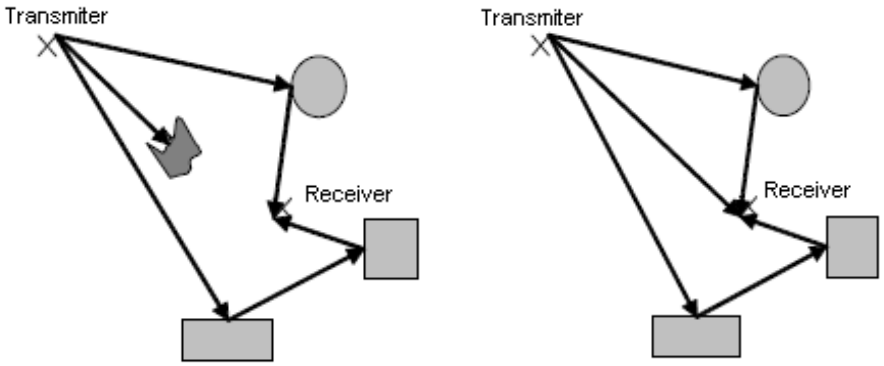

(a) Rayleigh configuration (b) Rice configuration

Figure 1.3: Typical Rayleigh and Rice configuration examples

A Rice distribution is usually parameterised by its parameter K, also called the Rice factor, representing the power ratio between LOS and multipath. Null K represents NLOS configurations. In this particular case, the Rice distribution is equal to the Rayleigh distribution. Infinite K represents the absence of multipath where only the LOS component reaches the receiver. Note that in practice, the K factor is hardly extractable from measurement campaigns although several estimating methods have been developed [Tepe 03]. The Rice pdf is given by Eq.1.5 where σ represents the Rayleigh parameter representative of MP power and I_0 the modified Bessel function of the first kind with order zero.

$$f(r) = \frac{2(K+1)r}{\sigma^2} e^{\left(-K - \frac{(K+1)r^2}{\sigma^2}\right)} I_0\left(2r\sqrt{\frac{K(K+1)}{\sigma^2}}\right) \tag{1.5}$$

1.1.1.1.3 Loo

The Loo distribution is a general statistical law having as particular cases Gauss, Rayleigh and Rice. This property gives to the Loo distribution a wide range of possible masking conditions

for a high versatility in the modelling. Contrary to Rayleigh and Rice distributions, the Loo distribution makes the difference between coherent (LOS) and incoherent (MP) components of the total signal. The coherent component is represented by a log-normal distribution of mean α and standard deviation Ψ both expressed in dB. The incoherent component follows a Rayleigh distribution parameterised by the multipath power σ expressed in dB relatively to the coherent component. Note that a correlation is observed between coherent and incoherent components due to the formulation of the Loo distribution as presented in Eq.1.6 from [Pere 01].

$$f(r) = \frac{r}{b_0\sqrt{2\pi d_0}} \int_0^\infty \frac{1}{z}\, exp\left(-\frac{(ln\, z-\mu)^2}{2d_0} - \frac{r^2+z^2}{2b_0}\right) I_0\left(\frac{rz}{b_0}\right) dz \tag{1.6}$$

$$\alpha = 20\, log_{10}(e^u) \tag{1.7}$$

$$\Psi = 20\, log_{10}\left(e^{\sqrt{d_0}}\right) \tag{1.8}$$

$$\sigma = 10\, log_{10}(2b_0) \tag{1.9}$$

1.1.1.1.4 Nakagami

The Nakagami distribution is based on Γ distributions to reproduce the fading considering two parameters: m, a shape parameter and Ω a spreading parameter. The Nakagami distribution has been used in the next presented study of [Li 10]. Its pdf is given by Eq.1.10 in [Saun 07]:

$$f(r) = \frac{2}{\Gamma(m)} \frac{m}{\Omega}\, r^{2m-1} e^{-m^2/\Omega} \tag{1.10}$$

1.1.1.1.5 Corazza

The Corazza distribution can be seen as a Loo distribution where coherent and incoherent components are modelled using log-normal distributions.

Model	Coherent comp.	Correlation (Coh./Incoh.)	Incoherent comp.
Rice	Constant	zero	Rayleigh
Loo	Log-normal	Variable	Rayleigh
Corazza	Log-normal	Unity	Log-Normal/Rayleigh

Table 1.2: Comparison between Rice, Loo and Corazza distributions [Saun 07]

1.1.1.1.6 Log-normal

Although not used to represent fading, the log-normal distribution is commonly used to describe virtual cities, e.g. buildings height or street width. The log-normal distribution can be seen as a normal distribution on logarithm scale. Pdf and cdf of the log-normal distribution are respectively presented in Eq.1.11 and Eq.1.12.

$$f(r,\mu,\sigma) = \frac{e^{-(ln\, r-\mu)^2/(2\sigma^2)}}{r\sigma\sqrt{2\pi}} \tag{1.11}$$

$$F(r) = \frac{1}{2} + \frac{1}{2} erf\left(\frac{ln(r)-\mu}{\sigma\sqrt{2}}\right) \tag{1.12}$$

1.1.1.2 Narrow-band state-oriented models

As shown in Fig.1.2, using one single fade distribution model is hardly acceptable if the masking condition of the direct signal is highly variable. The goal of state-oriented narrow-band models is to dissociate shadowing from multipath fading contrary to narrow-band fade distribution models. Thus, a state machine reproduces the shadowing conditions (random sequence of discrete states linked to some kind of virtual environment) while parameterised fade distributions reproduce the fast fading fluctuations associated to each discrete shadowing state.

State-oriented models are mainly based on Markov chains to reproduce the state alternation. Markov chains present the advantage of being a stochastic process which formulation allows predicting future states by knowing present and past states. Those chains can have more or less high orders and more or less discrete states. The order of the Markov chain corresponds to the memory of the system. For a first order system, the future state depends only of the present state while for second order, the future state depends of the present state and last past state. The number of states of the Markov chain corresponds to the number of possible discrete solutions of the system. For LMS channel modelling, the number of state corresponds to the number of possible shadowing conditions. In practice, 2 or 3 states Markov chains are commonly used.

One other advantage of Markov chains is to be fully characterised by two matrices: P and W. The matrix P is the transition probability matrix. This N by N matrix, where N represent the number of discrete states, represents the probability to switch from a state i to a state j. The matrix W is the absolute probability matrix. This 1 by N matrix represents the absolute probability of being at one particular state. Note that in the case of stationary process [Pere 05]: $W.P = W$.

In the following, a conventional two states first order Markov chain is presented as an illustrating example for LMS applications. This simple narrow-band state-oriented model is presented in Fig.1.4. The two states correspond either to LOS conditions (ON state) or NLOS conditions (OFF state). The Markov chain has to be tuned depending on the scenario, e.g. type of environment, elevation and azimuth of the satellite, which is usually derived from measurement campaigns to extract P and W matrices. Several extraction methods have been proposed in [Abel 09] and [Huss 02]. After having generated the random ON/OFF sequence, the fading fluctuations are added. Depending of the shadowing state, two typical fade distributions are used; Rice distribution for LOS states and Rayleigh distribution for NLOS states. The parameter L_{Frame} presented in Fig.1.4 represents the distance at which transitions may occur. Typical values are in the order of 3 m to 5 m. This parameter also has to be extracted from measurement campaigns and depends on the scenario. New developments have introduced the concept of pseudo-Markov chains where the L_{Frame} parameter is replaced by a randomly generated length of each state for more versatility.

Several variants of the first order Markov chain can be found in the literature. A first one was introduced by Perez-Fontan in [Pere 97]. It is based on three states first order Markov chains. Contrary to two states, LOS and NLOS conditions, using three states allow in principle a more realistic simulated time-series generation with better dynamics. The third state is representative of slight shadowing conditions mainly caused by vegetation. Another model has been introduced by Lutz in [Lutz 96] where the goal is to correlate two states first order Markov chains to reproduce realistic satellite diversity scenarios. More recently, time varying order Markov chains have been introduced in [Milo 09] to make the state duration L_{Frame} vary. One last approach was presented in [Pere 01] where Markov chains, fade distributions and wide-band WSSUS assumption are combined. This model is presented at the end of this section relative to statistical approaches.

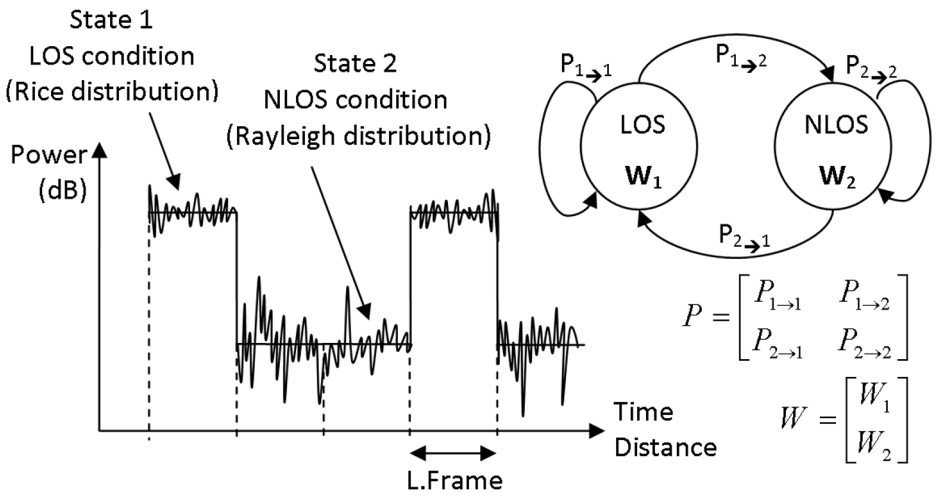

Figure 1.4: Example of a two states first order Markov chain

1.1.1.3 Wide-band models

Several wide-band models based on statistical approaches have been introduced in the literature. Only two of them are presented in the following. A summary of some others can be found in [Satn 08] and [COST 02].

For wide-band channel modelling, a common approach is to use the Wide-Sense Statonarity for Uncorrelated Scatterers *(WSSUS)* assumption detailed in [Bell 63]. This approach was used in many models and in particular in the COST207 project [Fail 89] for terrestrial applications such as GSM. The WSSUS relies on two main assumptions:

- Invariance of the channel autocorrelation function across time. This assumption remains true only if Doppler frequencies of the echoes are uncorrelated [Bell 63].
- Position and delay of the scatterers are uncorrelated

Due to both assumptions, the WSSUS have a limited validity domain and LMS channel modelling does not necessarily fulfil stationarity and invariance conditions. Furthermore, measurements have confirmed that scatterers may not be uniformly distributed in the azimuthal plane.

The first wide-band statistical model presented here has been introduced by Saleh and Valenzuela in [Sale 87]. This model has been designed for indoor wide-band propagation using a discrete process. It is based on wide-band channel measurement campaigns at 1.5GHz with 10ns delay resolution. From the measurements, it has been observed that multipaths are clustered, depending on the building configuration (walls, halls, corridors). Saleh Vanlenzuela model reproduces this observation as presented in Fig.1.5.
The principle is to model the delay of each cluster by using a Poisson distribution with a fixed rate Λ depending of the indoor environment. In each cluster, the delayed multipaths are also following a Poisson process with parameter λ. Note that one cluster contains many multipaths, $\lambda \gg \Lambda$. The received multipath amplitudes are independent Rayleigh random variables with variances exponentially decaying with cluster delays as well as with multipath delays within a cluster.

A second model has been introduced by Jahn in [Jahn 96] addressing the outdoor LMS channel. Similarly to Saleh Valenzuela model, it is based on measurements made by DLR in 1994 and also lies on the WSSUS assumption. The channel is represented by a tapped-delay line divided into three sections: LOS, near echoes, far echoes as presented in Fig.1.6. The LOS power follows a Rice or Rayleigh distribution depending respectively if LOS or NLOS conditions are achieved. For close echoes, their number follows a Poisson distribution, their delays

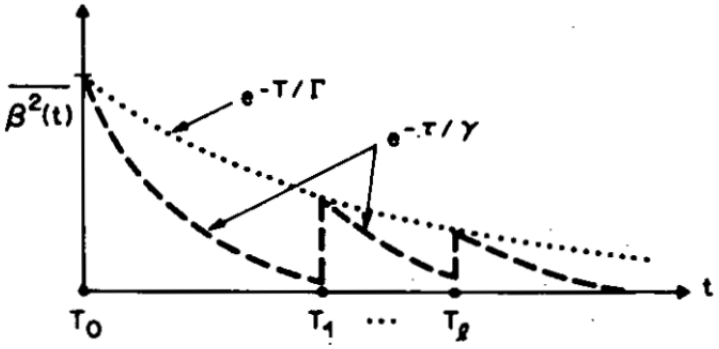

Figure 1.5: Cluster approach used in Saleh Valenzuela modelling [Sale 87]

an exponential distribution and their amplitudes an exponential decreasing distribution. For far echoes, their number follows a Poisson distribution, their delays a uniform distribution and their amplitudes a Rayleigh distribution. The Doppler spectrum is a Jakes spectrum [Jake 94] supposing a uniform repartition of the angle of arrival of the multipath.

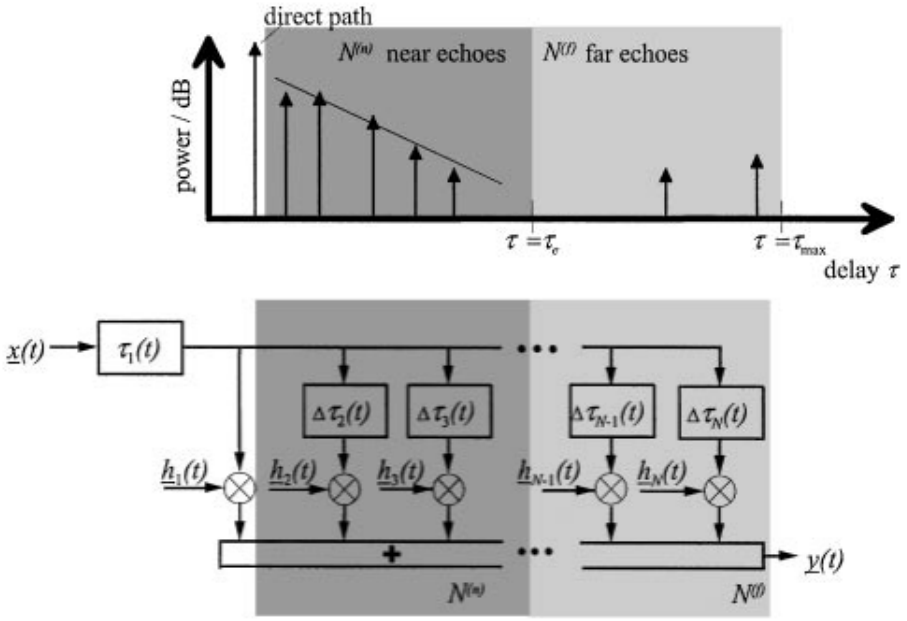

Figure 1.6: Tapped-delay line approach used in Jahn model [Jahn 01]

1.1.1.4 Perez-Fontan, University of Vigo, 2001 [Pere 01]

This model has been introduced by Perez-Fontan in [Pere 01] and reuses Jahn's approach [Jahn 01]. This model has been designed for wide-band LMS issues using a statistical approach. The approach is to model separately the LOS from the multipath as presented in Fig.1.7. The reader is advised that only the wide-band approach described in [Pere 01] is here treated.
The LOS component is modelled according to a three states first order Markov chain representing LOS, moderate shadowing and NLOS propagation conditions. The Markov chain is tuned following measurement campaigns where P and W matrices were extracted. They are described as related to the environment, e.g. urban, suburban, wooded, and detailed in [Pere 01]. Note that P and W matrices have also a particular dependency on the elevation of the satellite since low and high elevation configurations show significant differences in terms of LOS/NLOS state probability. A log-normal random process is applied next to the Markov chain to reproduce the slow LOS fluctuations within each state. In practice, those fluctuations are due to non uniform antenna patterns or changing orientation of the mobile. The model also includes a generator of

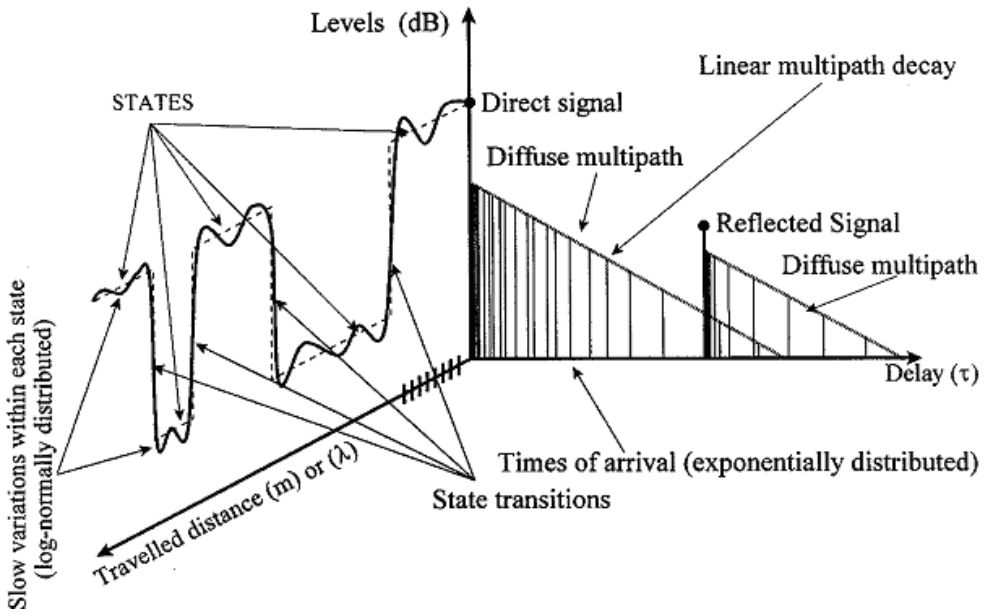

Figure 1.7: Example of wide-band statistical model based on Markov chains [Pere 01]

correlated Markov chains for satellite diversity purposes as in [Lutz 96].

The multipaths are modelled according to a cluster approach where each main contribution, LOS and major reflected rays, are followed by a cluster of smaller multipaths as presented in Fig.1.7. Since the time dispersion of the LMS channel is much smaller than the one of the terrestrial cellular channel, the case of reflected signals is not treated and only LOS cluster is assumed. The multipath delays are randomly generated following an exponential distribution as in Jahn model [Jahn 01]. The number of multipaths follows a Poisson distribution. However, for the sake of simplicity, the number of multipaths is fixed to 50. The multipaths amplitude follows a linear power decay expressed in $dB/\mu s$. The total multipath power follows a Loo distribution, tuned for each Markov state and each propagation scenario (urban, rural ...). Due to this random process a normalisation step has to be performed to tune the power of each individual multipath to fit the total multipath power.

1.1.1.5 Carrie, ONERA, 2012 [Carr 12]

Very recent work in the field of statistical modelling has been introduced by Carrie in [Carr 12] addressing the issue of MIMO LMS fading channels and completes King's approach [King 07a] presented hereafter with hybrid physical-statistical approaches. The starting point of this model is to use a two states first order pseudo-Markov chain for generating one SISO *(Simple Input Simple Output)* LMS channel where the dynamic of both large scale and small scale parameters have been studied. The large scale parameter refers to the commonly used L_{corr} parameter representing the slow variations within each state while the small scale parameter is related to the Doppler spectrum and multipath recombination. In a second step, the SISO LMS channel approach is extended to MIMO (Multiple Input Multiple Output) dual polarised channels using MIMO correlation matrix where the main assumption is that all MIMO channels are in the same state. Note that the specificity of this model is that each scale effect is pounded by a different correlation matrix, $\mathbf{R_{SH}}$ and $\mathbf{R_{MP}}$ describing the cross-correlation of shadowing and multipath effects respectively. The block diagram of the model is presented in Fig.1.8 where $G(0,1)$ is a Gaussian process with zero mean and unit variance, $C(.)$ denotes the Cholesky factorisation, $H(.)$ is a low pass filter, A_i the shadowing time-series, a_i the slow variations, ν_i the fast variations and finally h_i the channel complex envelope.

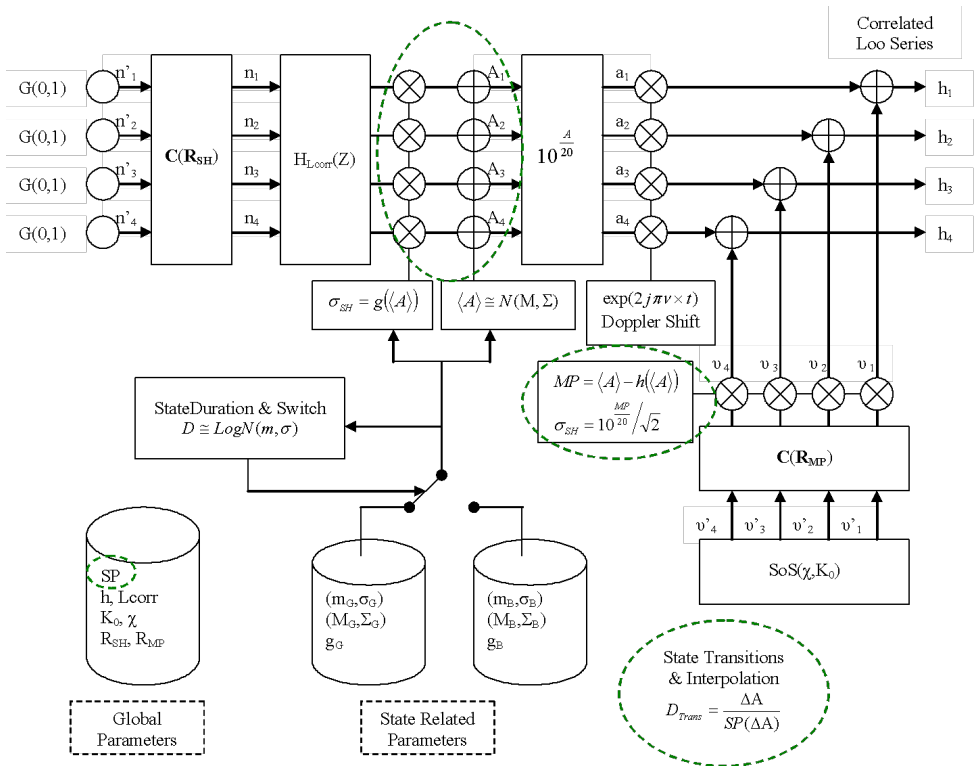

Figure 1.8: Block diagram of the MIMO channel model introduced by Carrie [Carr 12]

The last part of this work addresses the satellite diversity MIMO channel, encompassing both polarisation diversity and spatial diversity. The main difference with the single satellite MIMO channels is that in the case of satellite diversity, the various channels can be in a different state. This results in different correlation lengths which distort the correlation between channels. However, this distortion can be quantified and compensated by pre-processing the MIMO correlation matrices $\mathbf{R_{SH}}$ and $\mathbf{R_{MP}}$.

Critical review of statistical approaches :

In this subsection, three types of statistical approaches are presented, narrow-band fade distributions, narrow-band state-oriented and wide-band state-oriented models. Narrow-band fade distribution models are able to represent the total narrow-band attenuation combining medium scale, i.e. shadowing or blockage, and small scale, i.e. fading events. They present the advantage of being simple and efficient in terms of computation time. However, those models are extremely dependent on the environment, due to measurement based tuning requirements. The use of such models only allows system operating margin design for satellite communication systems and shows critical limitations in the case of high signal dynamics from LOS to blocked direct path. A more accurate approach is definitely required. Thus, narrow-band fade distributions are out of focus and discarded from the present critical review.

An alternative to narrow-band fade distribution models is to combine them with Markov chains to build state-oriented statistical models for more signal dynamic versatility. The principle is to associate a narrow-band fade distribution to each discrete state. This technique allows generating more realistic time-series with reduced time computation. The complexity of such models is still reasonable and the memory allocated to the required inputs is reduced (W and P matrices). The main drawback of such method is their dependence on measurement campaigns to tune the state machine and the narrow-band fade distributions. This tuning is mainly dependent on the type of environment and on the elevation/azimuth configuration of the source.

Those two types of modelling approaches are oriented toward narrow-band issues, which is a significant shortcoming. However, more advanced models have been introduced since with a wide-band extension as proposed in [Pere 01] based on the WSSUS assumption or MIMO LMS channels correlation as proposed in [Carr 12]. Still, although synthesising correlated time-series, those models suffer either from satellite diversity limitations or unrealistic multipath synthesis since no environment is generated.

As a conclusion, the main limitation of statistical models is that their internal parameters have to be tuned by extensive measurement campaigns.

1.1.2 Deterministic approaches

By opposition to statistical approaches which reproduce the global channel behaviour, deterministic approaches aim at reproducing real scenarios with physical EM models representing the interactions between the impinging waves and the local environment. With the major improvements made by computing tools during the last decade, deterministic approaches have considerably gained in feasibility. From simple and canonical objects treated few years ago, real complex and highly detailed objects and environments are now being considered with even better accuracy. In this subsection, two families of deterministic approaches are presented, exact methods, also called full-wave methods, and asymptotic methods. For both of them, the associated numerical methods are summarised in Tab.1.3 and briefly described in Appendix B. More details on the deterministic software tools used during this thesis can be found in Appendix B.3.

The common factors for all deterministic approaches are on one hand the realism of the environment description used as input for the computation and on the other hand the use of Maxwell equations to solve the EM interaction problem. Depending on assumptions and simplifications, the EM initial problem will conduct to different solving formulations, as summarised in Tab.1.3. Full-wave methods are less restrictive in terms of assumptions but unsuited for large areas. On the opposite side, asymptotic methods are to be used under specific assumptions but allow taking into account very wide environments. Note that both families require long computation time.

Full-wave	Integral Equations in Frequency Domain (IEFD, MoM) Finite Element in Frequency Domain (FEFM) Finite Difference in Time Domain (FDTD)	
Asymptotic	**ray-based**	**current-based**
	Geometrical Optics (GO, SBR, RT) Uniform Theory of Diffraction (UTD)	Physical Optics (PO) Physical Theory of Diffraction (PTD)

Table 1.3: Summary of the different numerical methods associated to the deterministic approaches

1.1.2.1 Full-wave methods

They are directly based on Maxwell equation solutions. Being assumption free in their formulation and due to numerical convergence criterion, those methods are called exact. Note that this convergence criterion is directly linked to the meshing constraints applied to the object (typical values are between $\lambda/5$ and $\lambda/10$), where the number of unknowns is proportional to the meshing, being the main limitation of such methods. They are grouped into several classes depending on Maxwell's equations formulation. The most popular ones are commented below.

Integral Equation in Frequency Domain (IEFD): This first class of methods is based on the radiation of the currents induced on objects by an incident wave. Those methods are also known as MoM *(Method of Moments)*. The modelling can be established on surfaces or on volumes and needs boundary conditions on the objects. Major improvements on computation time to overcome the matrix inversion issue have been introduced in [Rokh 90] with FMM *(Fast Multipole Method)* techniques.

Finite Element in Frequency Domain (FEFD): This second class is based on a differential formulation of Maxwell's equations. Those methods are mainly used to solve harmonic problems. They are particularly suitable for heterogeneous objects meshed with tetrahedral cells.

Finite Difference in Time Domain (FDTD): This last popular method is based on time domain formulation of Maxwell equations and exhibits wide-band capabilities for single incidence.

Because of the need of large computation resources (memory and CPU) all full-wave techniques described above are time consuming and limited in terms of problem size to a few tens of wavelengths. Very powerful, those methods are mainly used for antenna design or RCS *(Radar Cross Section)* computation on small objects. To improve time performance and to address larger problems, asymptotic methods are used.

1.1.2.2 Asymptotic methods

Contrary to exact methods, asymptotic methods do not rigorously solve the EM problem. They are divided into two classes and are only valid for objects large compared to the wavelength. This assumption comes from the fact that surface currents are supposed to be uniform over the surface of the object.

The first class of asymptotic methods is based on the optical-ray assumption which includes GO *(Geometrical Optics)* and UTD *(Uniform Theory of Diffraction)*. Considering infinite sized elements, the EM field propagates along ray path satisfying Fermat's principle. The EM problem is then solved using geometric formulations such as for example Snell-Descartes laws. Two ray-optical algorithms, different in their approach, are competing in the literature: the SBR algorithm *(Shooting and Bouncing Rays)* and the RT algorithm *(ray-tracing)*. The SBR philosophy is to launch rays in every direction from the transmitter to reach the receiver as presented in Appendix B.2.1. By opposition, RT builds a path from the transmitter to the receiver using

geometrical image theory. Both ray algorithms are presented in Appendix B.2.1.

A second class of asymptotic methods is based on the equivalent current method and regroups PO (Physical Optics) and PTD *(Physical Theory of Diffraction)*. Contrary to exact methods, instead of solving rigorously the EM problem, only first harmonic terms of currents are here considered using an integral formulation of Maxwell's equations. With PO based algorithms, the main limitation is that the current assumption aforementioned is valid only for objects larger than 3λ [Diaz 96]. Asymptotic current-based methods give rise to reduced computation complexity. Nevertheless, re-radiating equations and current integral calculations remain expensive in terms of time.

Critical review of deterministic approaches :

Two types of deterministic approaches are presented, full-wave methods and asymptotic methods. Even if assumption free, full-wave methods are restricted to few wavelength size problems which makes them unsuitable at street or city scale for high frequencies. Thus, they are discarded from this critical review.

At the present time, asymptotic methods remain the best solution considering the overall accuracy of the results and the number of possible outputs for parametric studies. DoA, power, delay or Doppler information are easily accessible using both, ray-based and current-based asymptotic methods. Close to the reality, asymptotic methods still suffer from a lack of environment modelling accuracy. For precise results, the environment has to be accurately represented in terms of geometry (usually complex) and materials (many types of materials). This modelling step becomes rapidly restricted to small environments (smaller than street scale). Note also that the simulations are oriented toward site specific scenarios, meaning that for each scene context, a new environment has to be produced. In terms of EM computation time, asymptotic methods are still prohibitive, even if ray-based methods are slightly faster compared to current-based methods. Nevertheless, asymptotic ray-based methods, such as GO, are not sufficiently accurate to reproduce the numerous contributions of the channel in urban environments and previous measurements [Arta 08] have shown that simulated GNSS receivers frequently lose track of the satellites consequently. PO based methods are more adapted for this issue but also more demanding in terms of computation time.

Regarding asymptotic methods, it has been shown that they are well suited for the LMS channel modelling issue but they remain time consuming. Nevertheless, asymptotic current-based methods (PO+ECM) are a good comparison point, for street scale environments, and those methods will be used in this document as reference methods through the use of the SE-WorkBench software suite presented in Appendix B.3.

1.1.3 Hybrid physical-statistical approaches

1.1.3.1 Oestges, UCL, 2000 [Oest 00]

A first presented hybrid physical-statistical approach has been introduced by Oestges [Oest 00] in 2000. This work entitled *Propagation Modelling of Low Earth-Orbit Satellite Personal Communication Systems*, tries to model the LMS propagation channel for low earth-orbit telecommunication systems from L to Ku bands with a particular focus on system performances. In this work, the influence of the EM propagation channel on system performances has been divided into two components. The first component can be described as a very large scale path attenuation taking into consideration on the one hand the ionospheric effects such as scintillation, and, on the other hand, tropospheric effects such as attenuations due to gases and rain falls, or absorption and scattering due to particles. The second component is more related to our concerns and deals with propagation in built-up areas for medium and small scale attenuation.

The proposed hybrid model for propagation in built-up areas is based on a deterministic approach to reproduce EM wave interactions with the environment. Interactions are computed using a ray-based algorithm (RT) coupled to a GO processing for reflections and UTD *(Uniform Theory of Diffraction)* and ECM *(Equivalent Current Method)* for diffractions. The proposed model handles also multiple interactions. The statistical part of this model comes from the use of the virtual city concept, detailed in Section 1.1.4. The main idea is to generate some virtual environment based on statistical distributions of building size or street width.

For narrow-band channel characterisation, the Oestges's hybrid model proposes to generate a random Rice time-series tuned by two parameters, c and σ^2, as presented in Eq.1.13, where both parameters are extracted from deterministic ray-based simulations.

$$T_{R_b}(r) = \frac{r}{\sigma^2}\, exp\left[-\frac{r^2+c^2}{2\sigma^2}\right] I_0\left[\frac{rc}{\sigma^2}\right] \tag{1.13}$$

where $T_{R_b}(r)$ represents the Rice probability density function of the received amplitude in built up areas, r the received amplitude and I_0 the modified Bessel function of the first kind with zero order. Parameter c represents the coherent component of the received field. For LOS conditions, c equals the amplitude of the LOS ray. For NLOS conditions, pseudo-LOS is assumed and the coherent component c equals the amplitude of the diffracted ray coming from the top edge of the masking building. c parameter is slow varying across time. Parameter σ^2 represents the incoherent component of the received field or total MP power. In order to estimate σ^2, all MP contributions, due to reflection and diffraction, are power added except the pseudo-LOS ray for NLOS cases. This parameter is also slow varying across time. However, since σ^2 represents the variance of the Rice process, σ^2 is responsible for the fast fading fluctuation. Note that c and σ^2 are tightly related to the environment.

A parallel can be made here with Markov chains presented in section 1.1.1.2. The first difference is that the Markov process generating the On/Off states is replaced by a real ray-based algorithm. The second difference is that the Rice fade distribution is directly tuned using physically simulated variables, c and σ^2, instead of measurement fitting. Contrary to Markov approaches, the Oestges hybrid model is related to the virtual scene with EM interactions between wave fronts and the environment making it more suitable for satellite diversity without using empirical correlation.

Being ray-based, this hybrid model is also inherently suitable for wide-band characterisation of the propagation channel. As implemented, the model takes into account second order GO reflections and single UTD diffractions. The equivalent base-band impulse response is presented in Eq.1.14 where M represents the total number of ray-contributions, α_m the complex amplitude of each ray-contribution, τ_m the delay, $\Delta\omega_m$ the Doppler shift and ω_0 the carrier frequency. For system behaviour simulations, the computation of $H(\Omega, t)$ is only needed over a limited bandwidth. The infinite-band equation presented in Eq.1.15 is then filtered by transmission and reception filters using for example square-root raised cosine filters.

$$h(\tau, t) = \sum_{m}^{M} \alpha_m(t)\, \delta\left[\tau - \tau_m(t)\right]\, exp\left[-\jmath\omega_0\tau_m(t) + \jmath\Delta\omega_m t\right] \tag{1.14}$$

$$H(\Omega, t) = \mathcal{F}\left\{h(\tau, t)\right\} \tag{1.15}$$

A common wide-band parameter describing the delay spread of the impulse response has been investigated, namely the RMS delay spread. It has been noticed that the RMS delay spread is sensitive to the number of paths and consequently to the size of the considered scene and the number of buildings.

Eventually, Oestges hybrid model is suitable for narrow-band and wide-band simulations taking into account various environments from built-up areas to rural areas. Interactions with buildings

and vegetation are modelled using ray-based algorithms. However, terrain effects are neglected since the model is restricted to a limited number of rays and a limited number of interactions. This model has been validated against measurements on various channel parameters such as fade statistics and bit error probability.

1.1.3.2 King, University of Surrey, 2007 [King 07a]

The models proposed by King in [King 07a] are addressing the specific problematic of LMS-MIMO channels. The issue is mainly focused on the correlation between MIMO channels for telecommunications in vehicular context. The main parameter for evaluating the MIMO performance is the channel capacity which is investigated considering two parameters: the space diversity at both transmitter and receiver sides and the polarisation diversity. From this study, three models have been proposed adapted either to narrow-band or wide-band concerns. All of them have been validated with MIMO measurement campaigns realised in 2005 in Guilford neighbourhood, UK [King 07b]. These validations have been made considering both first order statistics, e.g. fading distribution, and second order, e.g. level crossing rate or fade duration.

The first physical-statistical model presented in [King 05] is similar to the one introduced by Molisch [Moli 04] for MIMO terrestrial issues. The goal is to model the environment by using cluster of scatterers around the receiver on which simple space algebra is used. In King's approach, the principle is to link those clusters to a statistically accurate virtual city on which simplified ray techniques are used. The main effects taken into account are blockage, shadowing, rooftop diffractions and multipath reflections in the vicinity of the receiver. This approach is well adapted to predict large scale On/Off nature of the LMS channel as well as small scale effects. Even more, this approach contains intrinsically satellite diversity information.

The second narrow-band statistical model mainly relies on a Markov stochastic process similar to the ones presented previously. The main difference is that the Markov state machine and large scale fading are correlated on a measurement basis to ensure coherent MIMO channel synthesis. Both components are then added prior to the fast fading. The fast fading synthesis is based on Rice distributions tuned by the large scale fading and also correlated for each MIMO channel. Note that extracted correlation matrices are dependent on the type of MIMO channel (space diversity, polarisation diversity) and on the type of environment. Fig.1.9 represents one validation example on second order statistics for the tree-lined road case in polarisation diversity conditions.
The third wide-band statistical model consists in correlating the delay domain over the MIMO domain in addition to the Markov chain, the large scale fading and the Rice fast fading. The global principle is presented in Fig.1.10.

1.1.3.3 Lehner, DLR, 2007 [Lehn 07b]

The model has been introduced by Lehner and the DLR team [Lehn 07b] in 2007. This model is called LMMC model for Land Mobile Multipath Channel model. This hybrid model is also referenced by ITU under recommendation ITU-R P.681-7 [ITU 09]. The originality of this model is its measurement campaign basis. The hybrid denomination comes from the use of real experiments coupled to some statistics to extend measurement campaign results to similar scenarios. This model is based on the virtual city concept with statistically distributed scatterers into the environment coupled with EM model for representing the LOS component. Note that this hybrid model has been specifically designed for satellite navigation purposes for vehicular and pedestrian applications.

The measurement campaign has been performed in 2002 in Munich vicinity. Four different types of environments have been investigated, namely urban, suburban, rural and highway, for vehicular and pedestrian applications. Urban environments are commonly characterised by dense

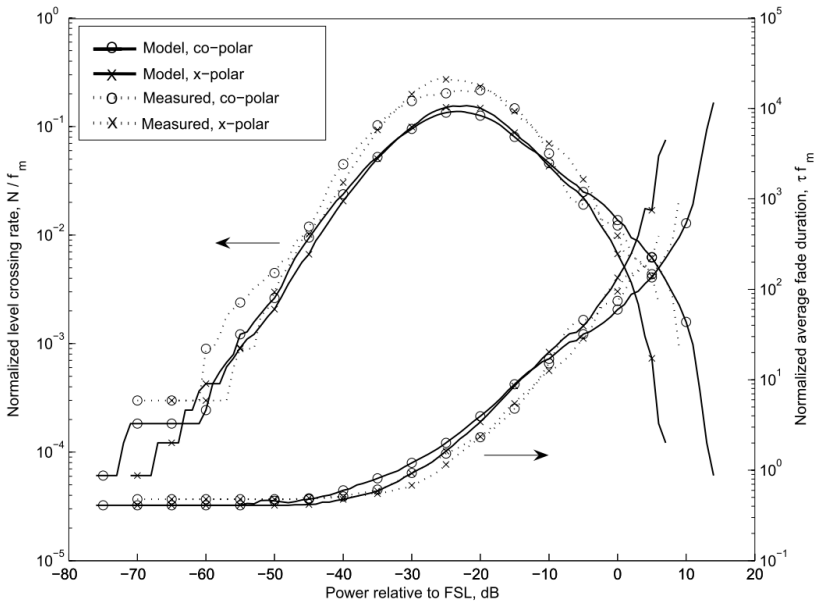

Figure 1.9: Validation example of the narrow-band model on second order statistics [King 07a]

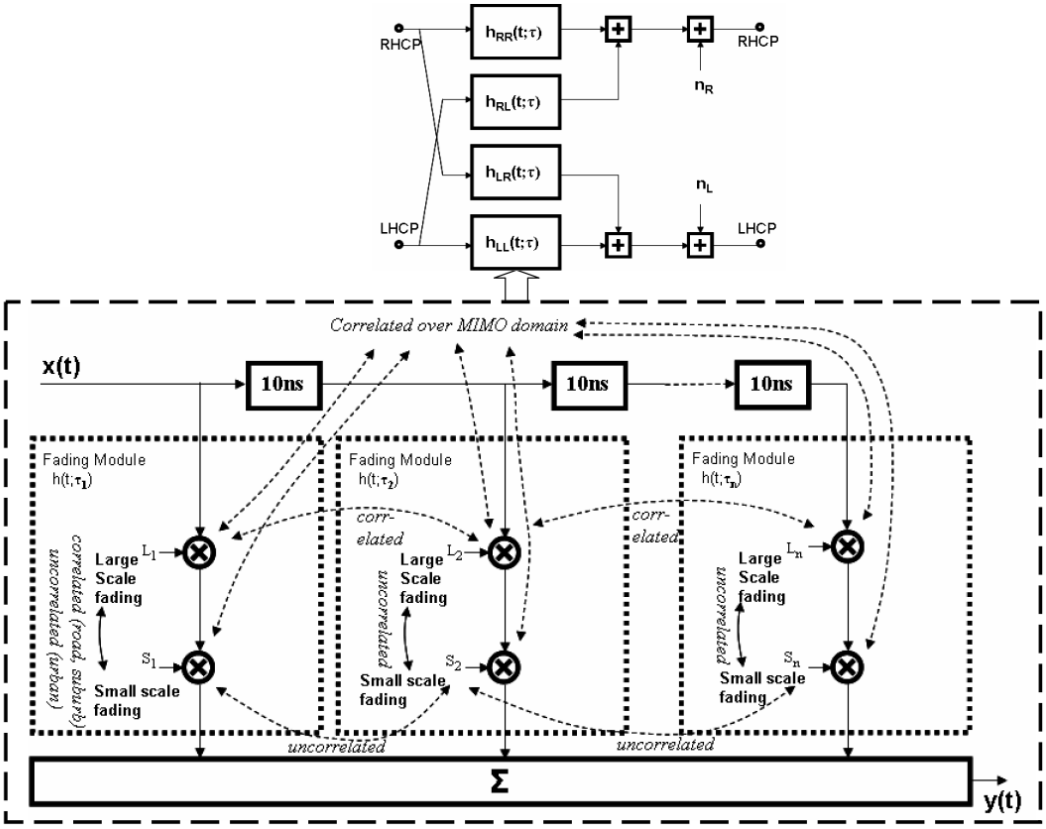

Figure 1.10: Principle of the wide-band model [King 07b]

habitation with high buildings and commercial office blocks while suburban environments are mainly composed of residential houses, gardens or commercial areas. Rural environments represent countryside scenarios with forest, farmlands and sparse buildings.

During this experiment, the transmitting equipment was loaded into a flying Zeppelin to reproduce LMS scenarios with various elevation angles rising from 5° to 90°. The centre frequency was chosen to be 1510 MHz, close to GPS L1 frequency. The receiving equipment was loaded

into a mobile van. For hardware design considerations, a single RHCP *(Right Hand Circular Polarised)* antenna has been used. DoA information are obtained from estimation techniques made during the post-processing step.

The channel sounder was using a spread spectrum technique with 100MHz bandwidth. The spreading code was 25.6μs long and repeated every 3.072ms. Due to the repeat period of the code, the maximum measurable Doppler frequency is 325.5Hz. The overall dynamic of the measurement system is around 30dB. Using ESPRIT *(Estimation of Signal Parameters via Rotational Invariance Techniques)* super resolution algorithm when post-processing the raw data allows to achieve 2ns time resolution for CIR *(Channel Impulse Response)*.

From those measurements, several propagation parameters were extracted to characterise both the total channel behaviour and the echoes. Those parameters are summarised in Tab.1.4. Note that all of them are elevation dependent.

Channel parameters	Echo Parameters
Power delay profile	Number of coexisting echoes
Fading characteristics	Power of the echo
Signal Doppler	Signal bandwidth of the echo
	Life span of the echo
	Reflector localisation
	Movement of the reflecting point

Table 1.4: Channel parameters of interest for LMMC model

The bases of the LMMC model are the following. The scenario is defined by the speed of the receiver, the satellite position (elevation, azimuth) and the type of environment (urban, sub-urban or rural). From those, a virtual scenario is created and tuned to be representative of a typical environment where measurements were made. This virtual environment is composed of building façades (two dimensional plates), trees and lamp post (cylinders). The total received power is divided into two components, one coherent, representing the LOS, and one incoherent representing the MP.

The coherent component is modelled using simple EM algorithm. In LOS conditions, the coherent component is equal to the LOS signal. When the direct signal is masked, in case of building blockage or tree shadowing for example, the coherent component is modelled using different EM methods. For building blockage, the diffraction taking place on the top horizontal edge of the building is calculated using a knife edge model. In the case of tree trunk and lamp post blockage, a double knife edge method is used to reproduce the double diffraction taking place at each vertical edge. For tree canopy shadowing, a linear attenuation model is used plus a random component to reproduce attenuation fluctuations. The linear attenuation is extracted from [Jong 04] [Torr 98]. The random process is tuned by measurements.

The incoherent component, reproducing MP contributions, is modelled using a geometry-based stochastic channel model (GSCM). All generated MP are based on a point-like scatterers approach meaning that each MP contribution is originated from one point placed into the environment. The strength of integrating static variables into the model is to give more versatility for extending the measurements to similar environments. As an example, statistics are here used to generate the number of echoes, their position, their life span, their movement or their mean power. The delay is calculated using a deterministic approach which is geometry based. Amplitude, phase and Doppler are calculated using semi-deterministic approach as presented in Fig.1.11.

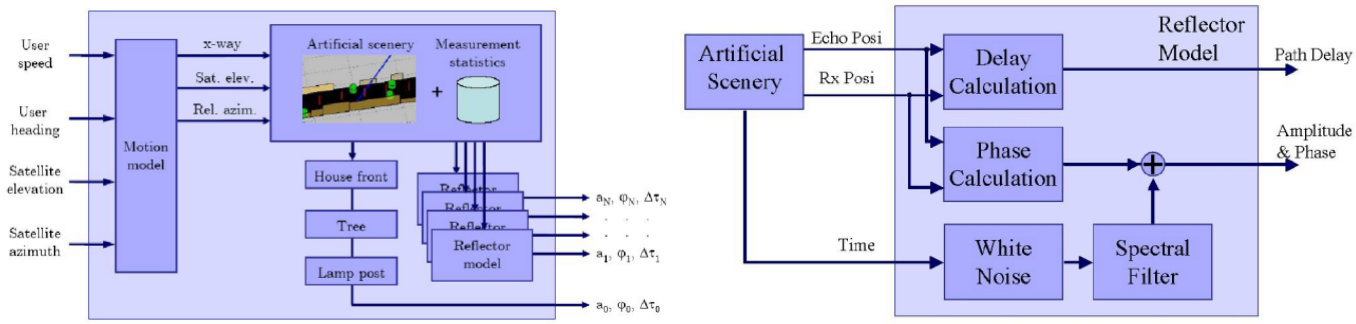

(a) LMMC model

(b) Reflector Model

Figure 1.11: Block diagram and reflector model of the Land Mobile Multipath Channel Model [Lehn 07a]

Several important differences can be observed comparing the pedestrian model [Stei 01] to the LMMC model for vehicular scenarios:

- The distribution of reflectors is different than for the vehicular model, since the pedestrian's position is commonly closer to the adjacent buildings due to the pavement position.
- The LOS blockage statistics is strongly affected by this positioning issue on the street.
- The movement profile of a receiver that is carried by a pedestrian is more stressful with respect to acceleration. Therefore the movement profile is rather shaky than smooth. This is expected to cause serious stress to the tracking loops, in particular for the phase locked loop.
- The correlation time of the channel is longer compared to a vehicular scenario, since the average/maximum speed of a pedestrian is much lower than the average/maximum speed of a vehicle.

Note that a new model of wide-band tree scattering has also been recently proposed [Schu 10] to complete the LMMC channel simulator.

Eventually, the LMMC model is suitable for various types of environments such as urban, sub-urban, rural or highway, various applications, vehicular or pedestrian and specifically designed for satellite navigation purposes. However, this model is not available publicly in its full version, is not able to compute satellite diversity and is restricted to L band.

1.1.3.4 Abele, ONERA, 2009 [Abel 09]

This model has been introduced by Abele and the ONERA team [Abel 09] in 2009. The goal was to reproduce the narrow-band LMS channel behaviour for satellite communication services in vehicular contexts. Abele model is based on the partition of the total narrow-band received power into one coherent component, coming from the LOS signal, and one incoherent component, coming from the diffuse multipath. This model involves several sub-models depending on the finally required precision and allocated computation time. The wave interactions with buildings and vegetation are described by using deterministic methods or stochastic processes. The principle of such a modular modelling approach is presented in Fig.1.12. The typical scenario handled by this model consists in a mobile receiver following a linear trajectory and surrounded by two building rows where each side of the road contributes either to the coherent component, i.e. LOS, vegetation shadowing, blockage, or incoherent component, i.e. diffuse multipath.

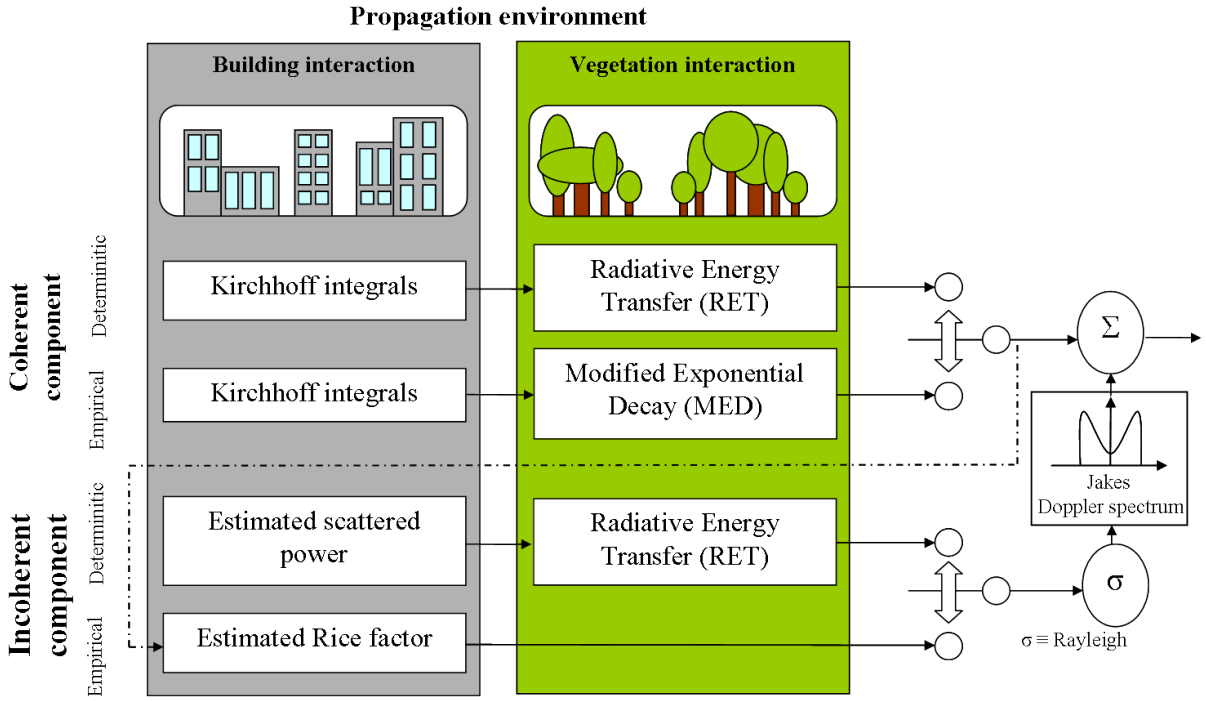

Figure 1.12: Principle of the Abele model

For the coherent component, wave interactions on buildings are modelled by using the Kirchhoff scalar diffraction theory [Pere 07]. Since the buildings are modelled considering 3D parallelepipeds, the total scattered E field is calculated as the combination of three apertures at the receiving point as detailed in [Abel 09]. This modelling allows a good estimation of the shadowed area by using 3D instead of 2D building representation with smooth transitions from LOS to NLOS regions by using Kirchhoff integrals contrary to On/Off ray-tracing models.

For the coherent component, two wave interaction models on vegetation are available following either a deterministic approach or an empirical process. The deterministic model is based on the RET model *(Radiative Energy Transfer)* [Schw 88] [Ishi 91] [Dida 00]. This model considers a sampled vegetation volume on which the diffraction phenomenon and the scalar attenuation experienced by EM waves while penetrating through vegetation can be computed by the mean of a complex transfer function. Note that this model is referenced by ITU under recommendation ITU-R 833-6 [ITU 07] and some tuning parameters can be found in [Pere 05]. The empirical model is based on the MED model *(Modified Exponential Decay)*. This model computes the total attenuation due to canopy crossing considering a modified exponential attenuation. The general formulation is given in Eq.1.16 where A represents the linear attenuation through canopy in dB/m, f represents the frequency in MHz and d the distance through the canopy in meters. Parameters η, ν and γ are given in [COST 02] [Bart 92] [ITU 86] depending on the frequency, leafs state, or canopy crossing distance.

$$A = \eta\, f^{\nu}\, d^{\gamma} \tag{1.16}$$

For the incoherent component, the principle is to generate a Rayleigh stochastic process filtered by a Jakes power spectrum [Jake 94] to reproduce respectively fading and Doppler effects on the time-series. This stochastic process can be tuned by using empirical or deterministic methods. Considering the empirical method, an estimation of the Rice factor is performed and is function of the type of environment and of LOS power coming out from the coherent component. Note that the estimated Rice factor is then representative of both interactions on buildings and vegetation. The deterministic method estimates power coming from the buildings and from the vegetation separately. For vegetation, the total scattered power is estimated by the means of

the RET model. For buildings, the total scattered power is estimated by the means of a new model based on equivalent RCS [Abel 08]. The principle is to map the normalised RCS of a typical rough surface at different frequencies depending on elevation and azimuth of the satellite as presented in Fig.1.13. This map of normalised RCS values has been established by using a PO algorithm on canonical rough surfaces presented in [Valt 09]. Since normalised RCS is given in m^2/m^2, the total scattered power is then proportional to the total surface of the surrounding buildings.

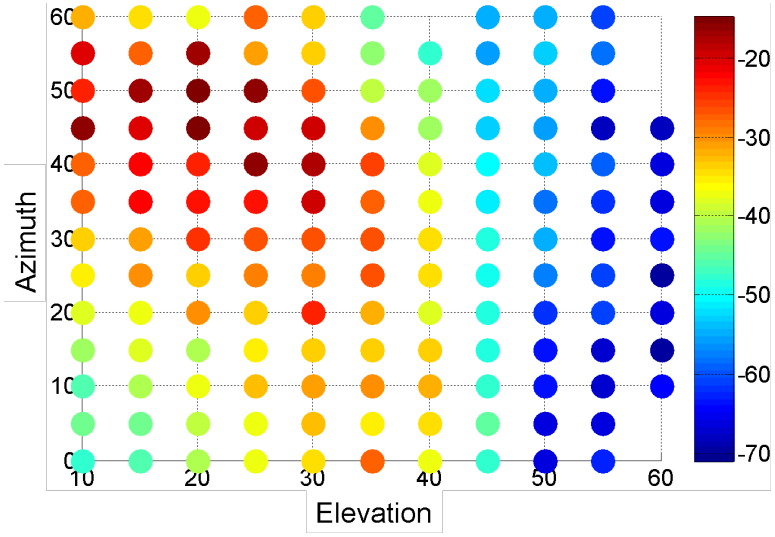

Figure 1.13: Example of mapping of the normalised RCS for a typical rough surface at 2.2GHz [Abel 08]

Abele model has been validated against two experimental data sets. The first one has been provided by CNES and was obtained during a measurement campaign carried out in Gaillac, France, in 2006 where narrow-band total power in S-band was recorded. One example is provided in Fig.1.14a which represents a typical road surrounded by trees. A second data set was provided by France Telecom Research and Development and was obtained during a measurement campaign carried out in Belfort, France, at 2.2GHz and 1.47GHz. One validation example is provided in Fig.1.14b corresponding to the cdf *(Cumulative Distribution Function)* of total attenuation for satellite elevation between 25° and 50° in Belfort at 1.47GHz.

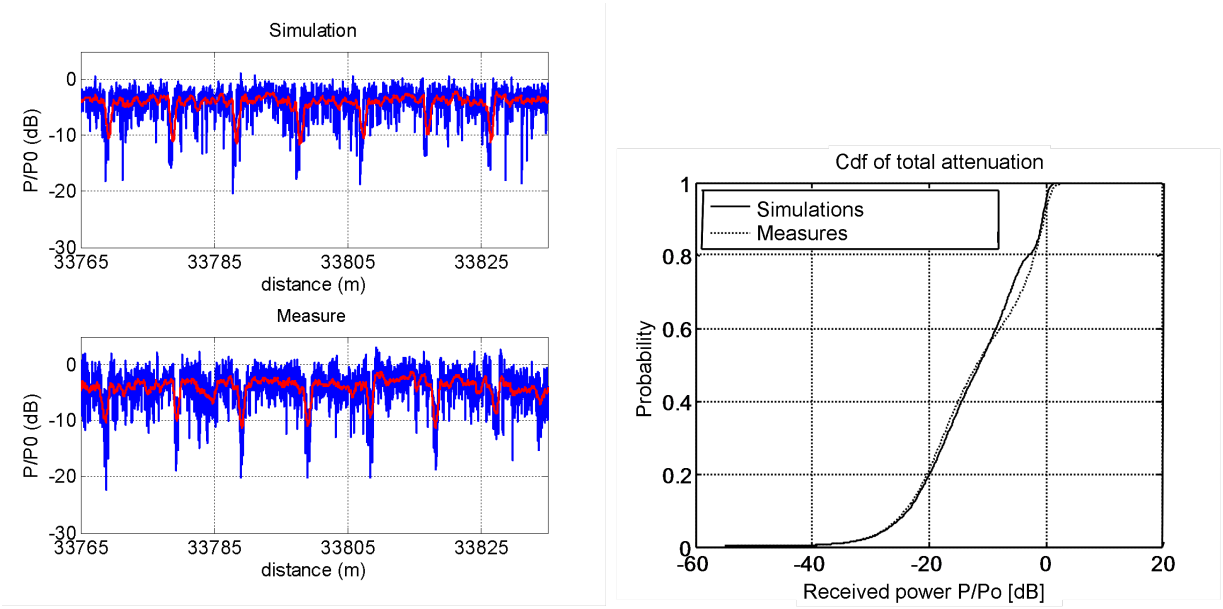

(a) (b)

Figure 1.14: Measurement validation examples of the Abele model [Abel 09]

1.1.3.5 Li, University of Poitiers, 2010 [Li 10]

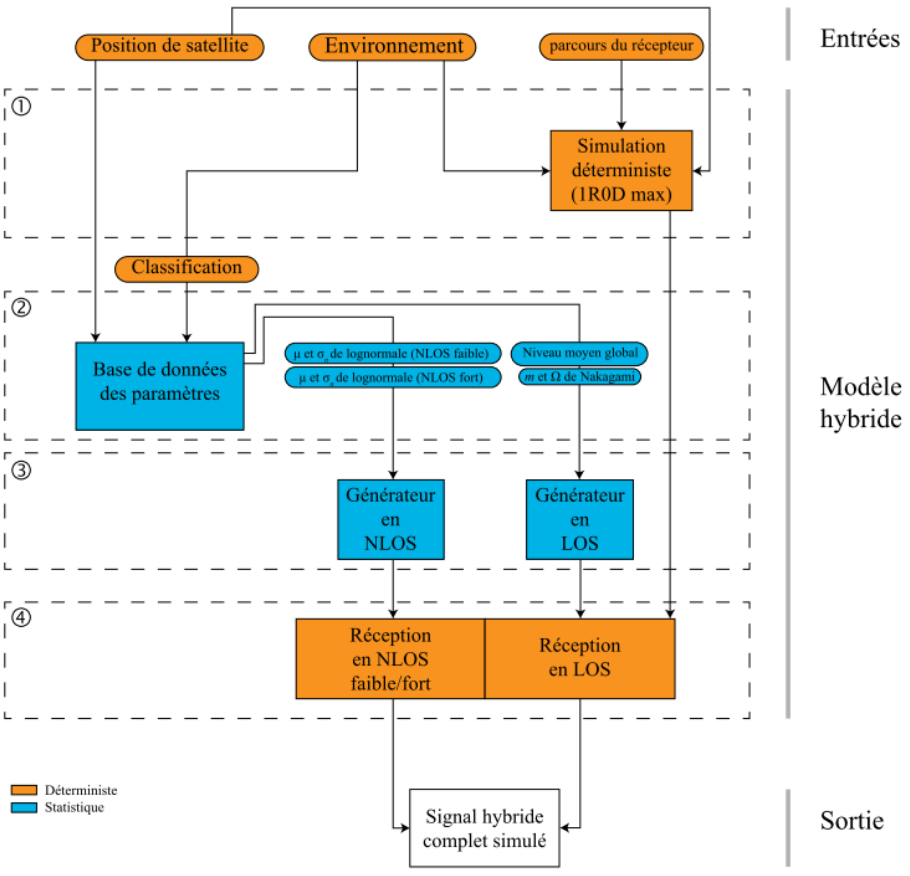

Figure 1.15: Principle of the Li deterministic-statistical model [Li 10]

Another model has been introduced by Li from the University of Poitiers in 2010 [Li 10]. This hybrid approach combines a deterministic ray-tracing tool with stochastic processes, generating narrow-band time-series in complex urban environments for vehicular purposes. The principle

of the model is depicted in Fig.1.15.

The inputs are the 3D environment of the considered scene, the mobile trajectory in the scene and a fixed satellite position. The first computation step consists in using a deterministic ray tracing algorithm, Ergospace. This software is based on ray-tracing techniques (RT) and handles multiple interactions which are a combination of specular reflections (GO) and multiple diffractions (UTD). In Li approach, only the direct path and first order reflections are calculated using Ergospace. The goal of this first computation step is to predict LOS and NLOS states all along the receiver trajectory. Note that the NLOS state is subdivided into two possible shadowing sub-states, light or deep. The NLOS light shadowing state corresponds to the case where at least one first order reflection is achieved. NLOS deep shadowing state is achieved otherwise. A parallel can be made on the Markov state model presented in Section 1.1.1.4.

Once LOS and NLOS states have been identified, a specifically tuned stochastic process is applied to each of the three states. The tuning of those stochastic processes is optimised using Ergospace simulations considering up to fourth-order interactions on the environment. The tuning parameters are then stored in a comprehensive database. This tuning database is parameterised considering the satellite position and the type of environment, i.e. urban, suburban or rural. A proposed alternative to tune the stochastic processes could be using wide measurement campaigns. From the analysis made in [Li 10], the synthesised time-series in LOS states follow a Nakagami-m distribution with a predicted constant mean. For NLOS states two different log-normal distributions are used.

Critical review of hybrid physical-statistical approaches :

Many different hybrid physical-statistical approaches are presented, where each of them is based on a specific balance between statistical and deterministic modelling. This balance is representative of a particular trade-off made considering each particular application. In the following, the targeted application of each hybrid model is recalled and the main advantages and drawbacks are highlighted regarding environment modelling and EM interaction modelling.

The first model was introduced by Oestges in 2000. It addresses the specific issue of LMS channel modelling for LEO satellite communication systems and is oriented toward system performance evaluation. The main advantage of such approach is the use of ray-tracing techniques to model shadowing and reflection. The use of the virtual city concept, introduced hereafter, is also one of its strengths handling natively satellite diversity issues. Mainly used for narrow-band time-series generation, this model is suitable intrinsically for wide-band purposes. However, wide-band limitations have been observed when modelling the multipath component, e.g. RMS delay spread or coherent multipath power, due to the use of simple GO methods.

The second model was introduced by King in 2007 and addresses the specific issue of MIMO LMS channel modelling. Among the three different proposed models, the wide-band LMS channel model suffers from the intensive use of statistics, derived from measurement campaigns, to generate pseudo-environments based on Markov chains or to tune the fade distributions and MIMO correlation coefficients. This measurement-based approach appears to be rigid and not versatile enough.

The third model was introduced by Lehner in 2007 and addresses the specific issue of LMS channel modelling for satellite navigation issues in various environments for pedestrian and vehicular applications. This model is standardised by the ITU. However, the LMMC model suffers from the use of statistics, also derived from measurements at L band, to model the multipath component (power, number and position of the scatterers, power delay profile ...). The approach, consisting in spreading point-like scatterers in the environment, depending on satellite position, makes satellite diversity results doubtful since different realisations of the same environment are used to model the multipath component. Also limiting, is the use of measured statistical distributions with specific tuning which make them inappropriate for environments different from the measured ones. Note that the EM interactions on the environment are calculated using simple EM models such as Kirchhoff integrals, MED for tree attenuation and point scatterers theory for multipaths.

The fourth model was introduced by Abele in 2009 and addresses the general issue of LMS channel modelling for satellite communication systems. The simulator was based on a modular approach which allows the user to choose the level of accuracy by using empirical or physical based methods. This model is however narrow-band oriented. Nevertheless, one interesting model has been proposed to quantify the total multipath power, reflected by complex urban environments.

The last model was introduced by Li in 2010 and addresses the specific issue of real-time site-specific LMS channel modelling for satellite communication systems. This model has the advantage of being based on 3D realistic environments handling natively the satellite diversity issue. However, this model suffers from the tuning process which is based on numerical simulations, replacing the conventional use of measurement campaigns. Finally, this model is also oriented toward narrow-band issues.

At the present time, even if designed for specific applications with specific needs, hybrid physical-statistical models seem to be a good trade-off optimising the computation time by adding statistics while maintaining realistic results by using EM physical models or measurement tuning. Considering each respective application segment*, hybrid approaches are sufficiently accurate with reduced computation time compared to all-purpose, but time consuming, deterministic approaches.*

1.1.4 Details on the virtual city concept

The virtual city concept has been introduced by Karasawa [Kara 94] in the late 90's and reused later and adapted by Saunders [Saun 96], Oestges [Oest 99a] and Lehner [Lehn 07a] for their own needs. This approach is now widely used by the scientific community. The principle is to generate statistical virtual environments, representative of real environments such as urban, suburban or rural, by the mean of distributions of building height and width, street width, tree position, probability of road crossing or building density index. This fast modelling approach is used for synthesising very wide and customised environments with few input parameters.

In Lehner approach, the virtual city is made of two dimensional flat buildings, lamp posts and trees. This virtual city is responsible of the attenuation of the LOS component. The multipath component is generated by spreading point-like scatterers into the environment depending on satellite elevation according to distributions tuned by measurements. This limitation has already been highlighted since point-like scatterers are linked to the satellite elevation instead of being linked to the environment. On example of lined tree synthesis is given in Fig.1.16, extracted from the user manual of the DLR LMMC model [Krac 07].

In Oestges approach, the virtual city is only made of two dimensional flat buildings on which physical EM models are computed. For a more realistic environment synthesis, Oestges has based the tuning of his virtual city on a qualitative study, performed by Saunders and al. from the University of Surrey, UK, to measure environment distributions. Two parameters were

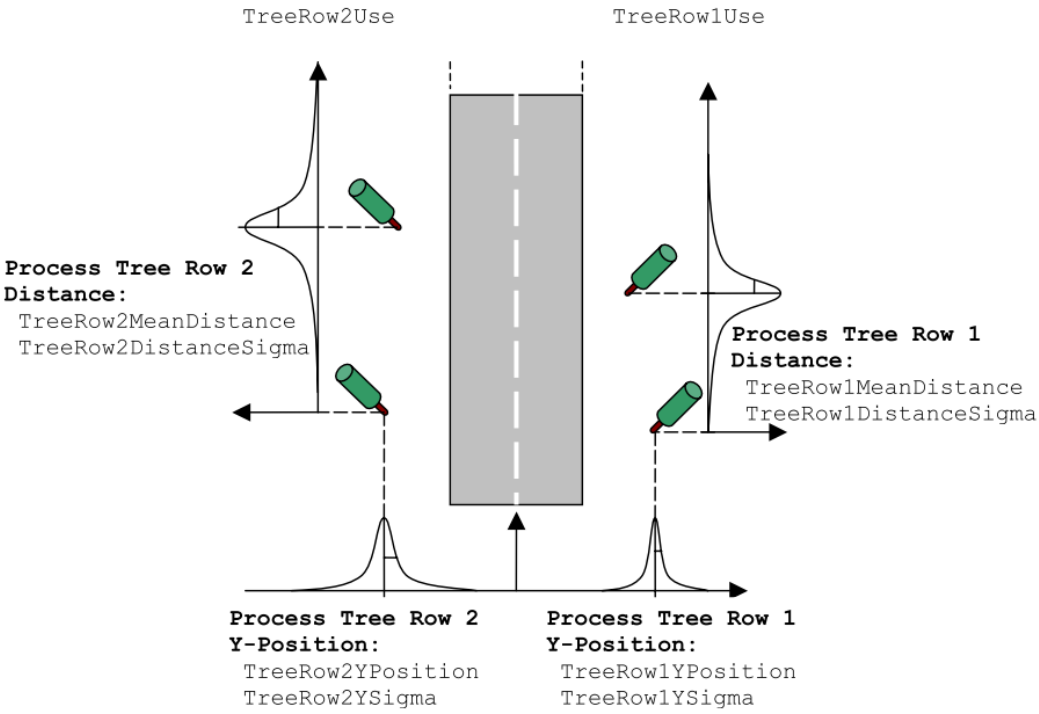

Figure 1.16: DLR virtual city approach for placing trees [Krac 07]

studied during those measurement campaigns [Saun 91] [Pars 00]: the building height and the street width. For this study, around 200 building heights were recorded in typical suburban environments in Guilford, UK during winter 1997. As a result, building height and street width follow a log-normal distribution as presented in Fig.1.17. Typical values for building heights are given in Tab.1.5 using Eq.1.17.

City	**Mean μ [m]**	**Std σ [m]**
Westminster	20.6	0.44
Guildford	7.1	0.27
Soho (London)	17.6	0.25

Table 1.5: Measured building height parameters for log-normal distributions [COST 02]

$$p(h) = \frac{1}{h\sqrt{2\pi\sigma}}\, e^{-\frac{1}{2\sigma^2}\ln\left(\frac{h}{\mu}\right)^2} \tag{1.17}$$

Even if very versatile and powerful in terms of computation time, the virtual city concept has some limitations. The main one is for site specific scenarios. Even if perfectly tuned, this approach is always generating virtual environments, similar and close to the original environment, without reproducing it deterministically. Furthermore, an infinite number of parameters can be added to better reproduce the targeted environments depending on each specific application.

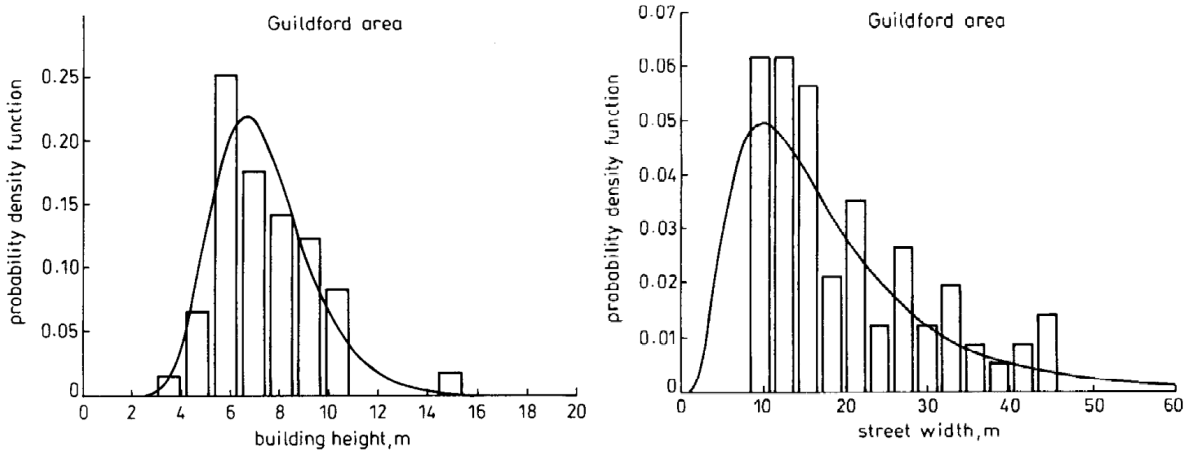

(a) Building height

(b) Street width

Figure 1.17: Guildford building height and street width statistics [Oest 99a]

1.2 Proposed approach for designing a new LMS channel simulator

The objective of this section is to explain the logic yielding to the design of a new hybrid physical-statistical LMS channel simulator. As a starting point, the objectives of the channel simulator and the constraints on the modelling are presented. From the previously made critical reviews, and to reach the formulated goals, a new hybrid physical-statistical channel simulator is proposed in the second subsection, where the positioning of the proposed simulator is presented as well as the macro-architecture and the typical outputs.

1.2.1 Objectives and constraints of the model

1.2.1.1 Objectives

The goal was to develop a fast software tool for reproducing the LMS channel behaviour for system simulation needs in very wide environments and without requiring extensive measurement campaigns for tuning the model. Since satellite navigation is currently an active scientific topic in the European community with the foreseen arrival of the Galileo system, and since navigation application are more and more demanding in terms of channel modelling (low tolerance to delayed multipath, important Doppler due to polar orbiting satellites, satellite diversity required for PVT *(Position Velocity Time)* computation, ...) the choice has been made to focus mostly in navigation issues to the detriment of satellite communication systems. However, satellite communication applications remain in the scope of this PhD work, and no critical assumptions have been made to restrict the use of the channel simulator to navigation issues only.

A second convergence point was the need of a channel simulator for designing future LMS services. This work on anticipating the future needs of potential LMS services has been oriented mainly toward navigation needs on multipath mitigation techniques and allocated frequency bands. Those considerations for futures services have lead to several constraints discussed hereafter.

One last objective was the computation efficiency. Since the developed tool will be used for system simulation purposes, a particular attention has to be paid to the computation time required by the channel modelling step, considering the use of wider system simulation chains.

1.2.1.2 Constraints

The objectives mentioned above have been translated into several concrete constraints for the design of the channel simulator. First, the channel simulator has to be free from any tuning requiring extensive measurement campaigns although experimental validations have been performed. The channel simulator has to be able to handle potentially very wide environments for system performance evaluation needs.

For satellite navigation systems, a particular emphasis is made on the wide-band representation of the channel and on multipath since they have a major impact on navigation receivers, especially in urban environmentsA.1.3. Several parameters of the multipaths, which have a substantial impact, have to be taken into account, namely amplitude, phase, polarisation, delay or Doppler. Due to their influence on navigation receivers, the need of reproducing realistic Doppler effects is also non negligible contrary to the assumptions made by some of the existing models. One other crucial point is the need of managing several satellites at the same time to perform realistic PVT computations in complete GNSS system simulation chains.

For satellite communication systems, the channel simulator has to be adapted to the frequency bands allocated for such services, S-band and C-band, slightly higher compared to the L-band allocated to GNSS systems. The reader is reminded that Ka and Ku bands are out of the focus of this work even if some of the modelling techniques could be extrapolated to those frequency bands. New solutions, based on diversity techniques, are currently being tested to ensure higher data rates. Several diversity solutions have then to be handled by the channel simulator such as satellite diversity, space diversity, polarisation diversity or frequency diversity. In reality, those constraints meet up the one introduced by the future developments for satellite navigation systems as discussed hereafter. With higher data rates, the involved signal bandwidths are also wider and multipaths, giving rise to inter-symbol interferences, become a critical issue which has to be taken into account.

Regarding the constraints imposed by the future evolutions of LMS services, a particular attention has been paid to multipath mitigation techniques for satellite navigation purposes. One already identified solution is the use of antenna arrays at the receiver side which meet up the already mentioned constraint on space diversity techniques for satellite communication systems. A second solution is the use of dual frequency systems and the probable adoption of higher frequency bands allocated to GNSS services at it is the case for some recent navigation systems (Indian IRNSS which operates in S-band). A third solution deals with the polarisation issue which is considered as a new way to discriminate LOS from MP. Finally, the channel simulator has to deliver a maximum number of outputs to ensure a maximum versatility. Several trails are already planed such as DoA or Doppler spectrum.

One last constraint, but not the least, is the computation time. The channel simulator has to be as fast as possible with almost real-time requirements. One criterion is to deliver one channel impulse response every 20ms, representing the integration time commonly used in navigation receivers. For system simulation needs, the simulator is also expected to have simple and standard inputs and outputs. In general, the simulation tool has to be as realistic and versatile as possible.

Section synthesis :
Regarding the expected capabilities of the channel simulator, the main constraints to be satisfied are summarised in a decreasing importance order:

- *Wide-band representation of the channel with a particular emphasis on realistic multipath modelling considering amplitude, phase, polarisation, delay and Doppler as key parameters.*
- *Real-time computation.*
- *Design not based on extensive measurement campaigns.*
- *Native handle of satellite diversity, space diversity, frequency diversity and polarisation diversity.*
- *Frequency scalable for L, S and C bands.*
- *Wide scenario management.*
- *Simple and standard inputs/outputs.*
- *Output versatile (DoA, Doppler spectrum ...).*

1.2.2 Presentation of a new hybrid physical-statistical LMS channel simulator: SCHUN

1.2.2.1 Positioning of the chosen approach

From the constraints mentioned previously and according to the critical review of existing LMS channel models, Tab.1.6 summarises the advantages and drawbacks of each model depending on our modelling constraints.
As suggested by Tab.1.6, none of the existing models is suitable directly for answering our needs. Nevertheless, some ideas from previously presented models deserve to be discussed and could be adapted to meet our requirements.

Deterministic approaches are the most suitable methods and almost fulfil all our needs. However, they are not adapted to wide scenario management, due to the cost of real CAD *(Cumputer Aided Design)* models at city scale, and suffer from long time computation.

The first issue on wide scenario management can be solved by using the virtual city concept. This modelling approach is particularly suited for generating very wide environments and long trajectories in a short time. Two variants of this concept have been described. The first one, proposed by Lehner, shows limitations for satellite diversity applications since multipath component is not linked to the environment but is dependent on each satellite position. The best solution is to force MIMO correlation by the environment as suggested by Oestges, Abele and Li. This solution implies generating only one environment, independently of the satellite position, so that shadowing and multipath are already correlated by the use of the same environment.

The second issue on computation time can be solved by using simple EM interaction models. Since using measurements has been avoided, the only alternative is to integrate more EM physics into the modelling. Note that physical EM models are usually time-consuming and a particular trade-off has to be made between precision and time computation. The use of physical methods provides also frequency versatility, position diversity and a wide range of possible outputs.

The final chosen approach is based on a hybrid physical-statistical approach, showing the best trade-off in terms of accuracy and computation time. Compared to the other hybrid models, the channel simulator embeds as little statistics as possible for generating almost real and static

environments independently of the simulation parameters (satellite position, MIMO, type of outputs ...). On the EM interaction side, the channel simulator embeds as much of EM physical modelling as possible to ensure EM propagation accuracy, without neglecting time computation issues. Finally, the positioning of the proposed LMS channel simulator SCHUN *(Simplified CHannel for Urban Navigation)*, is represented in green in Fig.1.18 among the existing LMS channel models.

		Wide-Band	Real-time	Measurement independence	MIMO oriented	Frequency scalable	Wide scenarios	Output diversity
Statistical	Markov	✗	✓	✗	✗	✗	✓	✗
	[Pere 01]	✓	✓	✗	✗	✗	✓	✗
	[Carr 12]	✗	✓	✗	✓	✗	✓	✗
Determinisitic	Asymp. Cur.	✓	✗	✓	✓	✓	✗	✓
	Asymp. Rays	✓	✗	✓	✓	✓	✗	✓
Hybrid physical-statistical	[Oest 00]	✗	✗	✓	✓	✓	✓	✗
	[King 07a]	✓	✗	✗	✓	✗	✓	✗
	[Lehn 07b]	✓	✓	✗	✗	✗	✓	✓
	[Abel 09]	✗	✗	✓	✗	✓	✓	✗
	[Li 10]	✗	✓	✓	✓	✗	✗	✗

Table 1.6: Critical review of the existing LMS channel models depending on imposed constraints

1.2.2.2 Macro architecture of the channel simulator

The concept of the developed LMS channel simulator SCHUN consists in generating the environment by using a virtual city approach and modelling the interactions by using simple EM interaction models. This trade-off, using simple EM interaction models, satisfies the real-time constraint, without using measurement-based tuning. This almost deterministic approach allows in principle to meet our requirements.

The macro architecture of the SCHUN LMS channel simulator is presented in Fig.1.19. The statistical component of the chosen approach is represented by the synthesis of the simplified virtual city. All other components of the modelling are based on ray techniques and simple physical EM models coming from deterministic approaches.

The simplified EM interaction models, on vegetation and on buildings, are based on EM physical

models such as GO and PO. The direct signal blockage model is based on UTD. The reader is advised that the simplified EM interaction model on vegetation has not been investigated and will not be presented in the following of this document since existing models have already been proposed [Chef 10] [Abel 09] and could be integrated in a later time.

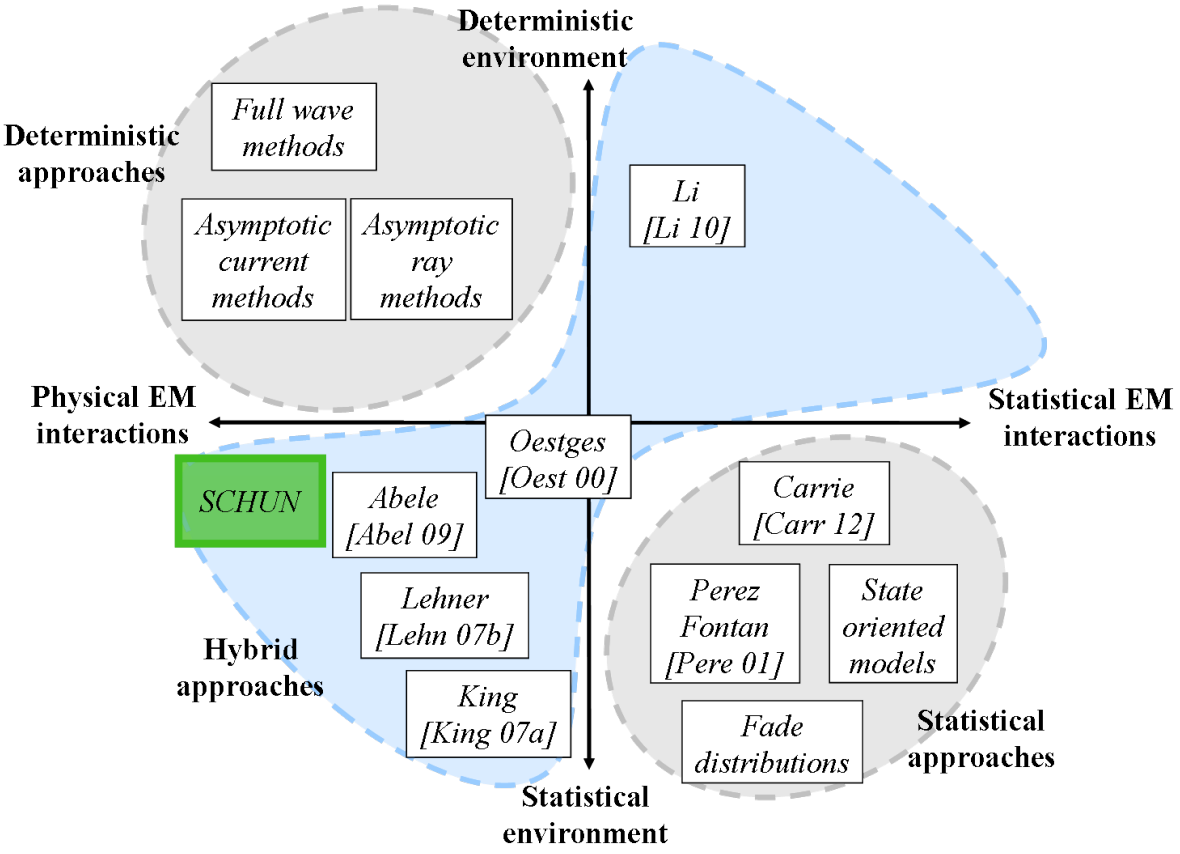

Figure 1.18: Positioning of the proposed approach

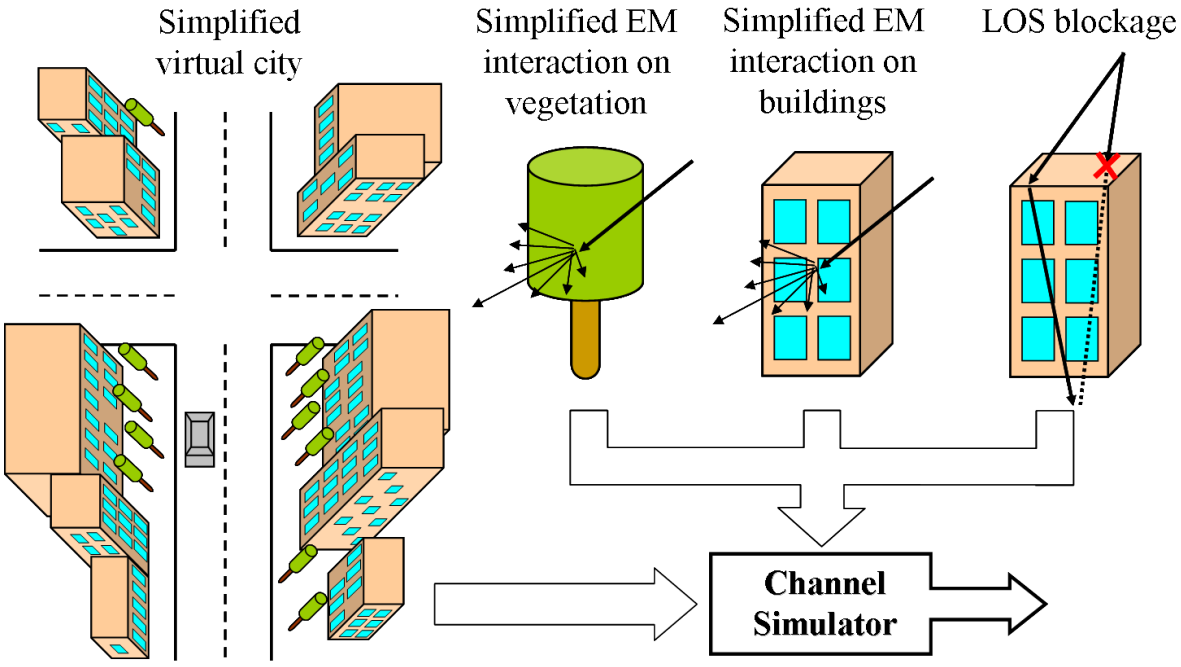

Figure 1.19: Macro architecture of the SCHUN LMS channel simulator

1.2.2.3 Typical outputs and signal model

The SCHUN LMS channel simulator is able to deliver a wide range of outputs such as instantaneous channel impulse response in delay/Doppler space, DoA information, complex narrow-band time-series, Doppler spectrum or On/Off blockage time-series.

The base-band signal model is presented in Eq.1.18 and Eq.1.19 where $h(t,\tau)$ represents the time delay impulse response of the channel, y(t) the received signal, x(t) the transmitted signal, N the number of multipath where 0^{th} represents the LOS, $\gamma_i(t)$ the ray amplitude, $\phi_i(t)$ the phase of the ray including delay and reflection shifts and $\tau_i(t)$ the delay.

$$y(t) = h(t,\tau) \otimes x(t) \tag{1.18}$$

$$h(t,\tau) = \sum_{i=0}^{N} \gamma_i(t) e^{-\jmath\,\phi_i(t)}\,\delta\left(t-\tau_i(t)\right) \tag{1.19}$$

1.3 Summary

This chapter has presented the main existing LMS channel models following statistical, deterministic and hybrid physical-statistical approaches. Each approach has its benefits and its drawbacks. According to our requirements and from the critical review made, none of the existing LMS channel model is directly suitable for our application and a new simulator has been proposed, mainly oriented toward wide-band modelling with real-time requirements. The proposed LMS channel simulator, SCHUN, follows a hybrid physical-statistical approach based on the virtual city concept coupled with simplified deterministic EM methods reproducing wave interactions with buildings.

The global approach followed by the next presented intermediate studies has been mainly driven by the real-time constraint. The guiding principle of the global approach is to observe and understand the different mechanisms to better reproduce them in a simpler way to reduce the computation time.

The starting point of our reflection deals with environment modelling. The main interrogation was on how to represent the environment and how it impacts the LMS propagation channel. As previously discussed, using deterministic tools requires to represent the environment with as much details as possible to be as realistic as possible. Thus, an infinite number of parameters can be considered in such modelling: object geo-referencing, dielectric materials, building architecture, tree species or urban furnitures, so that reproducing real environments becomes limitless and adding details may be unnecessary at some point.

In a first approximation, and according to existing LMS channel models, only macro objects such as buildings and trees seems to have a major impact on the channel behaviour since masking the direct signal. In this first approximation, the urban furniture's have been neglected. This can be justified by the fact that lamp pole and road signs do not require new developments since they are already integrated in some models. Furthermore they can be added in a later time to the simulator since using the already developed diffraction model. Moving objects, and especially moving cars, are also neglected since their multipath contributions are rapidly filtered by the DLL process taking place in navigation receivers due to high Doppler. In a second approximation, the vegetation effect has been discarded from the present study but is already considered as mandatory for further developments of the present simulator. As for urban furniture's, existing models for tree scattering have already been proposed [Chef 10] [Abel 09] and could be integrated in a later time.

For the present study, urban environments have been targeted and the main focus has been placed on building representation and wave interactions with buildings. Two approaches are commonly used when representing the buildings. On one hand, real three dimensional meshes of the buildings are used but not adapted at city scale mainly for modelling reasons and computation time. On the other hand, planar building representations are used, which is known to be limited in terms of realism of the scene. Next Chapter 2 is oriented toward this issue of generating simplified and realistic virtual buildings with a trade-off in terms of realism and computation time. The solution is an intermediate model, using a 2.5D façade approximation, to represent the buildings without using full 3D mesh but richer than only 2D planar surfaces. The focus is made on how to represent the façade architecture and how the small features present on real complex facades impact the overall channel behaviour. This study has been conducted by using a full wave method, namely Elsem3D based on MoM, and is oriented toward the targeted end applications, satellite communication and satellite navigation systems. Chapter 2 ends with some recommendations on how to simplify environment representation.

Chapter 2

Simplifying the representation of complex façades in urban environments

Contents

2.1 Details of the experimental protocol 38
2.1.1 Appropriate numerical method: Method of Moments 38
2.1.2 Definition of the façades 38
2.1.3 Definition of urban canyons 41
2.2 Preliminary observations made on isolated canonical façades 41
2.2.1 Analysis of surface currents 42
2.2.2 Analysis of Radar Cross Sections 43
2.2.3 Analysis of the near field scattering pattern 48
2.3 Influence of small features on MP power estimation 51
2.3.1 Simple narrow-band channel model 51
2.3.2 Qualitative analysis of MP power time series on simple urban canyons . . . 52
2.3.3 Statistical analysis of MP power time series on simple urban canyons 54
2.4 Influence of small features on navigation receivers 57
2.4.1 Simple wide-band channel model 57
2.4.2 Influence of resolution and speed 59
2.4.3 Influence of incidence 61
2.4.4 Influence of direct signal attenuation 62
2.5 Summary and recommendations 65

The objective of Chapter 2 is to quantify the influence of small features and scatterers present on complex façades with the aim of identifying what is the required level of detail for representing relevant reflection phenomena without using full 3D façade representations. This study has been performed using MoM tools adapted to model EM interactions with sub-wavelength elements. The conclusions of this chapter lead to significant time gains considering simpler CAD of complex façades for synthesising large virtual urban environments. This study could also validate the use of asymptotic methods such as PO on simple façade without restrictions after all small elements have been removed.

To address the issue of small features influence present on complex façades, Elsem3D code, based on MoM and presented in Appendix B.3.1, has been used. The approach is simple: two façades are represented with four levels of detail. By changing this level of detail, with more or less details on the façade, and by observing some parameters such as the surface currents, the near field scattering pattern, the total MP power or the GNSS pseudo-range error made, the contribution of insignificant scatterers can be isolated and removed from the complex CAD of the façade leading to a simplified representation. This simplification is called 2.5D façade

approximation in the rest of this document.

This chapter is organised as follows. The first section presents the immediate context of this study, the chosen approach and the simulation protocol. The second section presents observations considering isolated canonical façades. Narrow-band MP time series and wide-band results applied to the GNSS context are presented respectively in the third and in the fourth sections. Finally, in the fifth section, 2.5D façade approximation is presented where suggestions are given on what level of detail, i.e. minimum scatterer size, is required to reproduce accurately the EM behaviour of the LMS propagation channel.

2.1 Details of the experimental protocol

2.1.1 Appropriate numerical method: Method of Moments

As presented in Chapter 1, the PO algorithm is particularly suited for LMS channel modelling. However, since real complex environments do not necessarily fulfil the PO validity domain, e.g. object size compared to the wavelength, such asymptotic method is not adapted here to evaluate the impact of small features. To observe such impact of small scatterers, an adapted method has to be used, namely full-wave MoM, which does not have any restriction on object size contrary to PO. With this rigorous approach, sub-wavelength elements can be taken into consideration.

In the following, the EM code Elsem3D [Bark 00] [Soud 99] (Section B.3.1) of ONERA has been used to compute all the simulations discussed hereafter. It is based on the EFIE *(Electric Field Integral Equation)* solved with MoM techniques in the frequency domain. Thus, this chapter inserts itself in a global and rigorous process aiming at simplifying the EM interaction problematic from exact methods to asymptotic methods which are themselves reduced to simplified EM methods presented in Chapter 4.

As mentioned in Section 1.1.2.1 relative to full-wave methods, the MoM method is resource consuming (storage, memory, computation time) and only problems of limited sized can be solved. For this reason, the whole complex urban building case has to be reduced. For the results presented in this chapter, the elementary object used to model any urban canyon is called a *"canonical façade"*. This canonical façade represents one piece of the total building, also seen as one *"period"* of the architectural motive. Two examples are given in Fig.2.1 for two different types of buildings.

Even reducing the size of the CAD model of the building to the CAD model of one façade, from billions of edges to hundreds of thousands, the problem size remains too big in terms of unknowns to be treated on super-computer considering dielectric materials. Then, PEC *(Perfect Electric Conductor)* hypothesis has been applied to all constituting elements of the canonical façades reducing by a factor of two the number of unknowns. This conservative hypothesis does not affect the overall results presented hereafter. Indeed, those results are compared to each other based on the same assumption resulting in a relative comparison which is not function of the chosen materials. Even considering those simplifications, each canonical façade presents more than 700.000 edges and needs a computation time of about 36 h over 8 parallel processors on a super-computer. Regarding the PEC assumption, the reader is reminded that the interest is here focused on the simplification level. Model parameterisation for more realistic materials (lossy dielectrics) will be performed in Chapter 4, after having determined the level of simplification to be used and is out of the scope of this chapter.

2.1.2 Definition of the façades

To avoid loss of generality and better reflect urban diversity, the analysis has been carried out considering two types of canonical façades present in Toulouse, France. As presented in Fig.2.2,

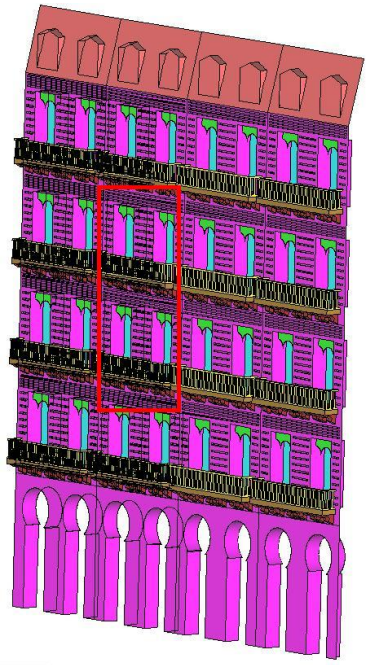

(a) City centre building type

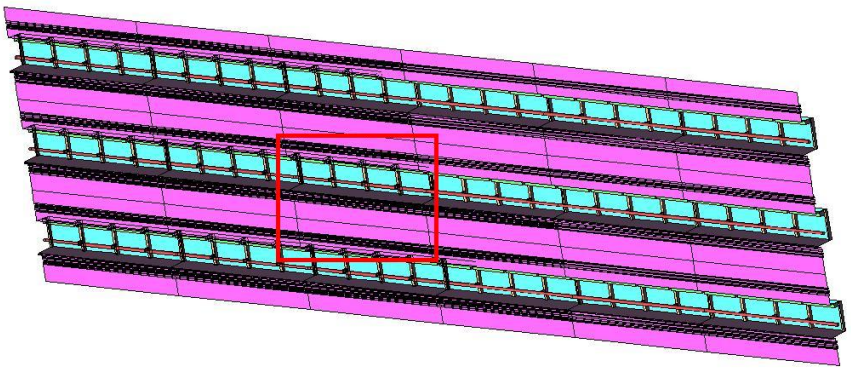

(b) ONERA office building type

Figure 2.1: Example of canonical façades extracted from periodic architectural motives on complex urban buildings

the first one (façade 1) has been extracted from a typical building of Toulouse city centre and is representative of a *rough* surface. Its size is 4 m in width and 6 m in height. The second one (façade 2) presented in Fig.2.3, has been extracted from an ONERA office building, smoother than the previous one, it has only a limited number of protruding and receding elements. Its size is 6 m in width and 3 m in height. To evaluate the impact of small scatterers on complex buildings, those two canonical façades have been reproduced four times using four different levels of detail as described next.

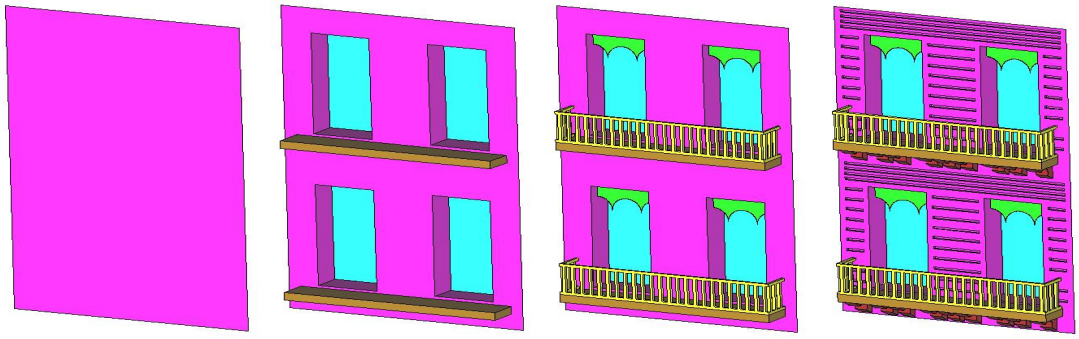

(a) Null resolution (b) Low resolution (c) Medium resolution (d) High resolution

Figure 2.2: Representation of the four level of details for the City centre façade in [m]

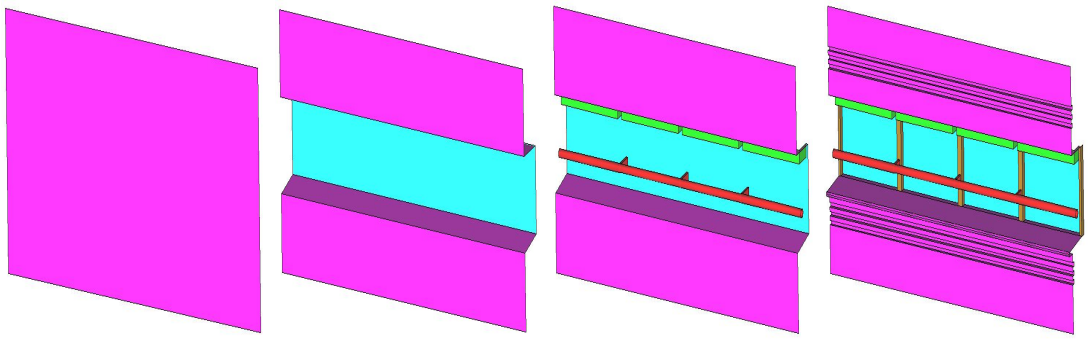

(a) Null resolution (b) Low resolution (c) Medium resolution (d) High resolution

Figure 2.3: Representation of the four levels of details for the ONERA office façade in [m]

As a convention, the four level of details are the following:

a - Null resolution: corresponds to a canonical plate. No details are present. This reference case has also allows calibrating the use of Elsem3D.

b - Low resolution: considers details much larger than one wavelength ($\lambda = 0.2$m at 1.5GHz). At this level of detail, only windows and balconies are represented.

c - Medium resolution: considers details in the range of the wavelength such as guardrails, window decoration and shutters.

d - High resolution: considers sub-wavelength details. Such small details can be seen as the architectural motives in walls due to its conception such as bricks, windows frame, balcony decorations or other details.

This progressive description principle has been also used for terrestrial applications for indoor [Pere 09] and outdoor [Ouat 11] environments. All canonical façades described in Fig.2.2 and Fig.2.3 are illuminated with plane waves. A total of nine distinct incidences are used, combination of three azimuths 0°, 40°, 80° and three elevations 0°, 40°, 80°. As a convention for a global interpretation, the incidences are grouped into three different sets: *normal incidence* for 0° elevation and 0° azimuth, *typical LMS incidence* for elevations and azimuths smaller or equal to 40° (three cases) and *extreme LMS incidence* for larger elevations or azimuths (five cases). The source is linearly polarized, θ and ϕ, at a frequency of 1.5 GHz. The θ polarisation represents a generalised case of vertical polarisation for non null elevations while the ϕ polarisation represents horizontal polarisation.

2.1.3 Definition of urban canyons

To generalise simple observations made in the next sections on isolated canonical façades, more complex scenarios are considered associating several canonical façades to reproduce complex buildings and urban canyons for mobile configurations. In the following, and particularly for statistical purposes, three urban canyons are used. Using three different canyons allows avoiding singular propagation effects due to particular building positioning to achieve uncorrelated statistical time-series. Those three canyons have been chosen since they are representative of typical urban environments from dense areas (canyons 1 and 2) to continuous building profiles (canyon3).

All three canyons are presented in Fig.2.4. The geometry of canyon 1 and canyon 2 represent typical discontinuous urban canyons in a dense urban area with buildings up to 12m high. Both scenarios are about 100m long. Blue blocks represent city centre façades while green blocks represent ONERA office façades. Canyon 3 differs slightly from the previous ones. Canyon 3 represents a continuous façade of 80m long for 12m high composed of both city centre façades and ONERA office façades. Since the main focus of this chapter is placed on scattering, the buildings are assumed to be on only one side of the street, the other one being building free. The LOS condition, from clear LOS to blockage, is simulated afterwards by attenuating the direct signal.

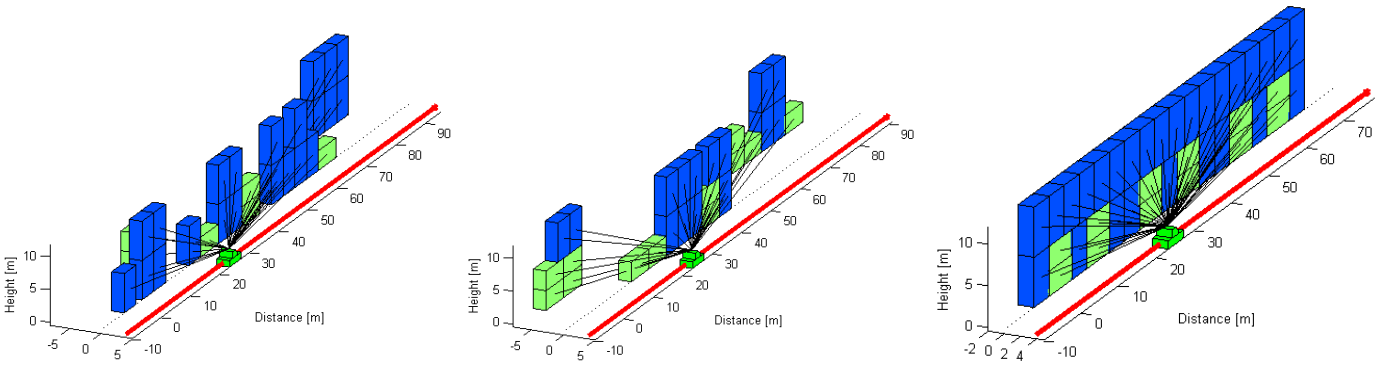

(a) Canyon 1 (b) Canyon 2 (c) Canyon 3

Figure 2.4: Representation of the three different urban canyons

Keeping in mind the mobile context for satellite navigation applications, the channel is assessed using different speeds: 5, 50 and 90 km/h. Those speeds influence the averaging process taking place in navigation receivers during signal integrations. To reproduce this process, a rectangular sliding window was used. The assumed integration time is 20 ms [Kapl 05] corresponding to one standard navigation data bit [Park 96].

2.2 Preliminary observations made on isolated canonical façades

The purpose of this section is to observe qualitatively the contribution of small features into the total MP power scattered by complex façades. Several parameters related to EM phenomena are observed such as surface currents, radar cross sections or near field scattering patterns. Preliminary observations made in this section allows to introduce better and understand conclusions made in Section 2.3 and Section 2.4, relatives to narrow-band and wide-band issues respectively.

2.2.1 Analysis of surface currents

This first visual analysis is based on surface currents calculated using Elsem3D. Surfaces currents are displayed in logarithmic scale. Since this first analysis remains qualitative, numerical values are of low interest and are not discussed. From the observation of many configurations, several particular phenomena are noticed and presented hereafter.

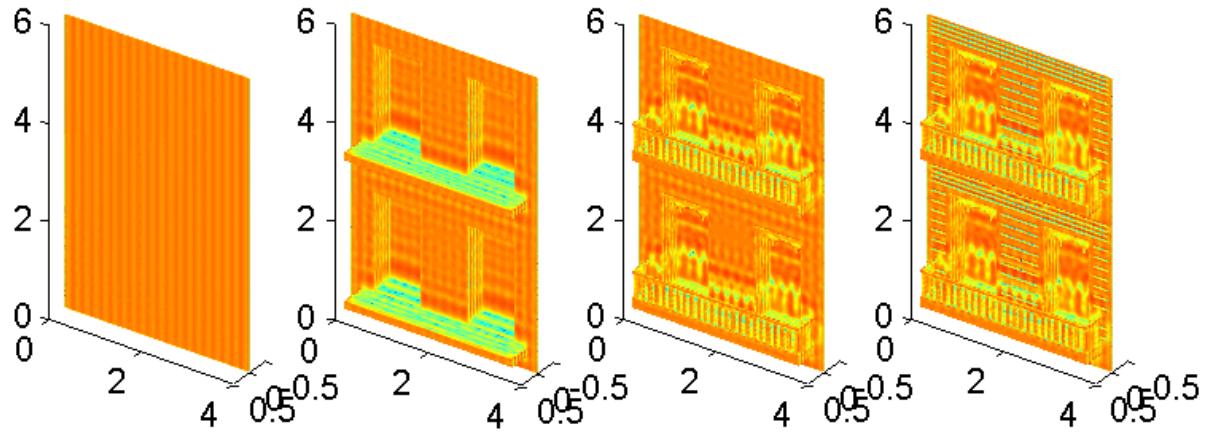

Figure 2.5: Quasi-optical inter-element shadowing visible on surface currents over the city centre façade in the case of a normal incidence with ϕ polarisation

Fig.2.5 represents surface currents on city centre façade with normal incidence and ϕ polarisation. Red parts represent high current densities over the surface while blue parts represent low current densities. As can be seen on the null resolution case (left diagram), some streaks are visible. They are oriented perpendicularly to the incident polarisation and are due to stationary surface currents. This observation is in agreement with the theory. Another phenomenon can also be observed for medium and high resolution (middle right and right diagram): the quasi-optical shadowing of the guardrail over the rear windows and the walls. This observation allows highlighting how discontinuous elements such as the guardrail can partly mask some others placed behind.

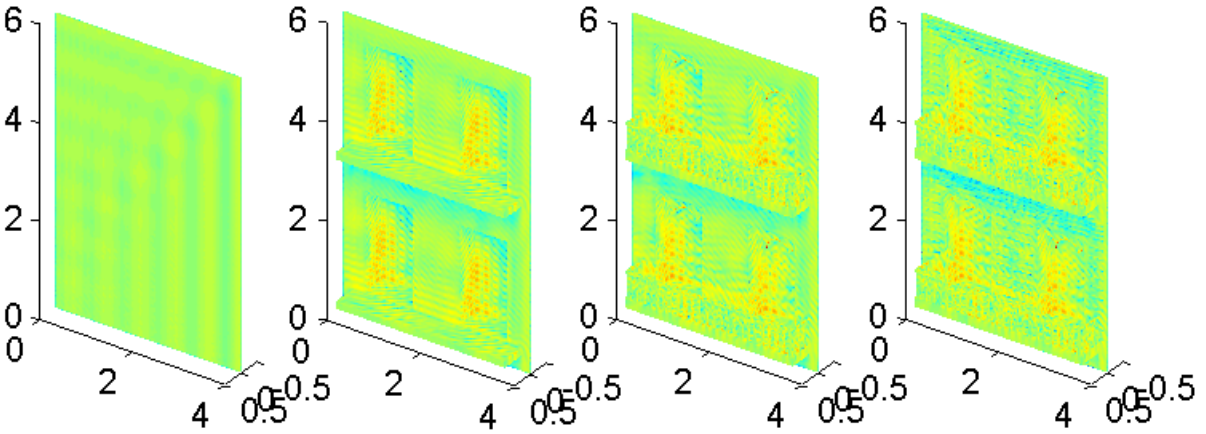

Figure 2.6: Dihedral reflections are visible on surface currents over the city centre façade in the case of a typical LMS incidence (elevation 40°, azimuth 40°) with ϕ polarisation

For typical LMS incidences (40° elevation) with non null azimuth, the streak pattern observed previously in Fig.2.5 are different and less visible in Fig.2.6. The inter-element shadowing mentioned previously, remains visible on low to high resolution where the top balcony masks the

underlying windows and some parts of the wall. For typical LMS incidences another interesting observation can be made. More visible on the low resolution, surface currents seem concentrated in the left bottom of each window representative of dihedral and trihedral effects. This observation is confirmed by observations made in the next section relative to radar cross sections and is of high interest for Chapter 4.

For extreme incidence configurations (elevation 80°) the main observation is that window frames (Fig.2.7) and protruding edges (Fig.2.8) are concentrating the currents contrary to other elements. This observation highlights the importance of edge diffraction on window frames and balconies when surface reflection decreases due to the incidence configuration. Also noticeable, the streak pattern on the null resolution is almost invisible for extreme incidences due to projection effects of incident wave polarisation which reduces the resonance phenomenon.

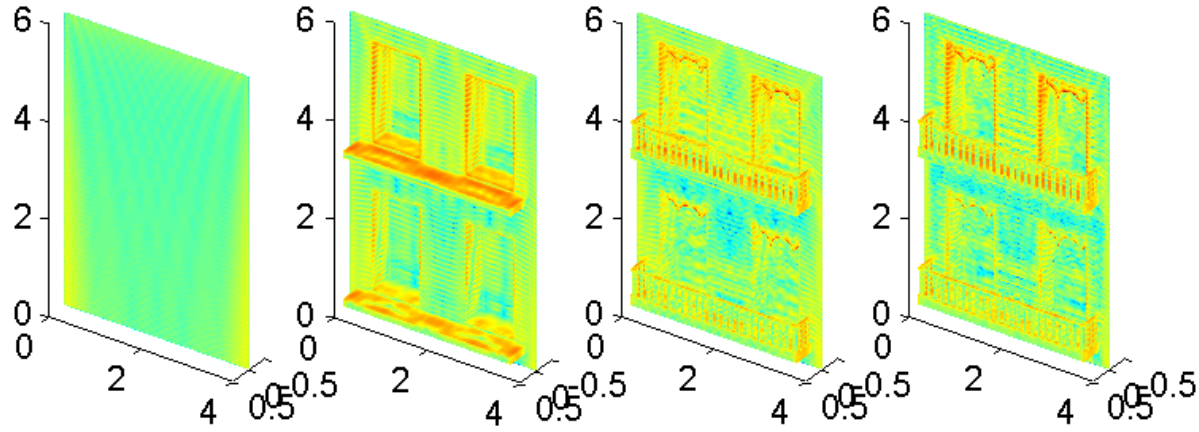

Figure 2.7: Edge diffraction is visible on edge currents on the city centre façade in the case of extreme incidence (elevation 80°) with ϕ polarisation

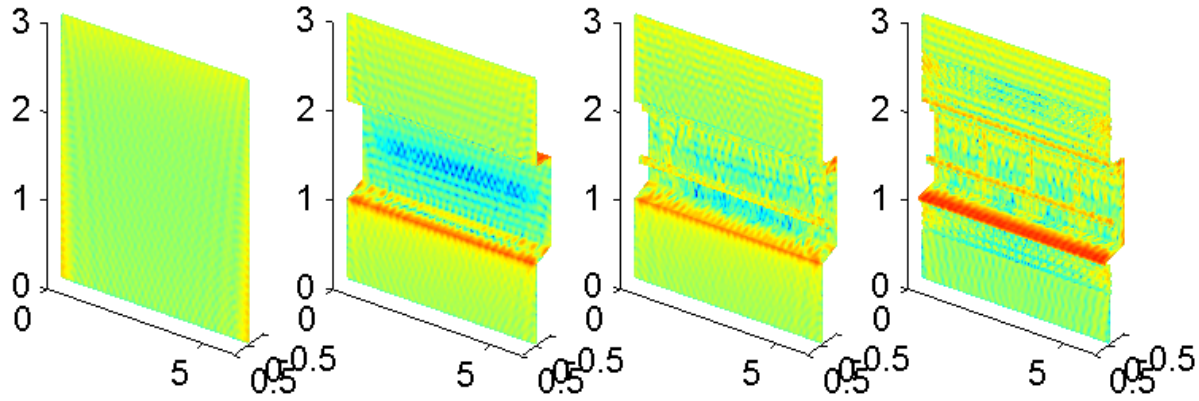

Figure 2.8: Edge diffraction visible on current distribution over the ONERA office façade in the case of extreme incidence (elevation 80°) with ϕ polarisation

2.2.2 Analysis of Radar Cross Sections

This second analysis is also qualitative and based on RCS analysis calculated using Elsem3D. The principle is to make radiating the currents previously presented and to observe the RCS in the case of far field, or the pseudo-RCS in the case of near field. Finally, a first estimation of the relative contribution of each type of detail into the total MP power scattered by complex façades is given.

Fig.2.9 represents the near field pseudo-RCS of city centre façade. The RCS representation considers all four resolutions of the city centre façade, from left to right, for co-polarisation and cross-polarisation, from top to bottom. Each RCS map is presented from -90 ° to 90 ° azimuth on x axis and from -90 ° to 90 ° elevation on y. The scattered EM fields are calculated at 20m from the façade and converted to pseudo-RCS using Eq.2.1. As a remark, the far field limit and the near reactive field limit are given respectively by Eq.2.2 and 2.3 [Knot 04] where r represents the distance from the object to the receiver, E_{inc} the incident field, E_d the scattered field and D the largest dimension of the object. The far field limit is equivalent to 520m for the city centre façade case, well above the 20m case here presented. In the following, RCS and pseudo-RCS are expressed in dBm^2.

$$RCS\left(\vec{u}\right) = \lim_{r\to\infty} 4\pi r^2 \frac{|\vec{E}_d\left(r,\vec{u}\right)|^2}{|\vec{E}_{inc}|^2} = \frac{|\vec{E}_l\left(\vec{u}\right)|^2}{|\vec{E}_{inc}|^2} \tag{2.1}$$

$$r_{Far\ field} > \frac{2D^2}{\lambda} \approx 520\,m \tag{2.2}$$

$$r_{Near\ reactive\ field} < 0.62\sqrt{\frac{D^3}{\lambda}} \approx 26\,m \tag{2.3}$$

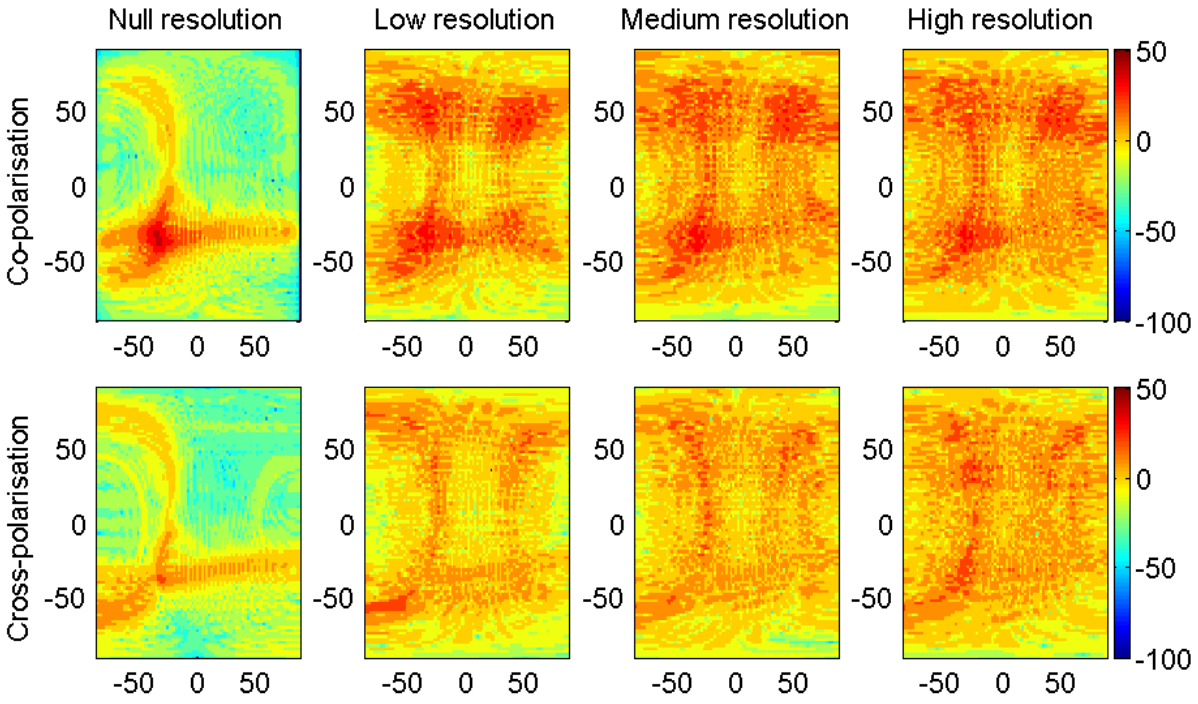

Figure 2.9: Near field pseudo-RCS of the city centre façade with polarisation ϕ in configuration 40° elevation, 40° azimuth for all four resolutions

As can be seen in Fig.2.9, the specular contribution is clearly visible at -40° elevation and -40° azimuth for the null resolution considering the co-polarisation diagram. Note that this specular zone is wide due to the near field effects and the almost guided propagation phenomenon taking place at this distance. When adding details to the representation of the façade, the 3D scattering function varies significantly. Considering low resolution diagram in co-polarisation, four zones are visible. The first one represents the specular reflection (-40° elevation, -40° azimuth). The second one represents a specular reflection on the top balcony (40° elevation, -40° azimuth). The third one represents a backscattering (40° elevation, 40° azimuth) due to trihedral effects in windows corners as mentioned in the previous section relative to surface currents. The last ones represent a backscattering (-40° elevation, 40° azimuth) due to dihedral effects also taking place near windows corners. For higher resolutions (medium and high), it can be noticed that

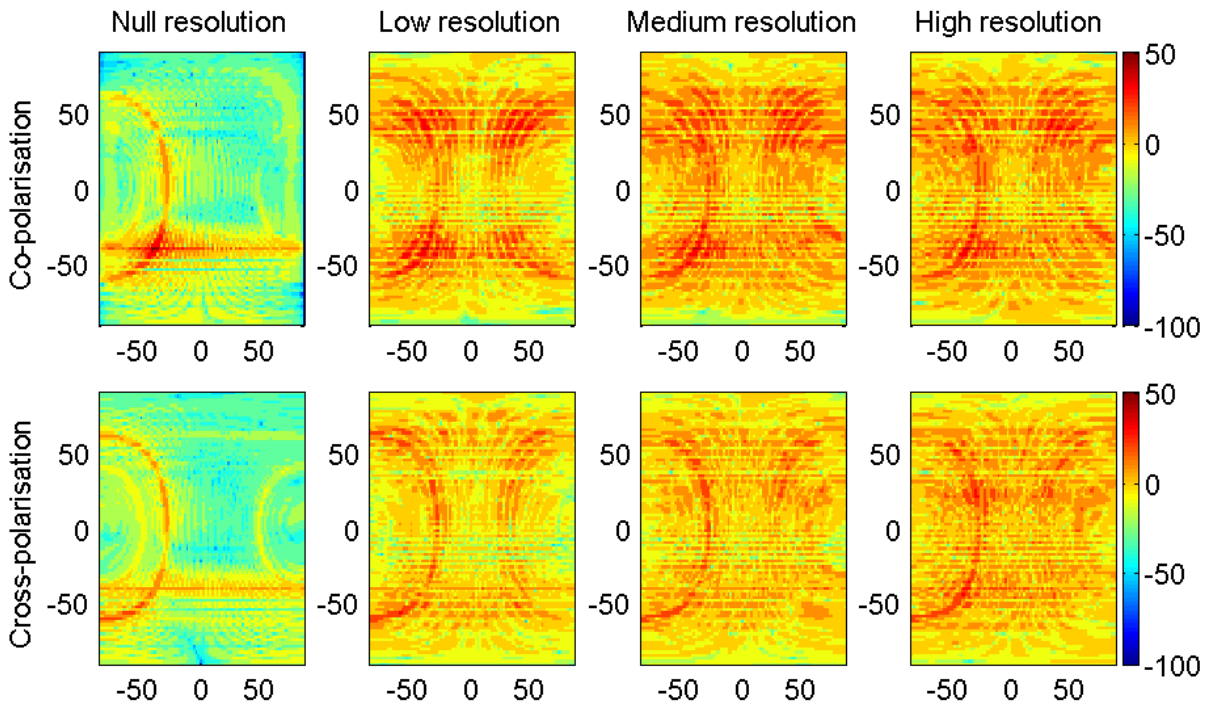

Figure 2.10: Far field RCS of the city centre façade with polarisation ϕ in configuration 40° elevation, 40° azimuth for all four resolutions

the four previously mentioned areas are less visible due to the augmentation of small features which reduces the specular phenomenon and increases the scattering phenomenon. This addition of small features contributes also to increase the cross-polarisation contribution as visible on bottom diagrams of Fig.2.9.

Fig.2.10, presents similar results in far field conditions. The main observation is that the wide specular zone becomes a specular point in the case of null resolution. Its power is also higher compared to near field results. For other resolutions, the three zones described previously are less visible. In addition, constructive and destructive interference patterns are clearly visible. To isolate and quantify the contribution of specific details into the total MP scattered power by comparing RCS maps from null resolution to high resolution, the previous results have been used. The first solution consisted in a RCS map difference. However, a metric of comparison using mathematical criterion has not been found and this approach has been discarded. The second approach is slightly different. The principle is to isolate surface currents on some details into the CAD model of the façade and make them radiate separately from the whole surface currents present on the façade. This allows quantifying the radiation coming from specific parts of the façade.

The following results have been obtained using Elsem3D in two steps. The first step consists in illuminating the canonical façades with the highest level of detail, Fig.2.2d and Fig.2.3d, to compute and store the induced surface currents over the whole surface. The second step consists in re-radiating only the currents from specific parts of the canonical façade up to the observation point. Thus, making each part of the building re-radiate one after the other, the contributions are separated and each one can be isolated from the total radiation pattern. Note that the currents on each detail are calculated at once all together in the first computation step, including neighbouring interactions, and neither discontinuities nor side effects occur when they re-radiate separately. It has been also verified that the coherent sum of all elementary contributions from the canonical façade to the receiver point is equal to the total radiation when the parts are radiating all together. One example of this procedure is presented in Fig.2.11 with the guardrail of the city centre façade where left diagram presents the surface cuurents on the iso-

lated guardrail, middle diagram presents the co-polar RCS map from -90° to 90° azimuth in the x axis and from 0° to -90° elevation in the y axis, right diagram presents the cross-polar RCS map.

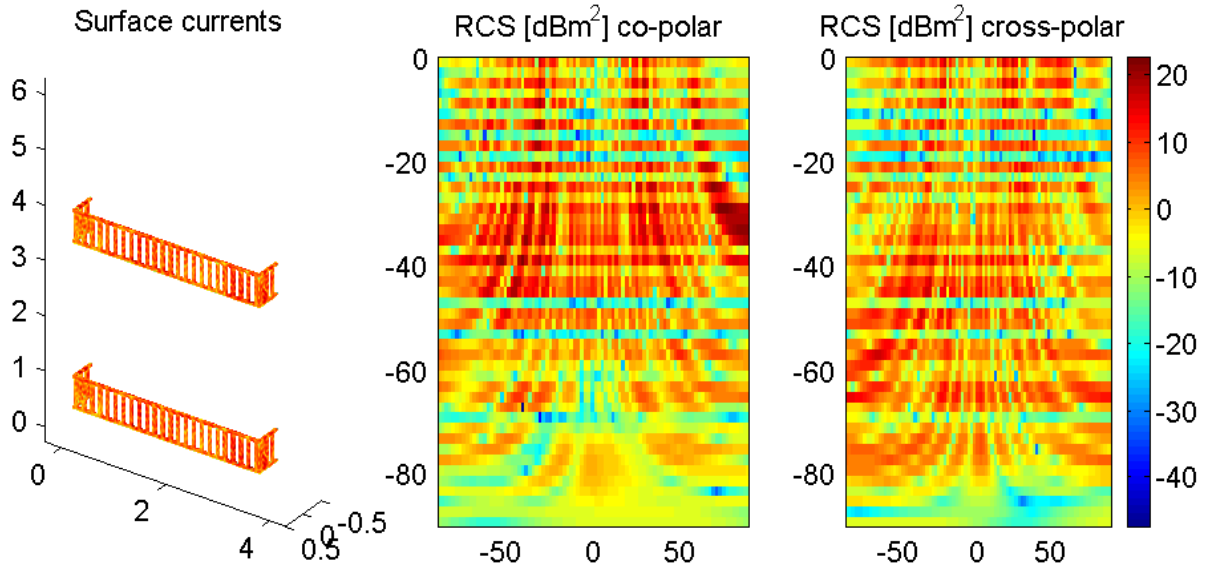

Figure 2.11: Illustration of the isolation principle of the guardrail contribution from the rest of the city centre façade.

The details present on canonical façades have been separated in four classes as illustrated in Fig.2.12. The class 1 (green) contains only the flat parts of the walls. The class 2 (yellow) contains windows and balconies. The class 3 (orange) contains shutters and guardrails. Finally, the class 4 (red) contains all smaller details. Note that each class of detail reproduces roughly the characteristics of each detail resolution from null to high. The contribution of each class of detail has been evaluated in the far field. To reduce computation time, only negative elevations are considered in the RCS map as presented in Fig.2.11. This assumption implies that the receiver can only be reached by contributions coming from above its horizontal plane. In practice, this assumption is commonly used since the receiving antenna diagram is normally hemispherical and oriented toward the sky, strongly attenuating the contributions coming from below its horizon [Kapl 05].

The studied re-radiating space is split in two zones: the specular zone and the non-specular zone. The specular zone is defined by ±2° around the geometric specular point. The non-specular zone represents all other angular regions. In the presented results, we consider only the magnitude of the scattered electric field without considering any polarisation loss at the receiver. The contributions in Tab.2.1 are presented in unit scale. One unit represents the total MP scattered power using a high resolution model. Note that the sum of each line equals one.

Unit	Flat walls (green)	Window+Balcony (yellow)	Guardrail+shutters (orange)	Small details (red)
Spec	0.50	0.21	0.25	0.04
Non-Spec	0.25	0.34	0.29	0.12

Table 2.1: Contribution of each class of details for specular and non specular zones for city centre façade in configuration 40° elevation, 0° azimuth, θ polarisation

From Tab.2.1, it can be observed that the scattered power received in the specular zone comes mostly from the flat parts of the wall, 50% in the presented case. The contribution of the smallest details is almost negligible in this zone, about 4%. However, in the non-specular zone,

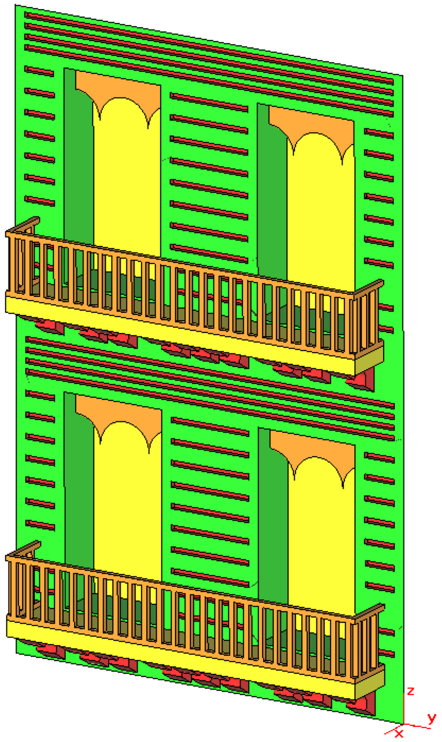

Figure 2.12: Illustration of the four different classes of details.

the contribution of the small details increases, reaching 12% of the total MP scattered power, while the contribution of the flat parts decreases. Also noticeable is the contribution of the intermediate details, yellow and orange, which increases in the non-specular zone compared to the specular zone. As expected, the above observations confirm the fact that large and flat surfaces dominate in the specular zone while the smaller objects and sub-wavelength details are dominant out of the specular zone.

The results from Tab.2.1 have been generalized for multiple incidences using both θ and ϕ polarisations over city centre type and office type façades. Fig.2.13 presents the generalised result in the case of a city centre building type for θ polarisation. Note that the RCS coefficient is given for each incidence angle to provide a better idea of the physical quantities involved. This RCS coefficient has been evaluated only at the specular point. It is noticeable that the RCS decreases with the angle due to projection and visibility effects from the source to the façade. As a comparison, RCS of a metallic plate of this size would be 52.57 dBm^2 for normal incidence and 47.94 dBm^2 in the case of 40° elevation, 40° azimuth.

In Fig.2.13, comparing RCS values to theoretical values for PEC plate, it is obvious that the details contribute to decrease the total RCS in the specular zone. Fig.2.13 reveals also that the details in the range of one wavelength and smaller, class 3 orange and 4 red, have a greater impact out of the specular zone. Those details, present in medium and high resolutions, re-radiate from 30% to 50% of the total MP scattered power out of the specular zone depending on the geometrical configuration. In the specular zone, the relative contribution of the same details is lower.

The conclusion is that details are more visible out of the specular zone even if their absolute contribution is not higher. Small details tend to scatter power in every direction almost uniformly. In the specular zone, those small contributions are masked by the strength of the specular reflection.

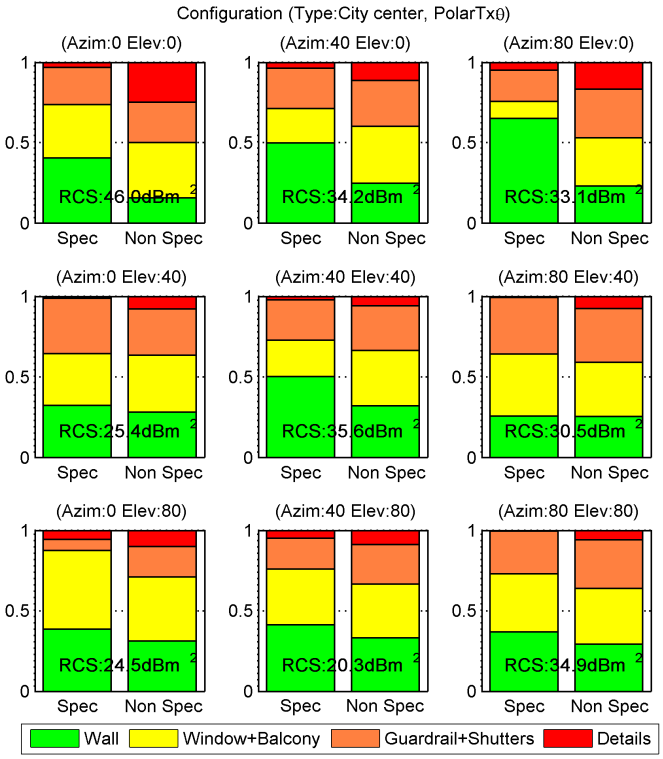

Figure 2.13: Contribution of the details for different source incidences. From left to right increasing azimuth (0°, 40°, 80°) and from top to bottom increasing elevation (0°, 40°, 80°). Case of the city centre façade illuminated with θ polarisation

2.2.3 Analysis of the near field scattering pattern

As mentioned previously, far field conditions will never be fulfilled for our final application in urban environments considering such sizes of façades. Even more, since echoes delayed of more than 300m are not seen by the loop inside the receiver [Kapl 05], modelling the far field contributions from those façades presents no interest for a navigation receiver. This subsection particularly addresses the near field issue. This subsection is focused on the power distribution coming from the reflection on canonical façades and observed in the horizontal plane in their close vicinity. The goal is to illustrate how small features impact the scattering pattern of such façades and how the energy flux spreads itself around the façades.

In this section all power maps are presented in dB scale w.r.t the LOS contribution. Fig.2.14 and Fig.2.15 represent a top view of the scene, where the city centre and ONERA office façades are respectively centred at x=0m, y=2m and x=0m, y=3m, x and y axis representing the horizontal coordinates of the horizontal plane. Each power map, from left to right, is representative of one resolution according to Fig.2.2 and Fig.2.3. The dashed blue line represents the geometric reflection zone where geometrically reflected rays are possible.

Fig.2.14 represents the scattering pattern around city centre façade for all four resolutions. The scattering pattern is dependent on the resolution of the façade. For the null resolution, the main contributions are included in the specular zone and are close to 0dB w.r.t LOS. This observation is mainly due to the PEC assumption made on materials. However, lower contributions are visible in the continuity of the geometric reflection zone and close to the façade. Constructive and destructive interference patterns are also observable for the null resolution. When adding details, the scattering pattern overlaps progressively the geometric reflection zone. Contributions in the geometric reflection zone are less powerful but spreader. The regular interference pattern have also disappeared due to the addition of small details increasing the scattering phenomenon.

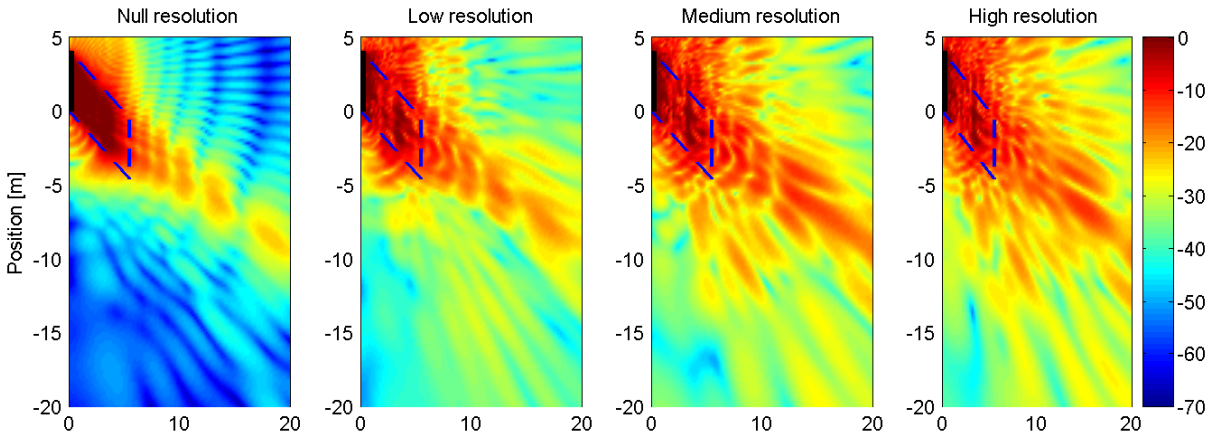

Figure 2.14: Near field scattering in the horizontal plane near the city centre façade with ϕ polarisation at 40° elevation, 40° azimuth

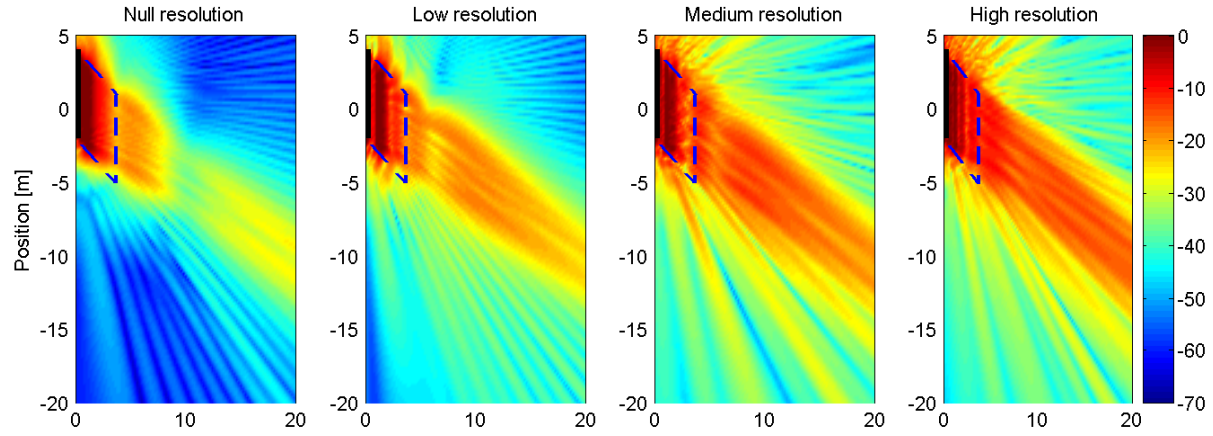

Figure 2.15: Near field scattering in the horizontal plane near the ONERA office façade with ϕ polarisation at 40° elevation, 40° azimuth

Fig.2.15 represents the scattering pattern around ONERA office façade for all four resolutions. As a comparison between Fig.2.14 and Fig.2.15, it is obvious that the architecture of the façade has a strong impact on the scattering pattern. Being smoother compared to city centre façade, ONERA office façade mainly reflects power in the continuity of the geometrical reflection zone. The addition of details seems to increase this phenomenon.

The last observation presented here deals with the energy flux and the Poynting vector. Since the E field and the H field are accessible with Elsem3D simulations, Poynting vectors are easy to compute using Eq:2.4. Poynting vectors can be used to identify where the main energy flux comes from. In practice, the resolution on the horizontal plane is too low to identify specific contributions. However, studying the energy flux reveals that small features have an important impact on the way EM waves propagate around the façade.

$$\vec{\mathcal{P}} = \frac{1}{2}\,\vec{E} \wedge \vec{H}^{*} \tag{2.4}$$

Fig.2.16 represents this energy flux using small arrays projected on the horizontal plane. The magnitude is represented by the colour map. The zoom at null resolution reveals that the energy flux fits almost perfectly the power zone. This phenomenon is relevant of some kind of EM guided wave propagation which is characteristic of near reactive field conditions. For low and medium resolutions, the addition of details allows to reduce the coherence of the reflecting surface avoiding almost guided propagation phenomena. Two directions of the energy flux are clearly visible. One is in the specular direction (negative y) while the other one is on the

opposite direction (positive y). This second direction is representative of the dihedral effect highlighted in previous subsections. This second direction is of high interest for the following chapters. Observing the high resolution map, the energy flux seems to be related to the small details and is almost chaotic when close to the façade. As for the three other resolutions, the steady propagation state is almost established by the end of the map where Poynting vectors are radially oriented w.r.t the centre of the façade.

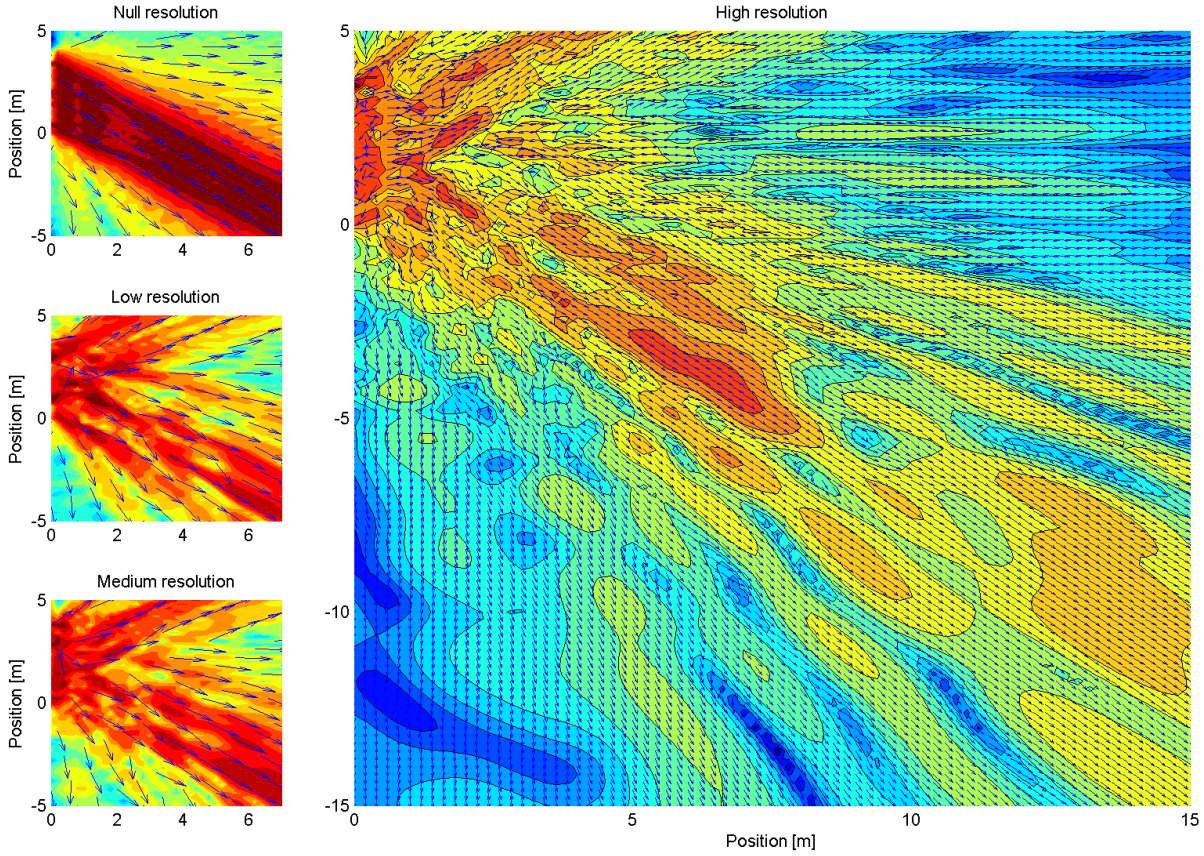

Figure 2.16: Scattering flux in the horizontal plane near the city centre façade with ϕ polarisation at 0° elevation, 40° azimuth

Section synthesis :
This section presents several preliminary observations on the influence of small features on the scattering phenomenon taking place near complex façades. This analysis is realised on isolated canonical façades. The main observations are listed below:

- *Surface currents are sensitive to source incidence with streak pattern for normal incidence and current concentration on protruding edges for high elevations. The analysis of the surface currents reveals also a quasi-optical shadowing between elements from one façade (top balcony on walls). This observation remains valid even when considering discontinuous objects (guardrails on walls).*
- *The RCS study shows that far field and near field results are different. It is noticed that small objects reduce the specular phenomenon while increasing the scattering phenomenon and cross-polarisation contribution.*
- *The specular reflection is the strongest contribution. It comes from wide surfaces and has a limited angular profile. The contribution of small features is lower compared to specular reflection and is only visible out of the specular zone.*
- *Dihedral and trihedral effects taking place in windows corners have been highlighted on surface currents, RCS and near field scattering patterns. This phenomenon will be described as* Backscattering *in Chapter 3.*
- *The architecture of the façade has a strong impact on all observed parameters. Classification from real façades to synthetic CAD façades has not to be neglected.*

Eventually, near field scattering is of high importance for the following work since far field conditions are never fulfilled.

2.3 Influence of small features on MP power estimation

After studying the case of isolated canonical façades, urban scenarios and mobile applications are addressed in the next two sections of this chapter associating the contribution of several canonical façades. This section is focused on narrow-band criterion. This section analyses and evaluates the influence of small features on synthetic MP power time series, followed by a statistical analysis for better representativeness of the results. This analysis is oriented toward mobile telecommunication systems and is useful for quantifying the total MP power difference due to the use of simple 2D surface models. As an example, a direct application of those results leads to tune more precisely Rice distributions as required in [Oest 99b] presented in Section 1.1.3.1.

2.3.1 Simple narrow-band channel model

To produce simple time series, the scattered EM field is calculated using Elsem3D along one trajectory. The receiver trajectory is parallel to the y axis at x=4m and is sampled every $\lambda/10$ over a range of $\pm$300 m around façade centre. This 300 m limit corresponds to the path difference beyond which multipaths will not interfere with the direct signal and will not introduce pseudo-range errors in navigation receivers as it will be eliminated by the DLL [Kapl 05]. A database of simple time series is then constituted considering the two canonical façades, the four resolutions, the three elevations, the three azimuths and the two polarisations. To produce complex time series, several façades are aligned one after the other. At each receiving point, contributions of all façades are summed coherently depending on the relative position of the receiver with respect to the façade. Note that one single contribution is assumed from each canonical façade.

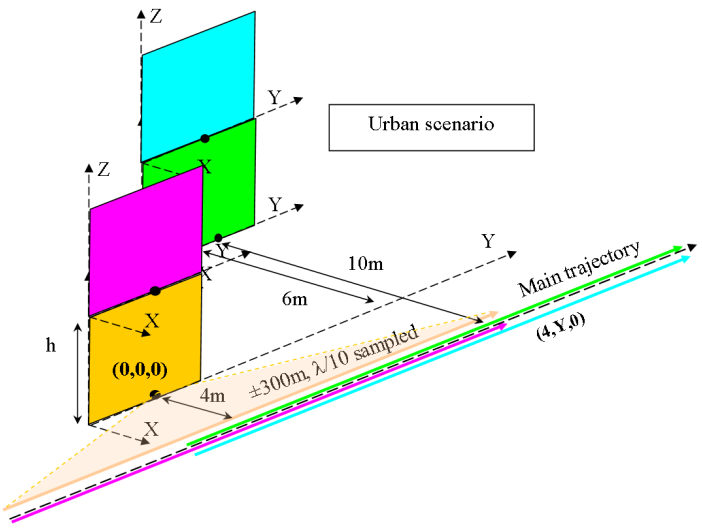

Figure 2.17: Complex narrow-band time series synthesis and summing principle used for simple urban scenarios

For more realism, the database of simple time series has been extended considering a total of four possible locations of the canonical façade as shown in Fig.2.17. This results in a final database taking into consideration two floor levels of façades and two rows of façades (x=0m, x=-6m) to consider higher buildings and different back settings from the road.

2.3.2 Qualitative analysis of MP power time series on simple urban canyons

The assumed scenario is the following: a receiver is moving along a linear trajectory parallel and at 4m from a row of buildings where each building may be made up of various canonical façades. While varying façades resolution, we obtain different time-series. It is this difference in terms of narrow-band MP scattered power that is analysed below to quantify the error made on estimated MP scattered power when simplifying the environment. For all the results presented below, the high resolution case is considered as a reference and all powers are represented relative to the unblocked LOS signal.

Fig.2.18 to Fig.2.20 are based on the same figure representation template. The top diagram represents the total MP power scattered by the façades to the receiver for all four resolutions of the canyon. Considering the high resolution as a reference, the bottom diagram displays the dB difference between null, low and medium resolutions, filtered using a sliding window of 20 ms. Note that the size of the window depends on the mobile speed since the trajectory is distance sampled. Fig.2.18 represents a standard incidence configuration for LMS applications while Fig.2.19 and Fig.2.20 illustrates the case of higher elevation of the source. From a visual inspection of all eighty-one configurations for each resolution (three canyons, nine incidences, three speeds and fixed θ polarisation) several statements can be made.

The first statement is that MP scattered power time series are dependent on the canyon profile. The influence of each building is obvious on times series and depends on its position and height. For example, on top Fig.2.18 the influence of the last blue building in canyon 1 (Fig.2.4a) is clearly visible between 65 m and 80 m.

The second statement is the lack of accuracy when using the plane surface compared to the high resolution. Typical observable differences are between +10 to -30 dB depending on the incidence configuration. For typical LMS incidences, below 40° in elevation and azimuth, the null resolution tends to over-estimate the MP scattered power in the specular zone, as shown at the bottom of Fig.2.18. This can be explained by the existence of specular points on façades

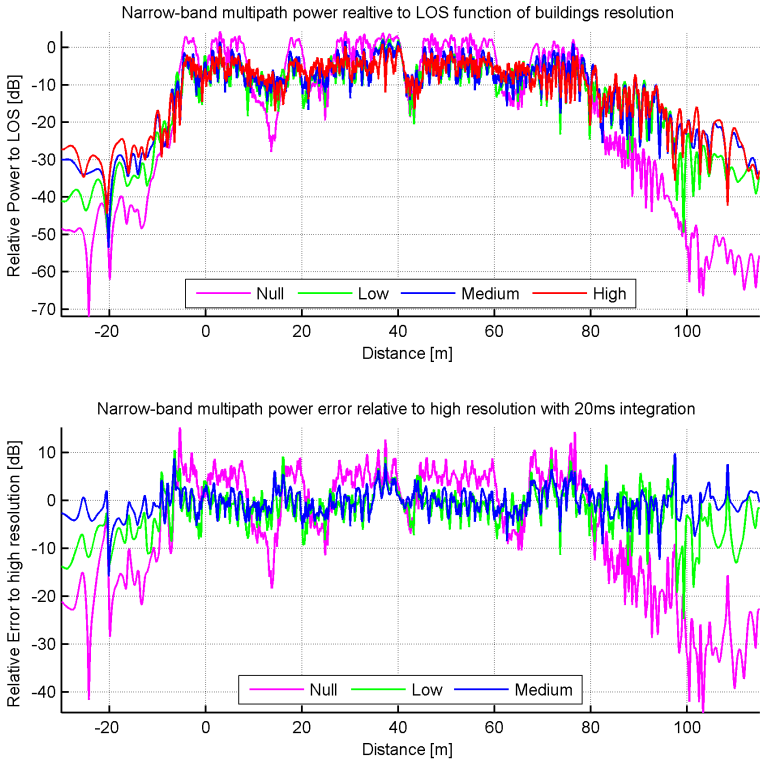

Figure 2.18: Multipath scattered power time series as a function of the resolution. Simulated case: urban canyon1, azimuth 40°, elevation 40°, Tx polarisation θ, speed 50 km/h

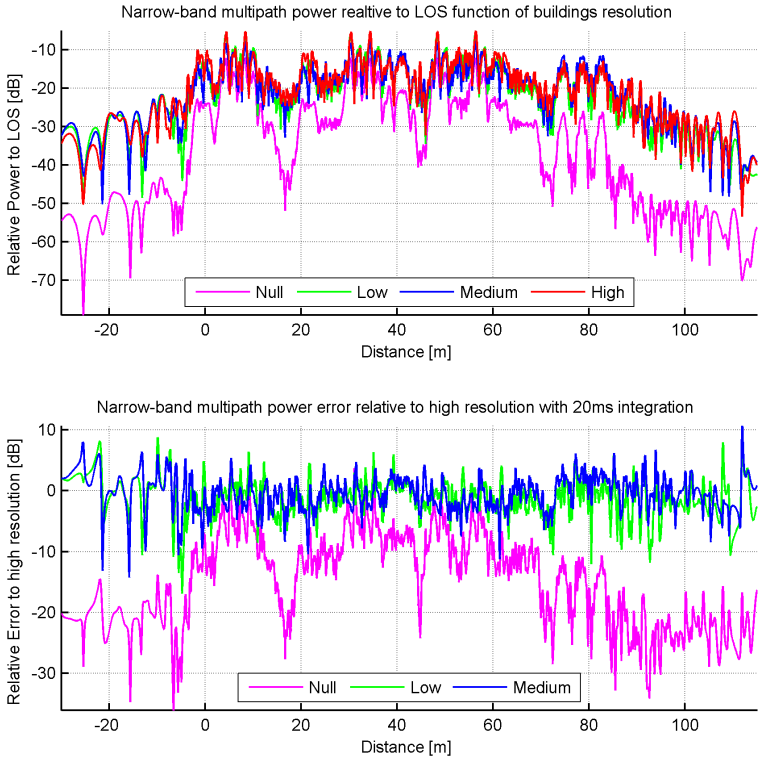

Figure 2.19: Multipath scattered power time series as a function of the resolution. Simulated case: urban canyon1, azimuth 40°, elevation 80°, Tx polarisation ϕ, speed 50 km/h

inducing a perfect geometrical reflection on the metallic plates. The region from -5 m to 80 m is then characterized by the presence of strong echoes. On the contrary, in non-specular zones, the null resolution tends to under-estimate the MP scattered power. This is particularly visible

for extreme incidences. Fig.2.19 and Fig.2.20 are a typical illustration of this phenomenon. At 80° elevation, specular points on façade do not exist anymore. The MP power scattered by the environment is then highly underestimated. It is also visible at the beginning and at the end of each time series when the receiver is out of the reflection zone of the canyon.

A last statement is about the speed of the mobile. It can be noticed comparing Fig.2.19 and Fig.2.20 that the integration time has a strong influence. For high speed, the deep fades are averaged and the dynamic range of the MP scattered power time series gets reduced.

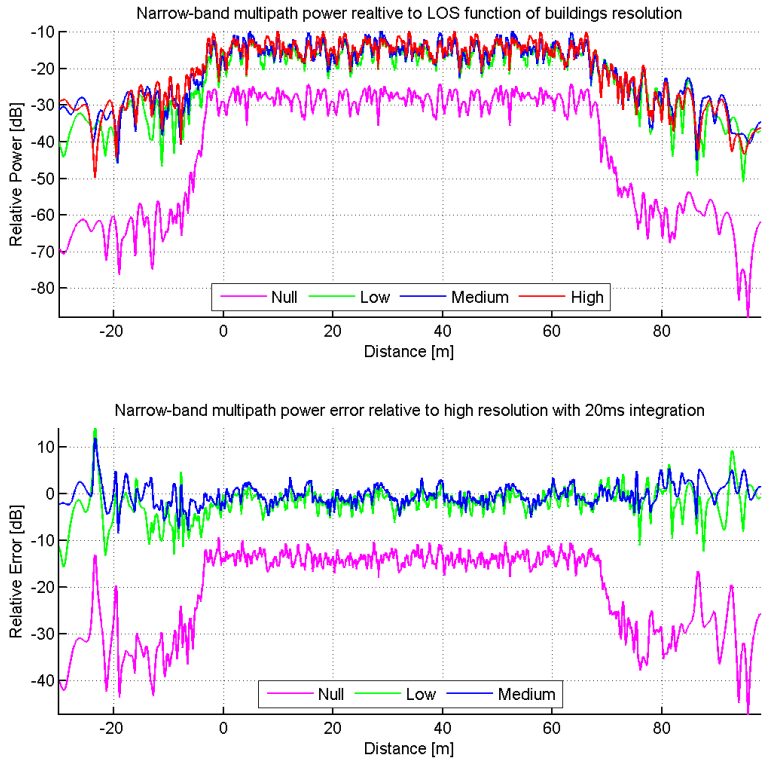

Figure 2.20: Multipath scattered power time series as a function of the resolution. Simulated case: urban canyon3, azimuth 80°, elevation 80°, Tx polarisation ϕ, speed 90 km/h

2.3.3 Statistical analysis of MP power time series on simple urban canyons

In general, the results for the low and medium resolutions show good agreement with respect to the high resolution case and it remains difficult to discriminate which one is accurate enough. Thus, to better compare them, a statistical analysis has been conducted. From each simulated configuration, two error parameters were extracted from the relative MP scattered power (bottom diagrams): the mean error and its standard deviation. Both parameters have been calculated only in the reflection zone, approximately from y=0 to 85 m depending on the incidence angle, where canonical façades have an influence.

The statistics shown in Fig.2.21 present the influence of the environment resolution on the MP scattered power. A cumulative density function based on all eighty-one configurations is here used to present both error parameters over the different resolutions. Left diagram presents the cdf of the mean error while right diagram presents the cdf of the standard deviation error.

The medium resolution shows the best agreement in terms of mean error and standard deviation. However, the mean error and the standard deviation for low resolution present similar slopes. The difference between both resolutions is about 2 dB for the mean error and less than

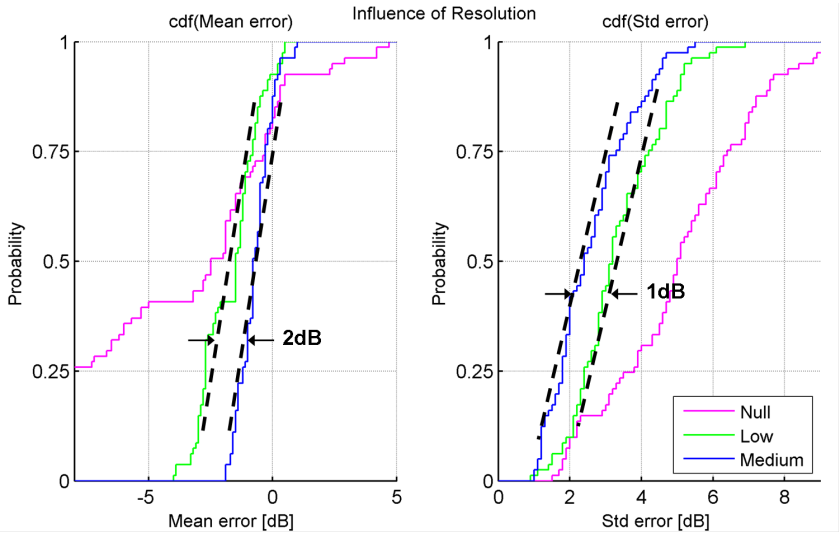

Figure 2.21: Influence of the environment resolution on the MP scattered power relative to the high resolution

1 dB for the standard deviation. Thus the low resolution could be acceptable for computing the MP scattered power. Indeed, by slightly filtering the time series when using low resolution to reduce the dynamic and by adding an empirical offset to the obtained MP scattered power of about 2 dB to compensate the mean error, the low resolution could be a good compromise to quickly obtain a reasonable estimate of the MP scattered power. Nevertheless, a major gap can be observed between the null resolution and other resolutions. As mentioned above, the null resolution over-estimates reflected power for some cases and highly under-estimates scattered power for the other cases. As a general comment, the mean relative errors for all three simplified resolutions are mostly negative due to a reduction of the scattering phenomenon when simplifying environment representation. For example, even for the medium resolution the median of the mean error is about -0.7 dB.

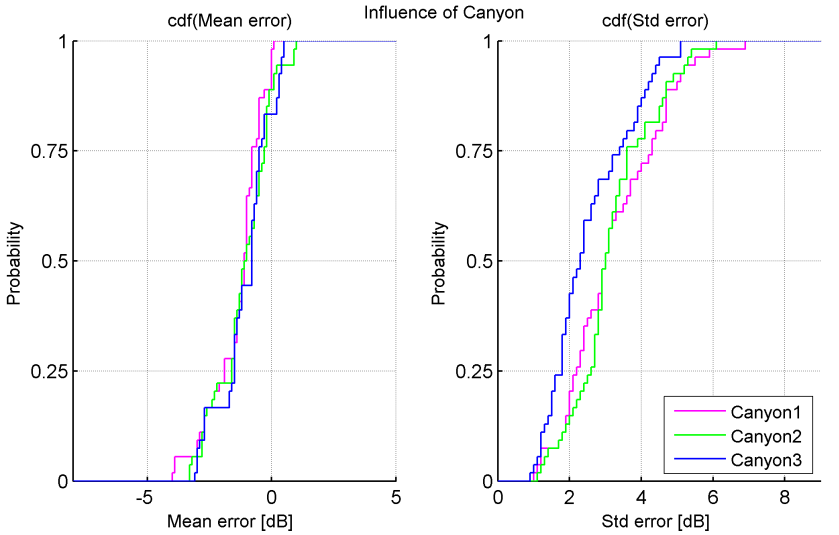

Figure 2.22: Influence of the canyon geometry on the MP scattered power relative to the high resolution

The statistics shown in Fig.2.22 present the influence of the canyon on MP scattered power. Those statistics have been established on fifty-four cases removing the null resolution from the eighty-one cases database since they were no more relevant. As can be seen, the impact of the canyon on the error made is not significant. The conclusion is that the influence of small details

is not dependent on the considered urban canyon.

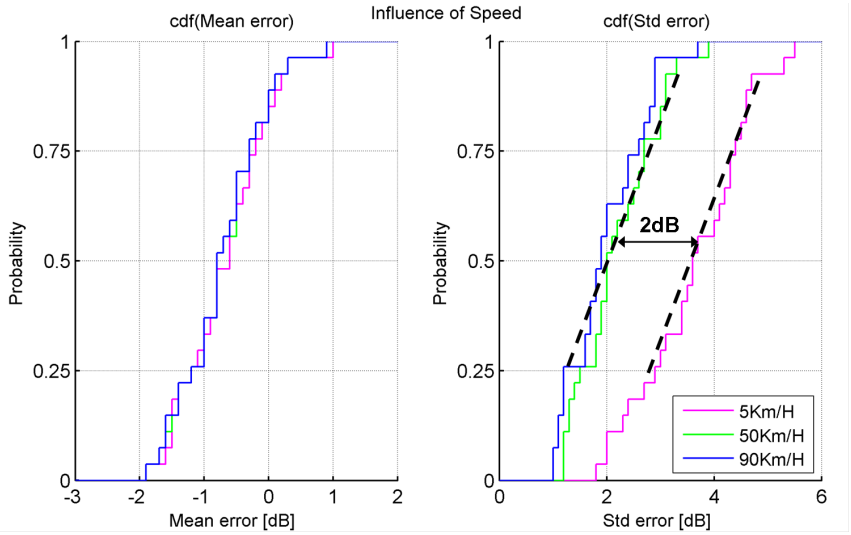

Figure 2.23: Influence of the speed on the MP scattered power relative to the high resolution

The statistics shown in Fig.2.23 present the influence of speed on MP scattered power. This figure has been produced using twenty-seven cases (three canyons, one speed and nine geometrical configurations) considering a fixed medium resolution to avoid the influence of environment representation. This figure reveals that the speed has no impact on the mean error since all cumulative density functions are almost equal. However, a constant difference of about 2 dB is observable for the standard deviation between slow motion, 5 km/h, and fast motion, 50 and 90 km/h. This phenomenon is due to the integration process which mitigates fading depth, decreasing signal dynamics and therefore the standard deviation of the error made.

Section synthesis :
To conclude this section on narrow-band issue in urban canyons, the following statements can be made.

- *The details in the range of the wavelength or smaller, contribute highly to the scattering phenomenon and are particularly visible out of the specular reflection region. Neglecting them by using a null resolution would unbalance the specular and scattering phenomena through favouring the strong reflections.*
- *The null resolution shows obvious limits. The null resolution does not reproduce any scattering phenomenon. It results in a MP scattered power over-estimation for typical LMS incidences and under-estimation for extreme LMS incidences. The null resolution is almost comparable to an on/off reflection model with significant transition effects.*
- *When using the low resolution where details are large compared to the wavelength, the specular reflection is well reproduced without fully reproducing the scattering phenomenon present on medium resolution. Low resolution seems acceptable if slightly corrected by empirical offset on the mean MP scattered power and filtered for decreasing the signal dynamic.*
- *The slow motion case (5 km/h) seems more restrictive since the integration process does not compensate deep fades as it is the case for fast motion (50 and 90 km/h).*
- *Medium resolution is the best compromise since high resolution is not applicable at city scale.*

2.4 Influence of small features on navigation receivers

To complete the above narrow-band analysis, a wide-band study has been performed addressing particularly the navigation applications. The goal is to quantify the influence of the resolution of the environment on the receiver performance when estimating the pseudo-range to a satellite. The simplified navigation receiver model used in this section has been described in Appendix A.2.1. This section is organised as follow. First, the wide-band channel model used to generate the CIRs is presented. Then, several analyses are performed to quantify the influence on navigation receivers of the environment resolution, the speed, the incidence or the case of direct path blockage.

In this section, the influence of the environment resolution is analysed from a navigation receiver point of view considering the pseudo-range error as the key parameter and using the simplified wide-band channel model next described. The pseudo-range to a satellite represents the estimated distance between the receiver and the satellite. The pseudo-range error represents the bias induced by multipath and corresponds to the difference between the estimated and the real distance. For the needs of this section, another comparison parameter is introduced: the relative error. Since the high resolution case remains the reference, this parameter represents the offset between the pseudo-range errors for the simplified resolution cases with respect to the high resolution case. The relative error can also be seen as the error of the pseudo-range error. In the following, pseudo-range error and relative error parameters are analysed as a function of the environment resolution for the eighty-one different configurations as used in the previous section.

2.4.1 Simple wide-band channel model

As for the narrow-band analysis, the MoM-based tool Elsem3D is used to determine the EM fields along a linear trajectory. The urban canyon under consideration here is built using the same principles as in Fig.2.17. However, contrary to the narrow-band analysis where the contributions of canonical façades were coherently summed together, each building contribution is now represented by one ray (delta function) discriminated in terms of power, phase, delay and Doppler. The power of each ray is assumed to be equal to the narrow-band power radiated by each canonical façade and depends on the façade resolution as presented in Fig.2.24.

Fig.2.24 represents the power evolution of each ray (grey curves) along the receiver route. The blue line represents the LOS contribution assumed to be constant and not shadowed. The red line represents the evolution of one specific ray chosen randomly to highlight the power evolution differences between the four resolutions of the canyon. For this simulation, the source is placed at 40° elevation 40° azimuth and transmitting ϕ polarisation. The receiver is moving at 50 km/h in canyon 1. Fig.2.24 allows a better understanding of how the chosen environment resolution could affect the navigation receiver considering the different power evolutions. The maximum power of the red ray slightly decreases when adding details to the façade.

The phase, delay and Doppler shift are determined using a geometrical approach where rays originate from the centre of each canonical façade. This construction implies that phase, delay and Doppler do not depend on the resolution employed for modelling the urban canyon. The power and the delay of each ray is considered relatively to the LOS signal. The phase and the Doppler are considered in their absolute values. Note that the transmitting satellite is supposed to be stationary and the observed Doppler shifts are only due to the receiver motion. Fig.2.25 illustrates the evolution of the channel parameters: power, delay and Doppler, while the receiver is moving through the canyon 1. Fig.2.25 left diagram presents the evolution of the delays of all echoes along the receiver route. Centre diagram presents the impulse response in power delay space at one specific position (y=32m). Right diagram presents the evolution of the Doppler of all echoes along the receiver route. The configuration is the same as in Fig.2.24.

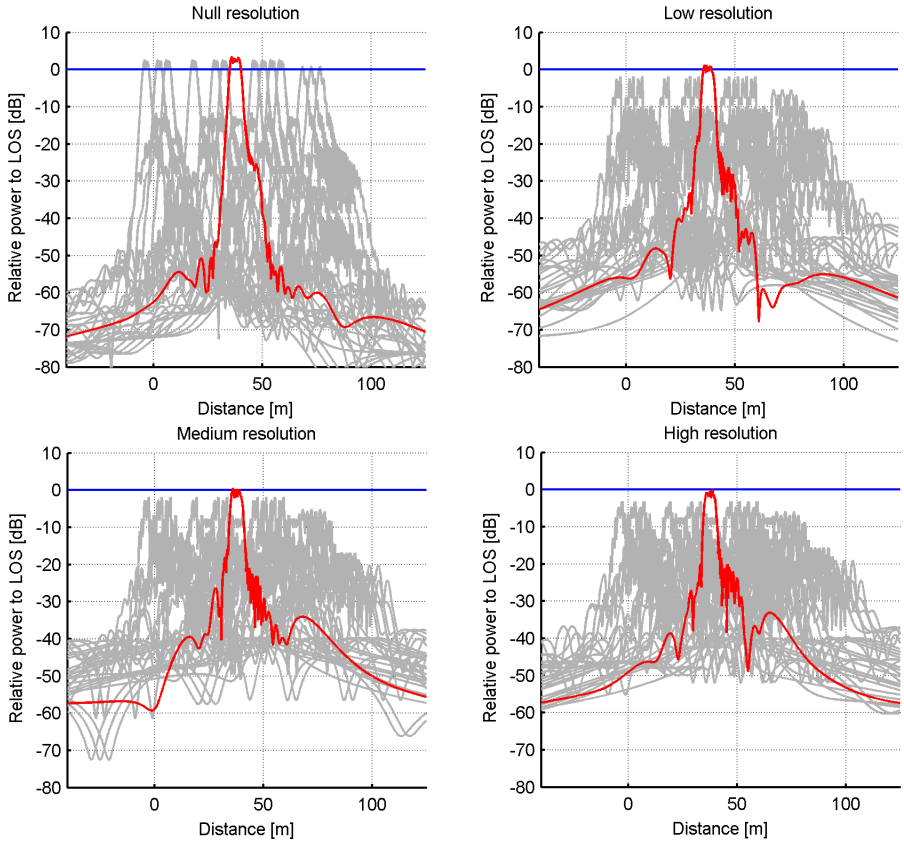

Figure 2.24: Power variation of all rays as a function of the environment resolution along a linear trajectory of the mobile in Canyon 1

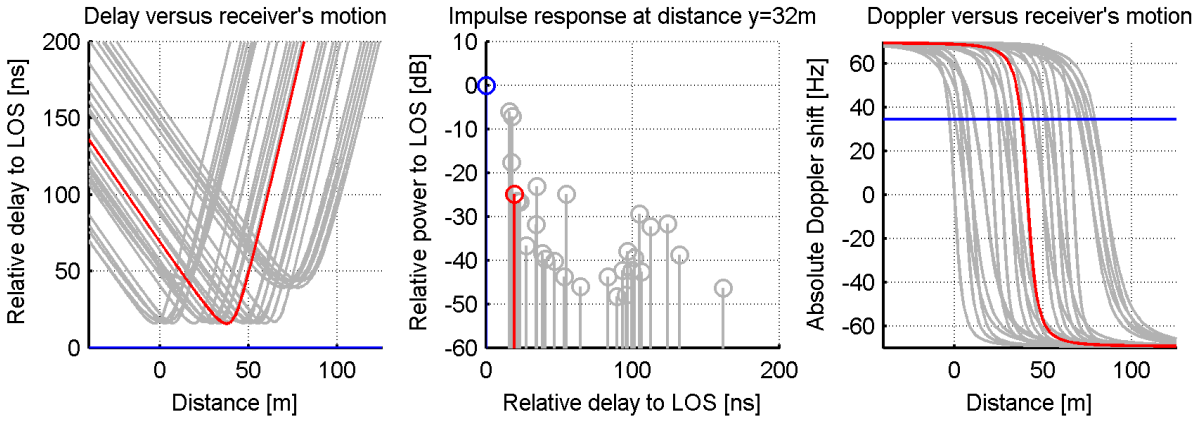

Figure 2.25: Evolution of the channel parameters along a linear trajectory of the mobile in Canyon 1

As expected, Fig.2.25 reveals that the strongest echoes comes from the specular reflection. Also noticeable are the deterministic evolution of the Doppler and the delay of each echo. Note that the considered red echo is the same as in Fig.2.24.

In order to model the wide-band channel, one major assumption is made in this simplified approach: each canonical façade gives rise to one single ray. This approach induces discontinuities since complex façades are reduced to one scattering point. This assumption comes from the MoM tool Elsem3D we used, which is frequency based and whose output only contains the EM fields considering monochromatic waves. One alternative solution has been found. The principle

is to divide each façade into smaller pieces and record their EM contribution. By merging the isolation principle described in Section 2.2.2 and the simple wide-band model presented here, we could have obtained up to sixty four rays per façade instead of one, leading to more than 1.500 rays for canyon 1 in the high resolution case. However, the navigation receiver we used is a software model and is not adapted to process such amount of data in a reasonable time. Even more, a statistical analysis based on numerous cases has to be performed and would not be possible with such constraints. Therefore, this solution has not been chosen for this part of the study. However, this alternative solution using multiple rays per façade have been used in Chapter 4.

Nevertheless, considering one ray per façade is reasonable considering that the spatial resolution of a standard 20 MHz bandwidth system is 15 m. This assumption is conservative since typical navigation receivers use bandwidths between 2 to 10 MHz. In our simulated scenarios, the maximum distance between two points from the same canonical façade is 7 m, half smaller than system's spatial resolution.

2.4.2 Influence of resolution and speed

The first part of the analysis presents the influence of the environment resolution on navigation receivers when the direct path signal is not attenuated. One example is presented in Fig.2.26 to illustrate a typical LMS configuration with 40° elevation, 40° azimuth, ϕ polarisation and assuming a constant speed of 50 km/h of the mobile in canyon 1. The top diagram presents the evolution of narrow-band MP scattered power relative to the LOS as presented in Section 2.3. The middle diagram represents the pseudo-range error depending on the environment resolution. The bottom diagram represents the relative error (error of the pseudo-range error) made when simplifying the environment resolution relative to the high resolution case.

A first remark can be made on the configuration presented in Fig.2.26, also relevant for some others not presented here. It has been observed that the receiver can be sensitive to specific wave combinations resulting in discontinuities visible around y=25 m for the high resolution case and y=35 m for the low resolution case on the pseudo-range error diagram. This phenomenon does not seem to be dependent on the chosen resolution. The consequence of this is a slight shift in the relative error (bottom diagram) while other resolutions are not affected in the same way. However, these discontinuities are negligible when extracting statistical parameters.

From the narrow-band analysis, it is shown how, for typical LMS configurations, the total MP scattered power is usually overestimated in typical LMS incidences considering the null resolution. With a wide-band approach, the same observation is made. For typical LMS incidences, strong echoes are present for the null resolution resulting in high and punctual biases visible from 40 to 60 m in Fig.2.26. Contrary to the medium and low resolutions, which show good agreement with respect to the high resolution case, the null resolution is not suitable for typical LMS configurations.

To get a better overview and generalise the observations made in Fig.2.26, statistical results are presented next. For all eighty-one scenarios, the mean and standard deviation error of the relative error is extracted in the canyon reflection zone, approximately from 0 to 85 m for the case of canyon 1. Fig.2.27 presents the cumulative density function of both error parameters. Left diagram presents cdf of mean error and right diagram presents cdf of std error. As can be seen here, the mean and standard deviation error for the medium and the low resolution are good approximations with respect to the high resolution. The null resolution has critical limitations with strong mean errors (positive and negative).

Fig.2.28 presents a parametric plot considering the {Mean;Std} error couple, showing the influ-

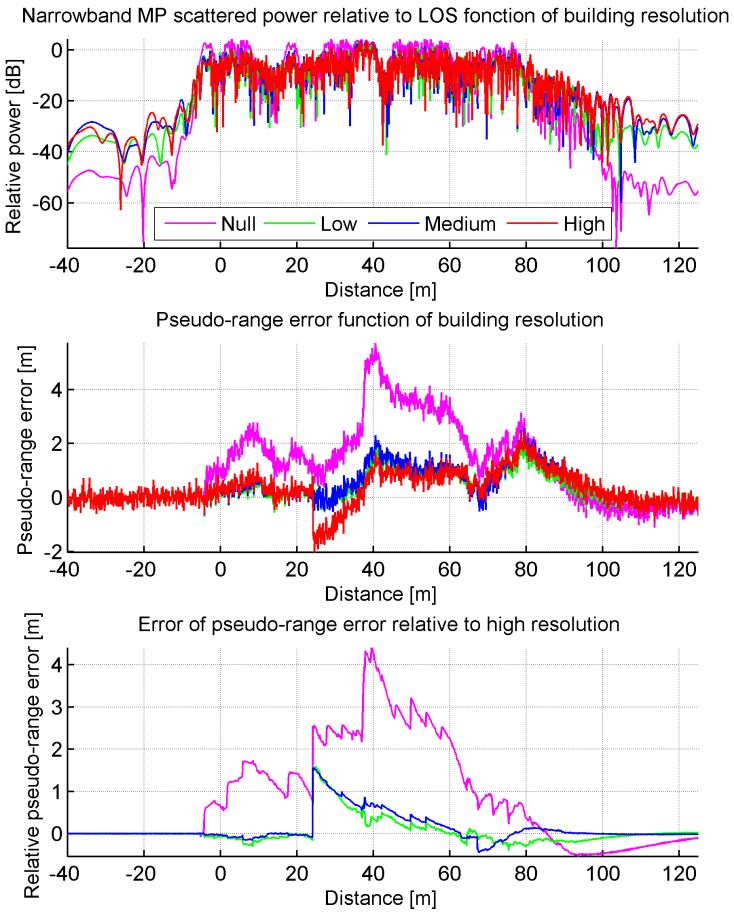

Figure 2.26: Example of pseudo-range estimations as a function of the environment resolution

ence of two parameters: the environment resolution and the receiver speed. The speed parameter is here taken into account since it has an important influence on the integration process taking place in the receiver as previously mentioned. From the analysis of Fig.2.23 it can be seen that slow motion is the most critical case. From the analysis of Fig.2.26 it has been shown that the null resolution is not suitable to represent the environment in navigation context. Removing both cases from Fig.2.28, the null resolution (pink) and the slow motion (circles), almost all other cases are in the dashed black square. This square represents a mean error in the interval of ± 1 m and standard deviation error inferior to 1 m. We can consider all these configurations as acceptable simplifications for the analysis of satellite navigation systems when the direct path is not attenuated.

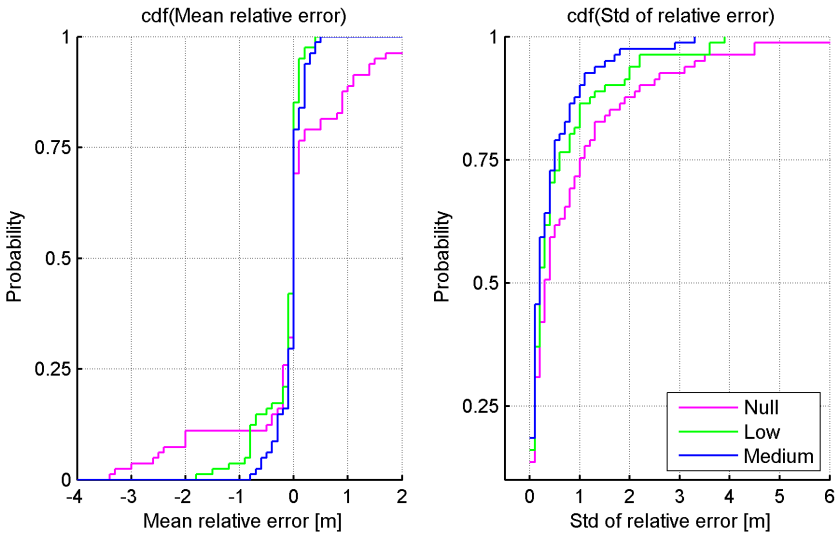

Figure 2.27: Influence of the environment resolution on pseudo-range errors in the case of unblocked LOS signal (0 dB attenuation)

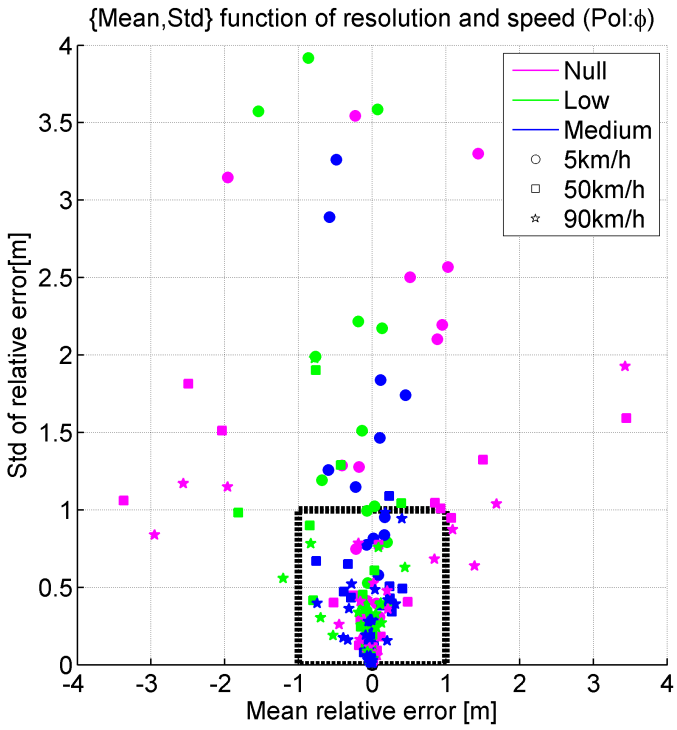

Figure 2.28: Parametric representation of the influence of the resolution and the speed on {Mean,Std} error couple

2.4.3 Influence of incidence

In a second step, the influence of the incidence angle is analysed. As a remainder of Section 2.1.2, incidences are merged in three categories: normal incidence, typical LMS configurations which represent all incidences with elevation and azimuth lower than 40° and extreme LMS configurations which represent all other incidences with elevation or azimuth higher than 40° . Fig.2.29 illustrates one extreme LMS incidence case with 80° elevation, 80° azimuth, ϕ polarisation and 50 km/h speed, using the same representation as Fig.2.26. Fig.2.29 is representative of the fact that for extreme incidences pseudo-range errors are small (±0.5 m) and behave like noise. Furthermore, relative errors are almost null and in the range of ±0.1 m. In general, for all configurations, it has been noted that pseudo-range errors occur when the MP scattered power

is larger than -15 dB relative to the LOS signal. This explains the low impact of MP for the extreme incidences. In this case, the environment resolution has no impact contrary to typical LMS incidences.

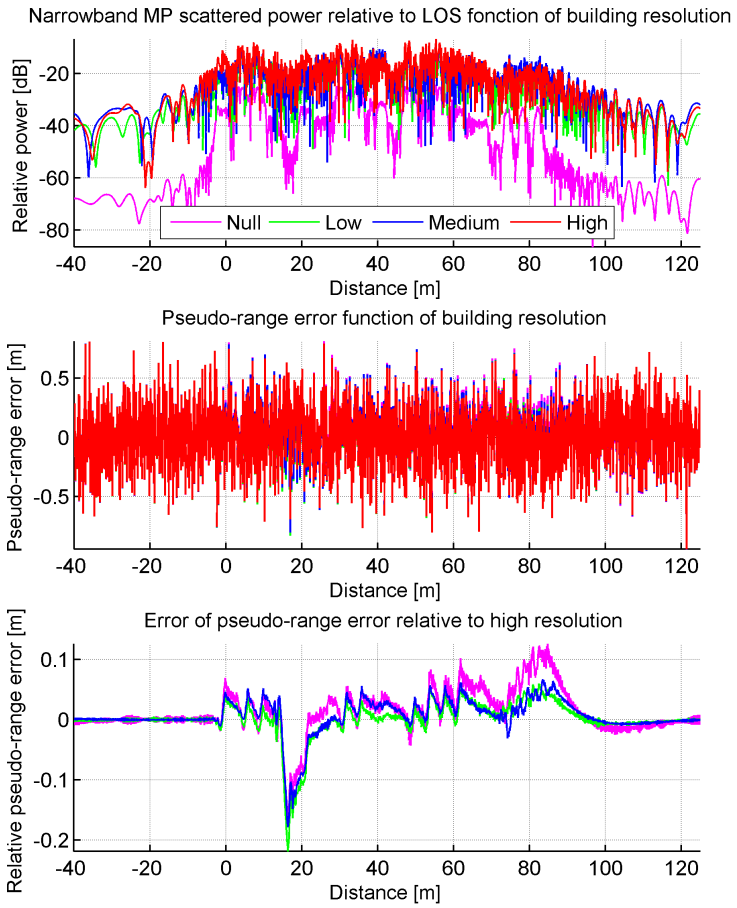

Figure 2.29: Example of pseudo-range estimations as a function of the environment resolution in the case of extreme incidence configurations

To confirm this statement, statistics are presented in Fig.2.30. They have been extracted considering the null resolution. This case is the most conservative one since the null resolution has the largest spread in the mean error as shown in Fig.2.27. From Fig.2.30 it can be observed how all extreme cases have a mean error almost equal to zero and standard deviation below 1 m, in agreement with Fig.2.29. This confirms the fact that for extreme LMS incidences, even the null resolution produces acceptable results.

2.4.4 Influence of direct signal attenuation

In the previous scenarios, the direct signal was not attenuated. To extend the domain of validity of this analysis and to take into account more realistic cases, the attenuation on the direct signal has been investigated. Two attenuations are considered: -5 dB and -20 dB corresponding to tree shadowing and building blockage respectively. . It is assumed that the direct signal is the only component affected by this attenuation. The consequence is that the power difference between the MP echoes and the direct signal is reduced. It may even occur that some echoes are stronger than the direct signal.

Simulations realised for -5 dB show similar results to those where the direct signal was not attenuated. Thus, for this case, the same conclusions are applicable.

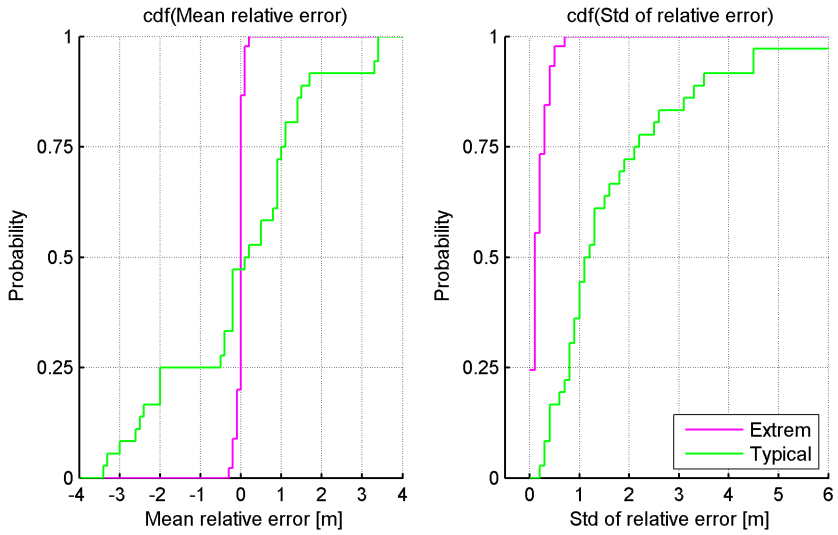

Figure 2.30: Influence of the extreme incidences on the pseudo-range error for the null resolution in the case of unblocked LOS signal

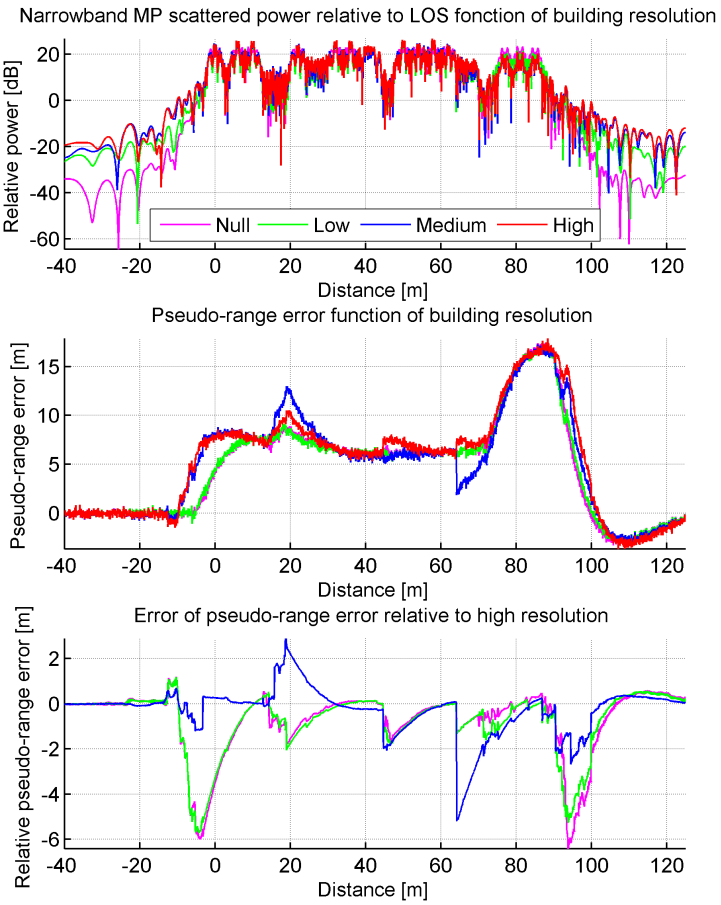

Figure 2.31: Example of pseudo-range estimations as a function of the environment resolution with 20 dB attenuation on the direct signal

However, results differ when considering a -20 dB attenuation as presented in Fig.2.31 where the configuration was 40° elevation 0° azimuth ϕ polarisation and 50 km/h speed. As can be seen on top diagram, the MP scattered power is about 20dB higher than the attenuated direct signal. When a long blockage event occurs, the receiver tends to track the strongest echo. This results in all resolutions being biased in the same way, the strongest echo coming from the façades. In

Fig.2.31, the pseudo-range error is about 6 meters, close to the distance between the receiver trajectory and the first row of buildings, situated at 4 meters from the receiver's route. We can also notice fluctuations around y=20 m due to the second row of buildings, situated 10 m from the receiver. A similar behaviour is particularly visible from y=70 m to the end of receiver's route. From point y=70 m to the end, specular reflections are not possible. While the receiver continues its route, the DLL keeps tracking the strongest diffuse contribution coming from last building. The result is that pseudo-range error increases until the diffuse contribution falls down at around y=90 m. Then, the attenuated direct signal becomes predominant over the MP, and the receiver recovers track of the LOS signal.

Finally, looking at the first half of the pseudo-range error diagram in Fig.2.31, for high and medium resolutions, the navigation receiver seems to be affected by MP earlier than for low and null resolutions. The explanation is that when the LOS signal is attenuated, any small MP contribution becomes noticeable by the receiver. Since scattering is almost absent in the low and null resolutions, both resolutions are affected later by MP, and only in the reflection zone. The medium and high resolutions show a longer impact, before and after. We noticed that the above observations are even more visible for very large azimuths where the details do not remain negligible when comparing the null and low resolutions to the medium and high ones.

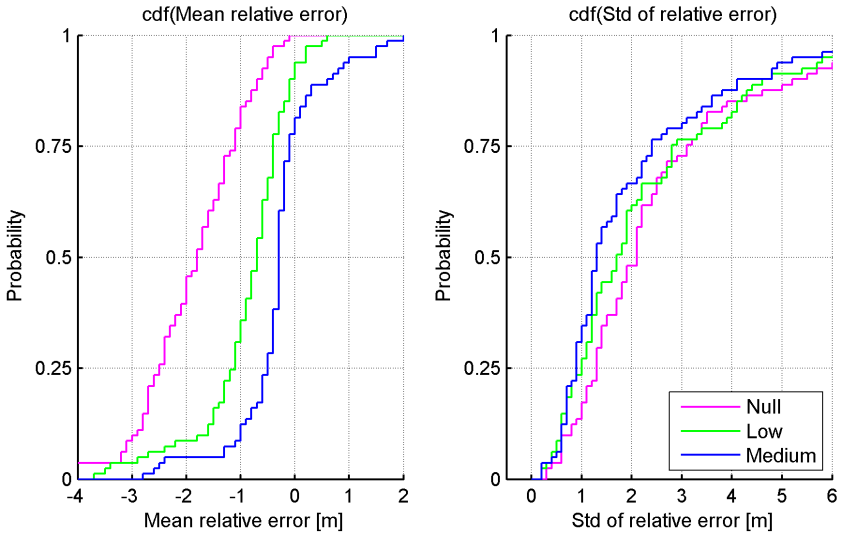

Figure 2.32: Influence of the environment resolution on the pseudo-range error for a 20 dB attenuated on the direct signal. Left diagram presents the cdf of the mean error. Right diagram presents the cdf of the std of the error

Fig.2.32 shows the statistics on the influence of the resolution when the direct signal is attenuated by 20 dB. Contrary to the unblocked case, the environment resolution has a significant impact on the receiver's performance. For attenuated cases, medium resolution seems to be the best option.

Section synthesis :
When considering the impact of building small features on navigation receivers, the following statements can be made.

- *As observed, the receiver seems to be impacted by MP as low as -15dB w.r.t the LOS contribution. When clear LOS conditions occur, the low and medium resolutions present similar results. For extreme incidence configurations with clear LOS conditions, null resolution is acceptable since MP power is low. When direct signal is highly attenuated, MP contributions become predominant and the resolution of the environment has a stronger impact on navigation receivers. The scattering phenomenon becomes important and the receiver may trace echoes signals. Those observations remain valid for low attenuations of the direct signal, e.g. -5 dB.*
- *The null resolution is not suitable since it over-estimates the pseudo-range error due to strong echoes for typical LMS incidences.*
- *The case of slow motion is restrictive since MP stay stable in a longer time and not averaged, inducing strong bias.*

2.5 Summary and recommendations

In this chapter, a rigorous method has been followed to evaluate the influence of small features present in complex façades for satcom and satnav applications. The goal of the study was to better understand what level of simplification is acceptable when representing complex urban environments used as inputs for EM tools. This work is useful in simplifying the representation of buildings to use asymptotic methods and, particularly, PO-based methods.

This analysis has been conducted with a rigorous EM tool based on the MoM, namely Elsem3D, which allows reproducing accurately the scattering phenomenon from small scatterers/features present on complex façades, without any object size restriction. Elsem3D has been used to simulate precisely the scattered EM field around canonical façades described following various levels of detail.

From the synthesis made in this chapter, several recommendations have been made considering either LMS satcom services with narrow-band constraints on MP power or satnav systems with wide-band constraints on delayed echoes.

As a recommendation for narrow-band systems, modelling the environment with details in the range of one wavelength and larger is advised for slow motion and extreme incidences. For other cases, fast motion and typical incidences, only details large compared to the wavelength could be sufficient to represent the environment if empirical adjustments are applied to the obtained MP scattered power. From our experience, +2 dB would be a typical offset value on the total MP scattered power. The canonical plate representation, equivalent to a null resolution, is hardly acceptable even for a first estimation of the total MP scattered power.

As a recommendation for wide-band applications and particularly for satellite navigation applications, details larger than the wavelength are sufficient to model the environment if the satellite is visible or slightly masked. For strong shadowing, the environment should contain smaller details in the range of the wavelength to produce some scattering. For particular applications where precise results are needed, a particular attention should be paid when the navigation receiver moves from the specular to the non-specular zone (transition from specular phenomenon to scattering phenomenon). Note that pedestrian and slow motion applications are the most critical ones since the integration process does not mitigate deep fades. Also for the slow motion case, environment sampling effects can be visible on navigation receiver performances when re-

ducing buildings to point-like scatterers has presented with the use of a very simple wide-band channel model.

Finally, it should be pointed out that the resolution has more impact on the total MP scattered power estimation than on the pseudo-range estimation. This study could be extended and completed by a similar work on the influence of dielectric materials when modelling complex environments.

According to the recommendations presented above, the modelling of complex urban environments can be simplified, in terms of details present on façades, without significant changes in the channel behaviour considering satcom and satnav applications. This study on simplifying the environment has lead to an intermediate resolution where 2.5D façade models are recommended. This trade-off is justified since contrary to full 3D models containing many small details and not adapted for modelling city scale environments, 2.5D models only contain the macro profile of the façades, mainly dependent on the architecture. On the other side, contrary to 2D façade models commonly used in existing models, 2.5D façade models are better suited for modelling the scattering phenomenon. Eventually, using 2.5D façade models allows then a faster and a more realistic synthesis of wide urban areas. The operated simplifications also allow the use of asymptotic methods such as PO since small objects have been removed and asymptotic assumptions are then fulfilled.

Still, PO asymptotic method is time consuming and a new approach to model building interactions with wave fronts has to be proposed according to the 2.5D façade approximation.

Chapter 3

Simplified EM interaction model for urban building scattering

Contents

3.1 Observation made in the vicinity of complex façades 68
3.1.1 Narrow-band observations - MoM 68
3.1.2 Wide-band observations - Asymptotic tool 69
3.1.3 DoA observation - Measurements campaigns 70
3.2 Proposed approach for a new building scattering model based on EM theory 72
3.2.1 Approach of the Three Component Model (3CM) 72
3.2.2 Physical base of the specular reflection component 73
3.2.3 Physical base of the backscattering component 75
3.2.4 Physical base of the incoherent scattering component 77
3.3 Numerical validation of the 3CM in simple cases 80
3.3.1 Narrow-band validation on isolated façades 80
3.3.2 Narrow-band validation on simple canyons 84
3.3.3 Wide-band validation on simple canyons 87
3.4 Summary 89

The objective of Chapter 3 is to present a new building scattering model, also called the Three Component Model or 3CM. This study was motivated by the trade-off that has to be reached to achieve fast computation, versatility and simple implementation when modelling the interactions between wave fronts and complex urban environments. Actual building scattering models are either empirical or deterministic. Fast and simple in their formulation, empirical models such as the ones presented in [Degl 07] and [Pong 04] are well adapted to represent the micro scattering due to surface roughness. However, they lack of versatility considering different surface types or different frequency bands and are disconnected from any EM physical theory. On the other hand, deterministic models such as PO or GO are more versatile in terms of geometry of the façade or frequency bands since they are based on parametric EM numerical formulations. Such models are particularly adapted to represent macro scattering due to architecture such as specular reflection, diffractions or dihedral effects but not adapted for micro scattering linked to surface roughness and small objects scattering. Even more, deterministic scattering models are resource consuming and their implementation is not straightforward.

From the above statements, a new physical simplified interaction model for urban building scattering has been designed and presented in this chapter according to the 2.5D façade approximation presented previously. This model is based on both empirical and physical deterministic EM models. The concept is to divide the total scattering phenomenon into three different propagation mechanisms taking place around complex façades, namely specular reflection, backscattering and incoherent scattering. Two of those propagation mechanisms, specular reflection and backscattering, represent a macro scattering phenomenon which is based on deterministic

method, namely PO. The last propagation mechanism, incoherent scattering, is closer to micro scattering and is based on empirical methods. Combining this hybrid approach with an efficient implementation of the PO algorithm allows substantial time computation gains in comparison with conventional deterministic methods while preserving a better representativeness of the micro scattering phenomenon compared to deterministic models alone.

Note that the approach using three propagation phenomena presented here can be integrated into existing ray-tracing tools without major modification but this discussion is out of the scope of this chapter. Only the simplified model for EM interactions on buildings is presented, LOS blockage being left apart and presented in Chapter 4.

This chapter is organized as follow. The first section presents several observations that have been made prior to the design of this simplified building scattering model. The second section presents the fundamentals and the main principles of the 3CM *(3 Component Model)*. For the readers who are interested in the validation steps, Appendix C presents a numerical validation of the implementation of each of the three propagation components against other numerical methods. The third section presents a numerical validation of the global implementation of the 3CM on various simple cases from narrow-band to wide-band. Note that those validations have been performed considering both references: Elsem3D, MoM based, and SE-WorkBench, asymptotic GO/PO based. Finally, the fourth section concludes and presents some features to be added to improve the actual implemented model.

3.1 Observation made in the vicinity of complex façades

3.1.1 Narrow-band observations - MoM

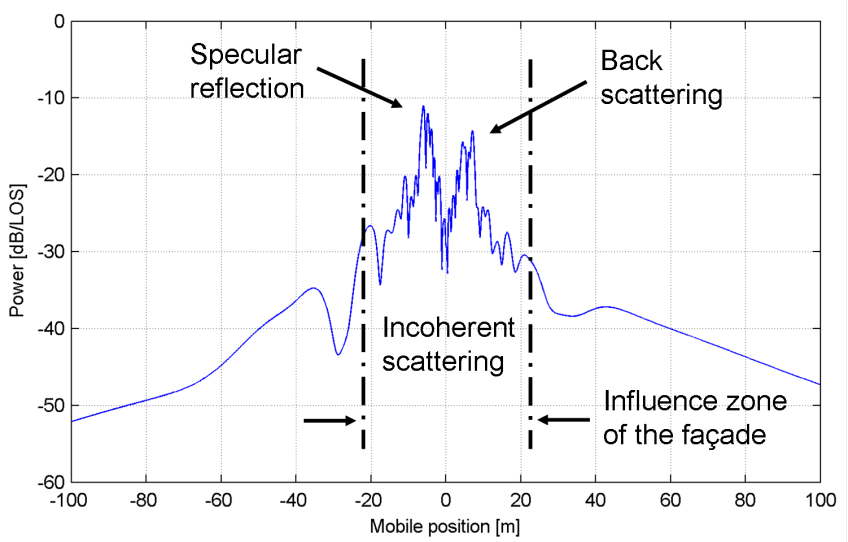

Figure 3.1: Narrow-band total scattered power received when passing close to a complex façade using MoM tool

The first observation presented in Fig.3.1 has been realised using Elsem3D, an EM research code based on MoM, developed by ONERA and presented in Appendix B.3.1. The scenario corresponding to Fig.3.1 is the following. A 4m width, 6m height façade (as presented in Fig.2.2d) is placed on the ground plane Z=0. The X axis is normal to the façade while the Z axis is oriented toward the sky. The bottom centre of the façade is placed at y=0. The receiver is moving from -100m to +100m following the Y axis at a constant distance x=10m. The source is placed at 20.000 km, 40° elevation w.r.t the ground plane, 40° azimuth w.r.t X axis. Fig.3.1 represents

the total power scattered by the façade when the mobile is passing in the vicinity on a logarithm scale w.r.t to the LOS level.

On Fig.3.1, two zones can be identified from the observation of the total scattered power; a zone where the façade has no influence (low scattered power with smooth variations) and a zone where the façade has an influence (strong scattered power with fast variations). The influence zone itself can be subdivided into three sub-zones. A first zone, specular zone, is located around y=-5m with a strong peak. The position of this peak can be linked, using simple geometric relation between receiver and transmitter positions, to a specular reflection on the façade. The second zone, around y=+5m, symmetrical w.r.t the specular one, is characterised by lower power. This zone is called backscattering zone and is detailed in Section 3.2. The last zone represents MP incoherent scattering from the façade. This zone seems to be characterised by a power threshold around -30dB w.r.t LOS with fast variations from y=-20m to y=+20m delimiting the influence zone of the façade.

3.1.2 Wide-band observations - Asymptotic tool

The second observation presented in Fig.3.2 is based on a commercial asymptotic tool. SE-WorkBench software suite is co-developed by Oktal-SE and ONERA [Mame 06] and is presented in Appendix B.3.2. The main processing software used here is SE-Ray-EM. SE-Ray-EM performs all basic operations such as the SBR *(Shooting and Bouncing Rays)* algorithm and the use of asymptotic techniques to model EM interactions with the environment such as PO and GO for multiple reflections or ECM for edge diffraction. This main processing unit is coupled to a more specific module oriented toward wide-band modelling for propagation issue and channel modelling in mobile context. This wide-band module allows the user to post-process the raw

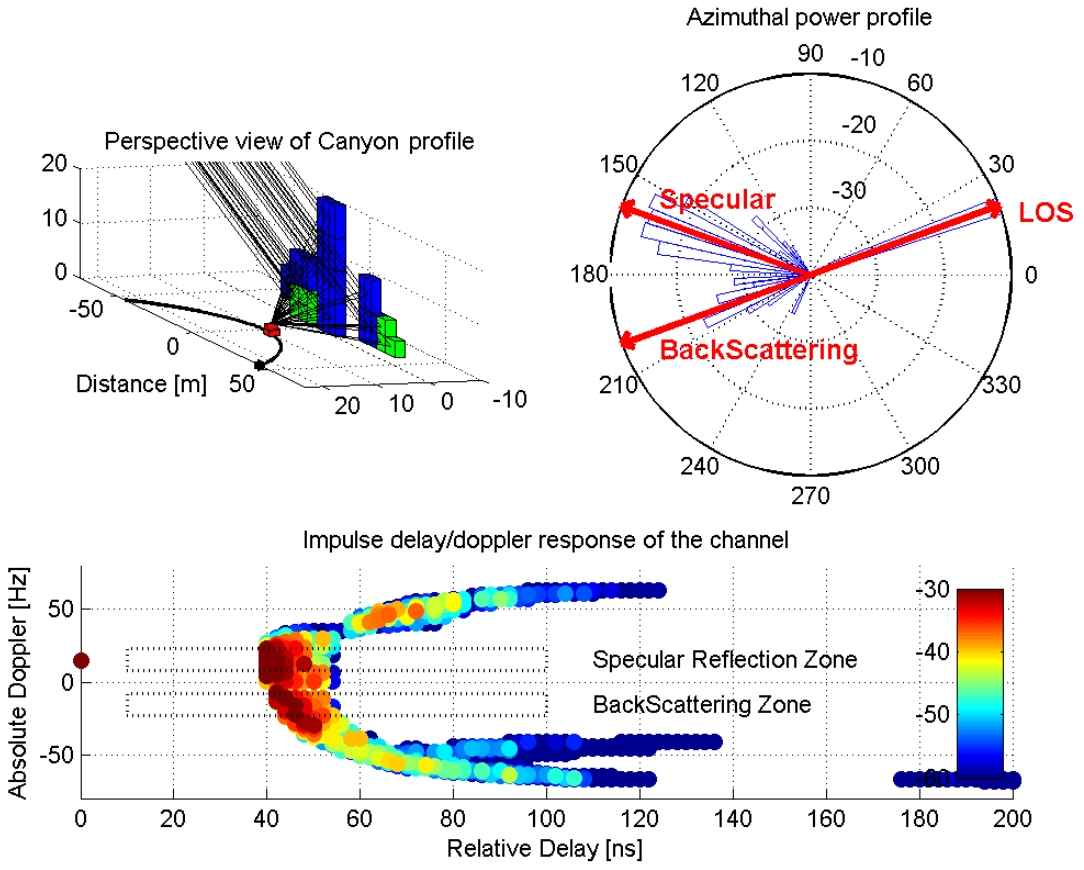

Figure 3.2: Wide-band delay/Doppler instantaneous channel impulse response when passing in a simple urban canyon using asymptotic GO/PO tools

EM field using information such as DoA or propagation path length of each ray to extract the CIRs of the channel. To reduce the number of rays from millions to thousands, a tapped-delay line approach is used where all rays belonging to the same tap are summed coherently together. For the purpose of GNSS channel modelling, the tapped-delay line approach has been extended to three dimensions: delay, DoA azimuth, DoA elevation where each sampled dimension has its own resolution. In the following of this chapter, SE-WorkBench will be used as a reference.

The scenario from which Fig.3.2 has been extracted is the following: a mobile receiver is moving into a simple urban canyon as presented in top left diagram of Fig.3.2. Only one side of the street is filled by buildings. The other one is building free. The transmitter is placed at 20.000 km, 40° elevation, 20° azimuth. The receiver is moving at a constant speed of 50km/h following the trajectory presented in top left diagram of Fig.3.2. In those conditions, perfect LOS is achieved all along receiver route. Bottom diagram of Fig.3.2 represents one example of instantaneous CIR. The abscissa axis represents the relative delay of the echoes w.r.t the LOS delay. The ordinate axis represents the absolute Doppler of each echo assuming a fixed transmitting point. The colour axis represents the power of each echo w.r.t the LOS level. Top right diagram of Fig.3.2 represents the instantaneous azimuthal power profile considering 5° beams in the horizontal plane. X direction is represented by 0° azimuth while Y axis (direction of the mobile) is represented by 90° azimuth.

From top right diagram of Fig.3.2, three directions are highlighted with major contributions: the LOS beam corresponds to the direction where the LOS signal is coming. The specular zone is symmetrical to the LOS direction w.r.t the direction of the mobile (Y axis, 90° azimuth). The specular zone has strong contributions. The last major contribution comes from the backscattering zone, opposed to the LOS direction. This zone contains also significant contributions. The influence zone of the façade with -30dB power threshold, not explicitly mentioned on top right diagram of Fig.3.2, can also be noticed between the specular zone and the backscattering zone.

Observations made on bottom diagram of Fig.3.2 confirm observations made in top right diagram. First, we can isolate the LOS signal with null relative delay and positive Doppler. Then, from the overall MP spread, two powerful zones can be isolated. The first one has a positive Doppler of around 15Hz. This zone contains the strongest echoes. The positive Doppler allows linking this zone to a specular phenomenon coming from the front of the receiver. The second zone is less powerful with negative Doppler. Still, this zone contains non negligible echoes. The negative Doppler and the symmetry w.r.t the specular zone indicate some kind of backward reflection coming from the back of the receiver. The influence zone of the street canyon can also be highlighted from -40Hz to +40Hz. Note that the delay/Doppler spread and CIRs shapes are site dependent and tightly linked to the canyon geometry. To conclude this observation, a parallel can easily be made with the first observation made in Subsection 3.1.1 for the specular, backscattering and incoherent scattering zones.

3.1.3 DoA observation - Measurements campaigns

The last observation presented in Fig.3.3 is based on a measurement campaign realised by DLR in 2002. The measurements aimed at providing real data to build an enhanced physical-statistical LMS channel model designed for satellite navigation purposes [Lehn 07b] later referenced by ITU [ITU 09] and presented in Section 1.1.3.3. Those measurements have been performed by using a Zeppelin for transporting the transmitter and a moving car carrying the receiver. Several environment types have been investigated such as rural, suburban or urban. From those data, various channel parameters were extracted such as the pdf of the scatterers position, scatterers lifespan, scatterers reflected mean power or the number of significant echoes.

Fig.3.3 represents a pdf of the scatterer positions for urban environment. In the presented case,

the source is placed at 25° azimuth, 30° elevation and the mobile is moving along the X axis. Four zones have been highlighted in Fig.3.3. The first three, specular reflection, backscattering and incoherent scattering, have been mentioned in previous observations. From an angular point of view, the specular zone is symmetrical to the incoming signal w.r.t receiver motion $\vec{v}$, the backscattering zone is in the opposite direction w.r.t the incoming signal and the incoherent zone makes the transition between the specular and the backscattering zones. The fourth zone is called diffraction and represents the edge diffraction taking place on building roofs when the direct path is masked. Since this situation is common, the probability density is high. However, in the following analysis of this chapter, we will assume that the direct path is always free and the façades only contribute to the reflection/scattering phenomenon and never to the masking/diffraction phenomenon. The diffraction issue will be treated in Chapter 4.

In the data analysis made in [Lehn 08], the authors pointed out some double reflection effects taking place mainly in urban environments which lead to backward propagation mechanism. Those observations are in accordance with the first two observations presented in this section.

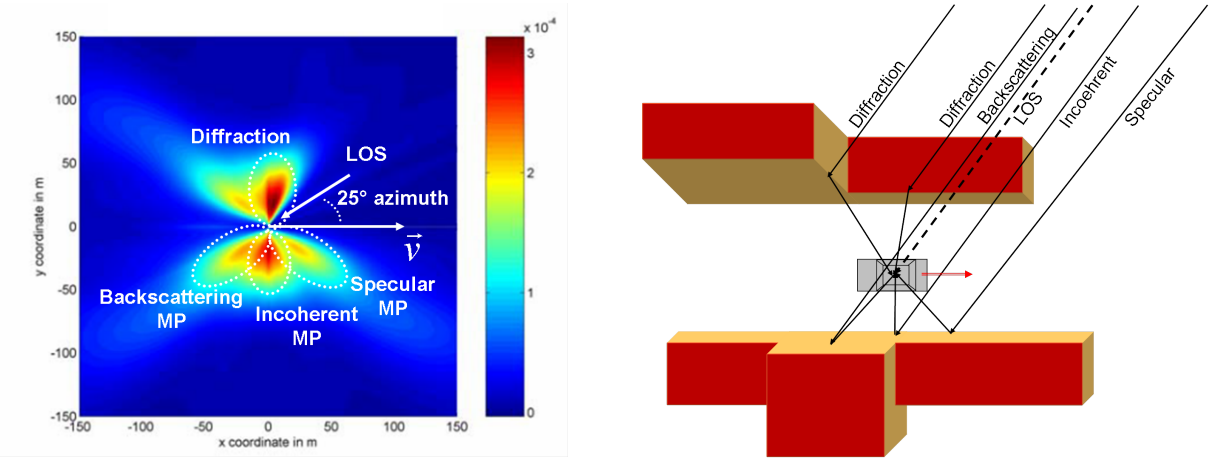

(a) (b)

Figure 3.3: Probability density function of the position of the scatterers extracted from measurements realised by DLR 2in 002 [Lehn 08] and physical interpretation of each scattering region

Section synthesis :
This first section relative to practical observations made on building scattering patterns considering both numerical and experimental results highlights several distinct propagation mechanisms:

- *A specular reflection of high power coming from the front of the mobile. This mechanism is commonly identified by the scientific literature.*
- *A backward propagation mechanism, also called backscattering, of medium power coming from the back of the mobile. This mechanism is not well identified in the scientific literature and usually integrated into the incoherent scattering component although different.*
- *A limited influence zone of the façade linked to the scattering mechanism due to small features present on complex façades which spreads power almost uniformly in façades vicinity.*

3.2 Proposed approach for a new building scattering model based on EM theory

3.2.1 Approach of the Three Component Model (3CM)

The problematic of building scattering and rough surface scattering has been previously studied in [Degl 07] and [Pong 04]. Other approaches aiming at homogenizing the different dielectric material present on façades into one equivalent material have been presented in [Most 11] and recent work to discuss the polarisation issue has lead to one empirical model extracted from measurement campaigns and presented in [Vitu 12]. Our goal in this study was to design a new building scattering model based on EM models with a minimum use of empirical approaches or measurement campaigns and satisfying the trade-off between computation time and versatility.

From the previous observations made in section 3.1, it has been shown that the scattering phenomenon taking place around complex façades can be divided into three propagation mechanisms, or components, each one being linked to a particular propagation scheme. The three components on which lies the 3CM (3 Component Model) are presented in Fig.3.4. Note that this scattering decomposition principle has the advantage of being potentially applicable to existent ray-tracing tools without major modifications.

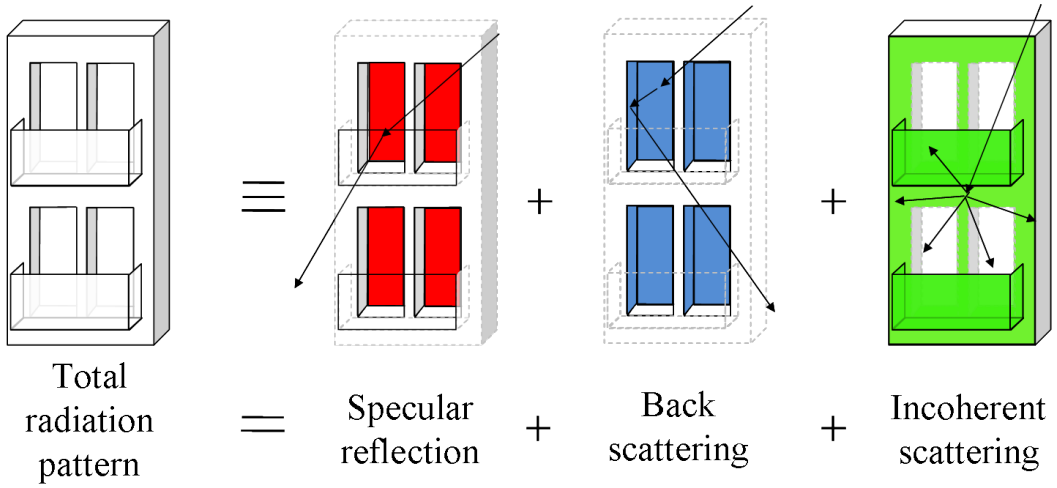

Figure 3.4: Decomposition principle of the 3CM

The 3CM model relies on the three propagation components:

- *The specular component:* reproduces the forward reflection mechanism taking place on wide and smooth surfaces such as windows and flat walls. This component is the most powerful. In its implementation, the specular component is based on a simplified version of the PO algorithm detailed in Subsection 3.2.2.

- *The backscattering component:* reproduces a double bounce reflection, or backward reflection, due to dihedral effects taking place near protruding and receding elements of the façade, i.e. receding windows or protruding balconies. The backscattering component is less powerful than the specular one but is responsible of significant contributions coming from the opposite side of the LOS signal. From existent models, this component is usually integrated into the incoherent scattering mechanism although the EM mechanism is coherent and different. The implementation of the backscattering component is also based on a simplified version of the PO algorithm and detailed in Subsection 3.2.3

- *The incoherent scattering component:* reproduces the scattering phenomenon coming from all small features present on complex façades. This component allows a smoother transition between the specular zone and the backscattering zone. It also characterises the

influence zone of the façade. Since small features are not supposed to be modelled using asymptotic methods such as PO, the implementation of this empirical component is based on analytical models extracted from [Ruck 70] and detailed in Subsection 3.2.4.

The main advantage of the approach chosen for the 3CM is the reduced computational effort: the total scattering pattern of any complex façade can be divided into three components, each one being easy to model. Reducing the computational effort allows low computation times. Another advantage of the 3CM is its physical EM base which gives it more realism and versatility. Contrary to empirical models, the 3CM is able to generate wide-band CIRs with realistic delay, Doppler and DoA information. Since it is based on the PO algorithm, the 3CM can also deal with dielectric materials, handle elliptic polarisations and is frequency scalable from 1 to 5GHz. Note that for higher frequencies, the 3CM would require more detailed environment inputs according to [Ait 12] which have not been investigated yet. Finally, the 3CM is suitable for MIMO studies with transmitting/receiving diversity, polarisation diversity or frequency diversity.

3.2.2 Physical base of the specular reflection component

The specular component is based on a simplified PO algorithm inspired from [Bala 89]. The *simplified* term is related to our implementation of the PO algorithm since coming from a trick when evaluating the current integral by using a *sinc* function instead of real integration to optimize time computation. Note that this simplified PO algorithm is equivalent to the conventional PO algorithm presented in Appendix B.1.1 under specific assumptions.

The first step of the PO algorithm is to calculate tangential $\vec{E}^t$ and $\vec{H}^t$ fields. E represents the electric field, H represents the magnetic field, superscript i is for incident field, r is for geometrically reflected field and t is for tangential field over the surface S.

$$\vec{E}^t = \vec{E}^i + \vec{E}^r \quad , \quad \vec{H}^t = \vec{H}^i + \vec{H}^r \tag{3.1}$$

From the tangential EM fields, surface currents are calculated. Note that EM fields and surface currents are expressed in the absolute xyz reference base of the scene. J_S represents the electric surface current while M_S represents the magnetic surface currents. $\hat{n}$ represents the unit normal vector to the facet.

$$\vec{J_s} = \hat{n} \wedge \vec{H}^t \quad , \quad \vec{M_s} = -\hat{n} \wedge \vec{E}^t \tag{3.2}$$

EM surface currents are then re-radiated using the radiating equations Eq.3.3 and Eq.3.4 where β is the wave number, $\hat{k}^s$ is the unit scattering direction, $\hat{k}^i$ is the unit incident direction both expressed in the absolute reference base.

$$\vec{N} = \iint_S \vec{J_s}\, e^{+\jmath\beta(\hat{k}^s - \hat{k}^i)\wedge\hat{n}} ds' \tag{3.3}$$

$$\vec{L} = \iint_S \vec{M_s}\, e^{+\jmath\beta(\hat{k}^s - \hat{k}^i)\wedge\hat{n}} ds' \tag{3.4}$$

The simplified denomination here used for the PO algorithm comes from the fact that instead of solving the integral equations presented in Eq.3.3 and Eq.3.4, a square plate of width c is assumed and the integral term becomes a sinc function as shown in Eq.3.5

$$\int_{-c/2}^{+c/2} e^{\jmath\alpha z} dz = c \left[\frac{\sin\left(\frac{\alpha}{2}c\right)}{\frac{\alpha}{2}c} \right] = c\, sinc\left(\frac{\alpha}{2}c\right) \tag{3.5}$$

Using projection relations to compute EM fields in spherical coordinates, $\vec{N}$ and $\vec{L}$ lead to Eq.3.6 to Eq.3.9 using notations described in Eq.3.10 and Eq.3.11. λ represents the wavelength, $\hat{\theta}$ and

$\hat{\phi}$ represent unit polarisation vectors.

$$N_\theta = (\hat{\theta} \,.\, \vec{J_s}) \prod_{xyz} sinc\left(\vec{\xi}\right) c^2 \tag{3.6}$$

$$N_\phi = (\hat{\phi} \,.\, \vec{J_s}) \prod_{xyz} sinc\left(\vec{\xi}\right) c^2 \tag{3.7}$$

$$L_\theta = (\hat{\theta} \,.\, \vec{M_s}) \prod_{xyz} sinc\left(\vec{\xi}\right) c^2 \tag{3.8}$$

$$L_\phi = (\hat{\phi} \,.\, \vec{M_s}) \prod_{xyz} sinc\left(\vec{\xi}\right) c^2 \tag{3.9}$$

$$\prod_{xyz} sinc\left(\vec{\xi}\right) \equiv sinc(\xi_x)\, sinc(\xi_y)\, sinc(\xi_z) \tag{3.10}$$

$$\vec{\xi} = \frac{\pi c}{\lambda}\left(\hat{k}^s - \hat{k}^i\right) \wedge \hat{n} \tag{3.11}$$

Finally, the E and H fields along both $\hat{\theta}$ and $\hat{\phi}$ polarisation vectors are calculated using Eq.3.12 to Eq.3.15.

$$E_\theta = -\frac{\jmath\beta e^{-\jmath\beta r}}{4\pi r}\left(L_\phi + \eta N_\theta\right) \tag{3.12}$$

$$E_\phi = +\frac{\jmath\beta e^{-\jmath\beta r}}{4\pi r}\left(L_\theta - \eta N_\phi\right) \tag{3.13}$$

$$H_\theta = +\frac{\jmath\beta e^{-\jmath\beta r}}{4\pi r}\left(N_\phi - \frac{L_\theta}{\eta}\right) \tag{3.14}$$

$$H_\phi = -\frac{\jmath\beta e^{-\jmath\beta r}}{4\pi r}\left(N_\theta + \frac{L_\phi}{\eta}\right) \tag{3.15}$$

One validation example of the simplified PO algorithm is presented in Fig.3.5 considering bistatic RCS of a PEC plate. Details of the simulation parameters and further validations are presented in Appendix C.1.

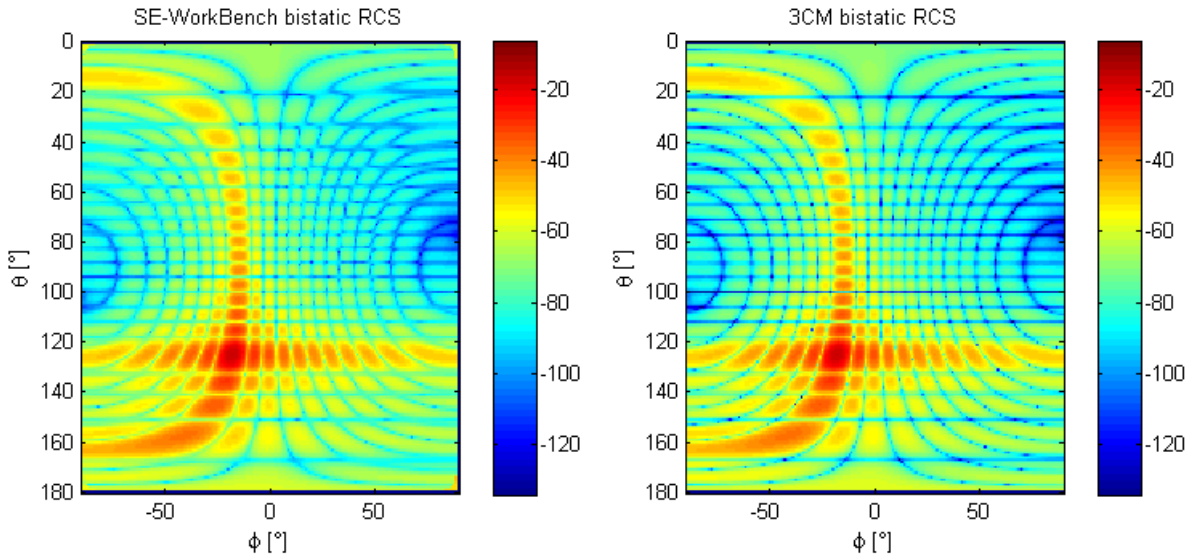

Figure 3.5: Validation of the simplified PO algorithm on 3D bistatic RCS of a PEC plate

To achieve time computation gain, this simplified PO algorithm has been vectorised using a Matlab implementation. In its current version, but not mandatory, each facet is characterised

by its material (ϵ_r, μ_r, σ) and its position. However, the simplified PO algorithm assumes the same normal for each facet and a constant square surface for time considerations, both parameters being tuneable.

3.2.3 Physical base of the backscattering component

The first attempt to model the backscattering component was based on a hybrid GO/PO algorithm which models rigorously the double reflection mechanism. This solution turns out to be consuming in terms of computation time and was discarded. The present implementation of the backscattering component relies on the previously presented simplified PO algorithm. The principle is to replace any dihedral by an equivalent plate in terms of size and orientation on which the simplified PO algorithm can easily be applied. This equivalent plate principle is presented in Fig.3.6.

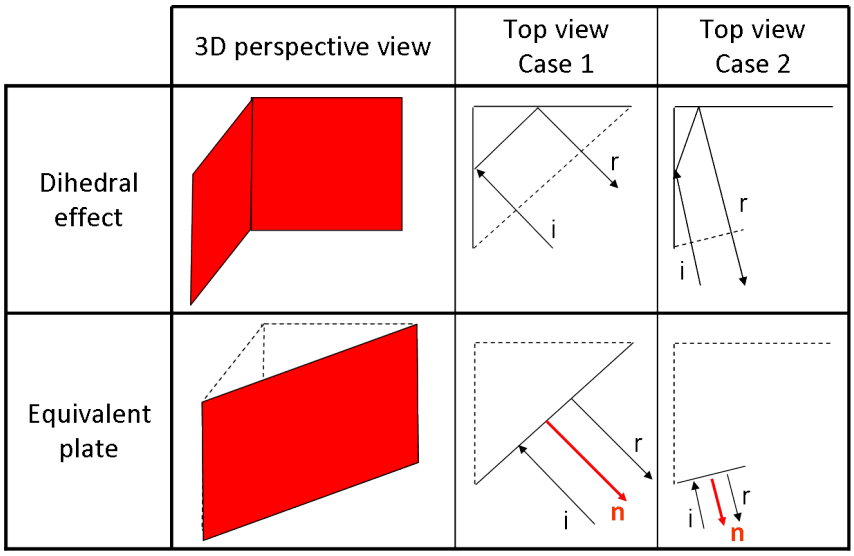

Figure 3.6: Principle of the equivalent plate to reproduce the backscattering component

To reproduce the double bounce reflection, the equivalent plate has been designed as follows.

- Its orientation corresponds to a rotation in the horizontal plane which satisfies Eq.3.16. Due to dihedral properties, the goal is to oppose the normal of the equivalent plate to the incidence direction taken in the horizontal plane. Including elevation angle in the rotation process of the equivalent plate would reproduce a trihedral mechanism reflecting power toward the source. This mechanism has no interest for the present study since reflecting power toward the sky instead of reflecting power toward the ground where the mobile receiver is.

- The height of the equivalent plate is kept constant w.r.t the original dihedral height while its width is a function of the azimuth and elevation of the incoming wave front as presented in Eq.3.17

- The polarisation is modified as if the first reflection occurs on PEC material before impinging on the equivalent plate. Nevertheless, for dielectric materials, the amplitude of the reflected signal is attenuated by ρ^2 presented in Eq.3.18. The square term comes from the double reflection mechanism which has to be taken into account in the total attenuation since only simple interactions are modelled using the PO algorithm.

$$\hat{n} = -\frac{1}{\sqrt{(k_x^i)^2 + (k_y^i)^2}} \begin{pmatrix} k_x^i \\ k_y^i \\ 0 \end{pmatrix} \tag{3.16}$$

$$w' = 2w \min\left(\cos\phi^i, \sin\phi^i\right) \cos^3\theta^i \tag{3.17}$$

$$\rho^2 = \left(\left(\sqrt{\epsilon_r} - 1\right) / \left(\sqrt{\epsilon_r} + 1\right)\right)^2 \tag{3.18}$$

where k_x^i and k_y^i represents the x and y components of $\hat{k}^i$ incident vector, w' represents the equivalent width of the plate, w the original width of the plate, ϕ^i the incident azimuth angle and θ^i the incident elevation angle.

Finally, the radiation pattern of the equivalent plate is empirically corrected to reproduce the side lobes around -50° and +140° as visible in Fig.3.7. Note that out of the specified angular range, the correction function equals zeros avoiding the backscattering component to radiate in a non-physical direction. The side lobes are due to edge diffractions which are not reproduced by the simplified PO algorithm. The empirical correction function α is presented in Eq.3.19.

$$\alpha = 1 + \sin\left[\left(\phi^s - \frac{\pi}{4}\right)\kappa\right]^{20} \tag{3.19}$$

where ϕ^s is the scattering azimuth angle and $\kappa = 105/90$ an empirical broadening coefficient.

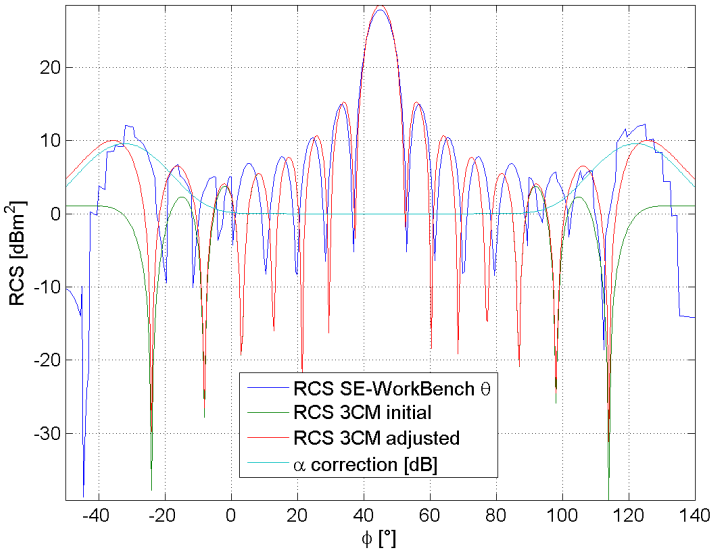

Figure 3.7: Illustration of the empirical correction function used to compensate the diffraction phenomenon when using the equivalent plate model to reproduce the backscattering component

One validation example of the double bounce reflection is presented in Fig.3.8 considering bistatic RCS of a PEC dihedral. Details of the simulation parameters and further validations are presented in Appendix C.2.

Even if empirically designed, the backscattering component is still suitable for dielectric materials including polarisation effects. The backscattering implementation has been also validated for various incidence angles with a reasonable agreement with the reference as presented in Appendix C while preserving time performances.

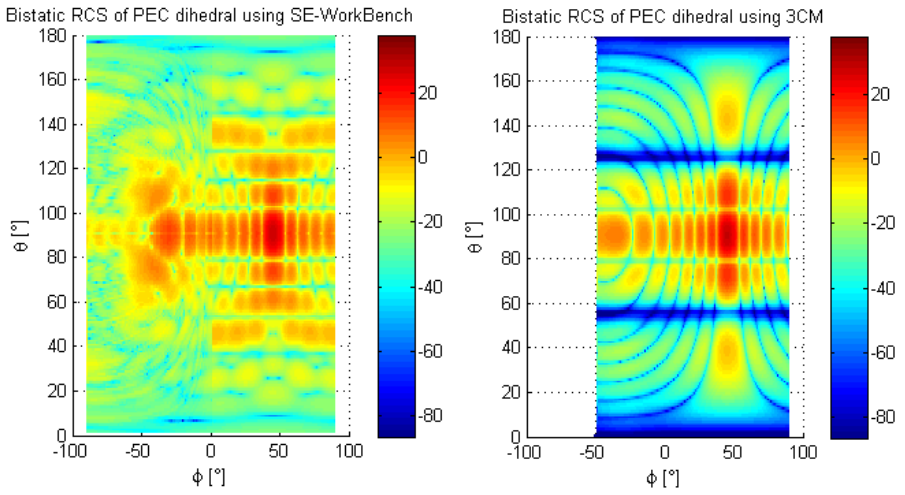

Figure 3.8: Validation of the double bounce reflection algorithm considering bistatic RCS on a PEC dihedral

3.2.4 Physical base of the incoherent scattering component

The incoherent scattering component is based on analytical formulas extracted from [Ruck 70] (in Chapter 9). Originally designed for sea surface modelling, four rough surface models have been implemented. The first two correspond to slightly rough surfaces with Gaussian or exponential roughness distribution. The last two correspond to rough surfaces with Gaussian or exponential roughness distribution.

All mentioned models have two-parameter dependence: h the RMS roughness height and l the correlation length of the surface roughness. All four models are based on normalised RCS, represented by γ_{pq}^{I} parameter in Eq.3.21 and Eq.3.31. The total radiated field is then calculated using Eq.3.20 where S is the total surface of the facet, Z_0 the vacuum impedance, R_1 and R_2 are respectively the distance between the transmitter and the facet and the distance between the facet and the receiver and $\hat{\theta}$ and $\hat{\phi}$ the polarisation vectors.

$$\vec{E} = \frac{S\sqrt{2Z_0}}{4\pi R_1 R_2} \begin{bmatrix} -\jmath\,\gamma_{p\theta}\, e^{-\jmath k_0(R_1+R_2)}\,\hat{\theta} \\ \jmath\,\gamma_{p\phi}\, e^{-\jmath k_0(R_1+R_2)}\hat{\phi} \end{bmatrix} \tag{3.20}$$

Let's first describe both slightly rough surface models. Several assumptions have to be verified prior to use this slightly rough surface scattering models. First $k_0 h < 1$ means that roughness height is small. Second $|\delta\xi/\delta x|, |\delta\xi/\delta y| < 1$ means that surface slopes are relatively small. Finally $\langle(\delta\xi/\delta x)^2\rangle = \langle(\delta\xi/\delta z)^2\rangle$ meaning that the roughness is isotropic. Eq.3.21 presents the computation of the normalised RCS of the surface, unit-less m^2/m^2, where k_0 represents the wave number, h the RMS roughness height, α_{pq} a coefficient dependent on polarisations p and q, and I a coefficient dependent on the surface roughness distribution. Note that in the following of this section θ_i represent the incidence angle, θ_s the scattering incidence angle and ϕ_s the scattering azimuth angle assuming that incident wave vector $\hat{k}_i$ is in the XZ plane oriented toward positive X [Ruck 70].

$$\gamma_{pq}^{I} = \frac{4}{\pi}\, k_0^4 h^2 cos^2\theta_i\, cos^2\theta_s\, |\alpha_{pq}|^2\, I \tag{3.21}$$

Eq.3.22 is used for slightly rough surfaces with Gaussian distribution of the scatterers while Eq.3.23 is used for exponential distribution of the scatterers. The other terms are defined from

Eq.3.24 to Eq.3.30 [Ruck 70].

$$I = \pi l^2 \, exp\left[\frac{-k_0^2 l^2 \left(\xi_x^2 + \xi_y^2\right)}{4}\right] \tag{3.22}$$

$$I = 2\pi l^2 \frac{1}{\left[1 + k_0^2 l^2 \left(\xi_x^2 + \xi_y^2\right)\right]^{3/2}} \tag{3.23}$$

$$\xi_x = sin\theta_i - sin\theta_s cos\phi_s \tag{3.24}$$

$$\xi_y = sin\theta_s sin\phi_s \tag{3.25}$$

$$\xi_z = -cos\theta_i - cos\theta_s \tag{3.26}$$

$$\alpha_{hh} = -\frac{\left[(\mu_r - 1)\left(\mu_r sin\theta_i sin\theta_s - cos\phi_s \sqrt{\epsilon_r\mu_r - sin^2\theta_i}\sqrt{\epsilon_r\mu_r - sin^2\theta_s}\right) + \mu_r^2(\epsilon_r - 1)cos\phi_s\right]}{\left[\mu_r cos\theta_i + \sqrt{\epsilon_r\mu_r - sin^2\theta_i}\right]\left[\mu_r cos\theta_s + \sqrt{\epsilon_r\mu_r - sin^2\theta_s}\right]} \tag{3.27}$$

$$\alpha_{vh} = sin\phi_s \frac{\epsilon_r(\mu_r - 1)\sqrt{\epsilon_r\mu_r - sin^2\theta_i} - \mu_r(\epsilon_r - 1)\sqrt{\epsilon_r\mu_r - sin^2\theta_s}}{\left[\mu_r cos\theta_i + \sqrt{\epsilon_r\mu_r - sin^2\theta_i}\right]\left[\epsilon_r cos\theta_s + \sqrt{\epsilon_r\mu_r - sin^2\theta_s}\right]} \tag{3.28}$$

$$\alpha_{hv} = sin\phi_s \frac{\mu_r(\epsilon_r - 1)\sqrt{\epsilon_r\mu_r - sin^2\theta_i} - \epsilon_r(\mu_r - 1)\sqrt{\epsilon_r\mu_r - sin^2\theta_s}}{\left[\epsilon_r cos\theta_i + \sqrt{\epsilon_r\mu_r - sin^2\theta_i}\right]\left[\mu_r cos\theta_s + \sqrt{\epsilon_r\mu_r - sin^2\theta_s}\right]} \tag{3.29}$$

$$\alpha vv = \frac{\left[(\epsilon_r - 1)\left(\epsilon_r sin\theta_i sin\theta_s - cos\phi_s \sqrt{\epsilon_r\mu_r - sin^2\theta_i}\sqrt{\epsilon_r\mu_r - sin^2\theta_s}\right) + \epsilon_r^2(\mu_r - 1)cos\phi_s\right]}{\left[\epsilon_r cos\theta_i + \sqrt{\epsilon_r\mu_r - sin^2\theta_i}\right]\left[\epsilon_r cos\theta_s + \sqrt{\epsilon_r\mu_r - sin^2\theta_s}\right]} \tag{3.30}$$

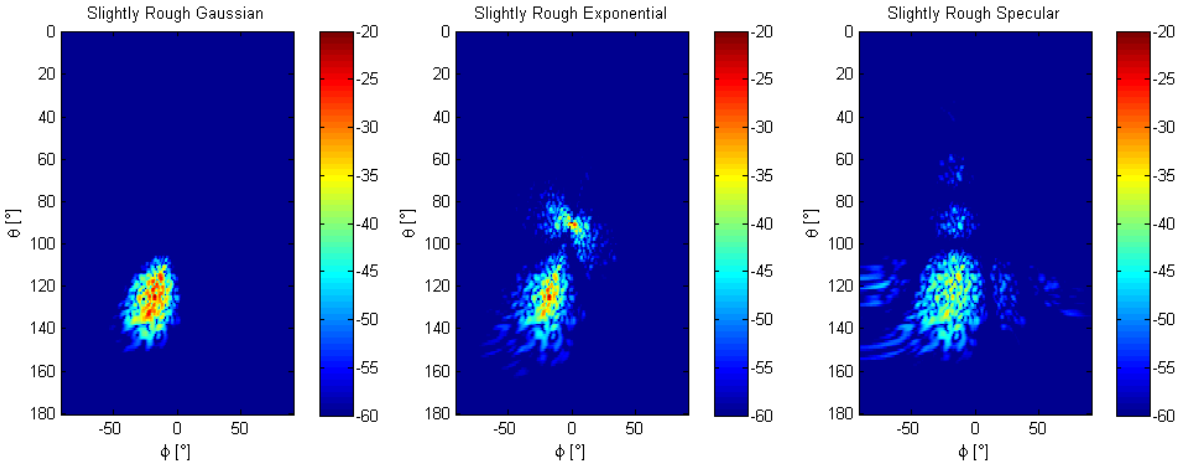

Figure 3.9: Example of bistatic RCS of a square of 5m width using the slightly rough surface models

The very rough surface scattering model is similar considering equations from 3.31 to Eq.3.43. Several assumptions have to be made. First, the surface radius has to be considerably larger than the wavelength. Second, the roughness is assumed to be isotropic in both surface dimensions. Third, $l \ll \sqrt{S}$ means that the correlation length of the surface roughness is much smaller than the length or the width of the illuminated area. This precludes the possibility of looking at only a portion of the scattering object, but rather demands that several facets of the object are included within the illuminated area. Finally, multiple scattering and shadowing are neglected.

$$\gamma_{pq}^I = |\beta_{pq}|^2 \, J \tag{3.31}$$

J function presented Eq.3.32 assumes Gaussian distribution while Eq.3.33 assumes exponential distribution [Ruck 70].

$$J = \frac{4}{s^2\xi_z^2} exp\left[-\frac{1}{s^2}\left(\frac{\xi_x^2+\xi_y^2}{\xi_z^2}\right)\right] \tag{3.32}$$

$$J = \frac{12}{s^2\xi_z^2} exp\left[-\frac{\sqrt{6}}{s^2}\sqrt{\frac{\xi_x^2+\xi_y^2}{\xi_z^2}}\right] \tag{3.33}$$

$$s^2 = \frac{4h^2}{l^2} \tag{3.34}$$

$$\beta_{vv} = \frac{a_2a_3R_{\parallel}(\iota) + sin\theta_i sin\theta_s sin^2\phi_s R_{\perp}(\iota)}{a_1a_4} \tag{3.35}$$

$$\beta_{hv} = sin\phi_s \frac{-sin\theta_i a_3 R_{\parallel}(\iota) + sin\theta_s a_2 R_{\perp}(\iota)}{a_1a_4} \tag{3.36}$$

$$\beta_{vh} = sin\phi_s \frac{sin\theta_s a_2 R_{\parallel}(\iota) - sin\theta_i a_3 R_{\perp}(\iota)}{a_1a_4} \tag{3.37}$$

$$\beta_{hh} = \frac{-sin\theta_i sin\theta_s sin^2\phi_s R_{\parallel}(\iota) - a_2a_3R_{\perp}(\iota)}{a_1a_4} \tag{3.38}$$

$$cos\iota = \frac{1}{\sqrt{2}}\sqrt{1 - sin\theta_i sin\theta_s cos\phi_s + cos\theta_i cos\theta_s} \tag{3.39}$$

$$a_1 = 1 + sin\theta_i sin\theta_s cos\phi_s - cos\theta_i cos\theta_s \tag{3.40}$$

$$a_2 = cos\theta_i sin\theta_s + sin\theta_i cos\theta_s cos\phi_s \tag{3.41}$$

$$a_3 = sin\theta_i cos\theta_s + cos\theta_i sin\theta_s cos\phi_s \tag{3.42}$$

$$a_4 = cos\theta_i + cos\theta_s \tag{3.43}$$

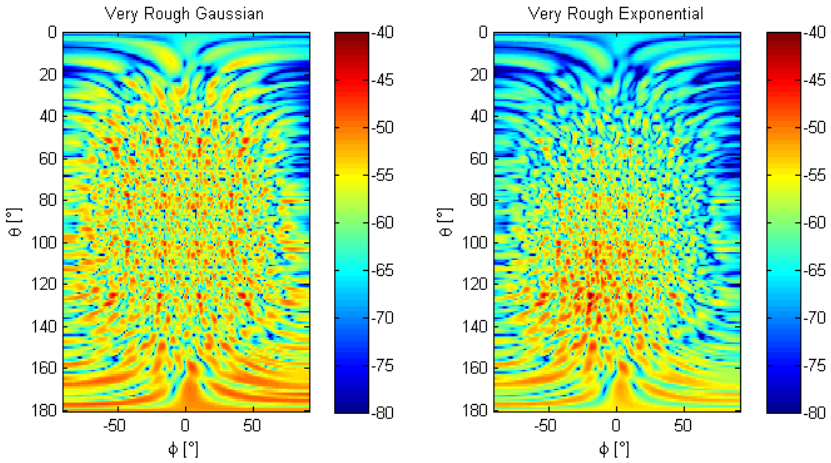

Figure 3.10: Example of bistatic RCS of a square of 5m width using the rough surface models

As visible, all four rough surface scattering models here presented are empirical. To compensate, one last rough surface scattering model based on the simplified PO algorithm has been introduced. The concept of this last model, also called *slightly rough specular* model, is to generate randomly distributed facets on which the specular reflection is applied. This approach allows synthesising roughness profile with a better control on polarisation effects. One validation example of such approach is provided in Fig.3.9. Note that the four previously mentioned rough surface scattering models are generalised analytical models reproducing the same experiment as the slightly rough specular model assuming Gaussian and exponential distribution of the facets. Further validation examples are provided in Appendix C.3.

3.3 Numerical validation of the 3CM in simple cases

3.3.1 Narrow-band validation on isolated façades

This first validation subsection is relative to the total power scattered by an isolated complex façade. Two different façades are here considered and presented in this validation exercise.

First the city centre façade presented in Fig.3.11. As visible several representations of the same façade are possible. Fig.3.11a is a photography of a real façade as it can be found in the city center of Toulouse, France. Fig.3.11b is an interpreted 3D CAD *(Computer Aided Design)* version of the same façade. This representation has been used in SE-WorkBench and Elsem3D when performing reference simulations. This façade is 4m in width by 6m in height and composed of 715000 edges. Due to restrictions on computation time when using Elsem3D (MoM based) on such a huge object, a PEC material was assumed. In the following, all simulations were performed using PEC material although the 3CM perfectly handles dielectric materials. Fig.3.11c represents the same façade translated into the 3CM formalism. This façade is composed of twelve objects (windows, balconies, corners...), each object being discretised into square facets of width 0.5m. The size of the facets has been chosen to be maximum, for computational effort reduction, but must satisfy the far field assumption. Facets of width 0.5m are a good trade-off for 1.5GHz systems, since they are large enough and satisfy the far field condition as close as 5m. The specular reflection component is applied to the red facets. The backscattering component is applied to the blue facets. The incoherent scattering component is applied to the green facets. As visible, the 3CM simplified version of this building has four windows on which the specular component is applied. It also has six backscatterers, four for receding window corners and two for protruding balconies. This façade also has two guardrails modelled using the rough surface model with exponential roughness distribution on each facet with parameters h =0.2 and l =0.5. Those facets are randomly thrown in a volume of depth equals to 0.5m. Finally the wall is modelled using slightly rough specular model. This surface has not been modelled using pure specular facets (red) since the real wall is not as smooth as a pure concrete wall. Using the slightly rough specular model allows to break the phase coherence to reduce the specular phenomenon and still reproduce the incoherent scattering phenomenon.

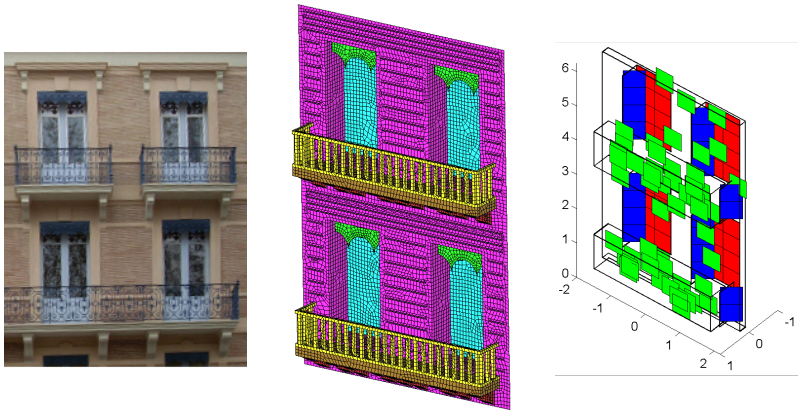

(a) Real façade (b) 3D CAD model (c) Simplified 3CM

Figure 3.11: Three different representations of a complex city center façade

This city centre façade has been used to perform the next validation example, presented in Fig.3.12. The simulation scenario is similar to the one presented in section 3.1.1. The façade is placed above the ground plane at position y=0. The transmitter is placed at 20.000 km from the façade centre considering 0° elevation and 40° azimuth. Even if not a typical incidence forLMS systems, 0 ° elevation and 40 ° azimuth allows to highlight the backscattering phenomenon. The transmitting frequency is set to 1.5GHz using θ polarisation. A mobile receiver is moving

following a linear trajectory passing in front of the façade at x=10m. Fig.3.12 presents the total power scattered by the façade, w.r.t the LOS incident power, as a function of receiver position. Five curves are displayed: Elsem3D which is the reference based on MoM method (plain black), the total power scattered by the façade using the 3CM model (plain cyan), the specular contribution of the façade (dashed red), the backscattering contribution (dashed blue) and the incoherent contribution (dashed green).

As expected, all three components have a different contribution into the total scattering function depending on the mobile position. In the specular zone, around -10m, the specular component is predominant while in the backscattering zone, around +10m, the backscattering component is predominant and between both the incoherent scattering component makes the transition. Also noticeable is the high power values reached by the incoherent component in the specular zone. This can be explained by the use of the slightly rough specular model to reproduce wall roughness in the 3CM formalism. By doing so, the contribution of the wall, almost specular, becomes predominant in the specular zone while the contribution of the guardrails, very rough exponential surface model, is predominant elsewhere.

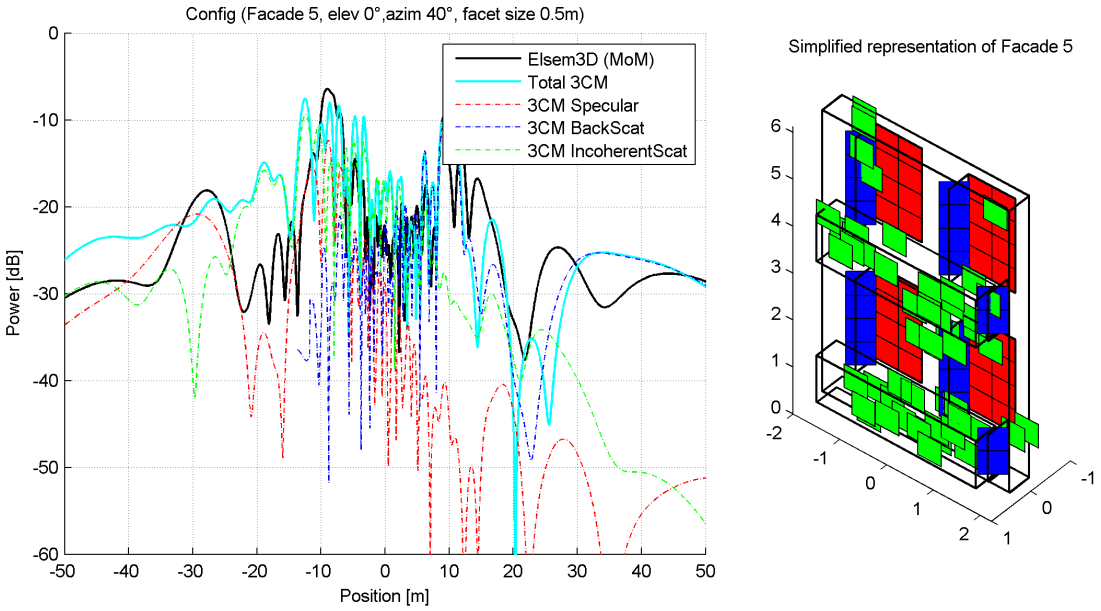

Figure 3.12: Repartition of the three component into the total narrow-band power scattered by a complex city centre façade.

To validate the representation of the city centre façade using the 3CM formalism, nine different incidences have been tested w.r.t both MoM reference using Elsem3D and asymptotic reference using SE-WorkBench. Results are presented in Fig.3.13 using the same scenario as detailed for Fig.3.12 except for incidence angles.

The critical validation zone is placed between 0dB and -20dB w.r.t the LOS level since MP in this range have a significant impact on navigation receivers. The range from -20dB to -40dB is also important in case of LOS blockage as it can frequently occur in urban environments. However, this second range is less critical in terms of validation. In general, all three models present a reasonable agreement in terms of scattering shape with slight differences from time to time on particular trajectory points due to constructive and destructive interferences. In Fig.3.13, for all non-zero azimuth configurations, the scattering pattern reveals two significant peaks, one for the specular reflection and the other one for the backscattering. Note that the backscattering peak is less pronounced for higher elevations. Also noticeable, the 3CM model fits better with Elsem3D results for high elevation and high azimuth cases. This observation can be explained by

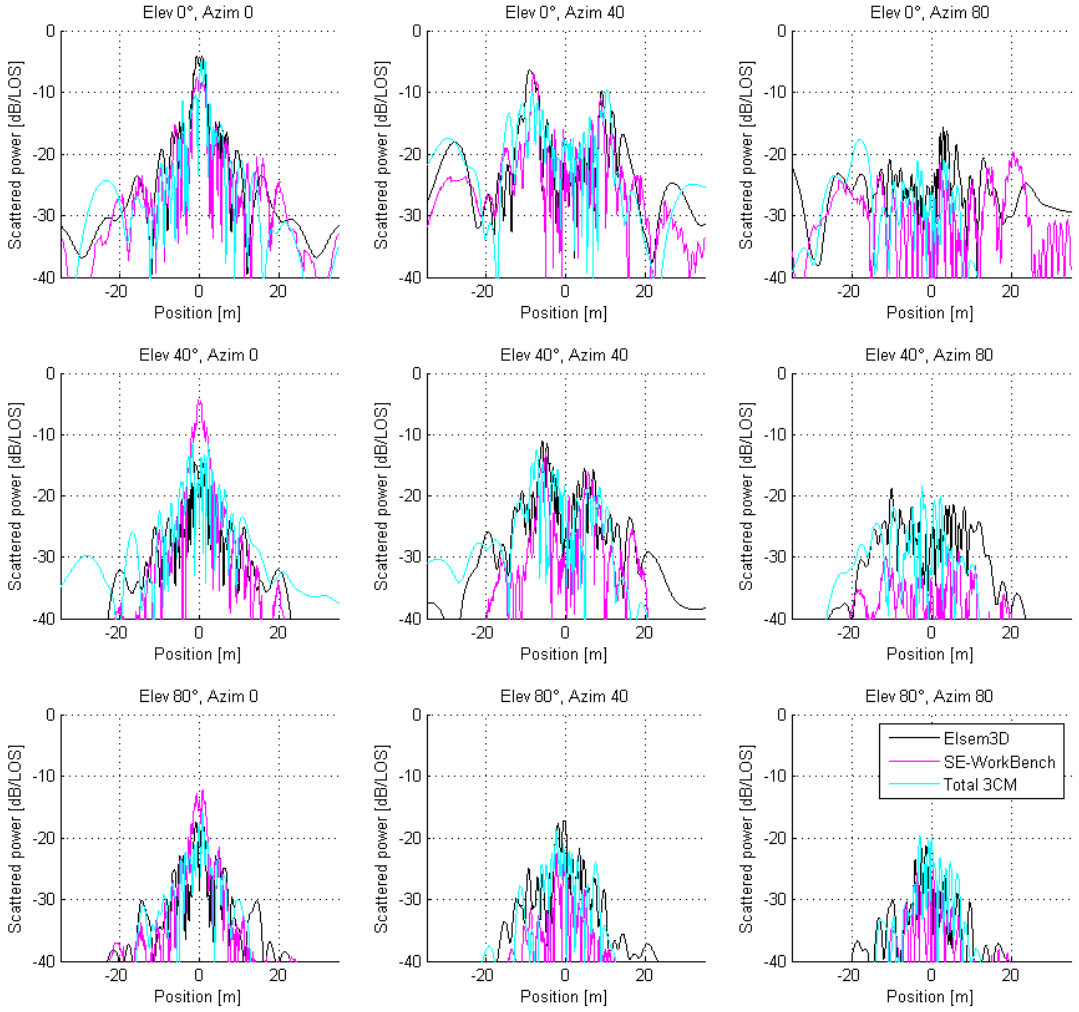

Figure 3.13: Total narrow-band power scattered by a complex city centre façade for various incidence angles

the fact that the asymptotic tool tends to under estimate the incoherent scattering phenomenon which is well reproduced by empirical rough surface models implemented in the 3CM. However, the scattered power is about -30dB which is negligible in LOS conditions.

To extend observations made on city centre façades, a second validation example has been detailed next for an ONERA office façade type following the same principle. Fig.3.14 presents the three different representation of an ONERA office façade from a photography to the simplified representation of the façade implemented in the 3CM. In Fig.3.14c uses the same representation convention as previously mentioned (red=specular, blue=backscattering, green=incoherent). The ONERA office façade is made of three objects, two specular representing the walls and one incoherent representing the windows plus all the small features. Note that this type of architecture does not require any backscatterer since protruding and receding elements are almost non-existent and only contribute to break the specular mechanism and increase the incoherent scattering near the windows.

As visible in Fig.3.15, a good agreement between Elsem3D and 3CM is achieved where the specular component is predominant. This phenomenon is due to the specular nature of this façade which is smooth compared to the city centre façade. Comparison made upon several incidence angles as presented in Fig.3.16 shows a reasonably good agreement for low elevation angles and typical incidence configurations. However, for high azimuths, both 3CM and SE-WorkBench show limitations in reproducing the incoherent scattering since this façade profile is mainly made of specular surfaces.

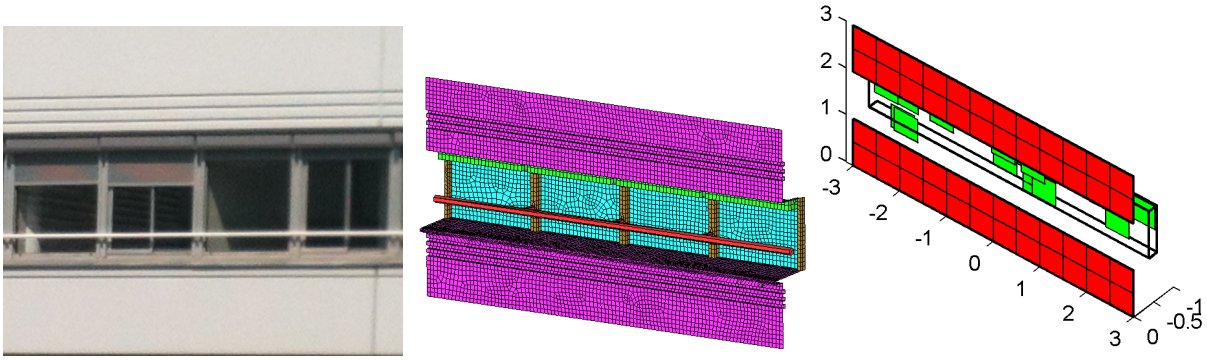

(a) Real façade (b) 3D CAD model (c) Simplified 3CM

Figure 3.14: Three different representations of a complex ONERA office façade

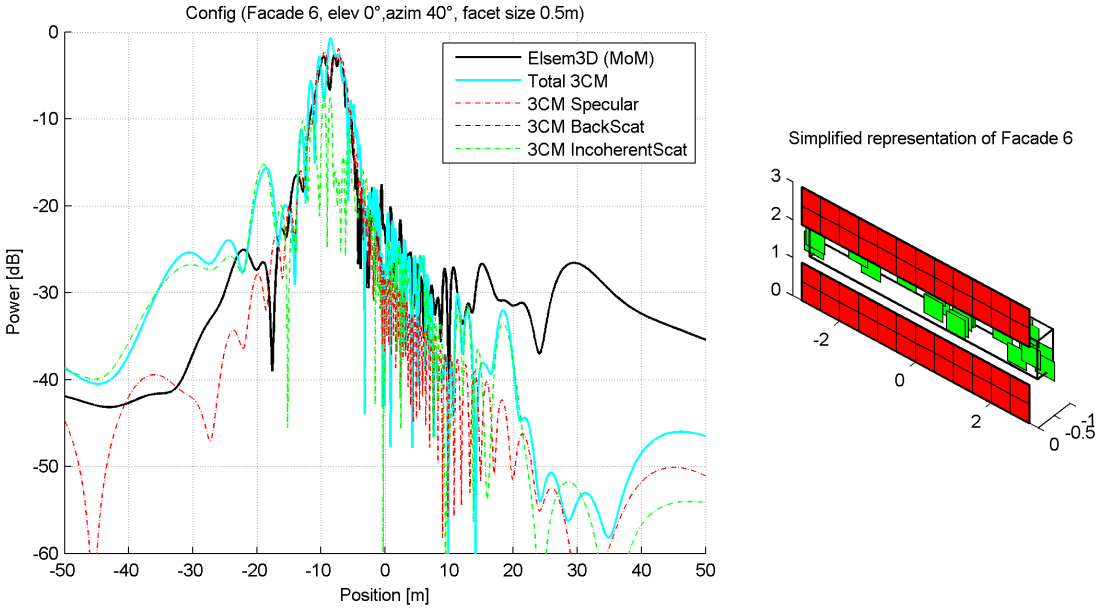

Figure 3.15: Repartition of the three component into the total narrow-band power scattered by a complex ONERA office façade.

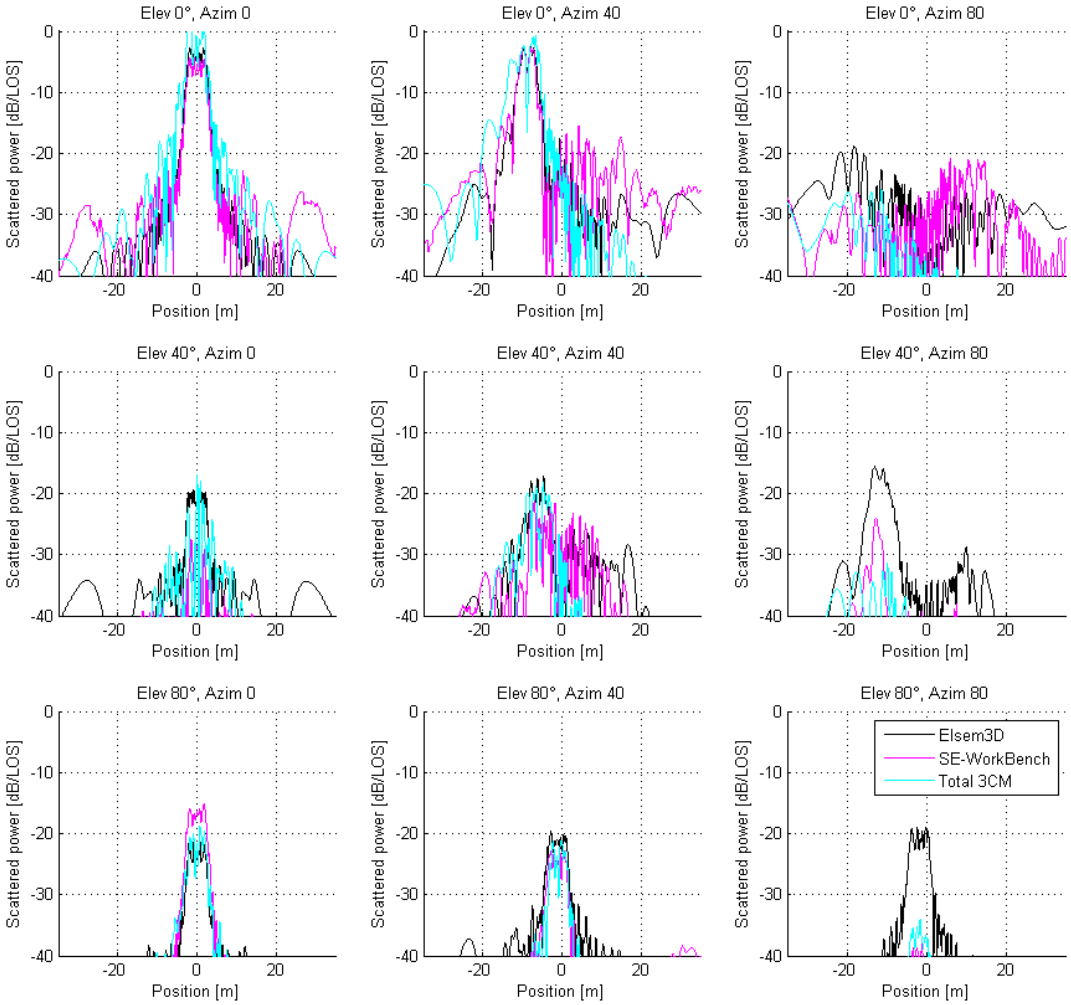

Figure 3.16: Total narrow-band power scattered by a complex ONERA office façade for various incidence angles

3.3.2 Narrow-band validation on simple canyons

The second validation example, performed in this subsection consists in associating several façades into a wider scenario to represent a simple row of buildings. The simplified representation of this urban canyon is presented in Fig.3.17. Equivalent simulation environments have been built for Elsem3D and SE-WorkBench using 3D CAD façades such as the one presented in Fig.3.11b and Fig.3.14b.

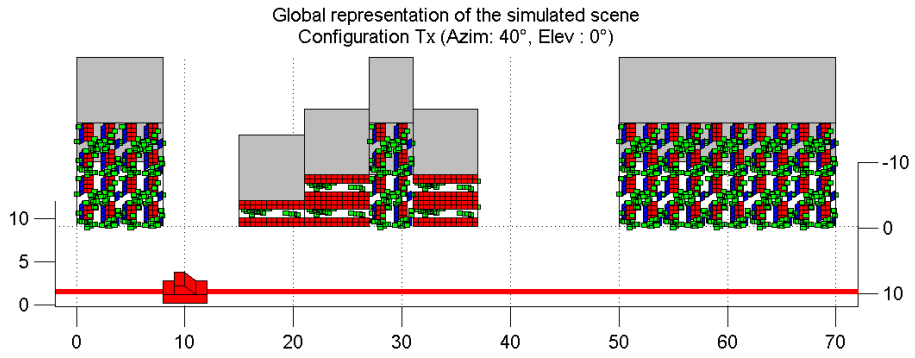

Figure 3.17: 3CM simplified representation of the simulated street canyon

The simulation scenario is the following. A street canyon is composed of several façades as presented in Fig.3.17. The right side of the street is building free. The mobile receiver is following

a linear trajectory at 10m from the building row at a constant speed equals to 30km/h. The source is θ polarised and placed at 20.000 km, 40° azimuth and 0° elevation. Fig.3.18 represents the total power scattered by all buildings without considering the LOS contribution.

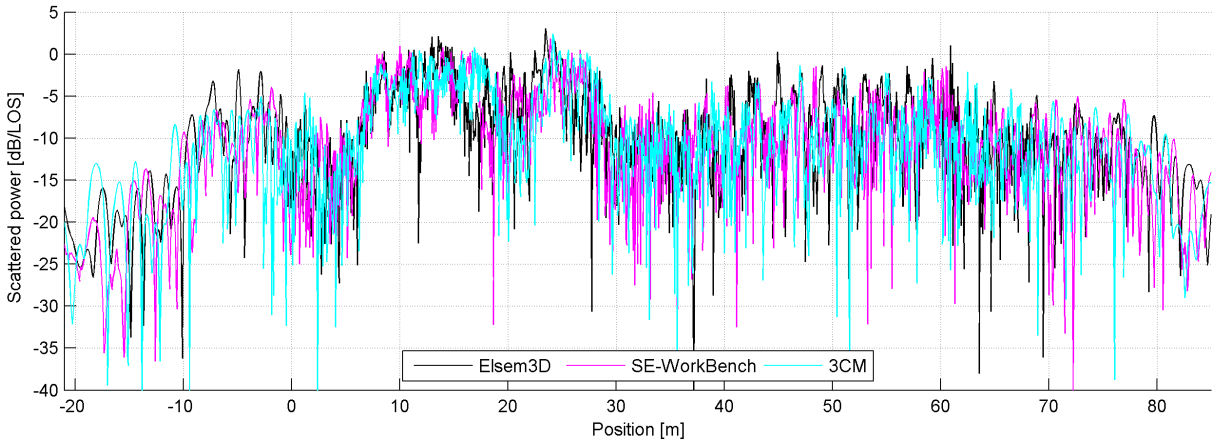

Figure 3.18: Total narrow-band scattered power in a simple urban canyon

On all three complex time-series presented in Fig.3.18, the influence of the environment can be easily seen on the total power scattered by the environment. From -5m to +2m and from +40m to +60m the specular reflection respectively on the first and third buildings is visible. From +60m to +80m, a relatively high power region can be noticed. This region can be related to the backscattering phenomenon taking place on the third building before decreasing after +80m. A particularly powerful contribution can be noticed from +5m to +30m due to a specular reflection taking place on the second building. As visible on Fig.3.17, the second building is mainly made of ONERA office façades which mainly consist of specular elements. It results that the scattered power in this zone is higher as compared to that near the first and third buildings. As visible, all three simulations present a good agreement in terms of dynamics and mean power scattered by the canyon.

From the complex time-series presented in Fig.3.18, a spectrogram and a power spectral density plot can be produced using the available phase information. Note that the LOS signal is still absent from those simulations and only the scattered power is considered. Fig.3.19 represents an interesting comparison point between reference methods and the 3CM on a spectrogram. The method here used is based on the short-time Fourier transform implemented in Matlab using the spectrogram function. The power colour scale is given in absolute dB values assuming EIRP= $1W$ at the transmitter side. From a first observation, a good agreement is noticeable. On all three figures, the footprint of all three buildings is clearly visible and comparable in terms of power. A strong component around +30Hz can be attributed to the specular reflection taking place on building faces. Some smaller contributions are also noticeable around -30Hz which can be linked to the backscattering phenomenon.

Fig.3.20 represents the power spectral density along receiver trajectory using the Welch method [Welc 67] which is equivalent to an averaged Doppler spectrum. The first observation that can be made is the power peak around 30Hz which corresponds to the specular reflection on façades. A second interesting peak is around -30Hz. Symmetrical w.r.t the first one, this second peak corresponds to the backscattering phenomenon as presented above. Once again, a good accordance is achieved between Elsem3D, SE-WorkBench and the 3CM.

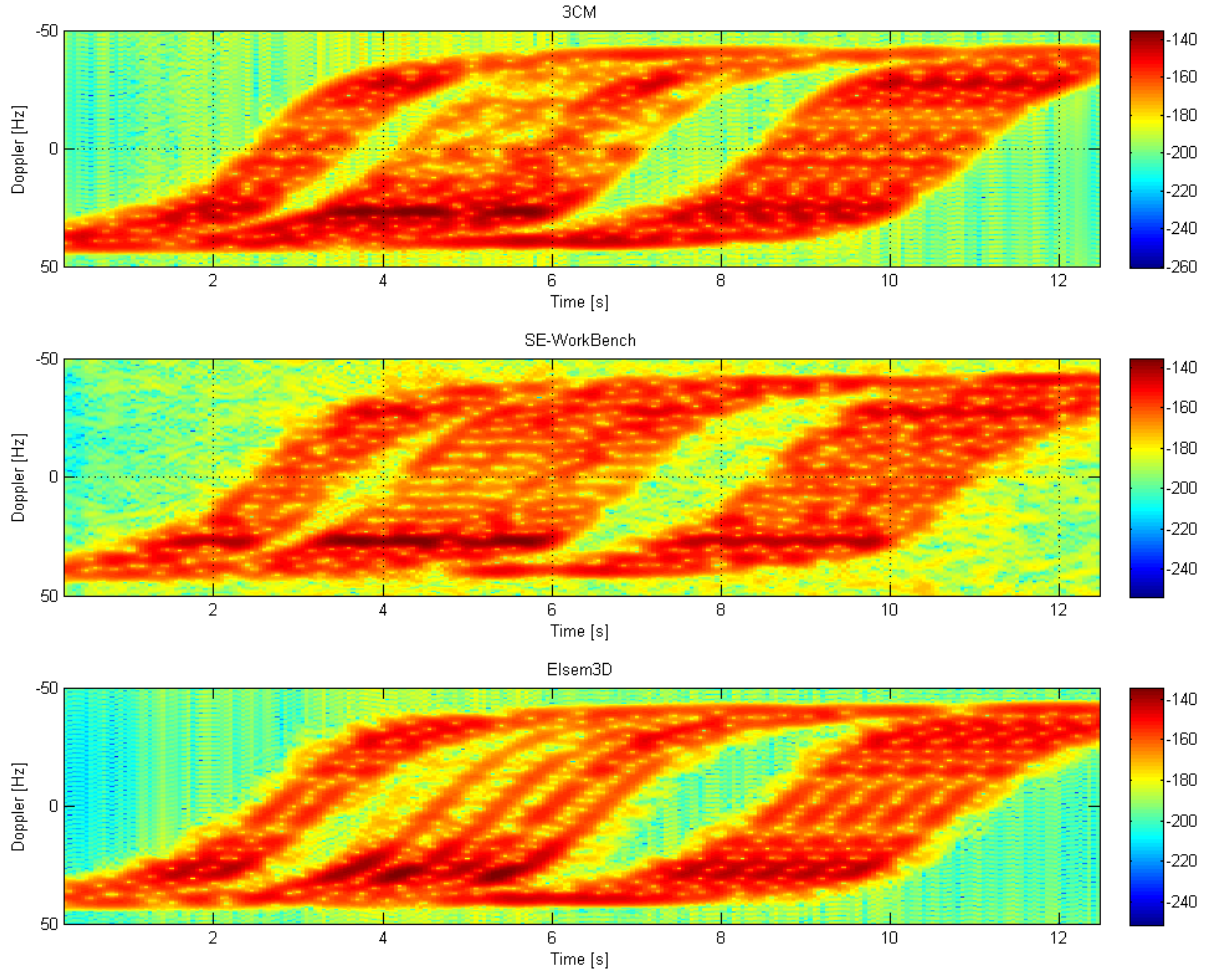

Figure 3.19: Spectrogram along the receiver trajectory

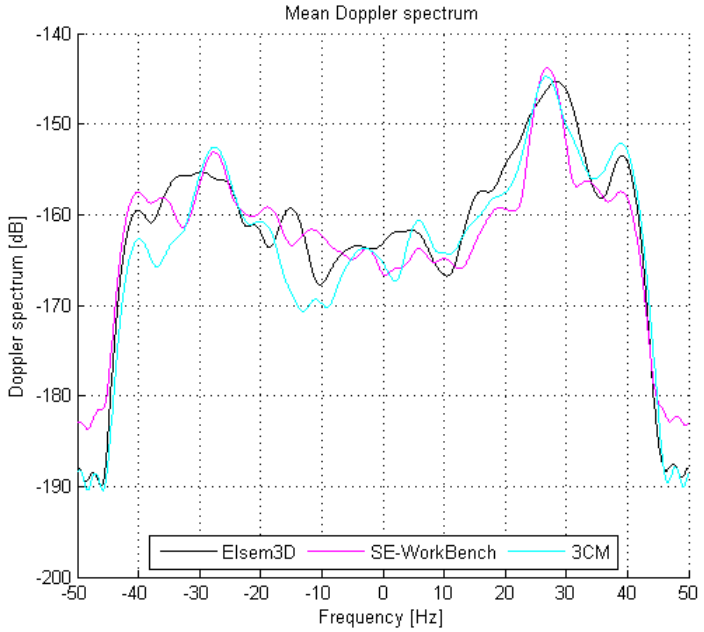

Figure 3.20: Power spectral density along the receiver trajectory

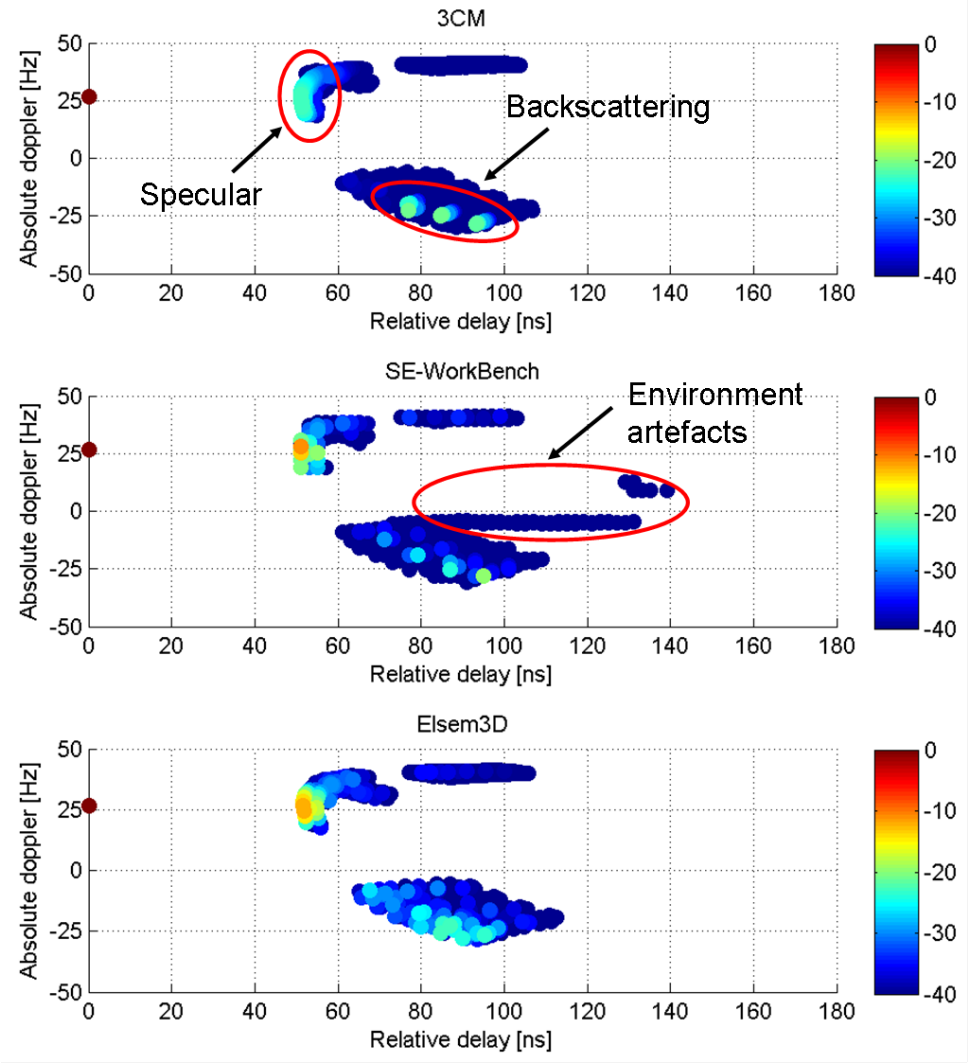

Figure 3.21: Power delay/Doppler channel impulse response

3.3.3 Wide-band validation on simple canyons

To complete the narrow-band validation performed in the previous subsection, a wide-band validation is here presented. All parameters from the previously described urban scenario are kept constant. The first validation performed in this subsection deals with a qualitative observation of instantaneous CIRs presented in Fig.3.21. For this snapshot, the receiver was at position y=10m as presented in Fig.3.17. In Fig.3.21 the X axis represents the relative delay of each echo w.r.t the LOS, the Y axis represents the absolute Doppler of each echo and colour axis represents the relative power of each echo. The power scale has been truncated to the zone of interest from 0dB to -40dB as previously explained. The wide-band technique used to produce pseudo CIRs using MoM Elsem3D has been presented in section 2.4.1. The reader is reminded that several rays per façades are assumed in this subsection as mentioned earlier.

For those simulations, the LOS signal has been taken into account. It is represented by a red dot with null delay and about 25Hz Doppler on each three plots in Fig.3.21. From a qualitative point of view, all three simulations give a comparable result in terms of delay/Doppler channel shape. However, a small difference is visible on SE-WorkBench simulation around 0Hz. This difference is due to environment artefacts since SE-WorkBench considers real 3D environments with buildings of 10m deep while the 3CM and Elsem3D consider only 2.5D environments where only façades have some depth while buildings depth is not taken into account. This results in multiple interactions taking place on those side walls before reaching the receiver with a longer delay and much more attenuation. Since the power is low and only few receiving location are

impacted, those echoes will not have any influence on the following observations.

The main significant difference is that 3CM seems to underestimate the specular reflection. Note that the specular region is characterised by its Doppler which is equal to the LOS Doppler. In this region, the 3CM shows echoes of about -20dB while SE-WorkBench and Elsem3D have stronger echoes of about -10dB. This phenomenon can be explained by the fact that the 3CM has a higher space resolution in terms of environment description, 0.5m. This results in numerous weak echoes which are radiating in phase to produce constructive interferences. If those echoes were summed together, it would result in fewer but stronger echoes as is the case for the Elsem3D and SE-WorkBench simulations. One other interesting observation is the backscattering contribution which can be highlighted in the negative Doppler region. Backscattering contributions seem punctual for 3CM and SE-WorkBench while they are more diffuse in Elsem3D simulation. In any case, using all three simulation tools, the backscattering component signs the CIRs confirming that this component has to be properly modelled and dissociated from the incoherent scattering component.

Regarding the time performances, the presented trajectory in Fig.3.17 has 937 sampling points. This simulation has been performed on a desktop computer with Intel Core2 Duo E8400 CPU 3GHz and 3Go RAM. The following computation times are only indicatives. The 3CM takes 18.80s to simulate all CIRs with more than 2000 rays per CIR. This represents one CIR every 20.06ms. Such computation time is considered as real time for navigation purposes since it is close to typical integration time (20ms). On the same computer, a SE-WorkBench simulation takes about 1730s, ninety times higher. The Elsem3D computation time is not representative since the initial computation has been performed on a super computer and IRs were pre-computed.

From Fig.3.21, qualitative observations can be made. To better observe the channel over the whole receiver route two channel parameters relative to the delay have been retained: the MP mean delay and the MP RMS delay spread. Each one is presented in Fig.3.22 using respectively Eq.3.44 and Eq.3.45 where Γ represents the power of the echoes and τ their delay relative to LOS.

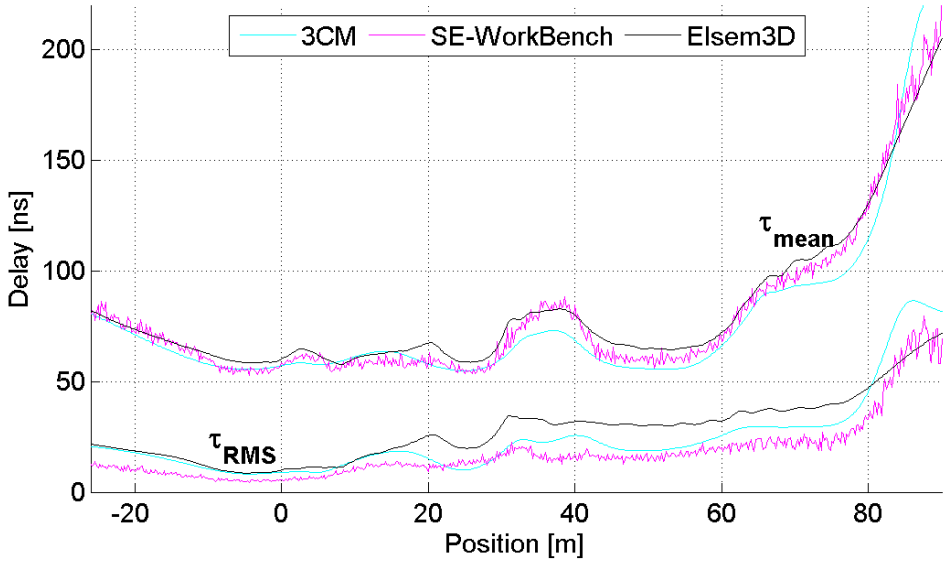

Figure 3.22: τ_{mean} and τ_{RMS} function of the mobile position

$$\tau_{mean} = \frac{\int_0^\infty \tau\,\Gamma(\tau)\,d\tau}{\int_0^\infty \Gamma(\tau)\,d\tau} \tag{3.44}$$

$$\tau_{RMS} = \sqrt{\frac{\int_0^\infty (\tau-\tau_{mean})^2\,\Gamma(\tau)\,d\tau}{\int_0^\infty \Gamma(\tau)\,d\tau}} \tag{3.45}$$

Since LOS is highly predominant in our simulations, it has been removed to better observe the temporal distribution of the delayed echoes. As visible on Fig.3.22, the RMS delay spread is low, in the order of few tens of nanoseconds in our simple case. The delay spread is in good agreement between all three simulations. Regarding the mean delay, it can be noticed that it is almost constant from -5m to 60m. This region corresponds to the specular region of the urban canyon. Observing Fig.3.21 we can see that 55ns corresponds more or less to the delay of the specular component. We can conclude from Fig.3.22 that the main power contribution comes from the specular reflection. It can also be noticed that the mean delay gets higher at the end of the trajectory. This is due to the geometry of the simulation. Since the mobile is facing the LOS, the delay spread is reduced when the buildings are in front of the mobile. On the opposite case, when the buildings are far behind the receiver, echoes have to pass the mobile to reach the buildings before being reflected back to the mobile. This extra path highly increases the delay. Also noticeable is the fact that the pink curve (SE-WorkBench) is not as smooth as the two others. Extra experiments have shown that this phenomenon is due to MP summation on a tapped-delay line (delay axis sampling of 2ns) taking place in SE-WorkBench processing. Elsem3D and 3CM are not affected since they do not use discrete but continuous delays.

3.4 Summary

This chapter presents a new simplified model to reproduce building macro-scattering pattern in urban environments. The 3CM - 3 Component Model - has been designed according to practical observations made on numerical simulations and experimental measurements. Three different wave propagation mechanisms have been highlighted in this chapter on which the 3CM relies. The specular component is originated from smooth and wide surfaces such as windows and flat walls. The backscattering component is a double bounce reflection mainly taking place on protruding balconies and receding window corners. The incoherent scattering comes from small objects present on façades such as guardrails or rough walls. This three macro propagation decomposition can be also implemented into conventional ray-tracing tools considering minor adjustments.

The 3CM model here presented is oriented toward MP wide-band representation of the channel with a strong emphasis on computation time reduction. Based on a simplified PO algorithm, the 3CM achieves around one-hundred time reduction factor w.r.t to conventional ray-tracing tools. Since the 3CM is based on EM asymptotic models, the 3CM perfectly handles dielectric materials and elliptical polarisations. It is also frequency scalable and particularly adapted for L, S and C bands without restrictions for higher frequencies, but not investigated yet. Typical outputs of the 3CM are delay, Doppler, DoA and polarised complex amplitude of each ray. Finally the 3CM is suitable for MIMO studies with polarisation diversity, frequency diversity and optimised for transmit/receive diversity.

In this chapter, the implementation of each three component has been detailed and some validation examples have been provided in canonical configurations. Further numerical validations have been performed and results are detailed in Appendix C. The three components have then been integrated into the 3CM model and several validation examples have been provided in Section 3.3. First, the total narrow-band scattered power in the case of two isolated complex façades followed by the case of a simple urban canyon. Very good agreement has been found

considering both MoM and asymptotic GO/PO tools as references. Those comparisons have been performed in terms of power, spectrogram and Doppler spread. Wide-band simulations have also been presented with a qualitative analysis of complex CIRs and a delay spread analysis.

As a limitation of the 3CM approach, the facade decomposition into the three components may be seen as a limiting aspect for non advised users. In the case of the presented validations on city center and office building facades, their synthetic representations were tuned and adjusted according to the MoM reference established with Elsem3D. In practice, and as shown in Chapter 4, the facade architecture can be easily broken down and each component can be identified on the facade representation. This approach is not formal and different users may design slightly different synthetic facades from the same facade picture. However, no particular sensitivity of the model has been noticed as far as all three components are roughly represented and dielectric materials are not PEC. For occasional users, a facade library may also be tuned by advised users and distributed to them to simplify their use.

The 3CM model, reproducing the EM interactions between wave fronts and complex buildings, is now ready to be integrated into a new enhanced simplified channel model handling LOS contributions with blockage and diffractions for better realism in more complex environments. This new enhanced simplified channel model is treated in the next chapter.

Chapter 4

Implementation and validation of the SCHUN LMS channel simulator

Contents

4.1 Implementation of the SCHUN simulator 92
4.1.1 The SCHUN LMS channel simulator 92
4.1.2 Virtual environment synthesis 93
4.1.3 Direct path blockage models 96
4.1.4 Introduction of a new multipath reduction method 98
4.2 Saint Lary experimental validation for satellite communication systems 102
4.2.1 Presentation of the Saint-Lary 2012 measurement campaign 102
4.2.2 Presentation of Saint-Lary virtual environment 105
4.2.3 Comparison with experimental SISO co and cross circular polarised channels in S-band 109
4.3 Toulouse Capitole experimental validation for satellite navigation systems 115
4.3.1 Presentation of the Toulouse-Capitole 2011 measurement campaign 115
4.3.2 Presentation of Toulouse-Capitole virtual environments 117
4.3.3 Indirect experimental validation on GNSS software receivers 122
4.4 Discussion 134

The objectives of Chapter 4 are to present the implementation and the validation of an enhanced physical-statistical simulator of the land mobile satellite channel for multipath modelling applied to satellite navigation systems.

Chapter 4 is the focal point of the previously presented material. As a reminder, based on the critical review of the existing models, Chapter 1 has introduced a new philosophy for the design of this new LMS channel simulator to meet specific requirements. Chapter 2 has recommended the use of the 2.5D façade approximations to take into account the specific architecture of the façades which has a significant impact on the macro-scattering pattern. Using the 2.5D façade approximation, Chapter 3 has introduced a new wide-band building scattering model based on EM theory and particularly on PO algorithm which allows to take into account macro roughness due to façade architecture and micro roughness due to rough surfaces. The present Chapter 4 merges the observations, conclusions and recommendations made previously conducting to the design of a new LMS channel simulator: SCHUN *(Simplified CHannel for Urban Navigation)*.

This chapter is organised as follows. The first section is dedicated to the implementation of the SCHUN simulator where the first subsection recalls the main characteristics of the SCHUN simulator such as its macro-architecture, its capabilities or the basic scenarios handled by the simulator. The second subsection details the adaptation and the implementation of the virtual city concept. The third subsection presents two direct path attenuation models to reproduce building blockage. The fourth subsection introduces a new method for reducing the number of multipath. The second and third sections are dedicated to the experimental validation of the

SCHUN simulator. The second section presents one direct experimental validation on channel measurements oriented toward narrow-band MIMO issues and performed in Saint Lary village in 2012. The third section presents one indirect experimental validation oriented toward satellite navigation performances in dense urban environments which have been performed in Toulouse Capitole in 2011.

4.1 Implementation of the SCHUN simulator

4.1.1 The SCHUN LMS channel simulator

4.1.1.1 The macro-architecture of the simulator

The macro-architecture of the SCHUN LMS channel simulator is presented in Fig.4.1. The interaction model for vegetation effects has not been developed yet and is not included in current version of the simulator as already discussed in Chapter 1. Nevertheless, the software architecture is already suitable for adding such model. Future development could also allow adding new interaction models with urban features such as lampposts or bus shelters.

The macro-architecture of the SCHUN simulator presented in Fig.4.1 reflects its hybrid physical-statistical design, where a simplified virtual city environment is generated from statistics while physical based methods are used to reproduce the interactions between the wave fronts and the buildings. This hybrid architecture also allows to fulfil all the objectives and constraints mentioned in Section 1.2.1.

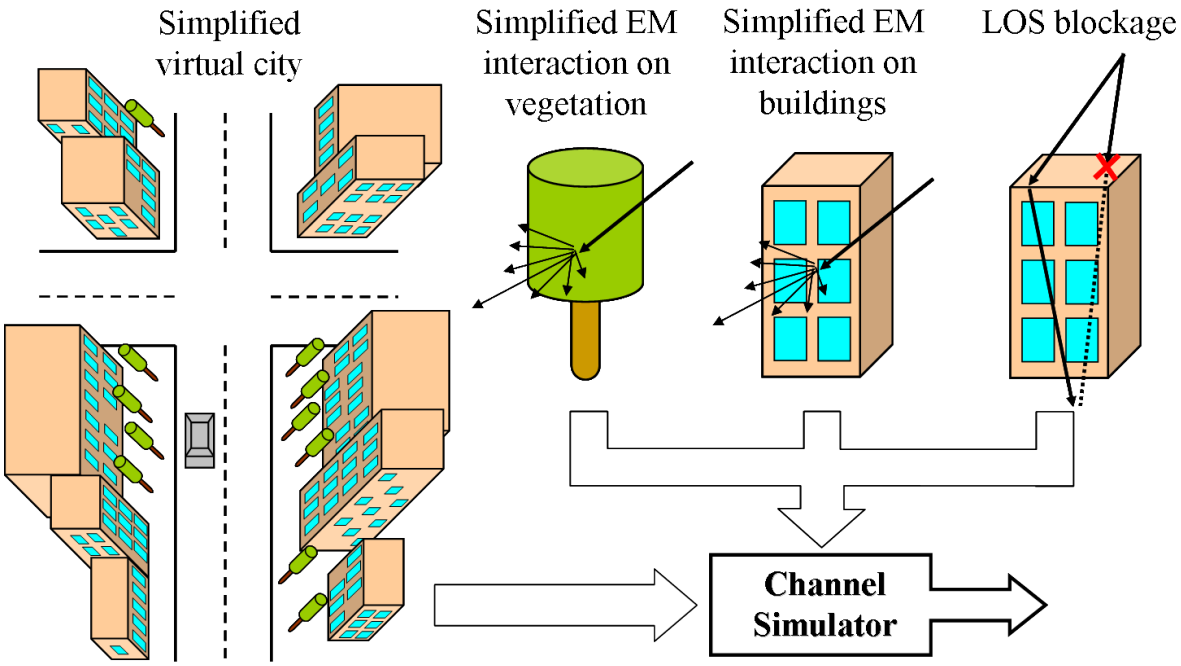

Figure 4.1: Macro architecture of the SCHUN LMS channel simulator

4.1.1.2 Capabilities of the channel simulator

At the present state, the SCHUN LMS channel simulator is suitable for a wide-band representation of the LMS channel in mobile contexts and particularly oriented toward realistic multipath synthesis considering amplitude, polarisation, phase, delay or Doppler as key parameters. A constant attention has also been paid to computation time requirements and the present SCHUN simulator achieves almost real-time channel impulse response synthesis on conventional desk

computers although implemented in Matlab. Having in mind future applications for next generation of LMS and GNSS systems, the SCHUN simulator includes several assets for MIMO issues since natively handling satellite diversity, receiving space diversity, frequency diversity or polarisation diversity. The SCHUN simulator is also frequency scalable for a wider range of possible uses, including satellite communication systems in C-band.

Since based on EM physical models and independent from any measurement tuning, the SCHUN LMS channel simulator is more versatile compared to other simulators and suitable for a very wide range of possible environments, either European cities such as Toulouse or Munich or US cities such as New-York. The use of the virtual city concept also allows generating very wide city-like environments for testing system performances. In the field of satellite navigation systems, the typical targeted applications are the design of new GNSS receivers, the study of multipath mitigation techniques or future improvements on signal modulations and satellite availability. In the field of satellite communication systems, the SCHUN simulator could also offer an efficient tool to predict MIMO correlated channels considering polarisation, frequency or position diversity either at the transmitter side or at the receiver side.

Finally, the SCHUN LMS channel simulator can be seen as an almost deterministic tool satisfying fast computation criterion.

4.1.1.3 Basic scenario

The SCHUN simulator relies on one basic scenario. In this basic scenario, the environment is composed of two rows of buildings where the position, the size and the architecture of the buildings are randomly generated as presented in Section 4.1.2.2 relative to the virtual city synthesis. Depending on the transmitting satellite position, one side of this street canyon is responsible for direct path blockage on the coherent component while the other side of the street is responsible for generating the multipath component. A mobile receiver is moving through this urban canyon following a linear trajectory parallel to the street axis with a constant speed.

More recently, this basic scenario has been extended to more realistic scenarios for validation needs. The main new features are the ability of the SCHUN simulator to handle smooth street changes with receiver orientation changes, speed changes of the receiver or moving satellites.

In the SCHUN formalism, the satellites are defined by their position, polarisation, frequency and EIRP. Their azimuth is defined with respect to the X axis (normal to the street canyon) toward the Y axis (representing the mobile direction and street canyon orientation). The reference for the elevation is the ground plane.

The mobile receiver is defined by its position and its speed. Several sensors can be attached to the receiver. The sensors represent each receiving antennas and are defined by their relative position to the receiver, polarisation and antenna diagram.

4.1.2 Virtual environment synthesis

The goal of this section is to present how the virtual city concept has been adapted and implemented to answer our problematic and how complex environments are generated in the formalism of the SCHUN simulator.

4.1.2.1 Layout of environment objects

In the SCHUN formalism, the virtual environment is composed of four hierarchical classes of objects, namely buildings, façades, architectural elements and facets. One example is presented in Fig.4.2. Each class of element is introduced in this subsection and further details are given

in the following.

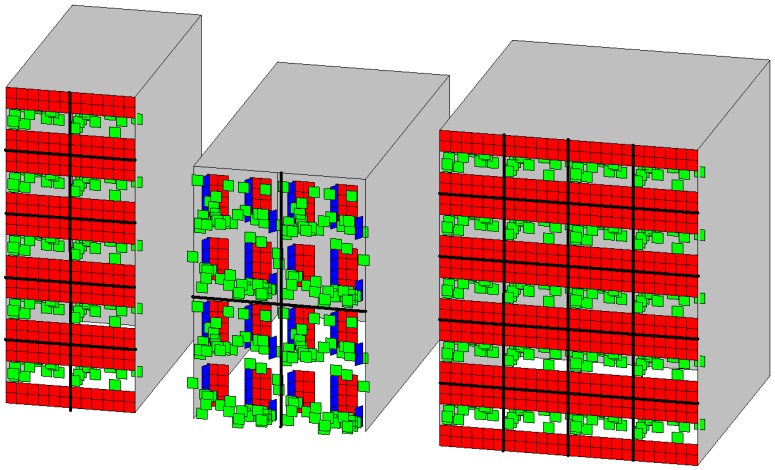

Figure 4.2: Example of the environment decomposition used in the SCHUN formalism

The building represents the largest object of the environment. It is modelled as a rectangular parallelepiped of width w, depth d and height h. The buildings are responsible for all shadowing and blockage effects experienced by the LOS signal.

Each building is composed of façades, representing the building macro-roughness due to its architecture using the 2.5D façade approximation. The façades, representing several square meters, are aligned on the building wall facing the street canyon as presented in Fig.4.2. On those façades, the macro-scattering model 3CM is used to synthesise the multipath component of the channel. For the needs of the SCHUN simulator, a library of façades has to be defined by the user. Several examples are given in next sections relatives to the experimental validations. This approach using the 2.5D façade approximation allows to represent the architectural details, large compared to the wavelength, as recommended in Chapter 2 contrary to the use of flat walls which turns out to be highly limiting. Note that this approach is also innovative compared to the existing virtual city generators where the importance of the architecture is here taken into account in the modelling of complex urban environments.

Each façade is made of several architectural elements representing walls, windows, balconies or dihedrals. For each architectural detail, one type of propagation phenomenon has been applied on it according to the three propagation phenomena described in Chapter 3 by the 3CM model.

Each architectural element is then broken down into facets. The facet represents the smallest object of the environment and all EM calculations are performed at this scale. From our experience, 0.5 m facet width is advised for performing the EM computation at 1.5 GHz since small enough to fulfil the far field conditions (4 m) and large enough to reduce the computation time. The higher the frequency, the smaller the plate.

4.1.2.2 Building synthesis

The buildings are synthesised using a conventional virtual city generator. Each building is characterised by six parameters, three size parameters and three positioning parameters in the street canyon referential according to the basic scenario formalism. The size parameters are based on log-normal distributions as previously discussed in Section 1.1.4. For the needs of the SCHUN simulator, the width and the height are rounded to obtain an integer number of façades for texturing the building. The type of façade to be applied on each building wall facing the canyon follows a uniform distribution where each façade has a certain probability to be chosen.

This parameter highly depends on the type of targeted environment. The positioning parameters are generated using a uniform distribution of building alignment and building spacing. The street changes of the receiver are also randomly generated using a normal distribution of street length and street orientation. Each of the mentioned distributions are characterised by their mean and their standard deviation. One example of statistically synthesised virtual city profile is given in Fig.4.3 for a 700 m trajectory length.

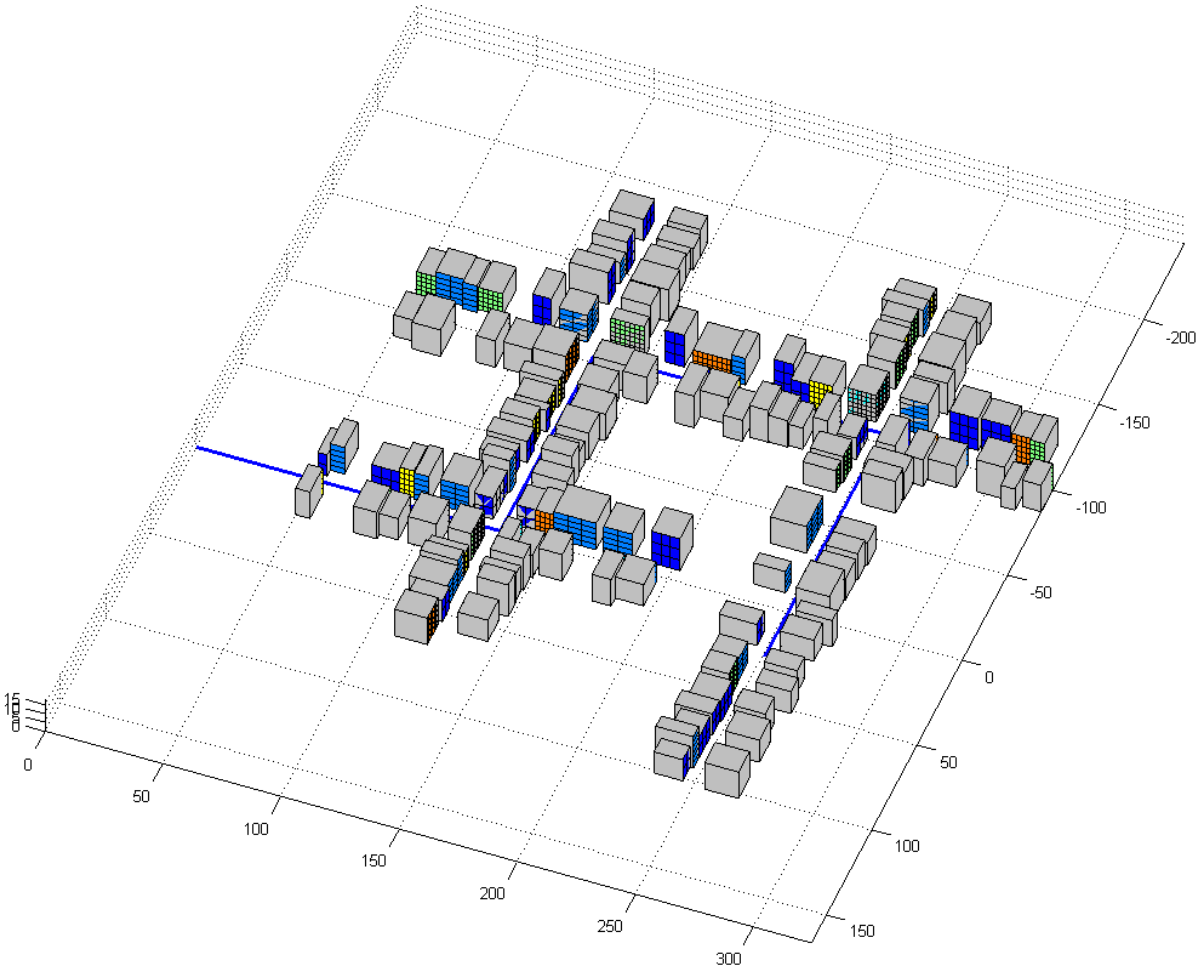

Figure 4.3: Example of statistically synthesised virtual city profile

4.1.2.3 Façade synthesis

To illustrate the concept of generating realistic façade library, two façades have been presented in Fig.3.11c and Fig.3.14c. Several others are presented from Fig.4.14 to Fig.4.17 and from Fig.4.33 to Fig.4.36. Each façade is made of several architectural elements represented by rectangles. Each rectangle is characterised by a different propagation mechanism, namely specular, backscattering and incoherent scattering. Each rectangle is then meshed into several smaller facets. Note that the meshing step, converting the architectural elements into facets, is done automatically by the SCHUN pre-processing module. Nevertheless, one should pay attention to that since contrary to meshing specular and incoherent scattering elements, which are independent of the satellite position, the backscattering elements are meshed depending on the azimuth of arrival of the transmitting satellite. This is due to the simplified formulation used in the 3CM model to reproduce the backscattering component. Due to this, all possible dihedrals in the façade architecture have to be defined when describing the façade. The meshing algorithm will then adapt itself to mesh the right backscatterers depending on each satellite position.

4.1.3 Direct path blockage models

This section is relative to the direct path blockage model described in Fig.4.1. Two models are proposed here depending on the final level of accuracy required.

4.1.3.1 Simple model for building blockage

This first building blockage model is very simple. The principle is to use a ray technique, basically the ray intersection algorithm, for determining if the receiver is visible or not from the satellite. In case of LOS, the amplitude of the ray is only affected by the propagation loss while in case of NLOS, a tuneable loss constant is added to reproduce the building obstruction, typically -20dB. In this modelling, the polarisation remains an important parameter since LOS rays are processed as multipath and are weighted by the antenna gain at the receiver side. Note that this simple model is very efficient and well adapted for generating correlated On/Off time-series for satellite diversity applications instead of using Markov chains for statistical approaches.

This simple direct path blockage model has also allowed validating the use of ray techniques on the environment and the SCHUN implementation of satellite and receiver diversity. Fig.4.4 presents one validation example considering three transmitters and two receivers moving in a dense urban canyon. The simulation parameters are summarised in Tab.4.1.

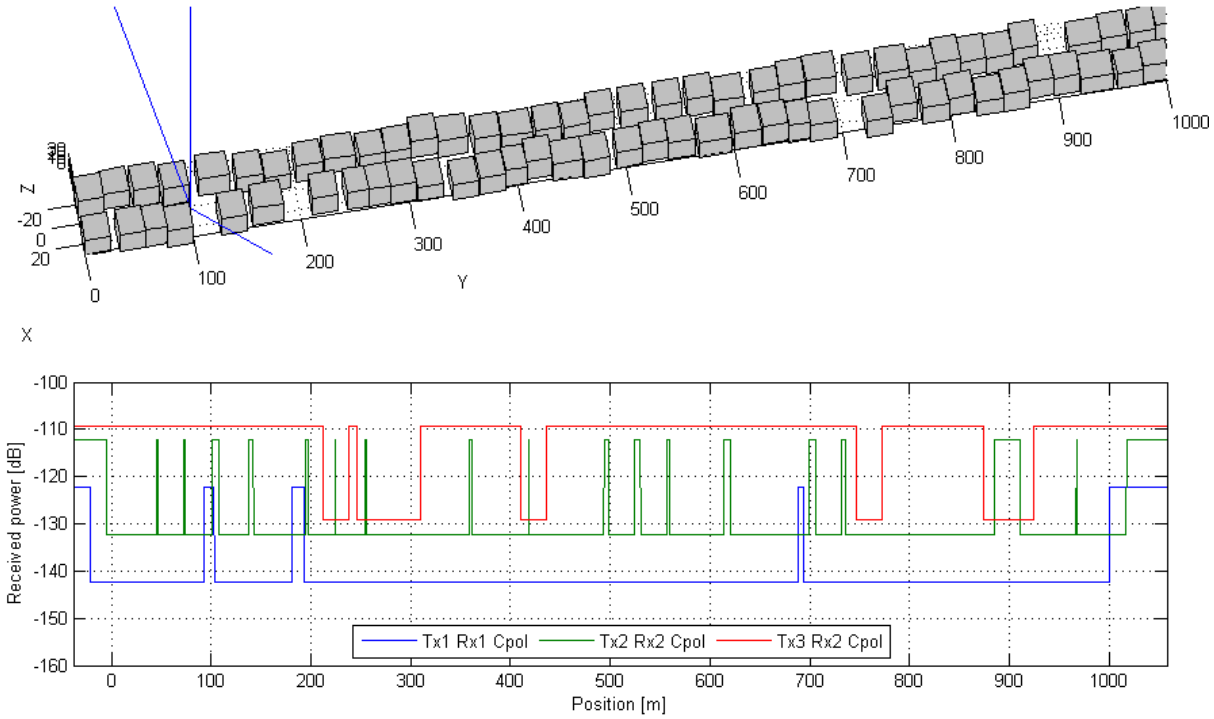

Figure 4.4: MIMO example using simple LOS blockage model

		1	2	3
Transmitters	Elevation	30	60	80
	Azimuth	35	170	-50
	Polarisation	RHCP	LHCP	LHCP
	EIRP	1	10	20
Receivers	Position	[0 -1 0]	[0 1 0]	
	Polarisation	RHCP	LHCP	
	Antenna Co-pol	Iso	Iso	
	Antenna X-pol	Null	Null	

Table 4.1: Simulation parameters for MIMO example using the simple LOS blockage model

4.1.3.2 Building diffraction model

Due to the limited accuracy of the simple direct path blockage model, a second model is proposed hereafter. This second model is based on the EM theory and particularly on UTD formulation to reproduce the diffraction phenomenon taking place on building edges.

In Fig.4.5, one validation example is presented comparing the implemented UTD method with PTD and ECM methods from SE-WorkBench software suite. The simulation scenario is similar to the one presented in [Oest 00]. A mobile is moving at 5 m behind one building row. The satellite is placed at 35° elevation, 0° azimuth using the SCHUN simulator convention.

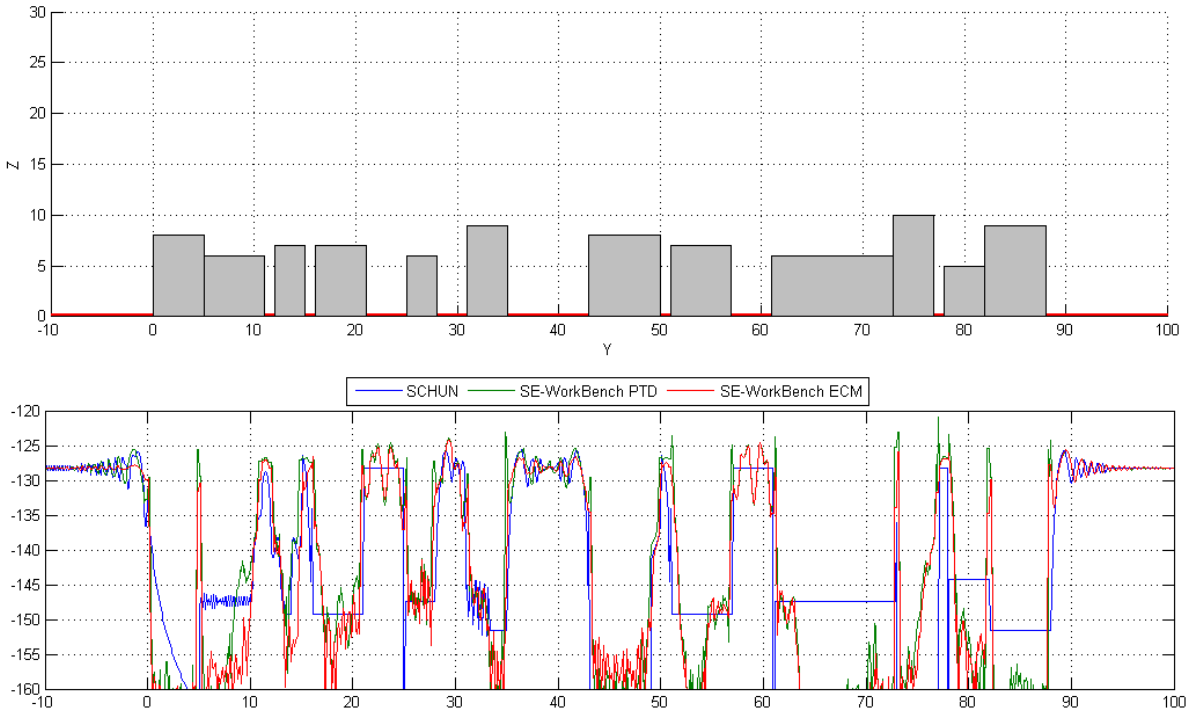

Figure 4.5: Validation of the building diffraction model comparing UTD from SCHUN and PTD and ECM from SE-WorkBench

As visible, results comparing the three methods are different even if macro phenomena are reproduced. The main difference comes from the small oscillations visible using PTD or ECM while UTD produces a constant diffracted power. This observation is due to UTD formulation assuming infinite edges. Note also that UTD is not adapted for corner diffraction while the simulated scenario displays a large number of corners. One upgrading solution could be to use a corner diffraction model instead of conventional UTD when diffraction points are close to corners.

4.1.4 Introduction of a new multipath reduction method

This section is relative to a common issue consisting in reducing the number of multipath to process the synthesised channel impulse responses. As it has been discussed, the SCHUN LMS channel simulator is able to deliver a very high number of multipath contributions. On one hand, generating such number of multipath brings more continuity and a certain richness to the channel behaviour, e.g. almost continuous power/delay profiles or smooth and rich Doppler spectrum. On the other hand, such amount of data can reveal itself to be hard to treat or simply not adapted for some specific applications, e.g. rapid calibration of new GNSS software receivers or hardware channel emulators for testing real GNSS receivers. Thus, this subsection is dedicated to the issue of reducing the number of multipath. This multipath reduction method particularly targets system applications for a wider range of use of the proposed LMS channel simulator.

Several methods are discussed in the literature among which [Ait 11], [Garc 10] or [Al B 07a]. They all have in common the issue of faithfully reproducing the channel behaviour by resorting to the minimum number of multipath contributions. Three types of approach can be found. The most basic approach consists in removing *irrelevant* multipath from the impulse response. The commonly used criterion is power, where multipaths under a certain threshold are considered as irrelevant contributions. This approach is highly limiting when considering a high number of weak multipath contributions where constructive and destructive phase effects are neglected. One other widely used method is to use the tapped-delay line approach where close multipath, belonging to the same tap, are coherently summed. This sampling approach is mainly used over the delay domain but can be extended to other dimensions such as Doppler or direction of arrival as used in the Onera wide-band module presented in Appendix B.3.2. This sampling approach is efficient and adapted to numerical tools since close to digital filtering techniques. Nevertheless, several issues have been highlighted in [Ait 11] and in the previously presented Fig.3.22, where discreet delays create discontinuities. Some new methods [Ait 11] [Garc 10], based on estimation techniques such as SAGE, seems encouraging although they require very long computation time.

The common point of all three presented approaches for reducing multipath number is to operate on the outputs, after performing the final step of the channel synthesis process. The typical input for such reduction algorithms is the channel impulse response. Those approaches are then very versatile since applicable to any generated channel, independently of the channel simulator used, although they present particular limitations as discussed above. Those methods have been judged as too restrictive and a new method is proposed hereafter.

As for the channel modelling step, the proposed approach for reducing the number of multipath has to remain in the boundaries fixed by the constraints mentioned in Section 1.2.1 and particularly the computation time constraint. The basic observation is the following, since the environment is responsible for generating the multipaths, what about using the environment for reducing their number. The idea is then to reduce the number of multipath directly from observing the environment during the channel synthesis process instead of operating on the outputs.

As previously presented in Section 4.1.2.1, the virtual environment is divided into four scale entities, namely buildings, façades, architectural elements and facets. The proposed method for reducing the number of multipath is based on those four scales. The principle is to process the EM modelling step of the channel at the facet scale and coherently sum all the contributions belonging to the same object to reduce the number of contributions, depending on the resolution scale chosen by the user. For instance, when using the building resolution (largest objects, lowest number of multipath, lowest channel resolution), the first EM step is realised at the facet scale. The contribution from each facet is tracked to identify from which building they are coming from. Those contributions are then coherently sum to give rise to one new ray, called virtual ray in the following. This virtual ray is originated from the barycentre of all facets. This origin

point allows calculating relative delay, DoA and geometrical Doppler associated to each virtual rays. Note that the use of the facet scale for the EM modelling step is very important and permits to keep all the phase effects (constructive and destructive interferences) into the virtual ray including the total Doppler spectrum related to each building. The use of the geometrical Doppler is relevant only for propagating the phase shift during the sampling time of the channel as a mean Doppler shift. However, reducing the Doppler spread due to one building to one frequency ray is not accurate and may present limitations in some specific cases. Note that the LOS component is not affected by this reduction process even if multiple diffracted replicas reach the receiver.

One example of such reduction method is presented in the following. The scenario is detailed hereafter and represented on top of Fig.4.7. The environment is made of 5 buildings. A clear LOS is always achieved. The mobile is moving at 50 km/h at 5 m from the building row. The trajectory is sampled every 20ms. This scenario results in 679 trajectory points with 2113 rays per impulse response (2112 facets into the environment plus the LOS). Tab.4.2 summarises the time performances of the SCHUN simulator to synthesise CIRs and the time performances of the GNSS MacroRx software receiver to post-process the CIRs as a function of the number of generated virtual rays. As visible, the strategy of reducing the number of multipath has a very low impact on the SCHUN computation time while drastically reducing the processing time of the software receiver. The computation time gain is then about 700 times.

Name	Resolution	Rays	SCHUN time	GNSS MacroRx time
Res 1	Building	6	14.90s	43s
Res 2	façade	29	15.52s	192s (3min 12s)
Res 3	Architecture	117	17.75s	805s (13min 25s)
Res 4	Facet	2113	15.16s	30 749s (8h 32min 29s)

Table 4.2: Influence of the MP reduction process on the computation time

About the SCHUN computation times, three mechanisms can explain those results. The first one is the intrinsic computation time at the facet scale. This time is constant for all four resolutions. The second mechanism is the adding process which differs for each resolution depending on the total number of objects (building, façade or architectural elements). The lower, the faster the adding process is since related to a finding algorithm. The third mechanism is the saving process which allows reshaping and exporting the results into a Matlab cell variable. The smaller the number of rays, the faster the saving process is. The Res4 is the reference time. This time is representative of a null adding process time plus a long time to store the synthesised data. The Res1 has a lower computation time compared to Res4 since the adding process is made on only six buildings. Furthermore, the adding process reduces the amount of data to store. Res2 and Res3 are longer compared to Res1 and Res2 since the adding process is made on a larger number of rays while the time for exporting the results remains almost constant.

As shown in Tab.4.2, reducing the number of multipath highly impacts the post-processing time of the GNSS software receiver. The simplified channel has however to be compared to the original channel. Fig.4.6 represents four instantaneous impulse responses of the channel in the power/delay/Doppler space function of the channel resolution. The bottom of Fig.4.7 shows the comparison in terms of pseudo-range error function of channel resolution. This result is at first surprising since almost no difference is observable in terms of pseudo-range error, meaning that the receiver does not see any difference between a channel with 2113 rays and a channel with only 6 rays. Further investigations have been made, and it has been found that the correlation function and the S curve are not modified by the multipath reduction process as shown in Fig.4.8 where the instantaneous correlation function has been calculated using Eq.4.1 and the S curve is based on the dot product discriminator given in Eq.4.2. Note that this representation has been

taken around 42 m where the differences are the largest. As presented in Fig.4.8, correlation functions are similar except normalisation issues and the difference of the S curve zero crossing is below 3 ns which represents about 0.9 m at speed of light. This difference is even more reduced due to the DLL processing which mitigates those instantaneous corrections.

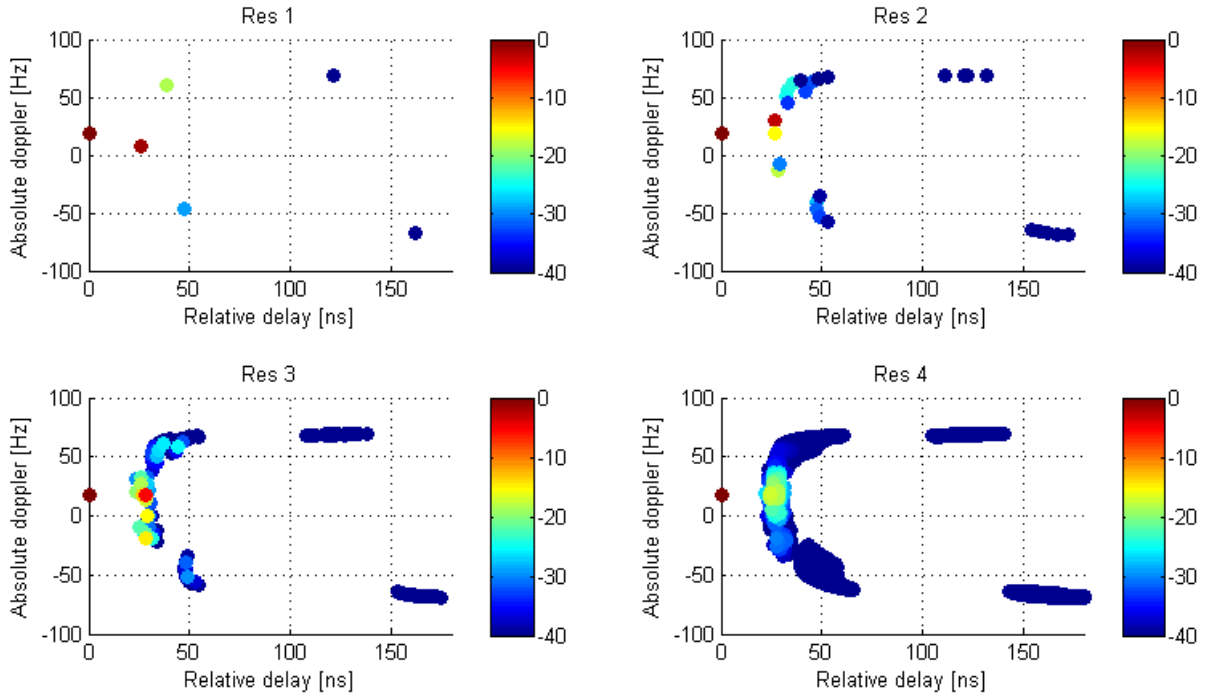

Figure 4.6: Example of reduced channel impulse responses

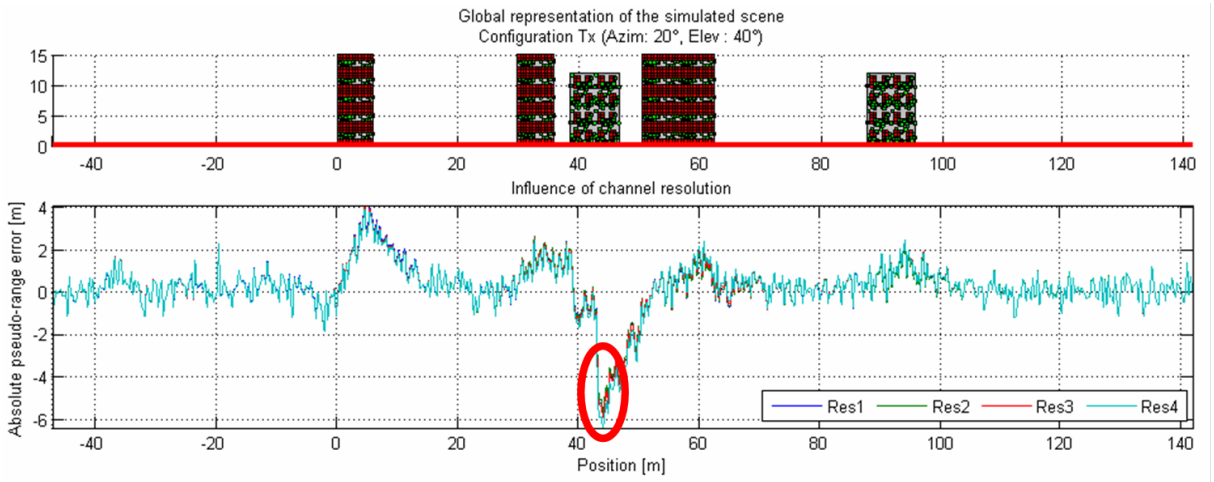

Figure 4.7: Influence of the MP reduction process on the GNSS pseudo-range error time series

$$R_c(\tau) = \sum_{i=0}^{N_{MP}} \gamma_i e^{\jmath\phi_i}\, sinc\left(\pi\nu_i T_{int}\right)\, Trig\left(\tau - \Delta\tau_i\right) \tag{4.1}$$

$$S(\tau) = \sum (I_E - I_L) I_P + \sum (Q_E - Q_L) Q_P \tag{4.2}$$

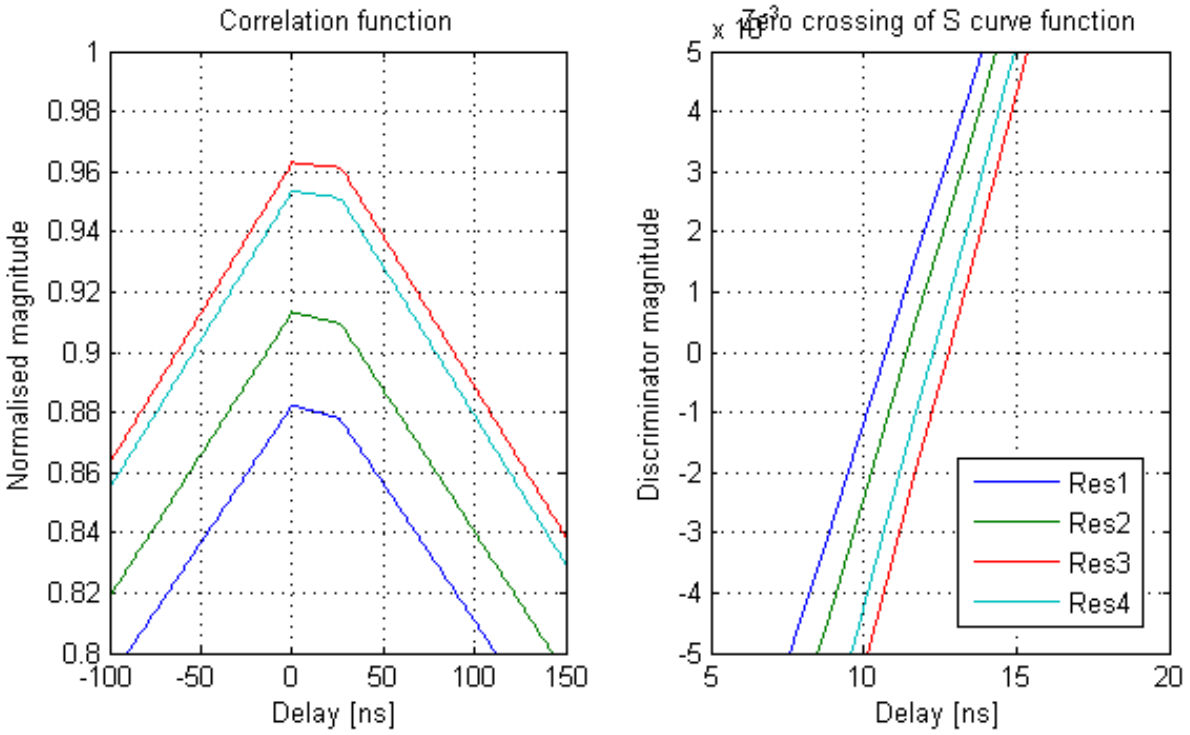

Figure 4.8: Influence of the MP reduction process on the GNSS correlation functions and S curves

Section synthesis :
This first section presents the final implementation of the SCHUN simulator as a complete and independent simulation tool performing both environment synthesis and EM computation to produce complex time varying channel impulse responses in mobile LMS contexts.

The first subsection recalls the main design choices which have led to the final SCHUN simulator answering both LMS satellite communication and satellite navigation needs. Its hybrid architecture is presented and its main capabilities are depicted.

The second subsection presents the virtual city synthesis algorithm and how buildings and façades are generated.

The third subsection presents two direct path blockage models from a simple attenuation model to a more complex diffraction model based on UTD algorithm. Contrary to the first model, more adapted to on/off correlated time-series synthesis, the second model allows to reproduce smooth transitions from LOS to NLOS for more realistic time-series synthesis.

The last subsection introduces a new method, based on the environment modelling, for reducing the number of multipath. This new approach has not been fully characterised yet but already presents interesting perspectives when post-processing CIRs. One of the main targeted fields of application of such technique is the simulation of complex system chains.

Now that the SCHUN simulator and its implementation have been presented, the next two sections are oriented toward experimental validations of the SCHUN simulator. For this purpose, two experimental measurement campaigns have been used. The first experiment was carried out by CNES and Onera in Saint Lary village, France, between 2011 and 2012 and addresses MIMO issues for mobile satellite communication applications using GEO links. This first experimental validation is oriented toward SISO co and cross circular polarised channels. Several parameters

such as narrow-band power time-series, Doppler spectrum, Rice factor estimation, level crossing rate or fade durations are compared and analysed. The second experiment was carried out by CNES and ISAE in Toulouse center, France, in 2011 and addresses satellite navigation issues in dense urban environments. This measurement campaign was focused on the overall influence of the channel on navigation devices and no direct channel measurements were performed. This second experimental validation is then oriented toward the use of the SCHUN simulator for system simulations considering an indirect validation comparing the influence of the channel on a satellite navigation receiver. Several parameters, internal to the receiver processing, are then compared and analysed, namely C/N0 and pseudo-range errors to a satellite.

4.2 Saint Lary experimental validation for satellite communication systems

4.2.1 Presentation of the Saint-Lary 2012 measurement campaign

The Saint Lary measurement campaign has been jointly carried out by CNES and Onera during fall 2011 and spring 2012 in the framework of the R&D study R-S09/TC-006-006. This measurement campaign completes the one carried out in 2008 in Auch [Laco 10] and addresses MIMO diversity techniques for LMS broadcast and telecommunication systems in vehicular and nomadic contexts for increasing the channel capacity. This experiment was performed over two frequency bands, S-band at 2.2GHz and C-band at 3.8GHz, and was focused on MIMO dual polarisation, MIMO dual frequency and SIMO receiver position diversity.

During this measurement campaign, a GEO satellite was emulated by two terrestrial transmitters deployed over a mountain surrounding Saint Lary village as visible in Fig.4.9. With about 800m height difference between the transmitter position on the mountain and the mobile receiver in the village, this configuration guarantees an elevation angle between 20° and 30°. In the case of the next performed validation, the elevation angle is about 22°. Note that the first Fresnel ellipsoid between the transmitter and the receiver is free of obstacle as visible on the terrain height profile presented in Fig.4.10.

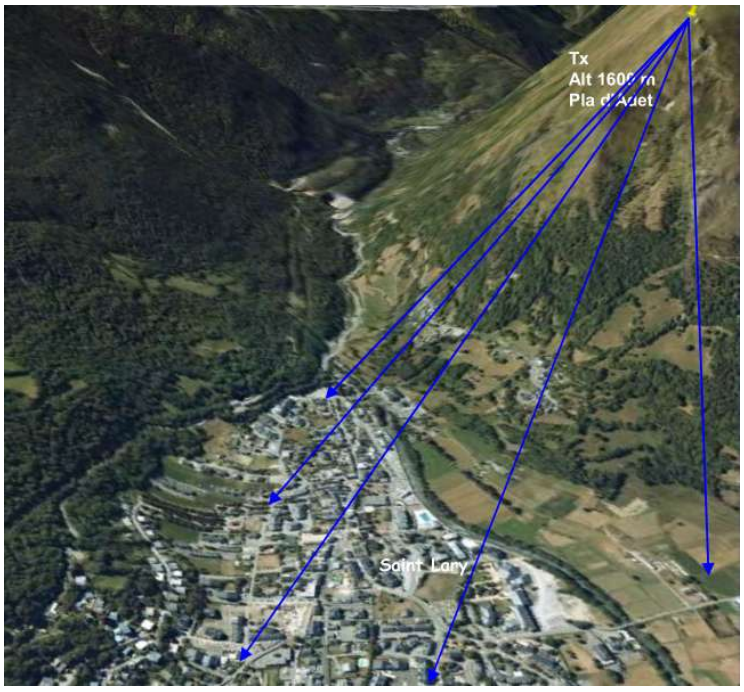

Figure 4.9: Emulation of a GEO satellite over Saint Lary village [Laco 12]

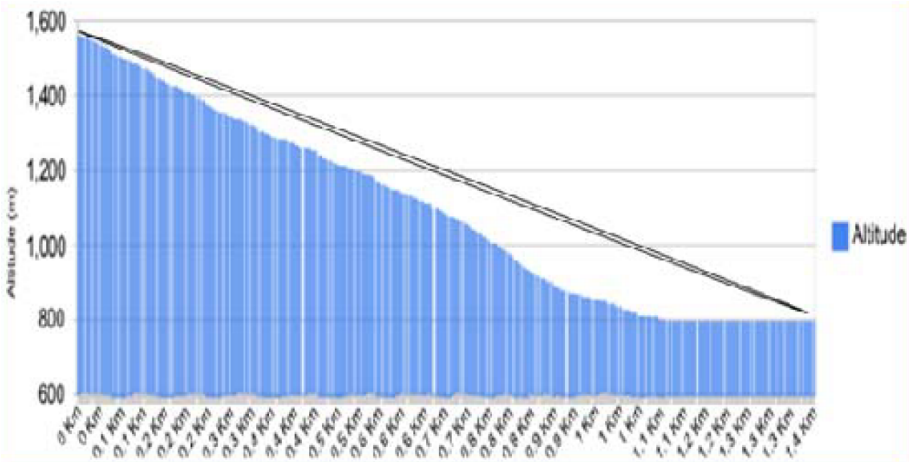

Figure 4.10: Terrain height profile for the Tx-Rx link and first Fresnel ellipsoid [Laco 12]

The transmitting antennas characteristics were the following:

- Two patch antennas at 2.2 GHz (RHCP and LHCP) : beamwidth = 80° x 20°, gain = 13 dBi, axial ratio = 3 dB
- Two patch antennas at 3.8 GHz (RHCP and LHCP) : beamwidth = 70° x 40°, gain = 10 dBi, axial ratio = 4 dB.

All beam widths were quite directive in particular in terms of elevation angle so that undesirable multipath effects coming from outside the measurement area were limited. For a given measurement frequency, the two circular polarization antennas were spaced out by about 20 cm on a mast and pointed manually to the centre of the measurement area. This manual pointing could have involved slight impairments on the axial ratio with respect to the nominal one in some cases. At the transmitter side, the transmitted power was monitored in real time so that fluctuations could be compensated when post-processing the collected datasets.

Transmitted signals were CW for each circular polarization. To be able to discriminate co and cross channels at the receiver side, the CW frequencies were spaced out by 200 kHz. This frequency lag was optimized to get no more than 30 dBc level interference between both CW. The frequency separation between CW was also kept lower than the assumed channel coherence bandwidth. Consequently, the exact RF frequencies of CW were: 2182.04MHz (RHCP) and 2182.24 MHz (LHCP) in S-band and 3824.04MHz (RHCP) and 3824.24 MHz (LHCP) in C-band.

At the receiver side, the measurement equipment was the one used for the past experiments [Laco 10] which performs received power measurements over several channels with user-defined bandwidths and complex signal snapshots (amplitude and phase of the propagation channel). Mobile measurements were triggered by an optical sensor measuring the travelled distance. The sampling distances are 2.4 cm at 2.2 GHz and 1.7 cm at 3.8 GHz representing between $\lambda/5$ and $\lambda/6$. A GPS receiver was also included in the measurement van to get an absolute time reference for data synchronisation and to record the van trajectory. It has also been used for the LOS level calibration.

Rx antennas were located on the van rooftop as visible in Fig.4.11. Two types of Rx antennas were used:

- Co-localised dual-polarised (RHCP and LHCP) antennas for MIMO measurements at 2.2 and 3.8 GHz. The typical RHCP-LHCP isolation exceeds 20 dB on the antennas axis. This isolation was not characterized at 30° elevation angle. They are not really optimised for GEO satellite but since negative elevation angles are filtered out, they could be considered as suitable for satellite reception.
- V-polarised dipoles spaced out by about 1m. Antenna patterns are typical dipole patterns. Nevertheless, for some azimuth angles, the van metallic rooftop could have distorted the original pattern.

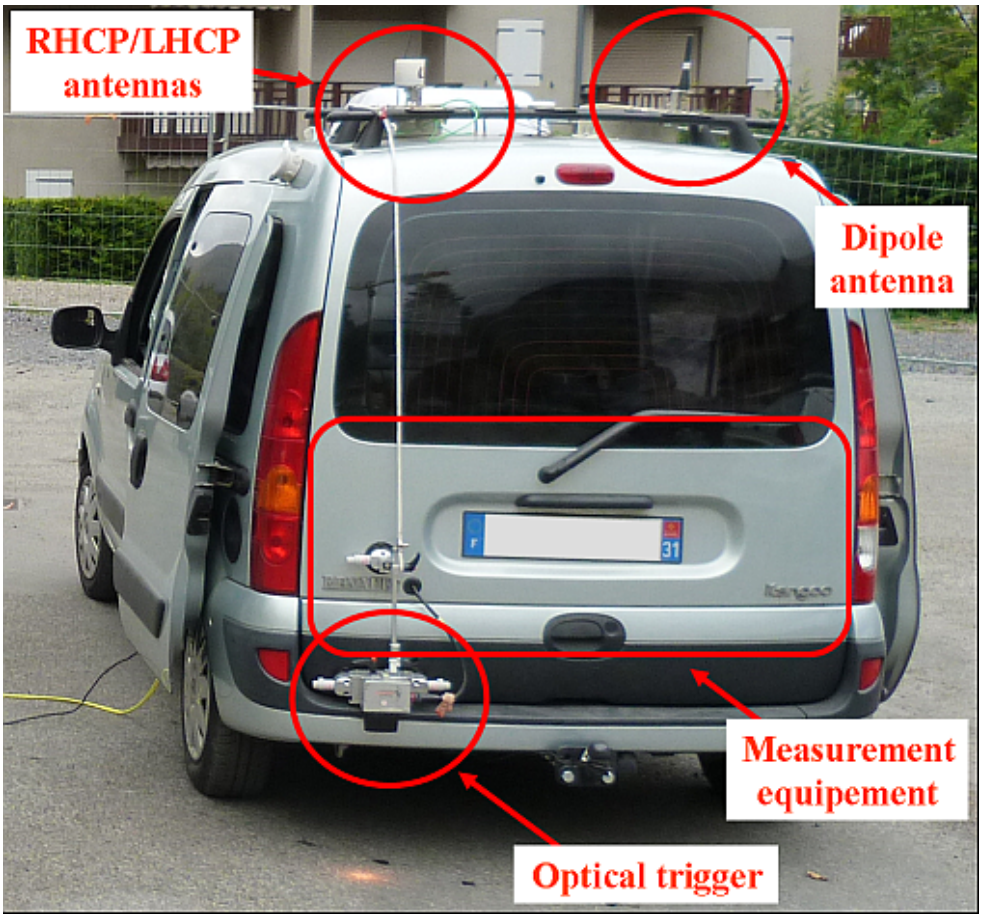

Figure 4.11: Measurement van used during the Saint Lary measurement campaign

About the experimental plan, many measurement configurations have been addressed during this campaign. The one used for the next presented validation is a SISO narrow-band power measurement of co and cross circular polarised channels in S-band. At the transmitter side, both RHCP and LHCP were emitted. At the receiver side, only the RHCP antenna was used. Thanks to the GPS measurements made, the reference trajectory has been recorded and is presented in Fig.4.12

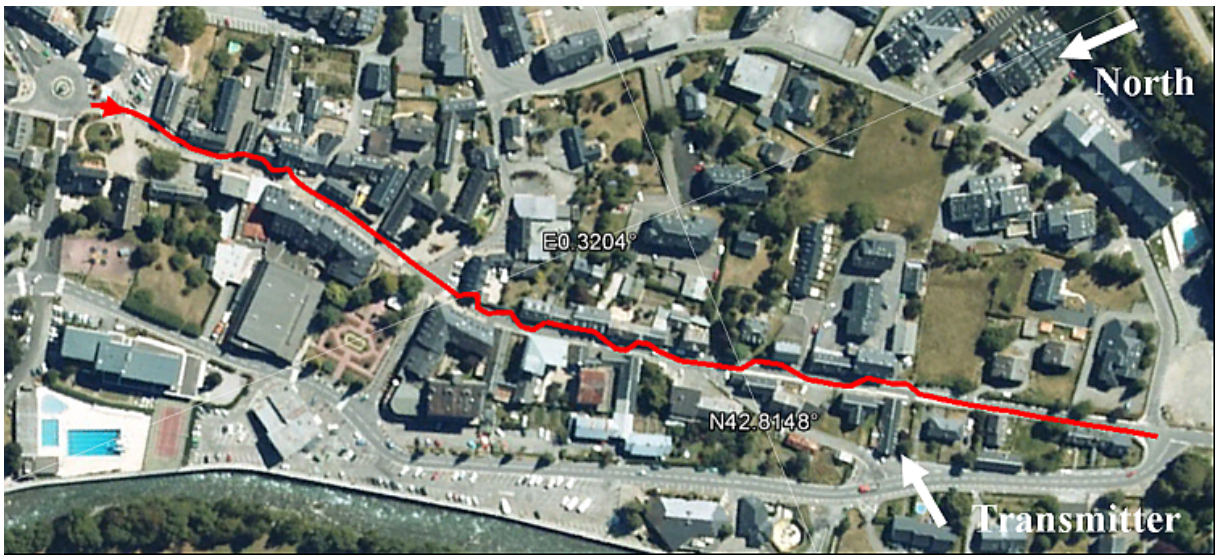

Figure 4.12: Reference trajectory in Saint Lary village

4.2.2 Presentation of Saint-Lary virtual environment

The first step prior to computing any propagation channel with the SCHUN simulator is to reproduce the experimental environment into the SCHUN formalism. In the following the main steps for importing the building footprint and creating the façade library are presented.

4.2.2.1 Modelling of the buildings

The first modelling step consists in synthesising the buildings (cuboids) from a footprint map. Since the basic scenario of the SCHUN simulator only handles linear trajectories of the receiver, the real trajectory has to be truncated into linear sections. For this purpose, the Saint Lary virtual environment has been divided into three linear sub-environments, as presented in Fig.4.13.

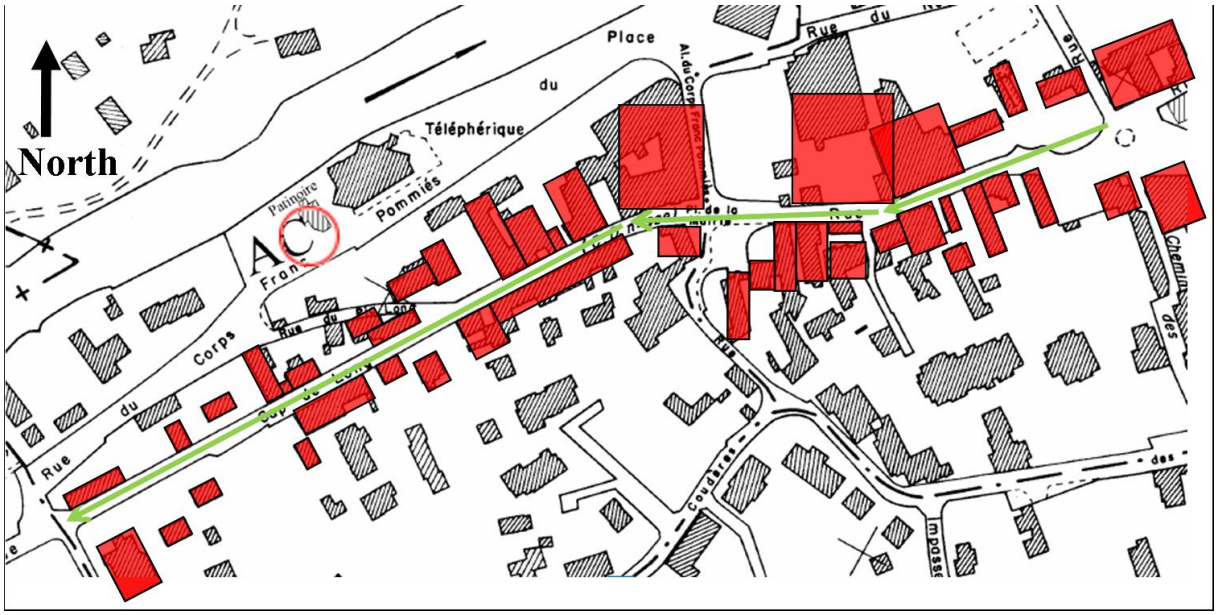

Figure 4.13: Saint Lary building footprints extracted from the official land register map

For reducing the computation complexity, only the buildings close to the receiver trajectory have been modelled. The reference footprint map presented in Fig.4.13 has been extracted from the governmental land register. From this map, the width, the depth and the position of the buildings (red rectangles) with respect to the mobile trajectory can be interpreted and translated into the SCHUN formalism.

However, the land register map does not deliver any building height information. The process for generating building height consists in stacking up façades depending on the number of observable floors. The number of floors is empirically tuned using a visual inspection of the buildings with Google street view tool. Although empirical, this process allows realistic building height modelling even if the height is rounded to a fixed number of façades. Even if not critical for the buildings on which the multipath component is generated, the heights of the buildings responsible for the LOS blockage are more critical and this empirical process may show limitations. The shape of the rooftops is also an important parameter since real geometries may be complex to reproduce and are modelled as cuboids in the SCHUN formalism.

4.2.2.2 Presentation of the façade library

Once the environment profile has been created, the second modelling step consists in creating a new library of façades to be applied on each building. This library is expected to represent the variety of the different architectures encountered in Saint Lary village. From our observation, this small village can be summarised into four types of façades.

The first type of façade represents a recent house front with smooth walls and receding windows. One example is presented in Fig.4.14. The specular object represents a window which is made of glass while the backscatterer due to the receding window is made of concrete. The façade wall is described as a slightly rough specular surface with 0.2m depth made of concrete.

The second type of façade represents an old house front made of stones. This façade is similar to the one presented above except that no backscatterer is present and the wall is assumed to be a slightly rough specular surface with 0.5m depth.

The third type of façade represents a typical chalet façade with large protruding wooded balconies. The guardrail is made of wood and is represented as a very rough surface with exponential distribution. One backscatterer is present due to the protruding guardrail. Finally, the window made of glass is represented as a specular surface.

The fourth type of façade represents a wide shop window made of glass. Those façades are mainly situated at the ground floor of the buildings. This type of façade is made of specular elements made of glass plus slightly rough specular elements with 0.2m depth made of concrete at the bottom.

(a) Real façade 1

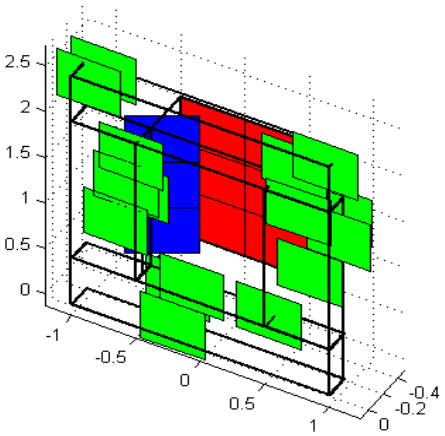

(b) Synthetic façade 1

Figure 4.14: Common brick house front (façade 1)

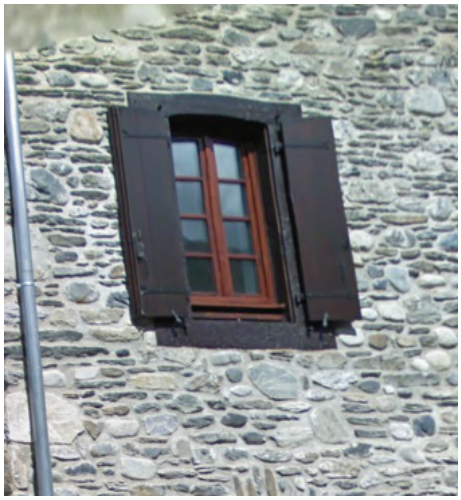

(a) Real façade 2

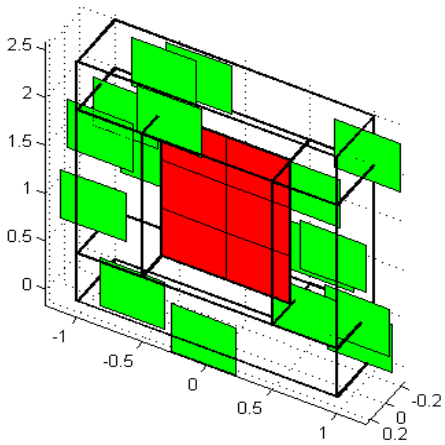

(b) Synthetic façade 2

Figure 4.15: Old stone house front (façade 2)

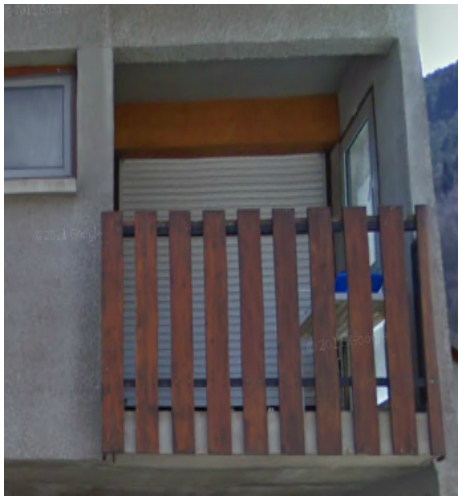

(a) Real façade 3

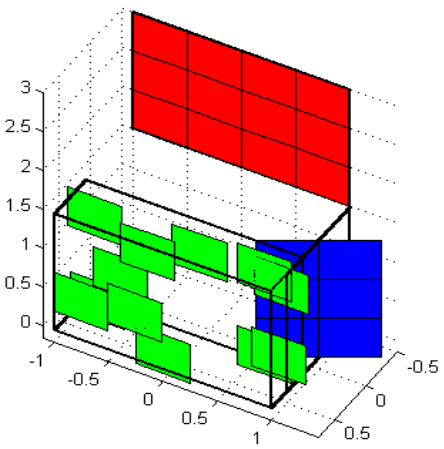

(b) Synthetic façade 3

Figure 4.16: Wooded balconies (façade 3)

(a) Real façade 4 (b) Synthetic façade 4

Figure 4.17: Shop window (façade 4)

For commodity reasons to apply the façade textures on the buildings, they all have been designed with 2m width. The height of façades 1 and 2 is 2.5 m while it is 3 m for façades 3 and 4. At the end, the resulting virtual environment in the SCHUN formalism is presented in Fig.4.18 where each type of façade texture has a specific colour. The building shapes are represented in grey. Note that the camera angle has been chosen on purpose since the scene is represented as viewed from the transmitter point of view.

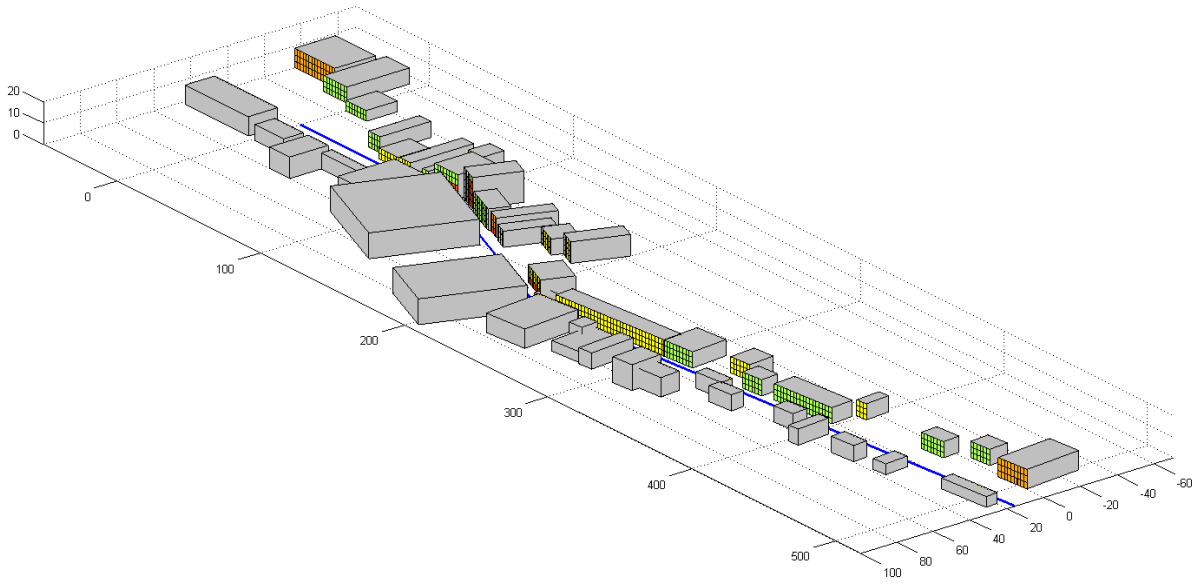

Figure 4.18: Saint Lary virtual environment in the SCHUN formalism from the transmitter point of view

4.2.3 Comparison with experimental SISO co and cross circular polarised channels in S-band

4.2.3.1 Narrow-band time-series

In the following, measured and synthesised time-series using the SCHUN simulator are compared. The first comparison point between the experiments and the simulation is the narrow-band power time-series for co and cross circular polarised channels. From a visual interpretation of Fig.4.19, measured and simulated time-series seem to present a reasonable agreement. However a slightly different dynamic in terms of fading depth is already observable. This observation will be confirmed later when analysing second order statistics.

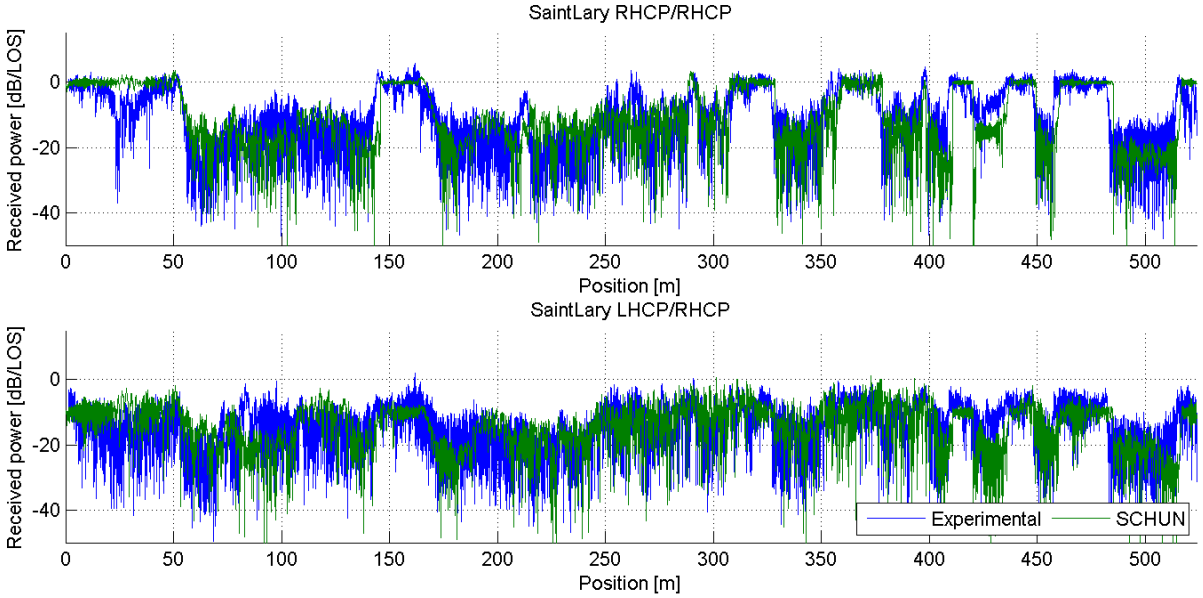

Figure 4.19: SISO narrow-band time-series for co and cross circular polarised channels

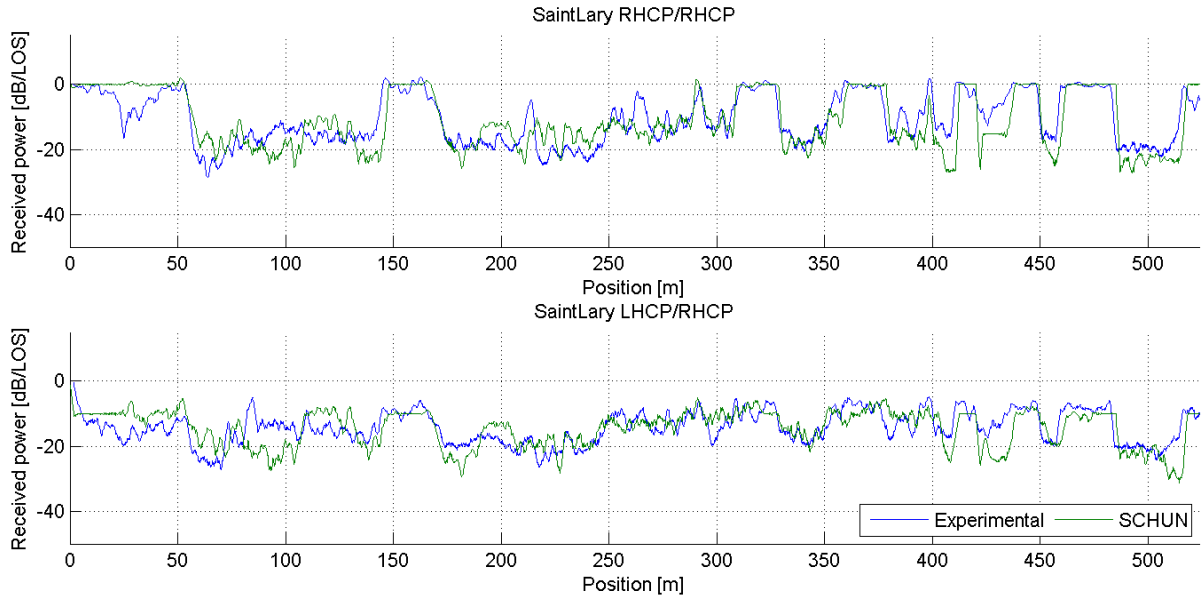

Figure 4.20: Filtered SISO narrow-band time-series for co and cross circular polarised channels

Figure 4.21: Presence of a tree on the LOS signal explaining the slight shadowing

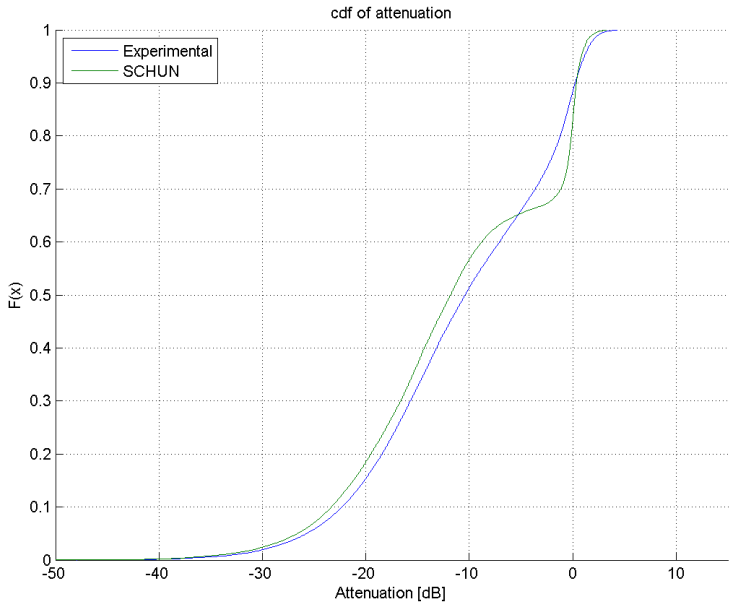

Figure 4.22: Cumulative distribution function of the total attenuation for co-polarised channels

To better observe slow variations and macro shadowing states into the narrow-band time-series, Fig.4.20 presents a filtered version of Fig.4.19. To perform this analysis, a sliding window equivalent to 2m width has been used along the receiver trajectory. In a first approximation, the two co-polarised time-series seem very close to each other even if small differences can be observed. For example around 25m, the measured time-series is affected by a slight shadow while the simulated time-series is not. This phenomenon can be explained by the presence of a tree on the direct path as visible in Fig.4.21 where the transmitter is on the top of the masked mountain. Even more, contrary to the picture in Fig.4.21 taken in March, the tree was in leaf at the time of the measurements. Other differences are observable around 275 m due to the complex geometry of the rooftops of one group of building which could not be reproduced by the cuboids formalism used in the SCHUN simulator.

On the cross polarisation diagram, the global accordance between measured and simulated time-series is also reasonable. A fine observation of co and cross polarisation diagram reveals that they are mostly correlated. This is even more noticeable at the end of the trajectory from 400 m to 550 m. This observation is probably due to the lack of polarisation discrimination at the transmitter side. Note that this phenomenon has been integrated into the simulation using 10dB polarisation discrimination.

Fig.4.22 represents the cdf of the total attenuation of both measured and simulated co-polarised narrow-band time-series. As visible, the simulated cdf of the total attenuation presents a major gap between -10 dB to -2 dB contrary to the experimental one. Nevertheless, this attenuation zone is characteristic of vegetation attenuation. Indeed, when observing the measurement areas in Fig.4.12, the reference trajectory is frequently surrounded by vegetation. This observation on the cdf can then be explained by the fact that the SCHUN simulator does not include vegetation effects in the present simulation. From -10 dB to -50 dB, the SCHUN simulator tends to slightly under-estimate the total received power of about -0.8 dB which remains in a reasonable accuracy interval.

4.2.3.2 Doppler spectrum

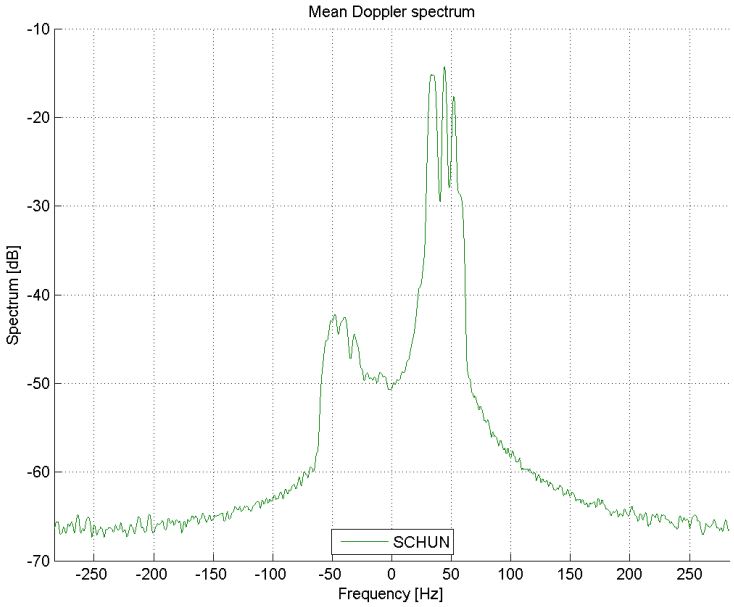

Figure 4.23: Mean Doppler spectrum along the receiver trajectory

The second comparison point is the Doppler spectrum of the time-series. Probably due to clock drifts into the measurement equipment, in phase and in quadrature acquisitions could not be interpreted and preliminary results show several incoherencies. Therefore, the experimental Doppler spectrum has not been used in the following. Nevertheless, this section presents mean Doppler spectrum and spectrogram using the synthesised time-series using the SCHUN simulator.

Fig.4.23 represents the Doppler spectrum averaged along the receiver trajectory. This spectrum has been realised using the Welch estimation method [Welc 67] on the complex co-polarised synthesised narrow-band time-series which has been LOS power normalised (no phase normalisation). As predicted by the theory, the Doppler spectrum is bounded at ± 60 Hz (v =30 km/h, $f_0 = 2.172$ GHz). Three rays are visible around +50 Hz which corresponds to the LOS contribution on each of the three parts of the trajectory. Also noticeable is the second lobe around -50 Hz due to the backscattering and incoherent scattering phenomena. Finally, this spectrum

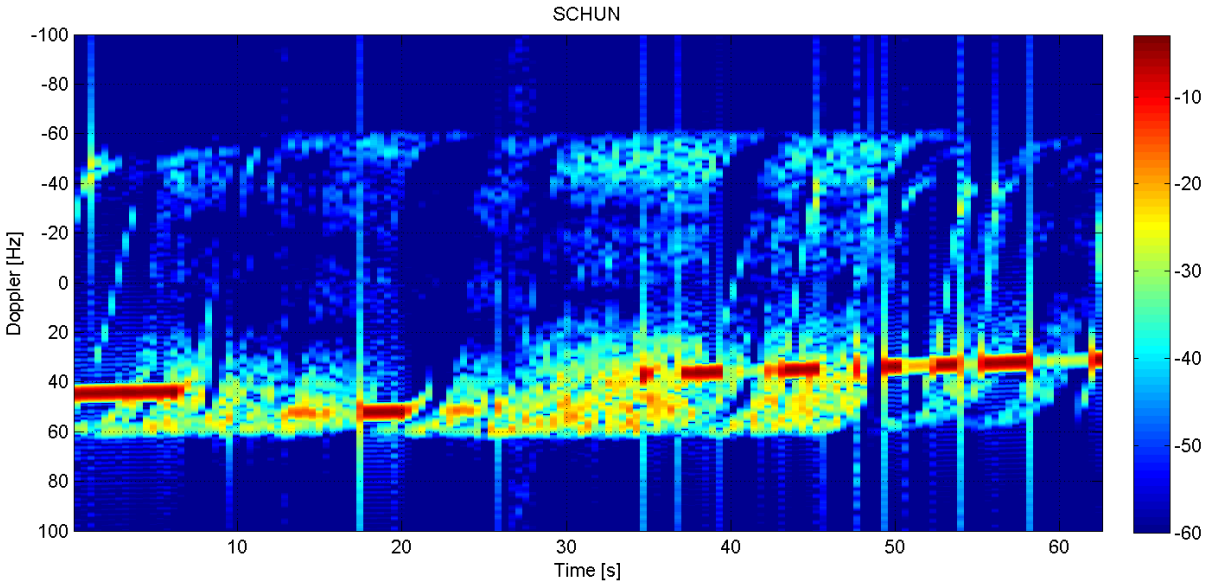

Figure 4.24: Spectrogram along the receiver trajectory

shape is in accordance with Jakes model [Jake 94].

The spectrogram presented in Fig.4.24 represents the time evolution of the Doppler spectrum. The phenomena observed in Fig.4.23 are still observable. Even more, the three parts of the trajectory can now be highlighted and the Doppler evolution of the LOS is clearly visible. This representation also allows highlighting the scattering and specular phenomenon taking place between +60 Hz and +40 Hz. The backscattering and the incoherent scattering are still visible around -50 Hz. One artefact is also visible on this plot when the mobile passes from LOS to NLOS. Indeed, the discontinuity between LOS and NLOS areas caused by the use of the UTD method which reproduces the diffraction is here visible in the frequency domain as a frequency flash over the whole bandwidth.

4.2.3.3 Estimation of the Rice factor

The third comparison deals with the Rice factor estimation using the method of moment. The results are presented in Fig.4.25 where the K factor is presented versus the estimated co-polarised coherent power.

In a first approximation, both plots present a reasonable accordance in terms of global shape. On the experimental plot, two zones are visible around A_{RR} = 0 dB and -20 dB. The 0 dB zone corresponds to the zone where the LOS is present. As visible, the K factor is spread as a small spot between 10 to 20 dB with A_{RR} centred on 0 dB. The interpretation of this result is that in LOS conditions, the multipath component is about 15 dB under the LOS. On the simulated plot, the equivalent region is characterised by a constant value of A_{RR} with a wider spread of K values between 10 dB to 30 dB. This observation shows that the coherent component A_{RR} is not as rich as in the experimental results and small variations of the LOS power are not reproduced. Analysing the K factor also reveals that multipath power is very weak in LOS conditions, about -20 dB, compared to the coherent power. This conclusion is in accordance when observing the time-series from 400 m to 550 m. In this zone, the LOS is very clear and multipath are very low since no vegetation effects have been taken into account by the simulation in this vegetated area. The multipath power is necessarily underestimated. The second zone, around A_{RR} = -20 dB, corresponds to NLOS conditions characterised by the fact that the multipath power is as high as the coherent power. In this zone, experimental and simulated results show a better accordance. An intermediate zone is also visible in the experimental plot around A_{RR} = -5 dB

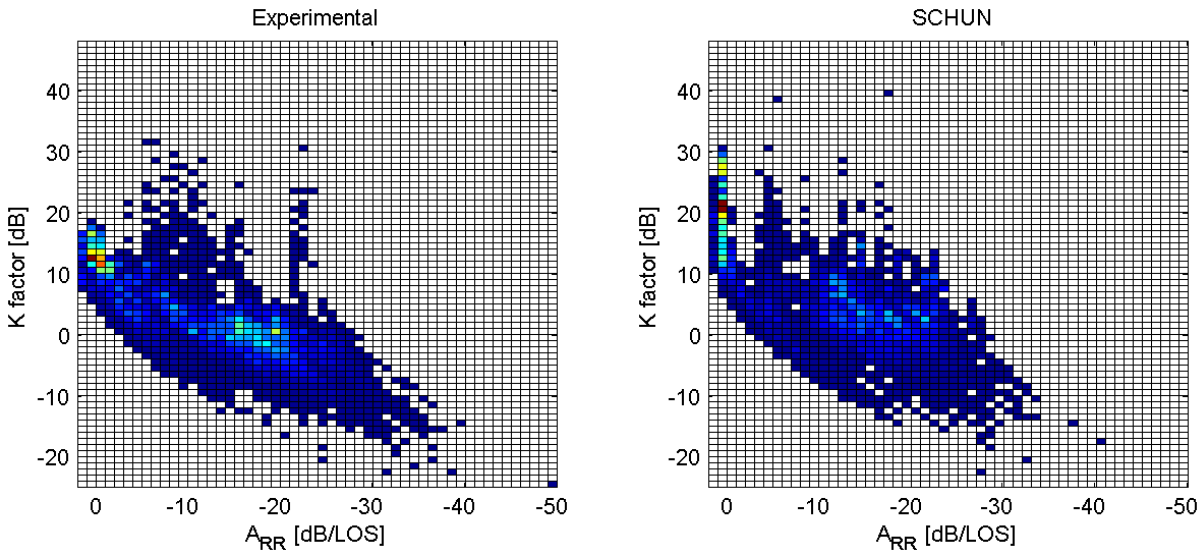

Figure 4.25: Estimated Rice factor K versus co-polarised coherent power

which corresponds to slight shadowing due to vegetation effects as discussed previously. This zone is not visible on the simulated plot.

4.2.3.4 Level crossing rate and fade duration

The last comparison presented here is oriented toward second order statistics and particularly on level crossing rate and fade duration. In a first approximation on level crossing rate, both plots in Fig.4.26 have a similar shape. However, a scaling coefficient seems missing. As a matter of fact, this is coherent with the observation made on Fig.4.19 where the dynamic of the synthesised time-series seems reduced. Looking closer into it, Fig.4.27, the synthesised time-series presents rounded fades instead of sharp and deep fades as the ones from the measurements. As a consequence, the level crossing rate is under-estimated. This result also affects the fade duration parameter as presented in Fig.4.26. Further investigations have to be done on this to correct the issue and improve the results for second order statistics.

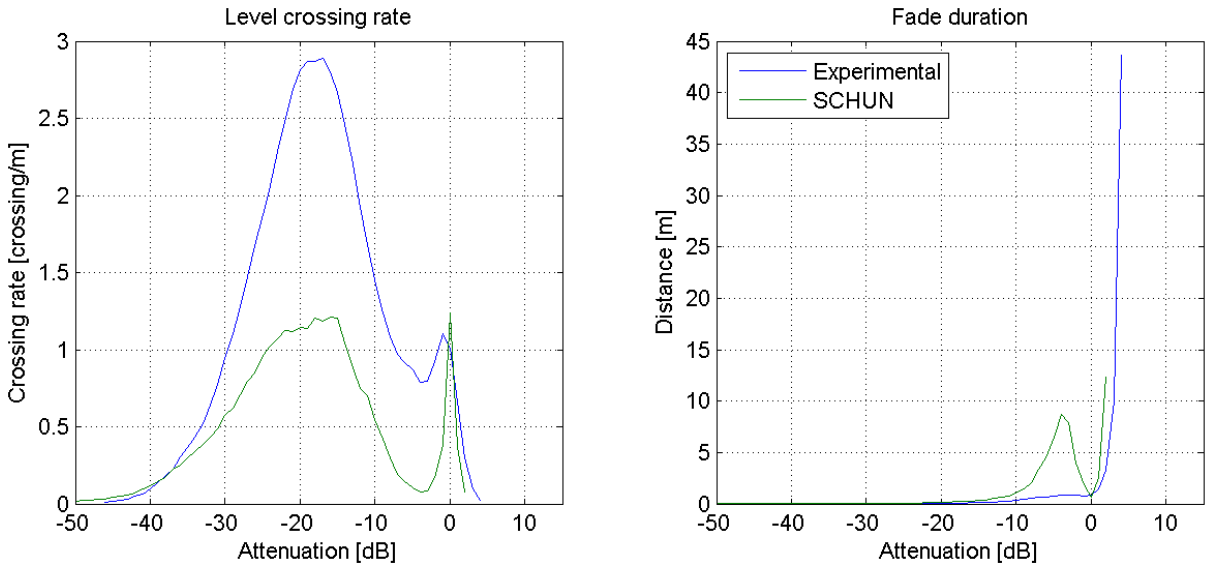

Figure 4.26: Level crossing rate and fade duration

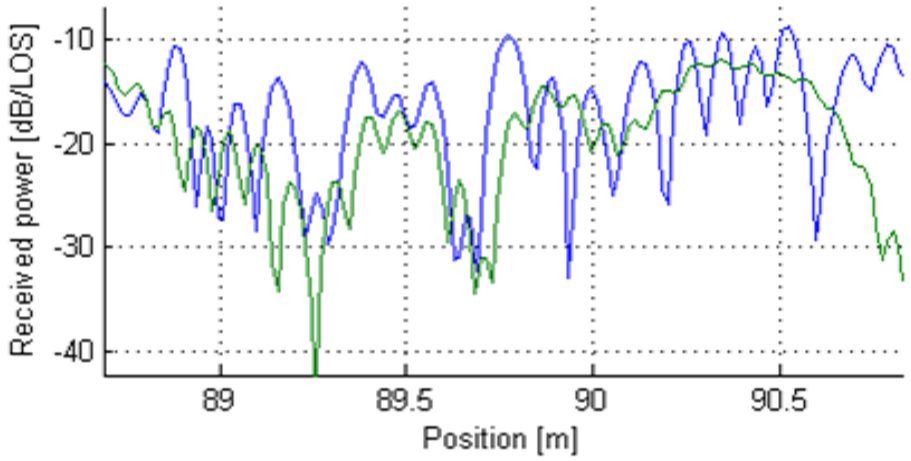

Figure 4.27: Zoom on the co-polarised narrow-band power time series (blue=experimental, green=SCHUN)

Section synthesis :
This first experimental validation has been established on a SISO co and cross polarised channel measurement in S-band performed in 2012 in Saint Lary village, France. The main conclusions are the following:

- *The real environment has been modelled using the SCHUN formalism. This virtual environment is based on the land-register for building footprints and on a visual inspection of the façades to tune buildings architecture and height. Due to the current limitations of the SCHUN simulator, no vegetation has been included into the virtual scene. The use of vegetation free environments is limiting as it has been highlighted during the comparison process. The cuboids assumption to represent the buildings may also be limiting when considering complex rooftops at some specific points of the trajectory.*
- *In general, the macro-shadowing effect due to building blockage is well reproduced by the SCHUN simulator. Mean multipath power is also coherent with the measurements when comparing co and cross polarised channels and cdf plots.*
- *On the fast fading component, the SCHUN synthesised results seem to lack of dynamic. Indeed, fading in the synthesised time-series are not as sharp and deep as the ones in the measured time-series. This observation has a high impact on second order statistics which affects level crossing rate and fade duration. This issue has to be further investigated and corrected.*
- *The Doppler analysis has not included any measurements due to clock drifts issues. However, the presented results from the synthesised time-series are in accordance with the expected results using both theory and geometric considerations.*
- *The K factor comparison has revealed a tendency of the SCHUN simulator to generate very clear LOS with low multipath. This observation may be biased by the end of the trajectory where vegetation may have a strong impact on the total multipath power. Nevertheless, simple rooftops as used in the SCHUN virtual environment may also have an impact on that phenomenon where LOS sub-states are not reproduced.*

4.3 Toulouse Capitole experimental validation for satellite navigation systems

4.3.1 Presentation of the Toulouse-Capitole 2011 measurement campaign

The Toulouse-Capitole measurement campaign has been jointly carried out by CNES and ISAE *(Institut Supérieur de l'Aeronautique et de l'Espace)* during spring 2011 in Toulouse center, France. The goal of this experiment was to quantify the influence of dense urban environments on GNSS receivers using real GPS signals. To do so, the channel was first recorded using specific wideband digitising equipment whereas commercial GPS receivers were also used simultaneously during the measurement campaign. The recorded channel is post-processed afterwards using different GNSS software receivers to compare their performances. The goal of the experimental validation presented hereafter slightly differs from the initial goal of the measurements. Indeed, in the following only one GNSS software receiver has been used, namely JGNSS, and presented in Appendix A.2.2. The goal of the next presented experimental validation is to replace the measured channel by a SCHUN synthesised channel and compare the overall behaviour of the software receiver. Contrary to Saint Lary measurements where channel information were available, this second experimental validation is indirect and based on parameters internal to the GNSS receiver processing, namely the estimated C/N0 and the pseudo-range errors.

The measurement area was located around place du Capitole, Toulouse. This environment has been chosen since typical of dense urban environments with narrow streets, high and continuous building profiles and the quasi-absence of vegetation. The absence of trees is an important feature as highlighted during the Saint Lary validation experiment since the SCHUN simulator does not handle vegetation effects yet. The reference trajectory is presented in Fig.4.28 where the colour of the points is related to the quality of the positioning estimated by the reference trajectory equipment. This route goes through several typical urban scenarios with narrow streets, wide streets or open squares. The measurements have been recorded during three consecutive loops of the reference trajectory. All trajectories were 1 Hz sampled with position, speed and orientation information. Even if the travelled distance is almost identical, the recordings last from 246 s to 373 s due to the traffic.
The receiving equipment, presented in Fig.4.29, was loaded into a car. The main features of the measurement equipment were one inertial sensor, one Novatel GNSS reference receiver for the precise positioning and the BitGrabberMobile. The car was also carrying several other equipments (two uBlox 5T + one uBlox 4T + one uBlox 6H + one Spirent GSS6400) used for unrelated purposes and which recordings were performed simultaneously. Note that uBlox 4T and 6H are used in the following as references for the C/N0 analysis. The IMAR-FSAS inertial sensor coupled with the Novatel Propack V3 GNSS receiver have been used to georeference the trajectory. Both devices were helped by a local augmentation system based at ISAE. The raw positioning data have been post-processed and merged using Kalman filtering techniques to achieve 0.7 m standard deviation on the positioning error and 0.1 m/s standard deviation on the velocity in the worst cases (red points).

The BitGrabberMobile (BGM) is the main experimental equipment of this setup. The BGM can be seen as an experimental channel digitiser which records gigabits of sampled received signal. The sampling process has been realised on four bits quantification on each I/Q signals with a frequency of 68 MHz. The received signal is close to noise and only the post-processing made by the GNSS software receiver is able to isolate each transmitting satellite of the GPS constellation. The input RF signal was coming from the same RHCP patch antenna on the roof as the one feeding the Novatel reference GNSS receiver.

Figure 4.28: Reference trajectory in Toulouse Capitole environment

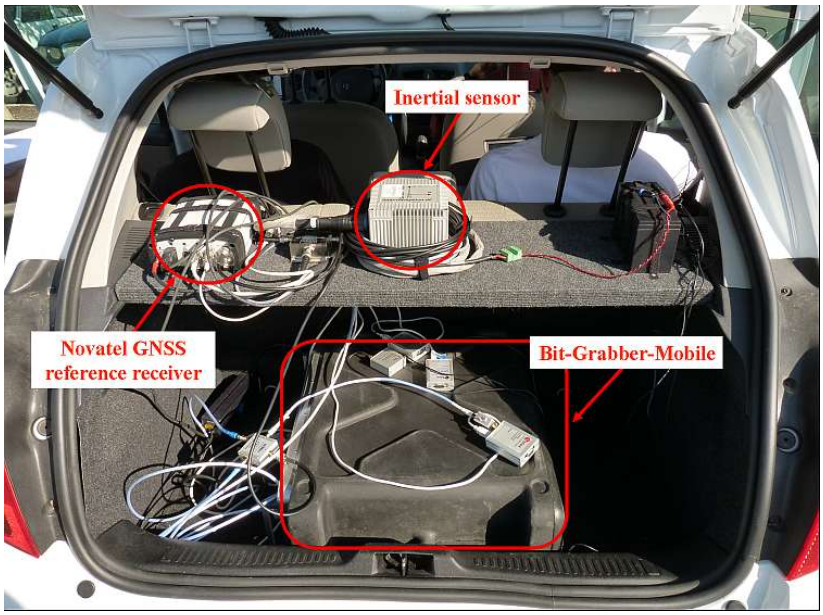

Figure 4.29: Measurement equipement during the Toulouse Capitole measurement campaign

The transmitters were the GPS satellites. In this experiment, the focus is made on GPS C/A signals. The carrier frequency is 1.57542GHz and the polarisation is RHCP. The state of the constellation at the time of the measurement is presented in Fig.4.30. As visible, twelve satellites were above the horizon but only six of them were above 30° elevation (PRN02, PRN04, PRN07, PRN08, PRN10, PRN13) and only the satellite GPS BIIA-26 (PRN10) was above 60° elevation. In the following, the satellites are called by their spreading sequence number since being unique for each satellite.

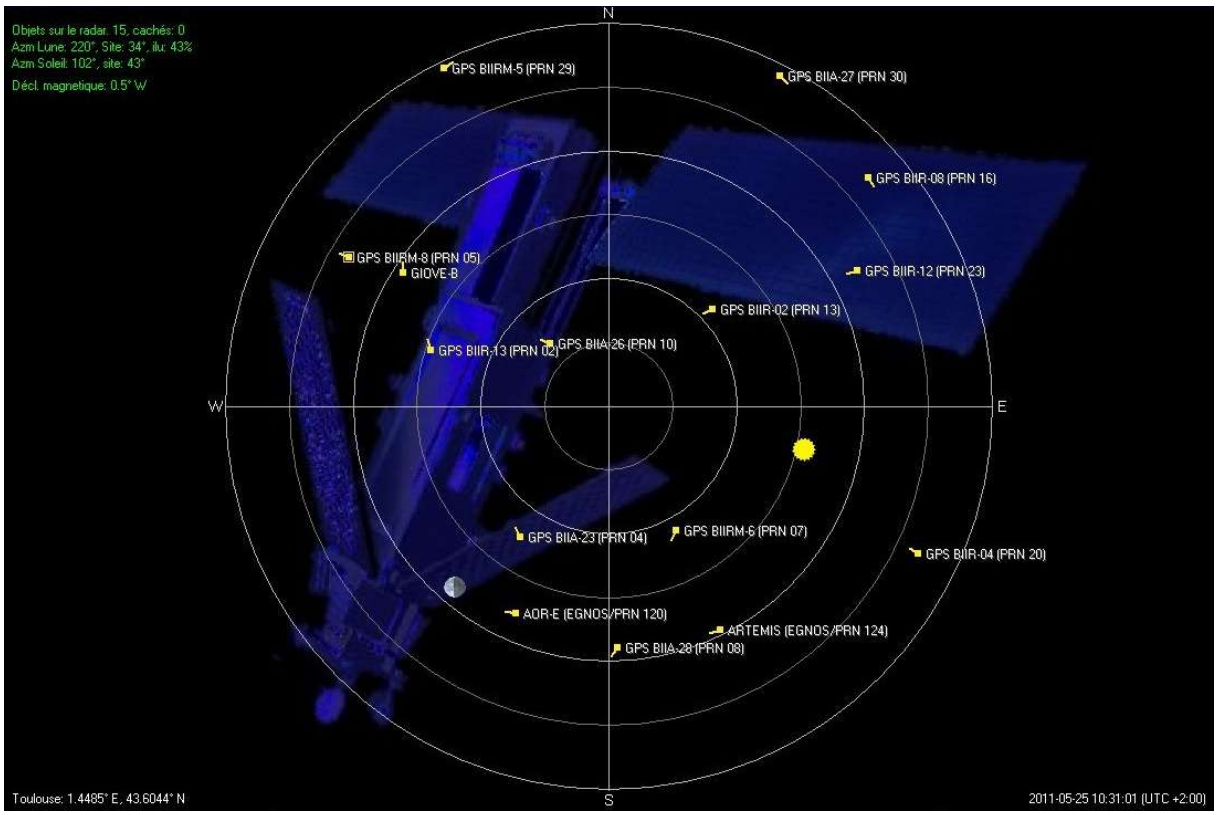

Figure 4.30: Skyplot of the GNSS constellation at the time of the measurement

4.3.2 Presentation of Toulouse-Capitole virtual environments

4.3.2.1 SE-WorkBench synthetic environment

The SE-WorkBench environment has been provided by Oktal-SE company, also responsible for marketing SE-WorkBench software suite. The Toulouse-Capitole commercial database uses a proprietary format, specific to SE-WorkBench software suite. Up to now, this synthetic environment is the widest and the most precise model of urban environment at street scale available at ONERA.

The Toulouse-Capitole database is georeferenced by the use of the governmental land register for generating building footprints. As for Saint-Lary virtual environment, building height information's are not provided by the land register and building heights have been extrapolated from in-situ photography's. The geometry of the buildings is made of planar surfaces reproducing walls and windows with protruding balconies and guardrails. The windows are considered in the same plane as the walls. Building textures are applied on building geometries to differentiate the continuing materials and to achieve a better visual rendering of the scene. Small elements such as lampposts, road signs, bus shelters and other street furniture's are present on this synthetic environment. Vegetation and trees are also present although in minority in such urban scene.

The first issue considering such synthetic environment was to reproduce the reference trajectory and satellite motion in the database referential. For the reference trajectory, thanks to the Kalman post-processing step, the reference trajectory is accurately known. However, the output is given in terms of longitude, latitude and altitude coordinates which have to be converted in ECEF *(Earth-Centred Earth-Fixed)* coordinates finally projected into the local (X,Y,Z) referential of the database. Finally, the quality of the reference trajectory is acceptable but not perfect and the car tends to overlap the sidewalks. It has also been noticed that the car was too close to the façades compared to the experimental conditions. The reference trajectory has then been manually tuned to keep the car in the centre of the street, closer to the experimental conditions.

This tuning is presented in yellow in Fig.4.31.

For the satellite positioning, the French RGP network *(Réseau GNSS Permanent)* has been used. The RGP sensor stations network records code and phase of each visible satellite. Those information's are transmitted to two central data centers which control their quality. They are finally publicly released. Two types of ephemerides are available, the ones broadcasted by the satellites and the ones post-processed by IGS *(International GNSS Service)* for a better accuracy. In the following, only the final post-processed ephemerides are used. Those ephemerides are sampled every 15 min and were available two weeks after the measurements. The expected precision of such ephemerides is inferior to 5cm on satellite position and about 0.1 ns on satellite clock. In order to interpolate satellite positions, an eleven order polynomial has been used according to Schenewerk method [Sche 03].

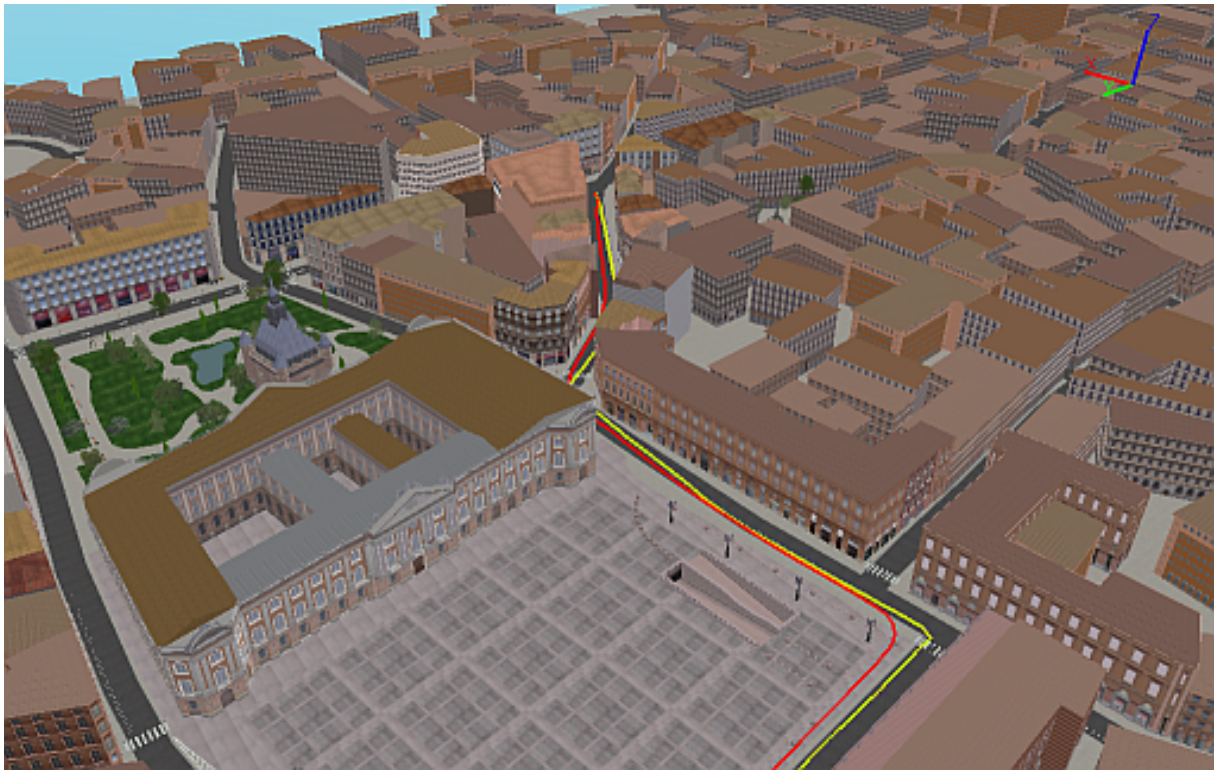

Figure 4.31: SE-WorkBench synthetic environment

4.3.2.2 SCHUN virtual environment

The reference trajectory has been split into four linear sections, Lafayette street, Alsace-Lorraine street, Remusat street and Capitole square. As for Saint-Lary, the Toulouse-Capitole virtual environment is based on the land register map from which building footprints have been extracted. The height of the building has also been empirically tuned using Google street view tool to fit the number of visible floors.

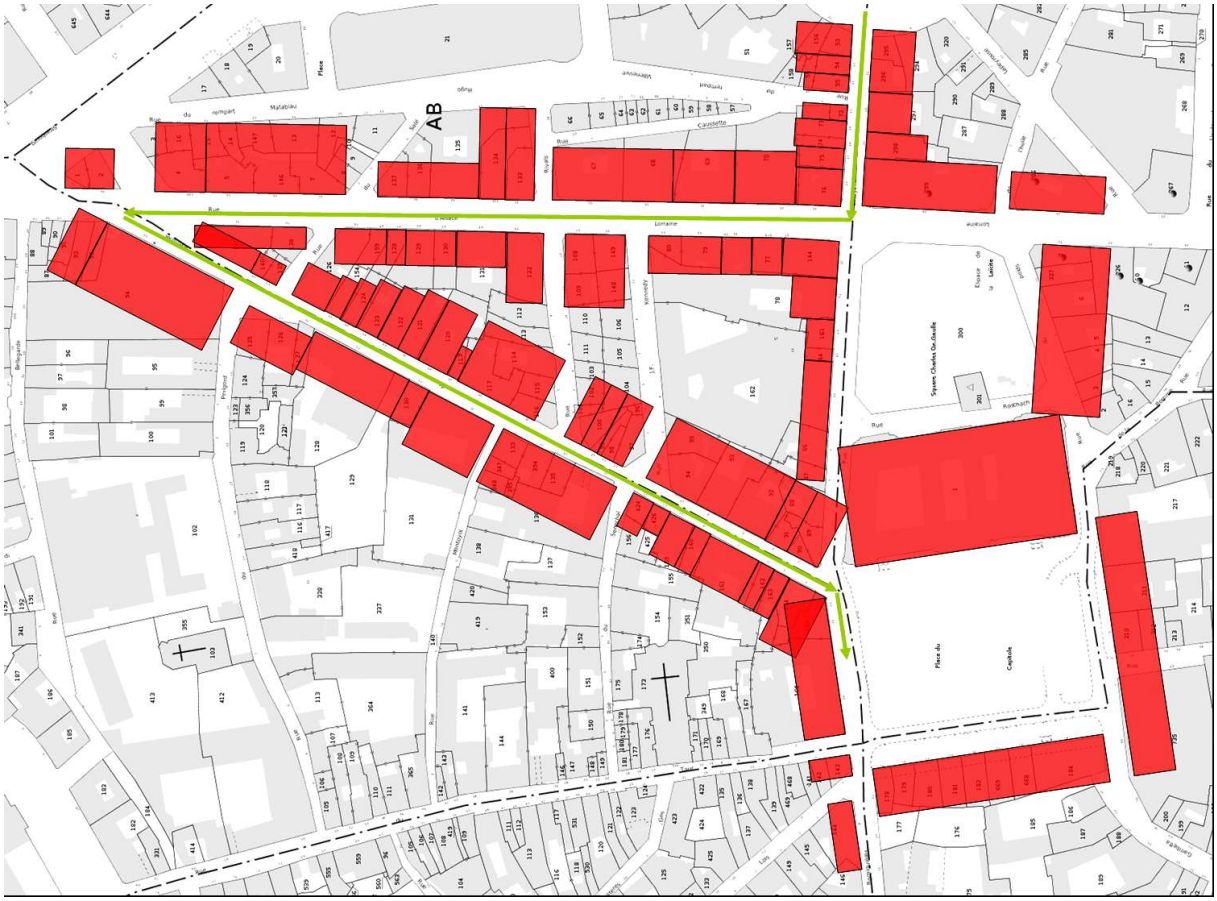

Figure 4.32: Toulouse-Capitole building footprints extracted from the official land register map

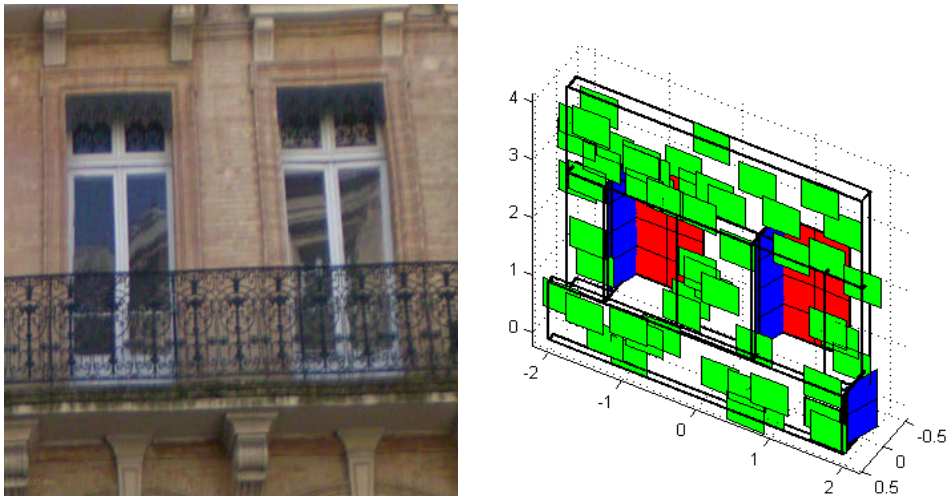

(a) Real façade 1 (b) Synthetic façade 1

Figure 4.33: Typical Toulouse Hausmanian house front (façade 1)

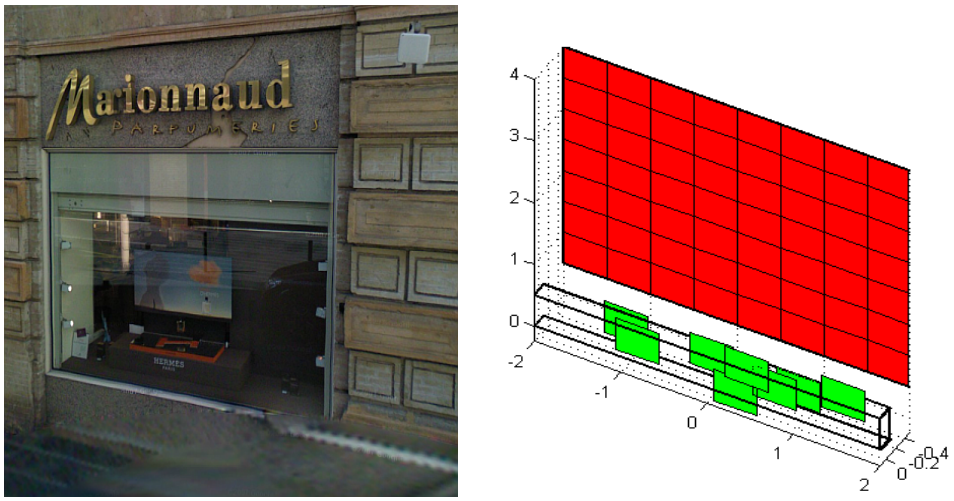

(a) Real façade 2 (b) Synthetic façade 2

Figure 4.34: Window shop (façade 2)

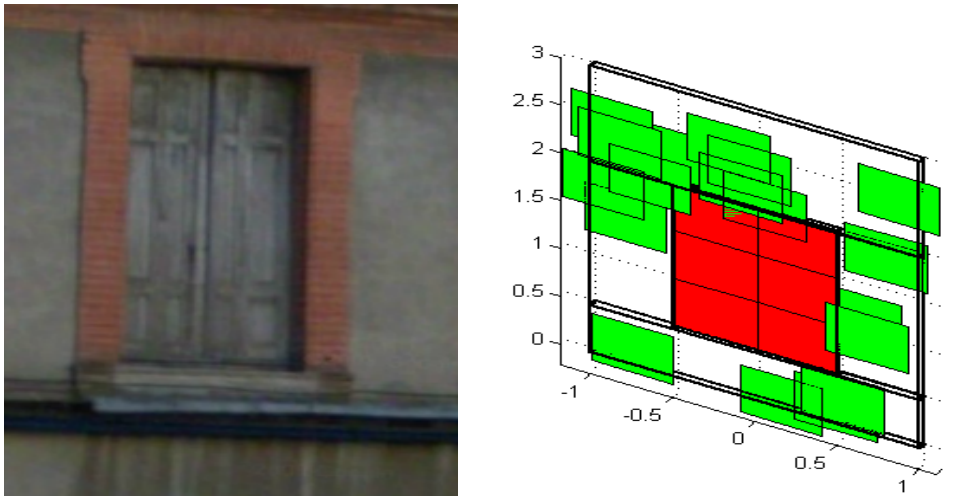

(a) Real façade 3 (b) Synthetic façade 3

Figure 4.35: Modern flat house front (façade 3)

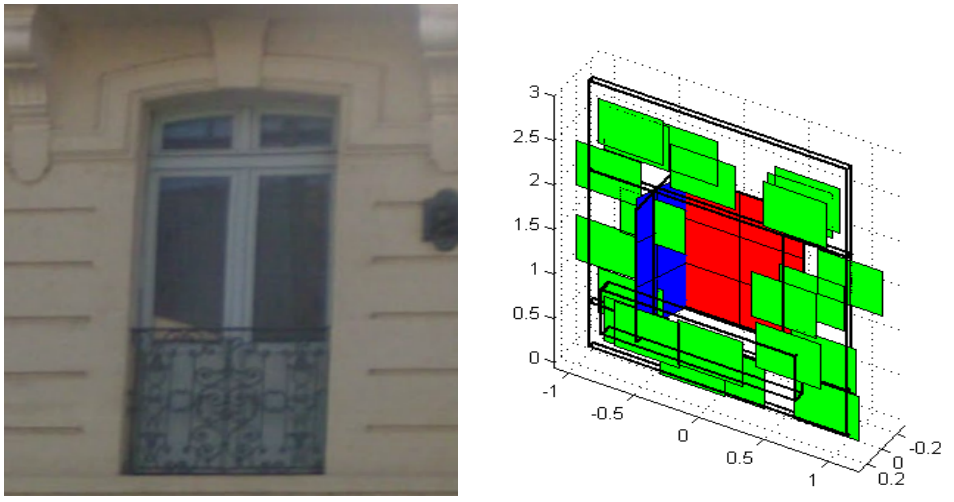

(a) Real façade 4 (b) Synthetic façade 4

Figure 4.36: Old façade with metallic guardrail (façade 4)

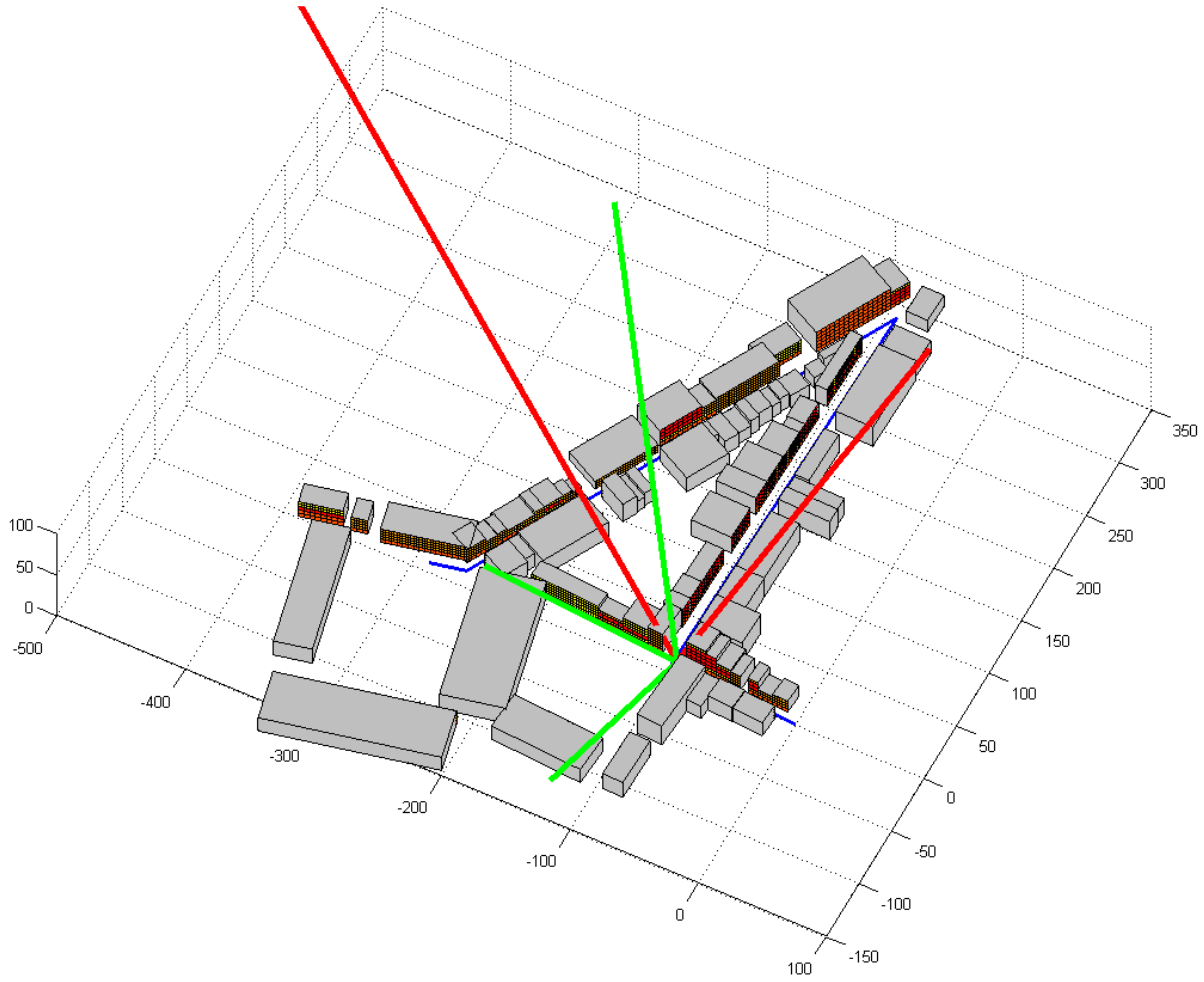

Figure 4.37: Toulouse-Capitole virtual environment in the SCHUN formalism from the PRN07 point of view

In this virtual environment, four types of façades have been used. This first one is representative of old Hausmanian architectures mainly present in Alsace Lorraine street. One example is presented in Fig.4.33. The simplified representation of this façade is composed of two windows made of glass, two backscatterers made of brick in the windows corners due to the receding windows, one backscatterer made of metallic material on the guardrail corner and one metallic guardrail represented as a very rough surface with exponential distribution. Finally, the walls are modelled as slightly rough specular surfaces with 0.2 m depth made of brick.

The second type of façade is representative of window shops mainly present on the ground floor of the buildings all along the receiver trajectory. Those façades are composed by one specular window made of glass plus one slightly rough specular surface with 0.2 m depth made of concrete at the bottom of the façade.

The third type of façade is representative of modern façades with smooth walls made of concrete. Those façades contain one window made of glass. The walls are modelled as slightly rough specular surfaces with 0.05 m depth and made of concrete.

The fourth type of façade is representative of old façades with metallic guardrails. They are made of one specular window made of glass, one backscatterer made of brick in the window corner and one very rough exponential surface made of metallic materials representing the guardrail. The walls are modelled as slightly rough specular surfaces with 0.05 m depth made of brick.

Finally, the Toulouse-Capitole virtual environment is presented in Fig.4.37 from the PRN07 point of view.

4.3.3 Indirect experimental validation on GNSS software receivers

4.3.3.1 Preliminary results

This subsection is relative to preliminary results and is focused on the use of synthetic environments when performing experimental validations. The first preliminary result is about environment stability. During the measurements, three loops of the reference trajectory have been performed successively in a 30 minutes interval. At the time of the measurements, a temporary market was rising up on Toulouse Capitole square. From one loop to the other, several trucks had moved and the stands were each time more numerous. This environment instability has caused severe impairments (DLL unlocking, deeper shadowing...) on the receivers as highlighted in Fig.4.38 in the red circle zone. Since this part of the measurement area was not stable and since this kind of temporary market is hardly reproducible by numerical simulation tools, this part of the reference trajectory on Capitole square has been discarded from the next presented indirect validation. The influence of other small objects such as cars or pedestrians has not been obviously detected on the estimated C/N0 time-series contrary to the influence of the market. Moreover, since the measurement conditions have not been filmed, they are not reproducible in the simulated scenario. Eventually, they have been neglected in the following analysis. The new reference trajectory is now 800 m long. It is materialised by the starting and the finish points in Fig.4.28. The loop 2 has been arbitrarily chosen for the following analysis since it is the shortest and reduces JGNSS post-processing time.

The second preliminary result highlights the importance of rigorously modelling the height of the building. The starting point of this observation presents the influence of the GPS constellation motion on the shadowing state at the receiver side. As discussed above, the three measurement loops have been made successively in a 30 minute interval. During that time, the satellites elevation had changed, from 5° to 20° depending on satellite trajectory, resulting in different shadowing conditions. Two examples are presented next for PRN10 and PRN13. As visible on Fig.4.39 the shadowing condition passes from a blocked state on loop 1 to a lighter shadowing state on loop 3. This observation can be linked to the sky plot presented Fig.4.30 where the PRN10 has an increasing elevation which reduces the depth of the shadowing. The opposite phenomenon is observable on Fig.4.40 for the PRN13 where the shadowing passes from a clear LOS on loop 1 to a deep blockage on loop 3 while PRN13 elevation decreases.

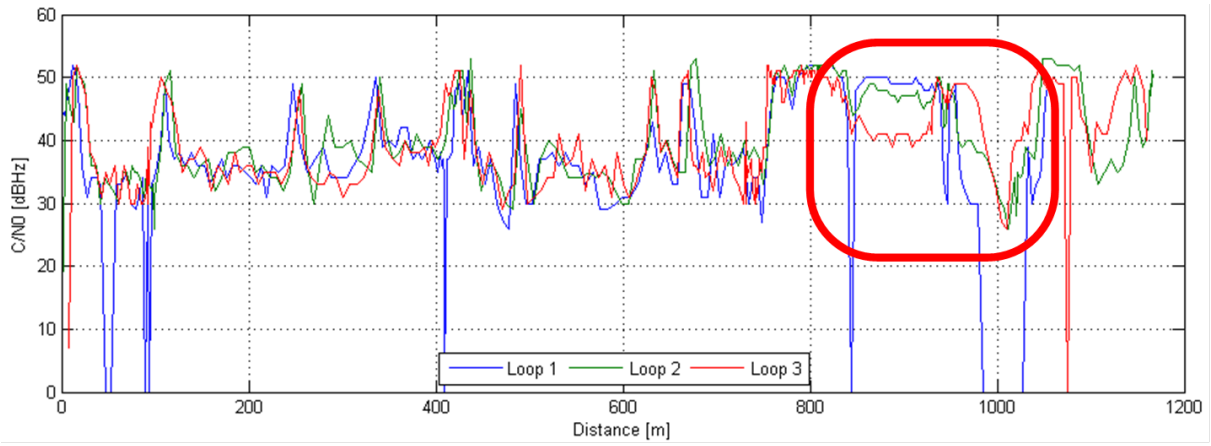

Figure 4.38: Influence of the environment instability on the C/N0 parameter estimated by one reference receiver (4T) for PRN07

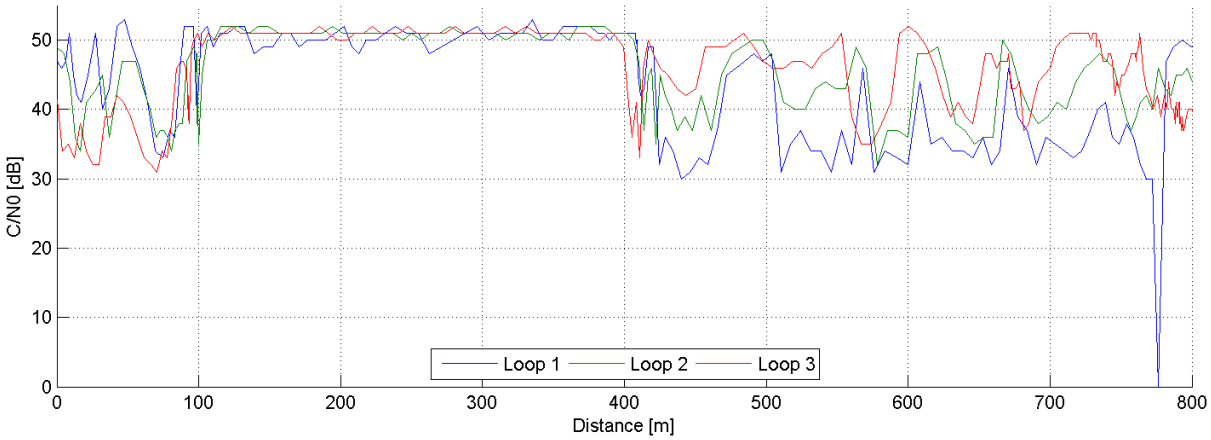

Figure 4.39: Influence of the elevation changes of PRN10 on the estimated C/N0 using Rx 4T during the three measurement loops

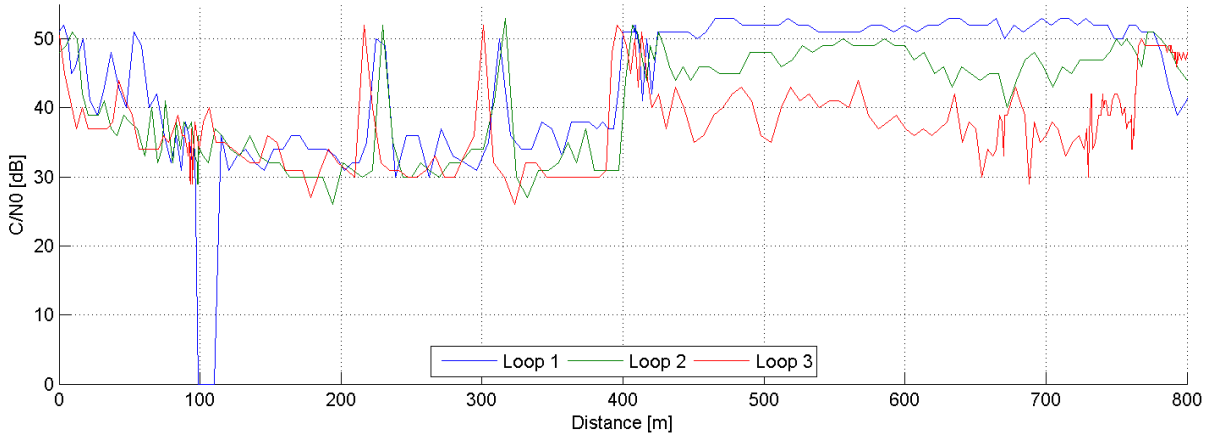

Figure 4.40: Influence of the elevation changes of PRN13 on the estimated C/N0 using Rx 4T during the three measurement loops

Observations made on Fig.4.39 and Fig.4.40 show how the macro-shadowing phenomenon at the receiver side is tightly linked to the satellite elevation and to the height of the buildings. Since the position of the satellites is accurately known, the only adjustment variable on the simulation tools is the height of the building. Fig.4.41 and Fig.4.42 present preliminary results of synthesised narrow-band time-series using both SE-WorkBench and SCHUN virtual environments with their respective EM tools.
As visible, major differences are observable between both synthesised time-series with respect to the reference time-series established using the BGM. The first difference is on the shadowing state. As visible, SE-WorkBench synthesised channel produces an obviously inaccurate alternation between LOS and NLOS states on both Fig.4.41 and Fig.4.42. From our interpretation, this is due to an inaccurate building height modelling which parameter is known to be empirically designed. Contrary to the SCHUN virtual environment which has been tuned, the SE-WorkBench environment is a commercial database which cannot be easily tuned without specific tools. The SCHUN virtual environment tuning consists only in adding or removing a maximum of one floor per building to modify the building height and reproduce the right LOS/NLOS alternation. The building footprint has not been modified, neither are the buildings architecture, the mobile trajectory or the satellite positions. Once tuned, the same SCHUN virtual environment has been used for all of the satellites.

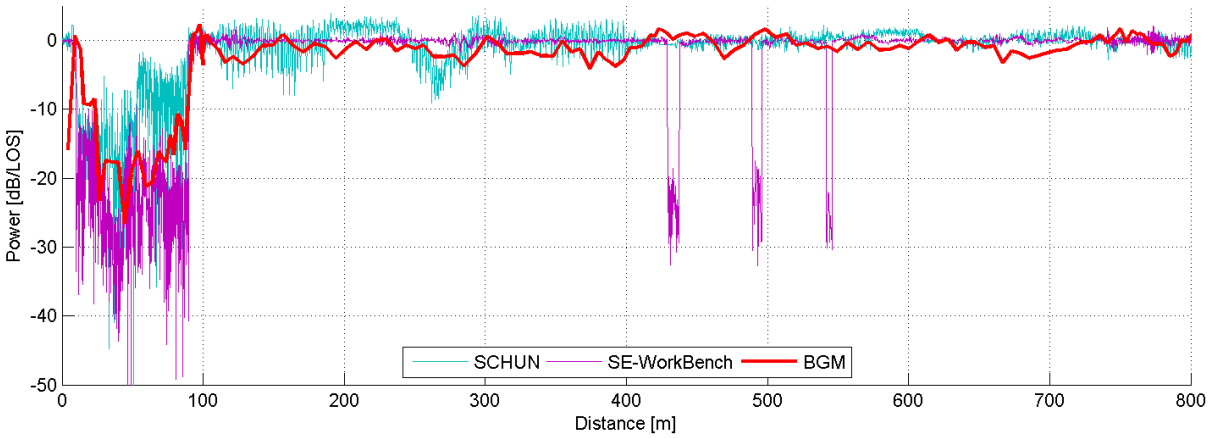

Figure 4.41: Comparison of narrow-band time-series using SE-WorkBench and SCHUN for PRN04. BGM is used as a reference

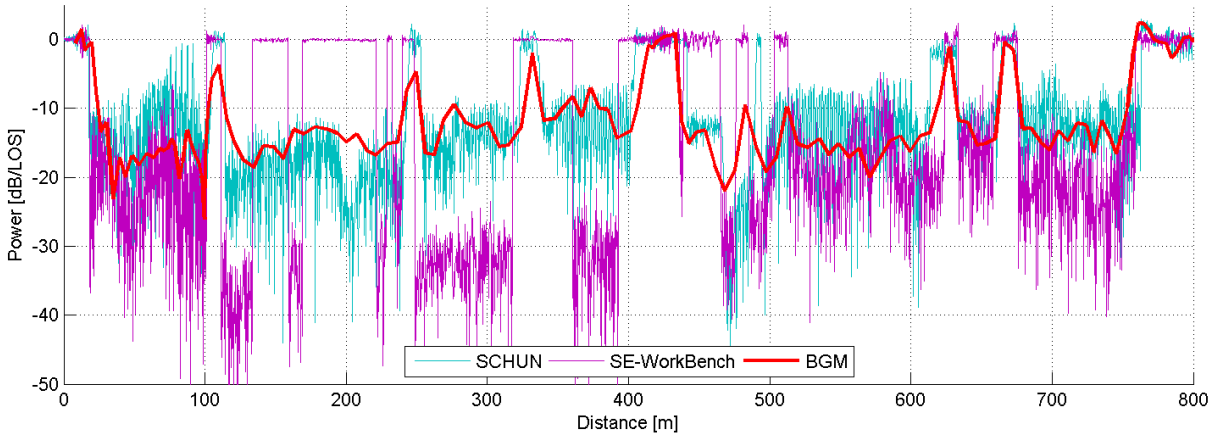

Figure 4.42: Comparison of narrow-band time-series using SE-WorkBench and SCHUN for PRN07. BGM is used as a reference

The second observation can be highlighted in Fig.4.42 between 100 m to 400 m. At those positions, the mobile is in Alsace Lorraine street and the PRN07 is almost aligned with the street axis, as visible in Fig.4.28. This configuration results in a very low multipath power estimation from SE-WorkBench contrary to SCHUN and BGM results. From preliminary simulations using JGNSS on such time-series, many DLL losses of lock were observable on this part of the trajectory contrary to BGM. An empirical offset of +15 dB was used to compensate this lack of power. The SE-WorkBench synthesised time-series presents a more reasonable accordance between 500 m to 800 m with SCHUN and BGM results where the satellite was no more aligned with the street axis. From our interpretation, the ray launching technique may present some limitations in the particular case of tangential incidences. Indeed, impinging rays coming from the initial ray launching grid are almost tangential to the building façades. This results in a very few interactions with the environment which conducts to an underestimation of the multipath power coming from the surrounding façades. The SCHUN simulator is not affected by this tangential limitation since using a different ray technique where each ray necessarily impinges each visible facet. The SCHUN approach allows preventing any facet miss and better reproduces the multipath power in such configurations.

At the end, SE-WorkBench synthesised time-series are not comparable to both BGM and SCHUN results mainly due to an unrealistic LOS/NLOS alternation. This lack can be imputed to the environment representation and particularly to the height of the buildings which is a critical parameter in such urban scenarios. SE-WorkBench is finally discarded from the next presented analysis and only BGM and SCHUN results are analysed and compared.

4.3.3.2 Estimated C/N0 time-series

The first experimental validation performed hereafter is based on the estimated C/N0 time-series. As introduced previously, the C/N0 parameter is a GNSS parameter, internal to the receiver processing, which estimates the quality of the received signal. The C/N0 is similar to a signal to noise ratio except it is independent from the receiver bandwidth. This allows comparing different receivers using different bandwidths. The C/N0 parameter is given in dBHz in the following. Between 50 dBHz to 40 dBHz, the C/N0 parameter is representative of clear LOS conditions or light shadowing effects at the receiver side. Between 40 dBHz to 25 dBHz, the C/N0 is representative of deep LOS blockage and dense multipath contributions. Usually, below 25 dBHz, the receiver looses track of the satellite and a new acquisition has to be performed.

In the following analysis, four curves are present on each plot. Two of them come from the spare receivers used during the measurements, uBlox 4T and uBlox 6H. The C/N0 time-series were directly processed during the measurements. The two others come from our GNSS software receiver JGNSS. The first one corresponds to the processing of the experimental propagation channel recorded by the BGM and the second one corresponds to the processing of the synthesised channel using the SCHUN simulator. In this analysis, six satellites have been chosen since having at least 30° elevation. The estimated C/N0 time-series are presented from Fig.4.43 to Fig.4.48 for PRN02, PRN04, PRN07, PRN08, PRN10 and PRN13 respectively.

In general a very good accordance is found between all six estimated C/N0 time-series. However, from time to time differences appear. They are summarised in Tab.4.3 and commented below.

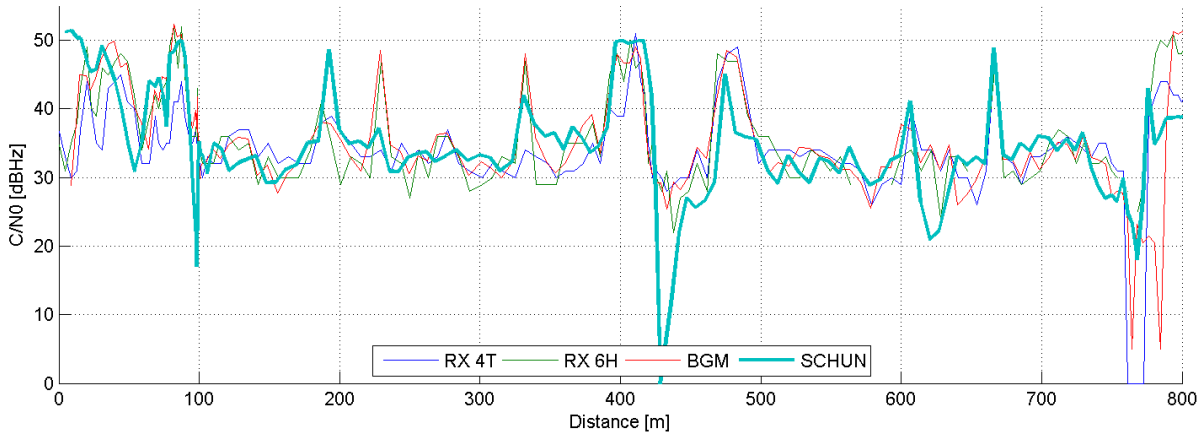

Figure 4.43: Comparison of the estimated C/N0 time-series for the PRN02

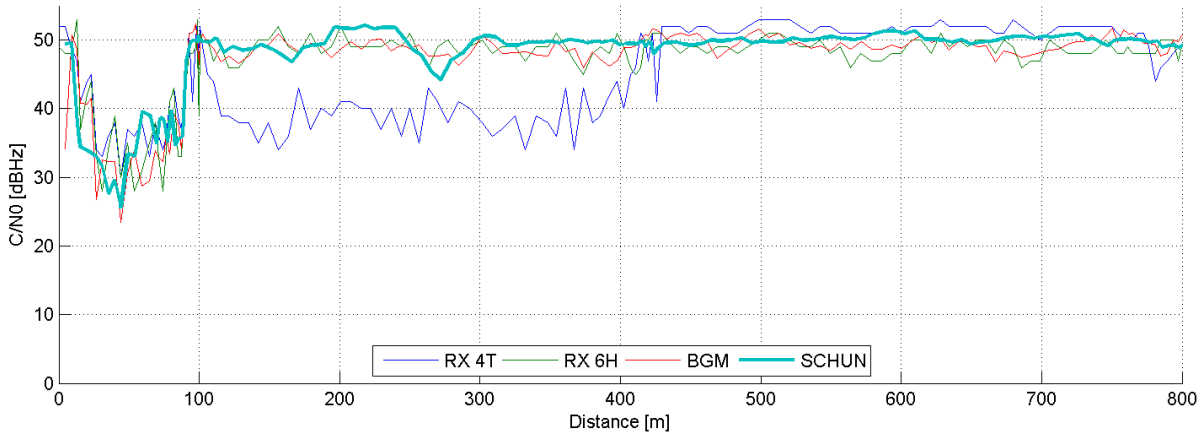

Figure 4.44: Comparison of the estimated C/N0 time-series for the PRN04

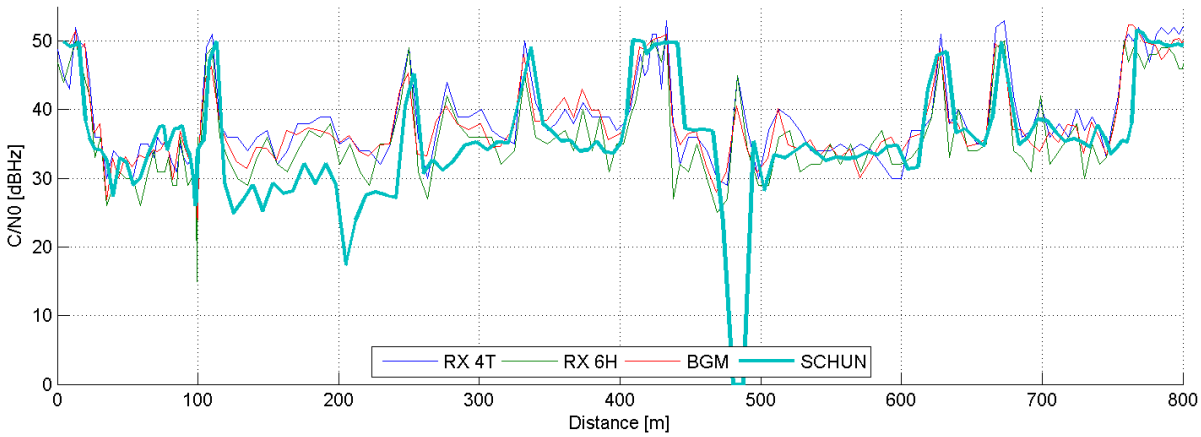

Figure 4.45: Comparison of the estimated C/N0 time-series for the PRN07

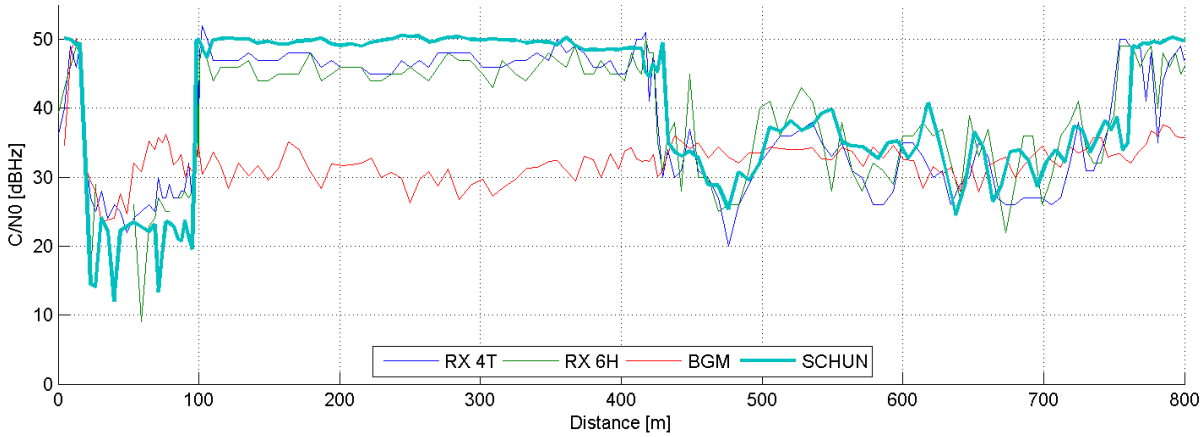

Figure 4.46: Comparison of the estimated C/N0 time-series for the PRN08

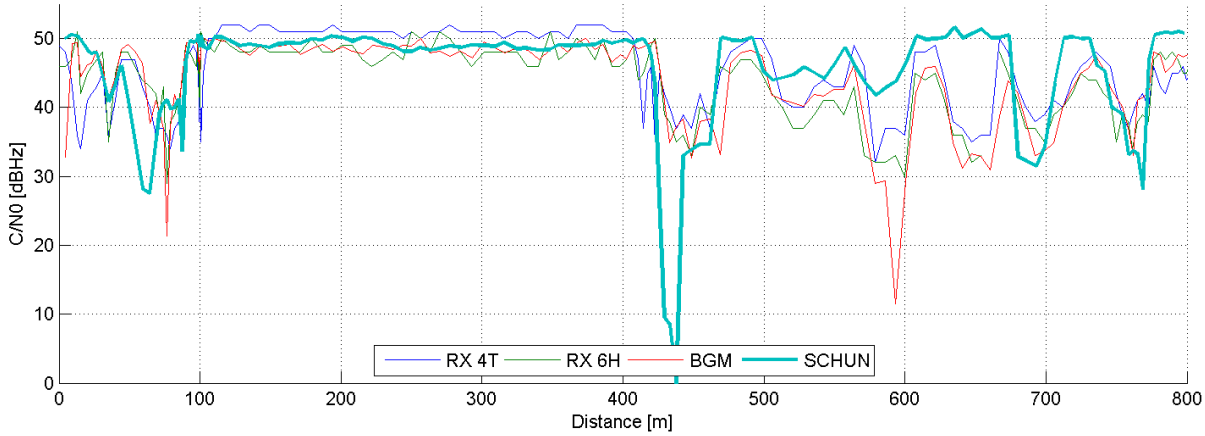

Figure 4.47: Comparison of the estimated C/N0 time-series for the PRN10

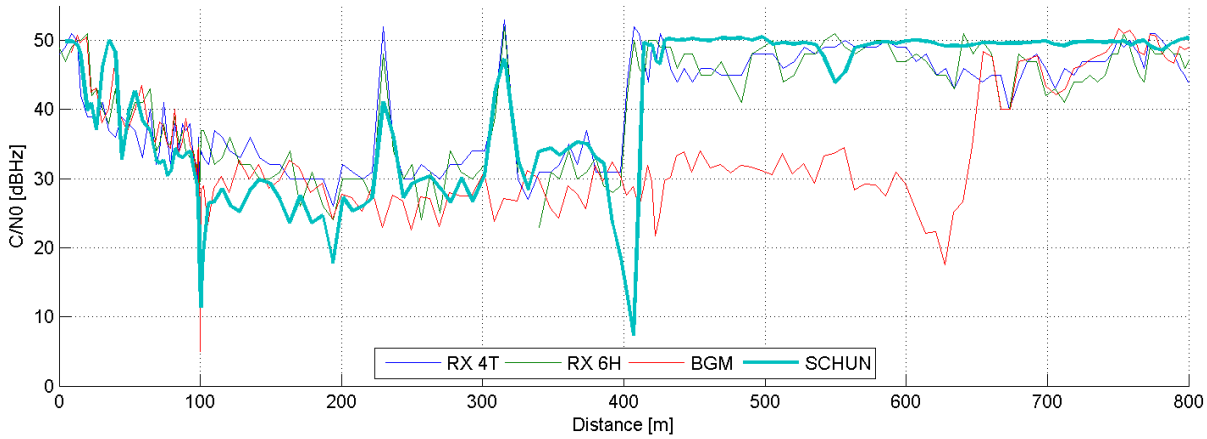

Figure 4.48: Comparison of the estimated C/N0 time-series for the PRN13

		PRN02	PRN04	PRN07	PRN08	PRN10	PRN13
In-situ	Rx 4T (Experimental)	✓	✗	✓	✓	✓	✓
	Rx 6H (Experimental)	✓	✓	✓	✓	✓	✓
Post-processed	BGM (Experimental)	✓	✓	✓	✗	✓	✗
	SCHUN (Simulation)	✓	✓	✓	✓	✗	✓

Table 4.3: Summary of the C/N0 comparisons for both in-situ measurements using reference GNSS receivers (Rx 4T, Rx 6H) and post-processed channels using JGNSS (BGM experimental, SCHUN simulation) for PRN02, PRN04, PRN07, PRN08, PRN10 and PRN13

The first noticeable difference is visible in Fig.4.44 for the PRN04 using the 4T reference receiver. As visible, 4T reference receiver seems masked when going through Alsace Lorraine street while 6H, BGM and SCHUN results are representative of clear LOS conditions. This observation cannot be explained without images of the measurements.

The second noticeable difference is visible in Fig.4.46 for the PRN08 using JGNSS to process the BGM raw data. As visible, the BGM looses track of the PRN08 at 25 m when entering the first canyon and never recovers the track, even in clear LOS conditions in Alsace Lorraine Street from 100 m to 400 m. A similar phenomenon is visible in Fig.4.48 for the PRN13 where JGNSS lags to recover the satellite track between 400 m to 650 m.

One last difference is visible in Fig.4.47 for the PRN10 using JGNSS to process the SCHUN synthesised channel. As for Saint Lary environment, the complexity of the rooftops in Remusat street, 450 m to 750 m, the LOS/NLOS alternation may have been impaired since using simple cuboids shapes in the SCHUN formalism. This results in slightly over predicting LOS states in this part of the trajectory.

Eventually, the SCHUN channel simulator presents very good results in terms of C/N0 time-series where LOS and NLOS states alternation is well reproduced and the multipath power seems coherent with the experimental data (C/N0 between 40 and 25 dBHz). However, JGNSS processing on PRN08 and PRN13 using BGM data seems impaired. PRN08 and PRN13 are discarded for the second part of the analysis based on pseudo-range errors.

4.3.3.3 Pseudo-range error time-series

The second part of the analysis deals with pseudo-range error comparisons using JGNSS to process BGM recorded channels and SCHUN synthesised channels. The range to a satellite represents the geometrical distance separating the mobile receiver from the transmitting satellite. Due to clock biases, atmospheric delays and multipath effects, the receiver is only able to estimate a pseudo-range to a satellite where all errors mentioned above are present. Finally, the pseudo-range error is the error made by the receiver when estimating its range to one satellite.

On one side, when using simulation tools, the pseudo-range error can be easily computed. The pseudo-range error is the difference between the geometrical distance separating the mobile from the satellite and the distance estimated by the receiver. In this experimental validation example, the focus is made on the influence of the channel close to the receiver and only pseudo-range errors due to multipath are of interest. Ionospheric delays and clock bias being out of focus, those error sources are not integrated into the SCHUN simulations.

On the opposite side, when using experimental datasets, the pseudo-range error to a satellite is hardly computable. The main steps which allow to isolate the pseudo-range error due to multipath are summarised in Fig.4.49 and described below.

The first step consists in synchronising time and positions of both the receiver and the transmitter. First of all, each measured sample has to be precisely dated. From this precise timing, the reference trajectory can be interpolated. At this state, both time and positions of the receiver are precisely known. Using the French RGP network as already mentioned, the position of the satellite can also be precisely known. However, this position corresponds to the satellite position at the receiving time. Since the satellite has moved during the signal propagation, the position of the satellite has to be determined at the transmitting time. After a first estimation of the geometrical distance, a new satellite position can be computed using interpolation techniques described in [Sche 03]. A looped process permits to accurately determine the satellite position at the satellite transmitting time.

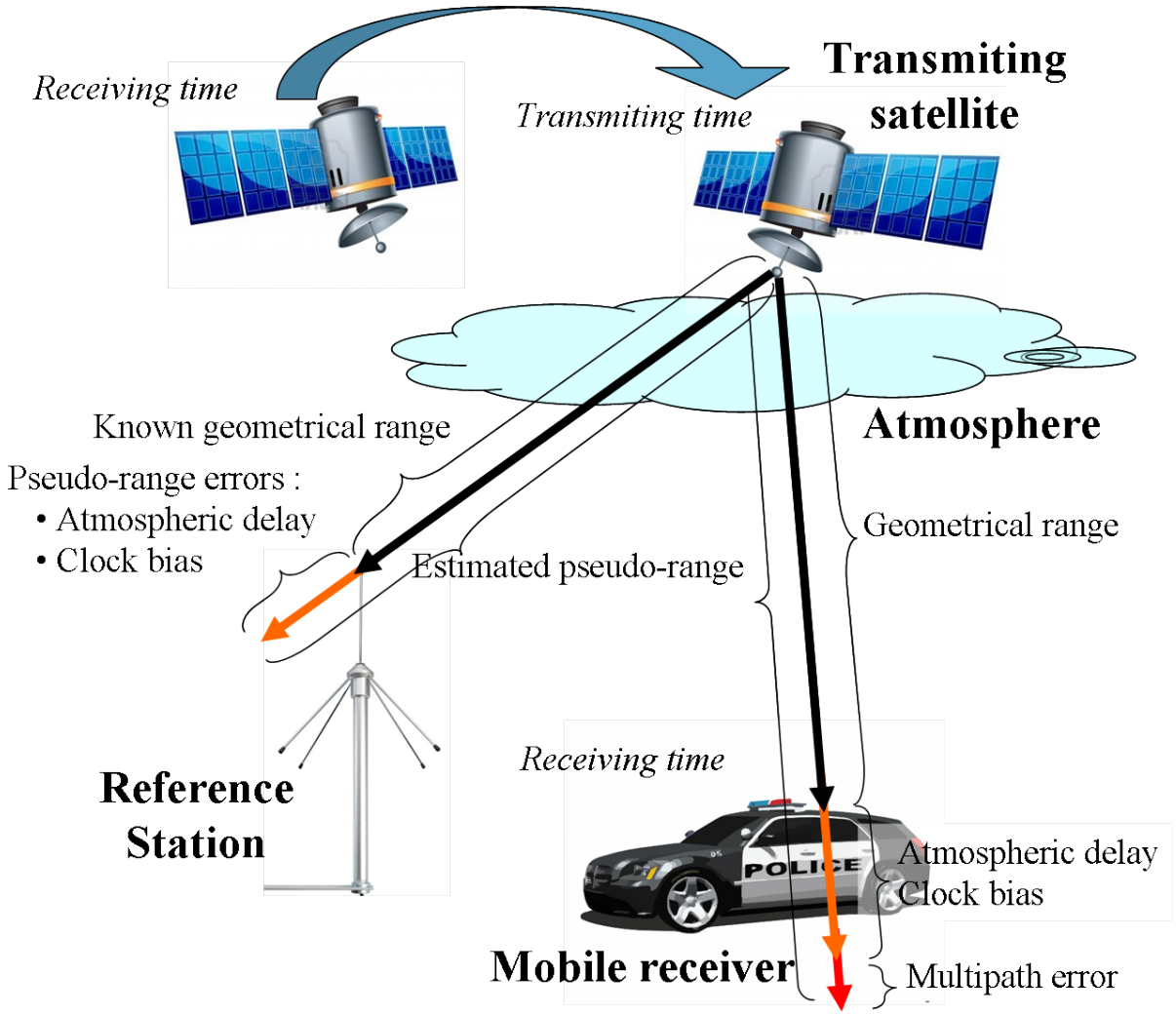

Figure 4.49: Estimation principle of the pseudo-range error due to multipath in experimental conditions

Once the satellite and the receiver are positioned and time synchronised, the second step consists in estimating the reference pseudo-range error. To do so, the reference station from CNES is used. The reference station provides measured carrier phases and pseudo-range from all visible satellites at the time of the measurements. Since the position of the reference station is precisely known, a geometrical range to each satellite can be computed. Removing the geometrical range into the estimated pseudo-range allows isolating the reference pseudo-range error at the reference station. This reference pseudo-range error mainly contains atmospheric errors and satellite clock bias. Due to its optimal receiving location, the reference pseudo-range error is assumed to be free of any multipath bias.

The last step consists in isolating the pseudo-range error due to multipath effects at the mobile receiver side. Using JGNSS allows estimating the pseudo-range error to each satellite. Since the precise positions of both the receiver and the transmitter are known, the geometrical range can be computed and removed from the estimated pseudo-range. Assuming that the atmospheric errors and the satellite clock bias are the same as the ones measured at the reference station, both error sources can be removed from the estimated pseudo-range. This assumption remains true only in a 10 km perimeter [Gunt 10] around the reference station. Finally, the pseudo-range error due to multipath in the vicinity of the mobile receiver can be isolated. The following of the analysis is based on the multipath pseudo-range error comparison between BGM measured channel and SCHUN synthesised channel.

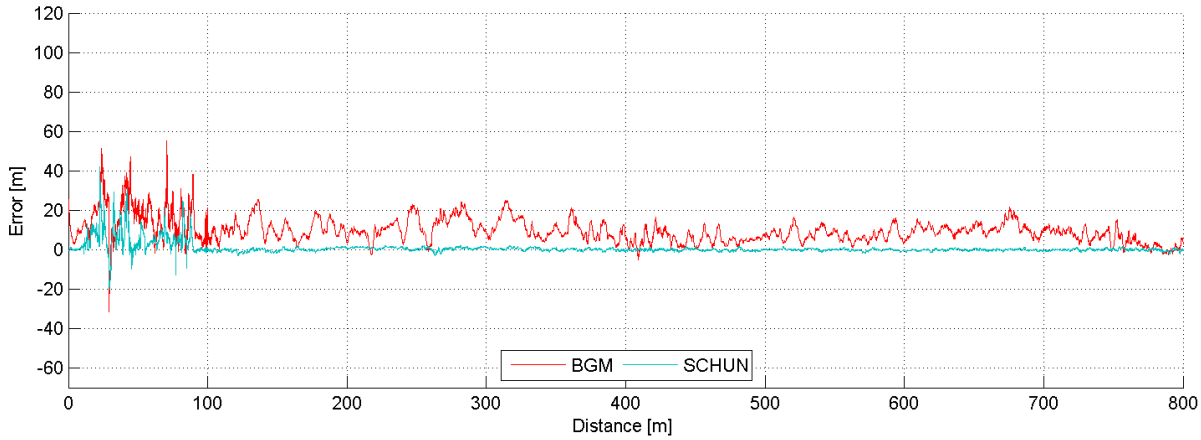

Figure 4.50: Raw pseudo-range error time-series for the PRN04

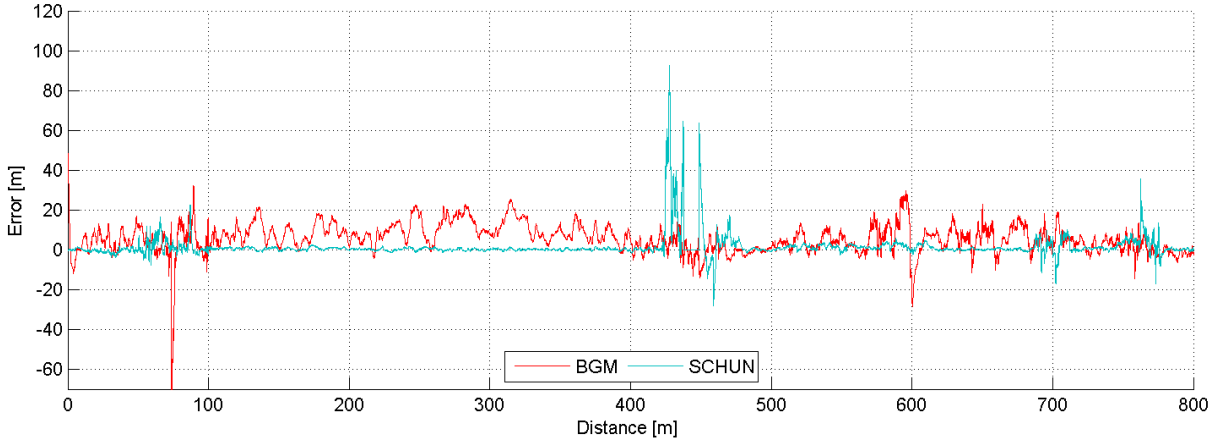

Figure 4.51: Raw pseudo-range error time-series for the PRN10

Fig.4.50 and Fig.4.51 present some preliminary pseudo-range error time-series for PRN04 and PRN10 respectively. Both time-series have been chosen on purpose since they are representative of long LOS sections as presented on the C/N0 time-series. As visible, both time-series are highly correlated and a similar pattern is visible on both time-series. Even more, the expected pseudo-range errors considering such C/N0 (about 50 dBHz) are too high and neither in accordance with the DLL jitter theory next presented nor with the SCHUN results which remain in the theoretical bounds. Note also that PRN04 and PRN10 have very different elevations and azimuths implying that the observed correlation does not come from the multipath environment. From our interpretation, some experimental biases may have not been corrected, or added, during the pre-processing step. To compensate those biases, which seem to be constant for at least those two satellites, the pseudo-range error time-series from PRN04 has been considered as a second reference to remove those biases on the other time-series. In the following of the analysis, PRN02, PRN07 and PRN10 pseudo-range time series are corrected. The new trajectory is now restricted from 100 m to 800 m where clear LOS is achieved on PRN04.

Fig.4.52 to Fig.4.54 present the corrected pseudo-range error time-series for PRN02, PRN07 and PRN10 respectively. As visible, pseudo-range error time-series behave like noise. However, one qualitative comparison can be made. Depending on the direct path condition LOS/NLOS, the dynamic of the time-series highly changes. This dynamic change seems to be well reproduced considering the SCHUN results for PRN02 and PRN07. For PRN10, it has been noticed when analysing the C/N0 time-series that SCHUN tends to over predict clear LOS propagation conditions at the end of the trajectory. This result is also visible on Fig.4.54 where the pseudo-range error from SCHUN is flatter compared to the one of BGM since mainly in LOS conditions.

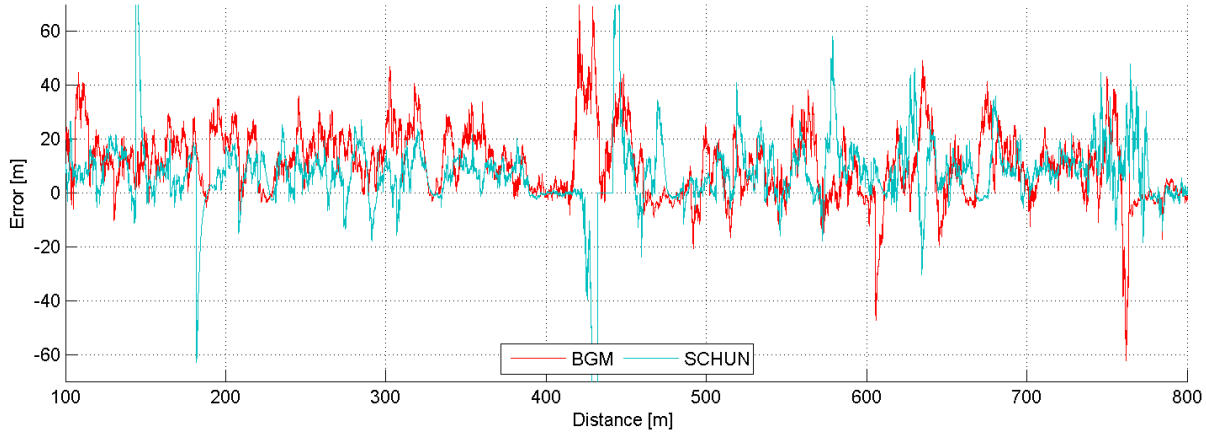

Figure 4.52: Corrected pseudo-range error time-series for the PRN02

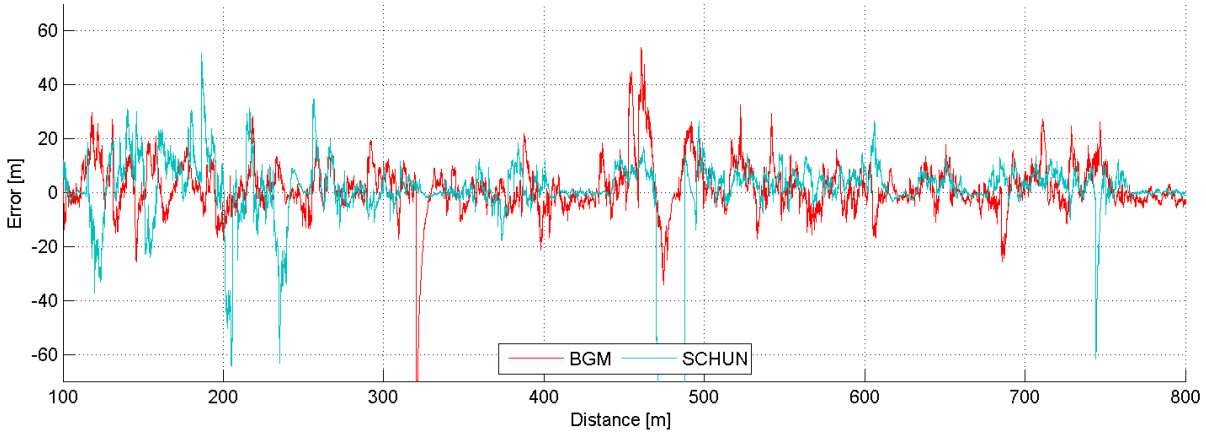

Figure 4.53: Corrected pseudo-range error time-series for the PRN07

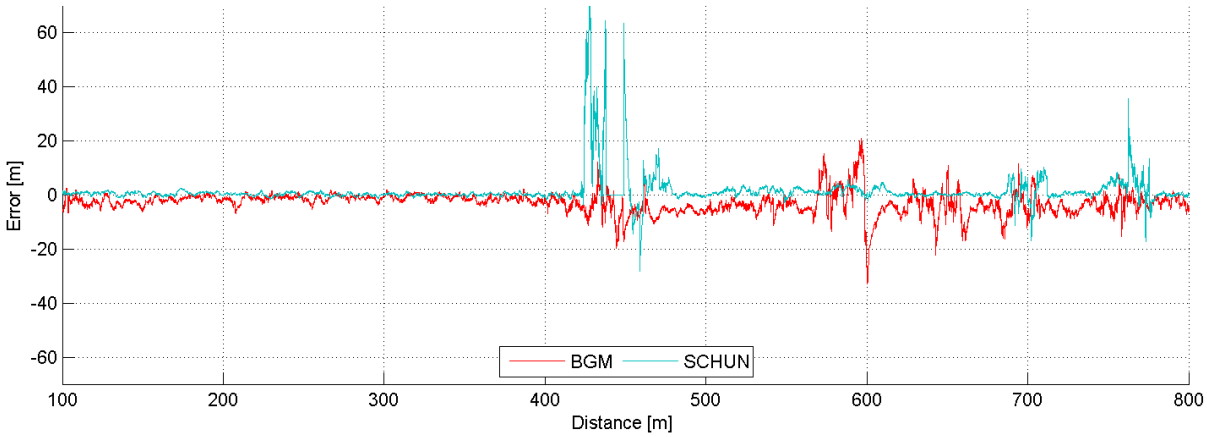

Figure 4.54: Corrected pseudo-range error time-series for the PRN10

To better compare noise-like time-series, a short statistical analysis has been performed. The first studied parameter is the pdf of the pseudo-range error. The second parameter is the DLL jitter, function of the estimated C/N0. The DLL jitter represents the standard deviation of the pseudo-range error in the case of a white Gaussian noise. The DLL jitter is a function of many parameters: the received power $C/N0$ in Hz, $B_n = 1$ Hz the equivalent DLL bandwidth, $D = 1$ the normalised early minus late spacing of the discriminator, $T_c = 1,023$ MHz the chip rate, $T = 20$ ms the integration time and $B_{fe} = 68$ MHz the double sided front end bandwidth. The DLL jitter formula is given in Eq.4.3 [Kapl 05]. In the following, the DLL jitter is represented by a black curve function of the estimated C/N0. Experimental results from BGM and SCHUN

are scatter plotted over the theoretical DLL jitter. Note that one scatter point corresponds to the jitter computed over a window of 2 seconds. This window length has been chosen in order to consider stationary conditions of the environment and of the DLL filtering process.

$$\sigma_{t\,DLL} = \begin{cases} \sqrt{\frac{B_n}{2\,C/N0}\,D\left[1+\frac{2}{T\,C/N0\,(2-D)}\right]} & , \quad D \geq \frac{\pi}{B_{fe}\,T_c} \\ \sqrt{\frac{B_n}{2\,C/N0}\left[\frac{1}{B_{fe}\,T_c}+\frac{B_{fe}\,T_c}{\pi-1}\left[d-\frac{1}{B_{fe}\,T_c}\right]^2\right]\left[1+\frac{2}{T\,C/N0\,(2-D)}\right]} & , \quad \frac{1}{B_{fe}\,T_c} < D < \frac{\pi}{B_{fe}\,T_c} \\ \sqrt{\frac{B_n}{2\,C/N0}\left[\frac{1}{B_{fe}\,T_c}\right]\left[1+\frac{1}{T\,C/N0}\right]} & , \quad D \leq \frac{1}{B_{fe}\,T_c} \end{cases} \tag{4.3}$$

On the pdf plots, all three presented results present a reasonably good agreement between BGM and SCHUN results. A slight difference is however visible on all plots at 0 m of the pseudo-rage error. For null pseudo-range error, the SCHUN results predict higher probabilities contrary to BGM results. From our interpretation, this result either comes from very clear LOS conditions (similarly to Saint Lary results), which are even more over predicted by the SCHUN simulator (end of the trajectory for PRN10), or, from the noise present in the measurements which has not been perfectly reproduced by the simulation. One other minor difference is the slight pseudo-range error offset, about -1 m, present for PRN07 and PRN10 while SCHUN results are centred on 0 m. This observation is also visible on the corrected pseudo-range error times series visible in Fig.4.53 and Fig.4.54. This result can be explained by the empirical adjustments made using PRN04 as a second pseudo-range error reference which may have introduce a new bias.

On the DLL jitter plots, it can be seen that the standard deviation of the pseudo-range error is function of the C/N0 and both BGM and SCHUN scatter plots present a reasonable agreement with the theoretical curve of the DLL jitter especially for high C/N0.

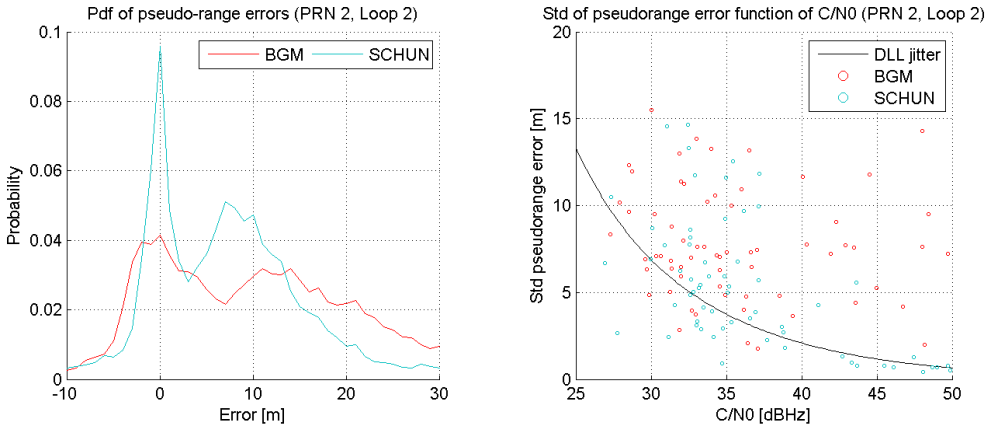

(a) (b)

Figure 4.55: Distribution of the pseudo-range errors and DLL jitter versus the estimated C/N0 for the PRN02

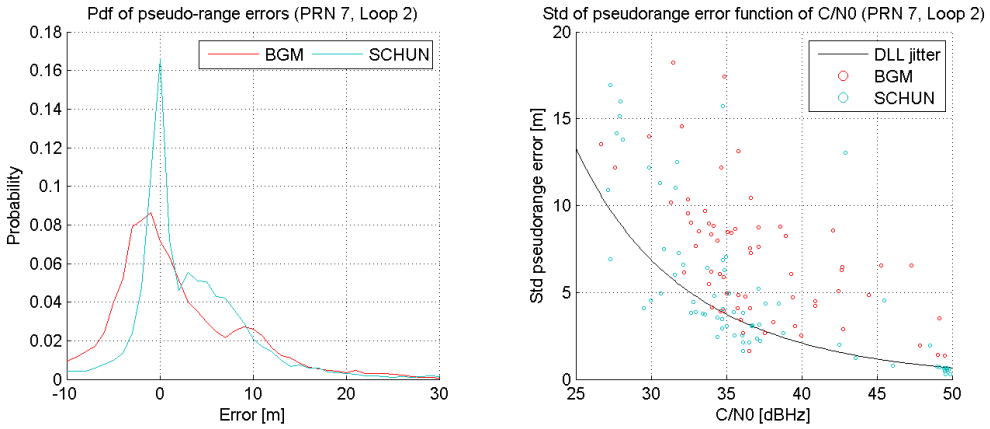

(a) (b)

Figure 4.56: Distribution of the pseudo-range errors and DLL jitter versus the estimated C/N0 for the PRN07

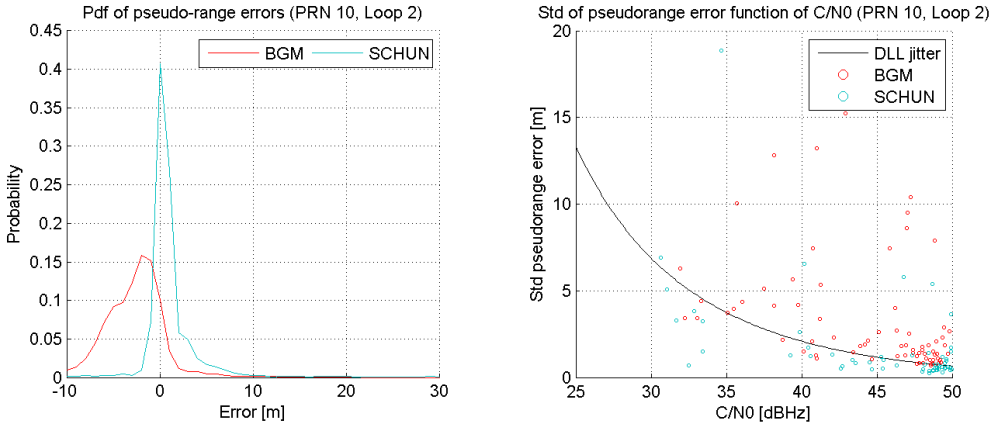

(a) (b)

Figure 4.57: Distribution of the pseudo-range errors and DLL jitter versus the estimated C/N0 for the PRN10

Section synthesis :
This second experimental validation is focused on the behaviour of GNSS receivers in dense urban environments. The measurement campaign has been performed by CNES and ISAE in Toulouse-Capitole, France during spring 2011. This second validation is an indirect validation. The comparison has been established considering the internal behaviour of one GNSS software receiver processing measured and synthesised propagation channels. The main conclusions are the following:

- *For the need of this validation, a very complex urban environment has been created and integrated into the SCHUN simulator. The complex mobile trajectory, with street changes and variable speeds, has been reproduced. The GPS satellite constellation has also been reproduced and six channel syntheses have been performed simultaneously by the SCHUN simulator.*
- *During the validation process, the importance to accurately reproduce the environment and particularly the building height in urban canyons has been presented as a critical issue. Due to building height uncertainty in the SE-WorkBench database, SE-WorkBench software suite has not been used to compute propagation channels.*
- *Using the SCHUN channel simulator to compute the propagation channels is a success and C/N0 time-series present a very good accordance using several references from the measurement campaign. As for Saint Lary, the SCHUN simulator tends to underestimate sub-states in the LOS state producing very clear LOS conditions.*
- *On the pseudo-range error analysis, processing real measurements appears to be very difficult and residual errors were still present in the preliminary results justifying an empirical adjustment using one satellite in clear LOS condition. Even more, the pseudo-range errors behave like noise and are hard to compare. A short statistical analysis using pdf and DLL jitter as comparison points presents a reasonably good agreement.*

4.4 Discussion

This last chapter has presented the final implementation and two experimental validations of a new LMS channel simulator: SCHUN. Based on a hybrid architecture, this LMS channel simulator is well suited for MIMO issues considering satellite communication applications and is able to generate realistic multipath for wide-band applications and satellite navigation systems. In its current version, the SCHUN simulator can be used as an independent tool synthesising complex urban scenarios and delivering continuous channel impulse responses. The virtual city synthesis allows the user to generate very wide environments while the use of deterministic methods based on EM theory such as PO and UTD allows a better accuracy and more versatility to the different uses of the SCHUN simulator. An extra feature, reducing the number of multipath, has also been presented. Not fully characterised yet, this new technique is promising since it allows to drastically reducing the post-processing time when integrating the SCHUN simulator into system simulations chains.

The SCHUN simulator has also been validated considering two measurement campaigns. The first one is oriented toward narrow-band issues for satellite communication systems while the second one is oriented toward wide-band issues for satellite navigation systems. All along both validations, the SCHUN simulator has presented a reasonable agreement with the measurements, even if some specific points require to be further investigated in a close future.

One of the main advantage of the SCHUN simulator is its particular emphasis on multipath modelling applied to system simulations and particularly to satellite navigation systems. Indeed, during the whole validation process, channel impulse responses have been post-processed

using different GNSS software receivers. This system approach has permit to validate the initial concepts and show reasonnable results considering real experimentations contrary to deterministic tools based on geometrical optic only. One other main advantage of the SCHUN simulator is its time efficiency. Thanks to its virtual city approach and its simplified EM modelling, the SCHUN simulator allows to process very wide scenarios with high sampling rates of the trajectory ($\lambda/6$ for the Saint Lary experimental validation) in a resonnable time contrary to SE-WorkBench deterministic tool based on complex EM methods which computation time is in the order of several months. The last main advantage of the SCHUN simulator is its native MIMO management. This feature is very important considering next generation uses of the SCHUN simulator where antenna arrays are now widely used and frequency diversity for satcom and satnav systems is investigated. The transmitter diversity is also an important feature and is mandatory to compute realistic PVT for satnav systems.

One of the main actual limitation of the SCHUN simulator is the vegetation which is not taken into account yet. From the author point of view, this new feature is mandatory for the next evolutions of the SCHUN simulator. One other limitation is the use of a façade library which have to be tuned depending on the targeted environment. At the present time, the façade library contains several façades which have been validated and which can be directly used by the SCHUN users. Advised users may also create their own façades to better represent specific environments. The façade labrary issue may also be solved by changing the virtual city generator. On the EM modelling part, one limitation comes from the use of the UTD when estimating the Doppler spectrum from the narrow-band time series due to the intrinsic discontinuities of this method. One solution is to use PTD or ECM methods but this solution would require more computation ressources and increases the number of received rays which is critical when post-processing CIRs. On the experimental validation part, it has been shown that the SCHUN simulator tends to over-predict LOS conditions with very clear line of sight. This issue may come from the cuboids shape used to represent the buildings. One solution is to better represent the building roofs and accurately model the building heights. Nevertheless, and according to SE-WorkBench results, this issue also affects deterministic simulation tools. The issue on second order statistics observed on the Saint Lary validation have also to be investigated and corrected.

Conclusion

This PhD work presents a new enhanced physical-statistical simulator of the land mobile satellite channel for multipath modelling applied to satellite navigation systems. As a starting point of the approach followed during this work, a critical review of the existing LMS channel models has been performed to highlight their respective limitations. From this analysis and to satisfy our requirements, a hybrid physical-statistical approach has been chosen and the macro-architecture for a new LMS channel simulator has been proposed. According to the proposed architecture, the first interrogation was on how complex environments, and particularly complex facades, should be modelled to remain realistic in simulation tools. This study has shown that the architectural elements have a strong impact on the propagation mechanisms taking place around complex facades. This study has lead to the 2.5D facade approximation where macro-details, objects large compared to the wavelength, have to be integrated into the facade modelling. From the 2.5D facade approximation, a new building macro-scattering model, the 3CM, has been proposed to reproduce wave interactions with buildings. This model proposes to separate the three identified propagation mechanisms taking place around the facades, namely specular reflections, backscattering and incoherent scattering, to reproduce the macro-scattering function, dependently of the facade architecture. The 3CM is based on the PO algorithm which handles dielectric materials, polarisation issues and frequency scalability for a better versatility of the model. As illustrated by the SCHUN simulator architecture, the 3CM model has been integrated into a standalone channel simulator, for a more versatile use. The SCHUN LMS channel simulator is able to synthesise very large virtual environments. It also performs the EM computation of the LMS propagation channel using both the 3CM and a direct path model based on UTD. Finally, the SCHUN simulator has been validated against two measurement campaigns oriented toward system designs for both satellite communication systems and satellite navigation systems.

All along this document, several innovative results have been presented. One of them is the 2.5D facade approximation and the associated recommendations. From a rigorous study using full-wave method, it has been shown that textured walls, representative of the facade architecture, do not behave like flat walls. Indeed, flat walls highly over-estimate the specular phenomenon to the detriment of the scattering phenomenon. As discussed, this imbalance has a strong impact when considering end applications such as satellite navigation systems.

The other originality of this work comes from the 3CM model where the total radiation pattern of a complex facade has been broken down into three different propagation mechanisms considering EM simulations and measurement observations. According to the 2.5D facade approximation, each part of the facade can be linked to a specific propagation mechanism where flat parts give rise to specular reflections, protruding and receding elements give rise to backscattering reflections and rough surfaces give rise to incoherent scattering. Finally, the 2.5D facade approximation has introduced a new way of representing complex urban environments and the 3CM has introduced a new way of performing simplified EM interactions between waves and buildings.

However, the main achievement of this work remains the SCHUN LMS channel simulator which merges observations, recommendations and partial conclusions made all along this document. This new channel simulator is based on a hybrid physical-statistical approach, taking advantage of low computation time from statistical approaches and versatility from deterministic approaches. The statistical component is mainly used during the environment synthesis step and allows fast and realistic site generic computation based on the virtual city concept. Contrary to existent virtual city generators, the SCHUN environment generator uses a 3D representation of the buildings and includes the facade architectures into the modelling of complex urban environments. A minority use of statistics is also present in the 3CM when randomly spreading

the facets responsible of the incoherent scattering component. The rest of the modelling comes from deterministic approaches and uses simplified EM models (PO and UTD in the 3CM and in the LOS blockage model respectively) and conventional ray algorithms (ray propagation, ray masking and stationary diffraction point). The overall design of the SCHUN simulator has permitted to meet our requirements in terms of wide-band representation of the LMS propagation channel, fast computation, independence from measurement campaigns, MIMO oriented with satellite diversity, space diversity, frequency diversity and polarisation diversity, frequency scalable at least from L-band to C-band, very wide scenario management and output versatility.

Finally, this work is innovative considering the validation process which merges numerical tools and experimental campaigns considering both propagation channel parameters and end applications, particularly oriented toward satellite navigation systems. During this work, the choice has been made to use the most accurate EM methods (Elsem3D based on the Method of Moments) to better understand the underlying propagation mechanisms prior to simplify the EM computation using asymptotic tools (SE-WorkBench software suite) to finally end up with a simplified model based on the PO algorithm and restricted to the most essential EM component. During this process, a continuous attention has been paid to satellite navigation applications, and partial validations using GNSS software receivers were considered as mandatory to go further in the modelling process. Once build, the SCHUN simulator has been strengthened according to two measurements campaigns based either on propagation channel parameters or through a satellite navigation receiver.

As a prospect for further developments of the SCHUN simulator, a particular and mandatory emphasis has to be made on vegetation effects since being the actual main limitation of the SCHUN simulator. Other urban features such as lamppost or bus shelters could also be integrated in a latter time. Adding such models would allow the SCHUN simulator to be used in a wider range of environments from urban to rural. This upgrade could also lead to new experimental validations to strengthen the new SCHUN simulator on some aspects which have not been experimentally validated yet. MIMO issues are one of the main priorities even if partial MIMO simulations have already been realised during the validation process, L-band and S-band simulations, multi-satellites computation for satellite navigation needs or co and cross polarisation issues. A second issue could be the use of higher frequencies in Ka/Ku bands to validate the new SCHUN simulator.

A new track to be investigated in further work could also consist in characterising the multipath reduction algorithm briefly presented in the last chapter. Solving this issue would permit to integrate the SCHUN simulator into complex system simulation chains or hardware channel emulators to characterise and standardise GNSS receiver prototypes or third generation of signal modulations.

Appendix A

Basics of satellite navigation systems

Contents

A.1 Satellite navigation systems 139
A.1.1 Different operating GNSS systems 139
A.1.2 GPS signal processing 141
A.1.3 Impact of urban environments on GNSS receivers 149
A.2 GNSS software receivers 151
A.2.1 GNSS Macro Rx 151
A.2.2 J-GNSS,[Arta 06] 152

A.1 Satellite navigation systems

With the emergence of new autonomous systems and the continuous evolution of the requirements made for precise positioning, integrity or availability, the market of global satellite navigation systems (GNSS) is in rapid mutation. The increase in performances of positioning systems allow to offer a wide range of new applications from civil engineering, to tourism, transportation or sports. To compete against the historical GPS *(Global Positioning System)* from the United States, many other nations, i.e. Europe, China, Russia, India and Japan, are now developing their own satellite navigation system for sovereignty reasons and to conquer new market shares. The acronym GNSS regroups all satellite positioning systems including regional services as for India or Japan. The main objective of such systems is to provide an estimated time and a worldwide position to the user.

In this section, the different operating GNSS systems are first described followed by the main signal processing steps dealing with modulations, triangulation principle and phase/code tracking processes. Note that a particular emphasis is made on GPS and European Galileo systems. The third subsection is dedicated to the impact of the urban environment on navigation devices.

A.1.1 Different operating GNSS systems

A.1.1.1 NAVSTAR, US

NAVSTAR system *(NAVigation System by Timing And Ranging)*, commonly called GPS, has been developed by the US DoF *(Department of Defence)* since 1973. Its main objectives were to provide three dimensional position, speed and time informations all over the world for US military needs. The first satellite was lunched in 1978 but the system was declared fully operational in 1994. Note that at this time, the cost of the first GPS receivers was about 150.000$. Even if designed for military purposes, the GPS system is now freely available for civil uses with a precision of about 13m in horizontal plane and 22m in the vertical plane with 95% confidence.

As for the majority of GNSS systems, the GPS lies on three segments, namely the space segment, the control segment and the user segment. The space segment represents the satellite

constellation in orbit around the Earth. It is composed of 30 satellites of generation IIA, IIR and IIR-M with at least 24 operational and 6 spare. The satellites are spread over 6 MEO orbits *(Medium Earth Orbit)* at approximatively 20.200km altitude with 55° inclination with respect to the equatorial plane. This repartition permits to optimise the probability to have at least four in sight satellites worldwide. Each satellite encompasses four atomic clocks, two based on Rubidium and two other on Caesium. The GPS system uses two frequencies bands, $L_1 = 1575.42$MHz and $L_2 = 1227.6$MHz broadcasting the navigation message discussed in the following and using a CDMA technique *(Code Division for Multiple Access)* to differentiate the satellites and a BPSK modulation. A third band, $L_5 = 1176.45$MHz, should be shortly used for safety services such as civil aviation.

The control segment, or ground segment, regroups all ground stations dedicated to the surveillance of the space segment, Fig.A.1. Each station has to collect informations from the space segment and send the informations to the master station in Colorado, US. Then, the master station controls satellites orbits, health, integrity, time shifts, ephemerids and other essential parameters of the system before broadcasting the corrections to the space segment by the intermediate of the other stations.

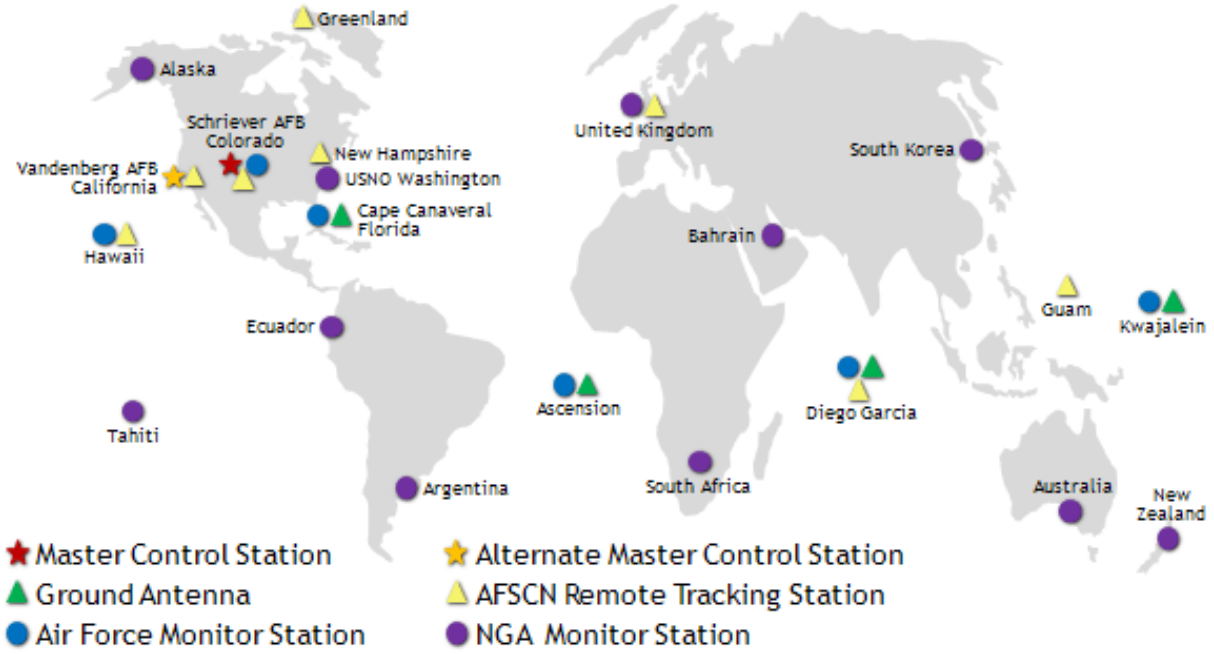

Figure A.1: GPS control segment [Offi 12]

GPS system handles two services: the standard positioning service (SPS) and the precise positioning service (PPS). The SPS is a positioning service available for any user across the world. It is based on a C/A code on L1 carrier frequency with a navigation message detailed in Section A.1.2.1. The PPS has been designed for military use only and delivers very precise positioning, time, and speed informations. It is encrypted by US DoF and restricted to US army and allied nations. It is based on a P code on L1 and L2 frequency bands.

The user segment represents all the users of the system, from military to civil. A common receiving architecture is based on parallel channel processing, where each channel is dedicated to the processing of one satellite.

A.1.1.2 Galileo, Europe

It is mainly for sovereignty reasons and to develop critical safety services that ESA *(European Space Agency)* involved itself in 2002 in the creation of new GNSS system: Galileo. This new

generation system, under civil regulation, permits to achieve highly accurate and guaranteed positioning services with redundancy, infrastructure upgrade and inter-operability services with GPS and GLONASS systems.

At the present date, Galileo system is at the *"In Orbit Validation"* (IOV) step with 2 test satellites (GIOVE-A and GIOVE-B) and 4 operational satellites of the IOV generation. By the end of 2015, the system should be composed of 16 satellites, *(Initial Operational Capability or IOC)* and deliver the first services. The final deployment should be reached by the end of 2019 with the FOC *(Final Operational Capability)* constellation composed by 27 satellites plus 3 spare. The satellites are spread over three orbital planes at 29.601km with 56° inclination with respect to the equatorial plane. As for other systems, Galileo uses a CDMA approach with BOC modulations. However, contrary to the others, Galileo has been enhanced to provide distress localisation and call features for the provision of the Search and Rescue service presented in the following.

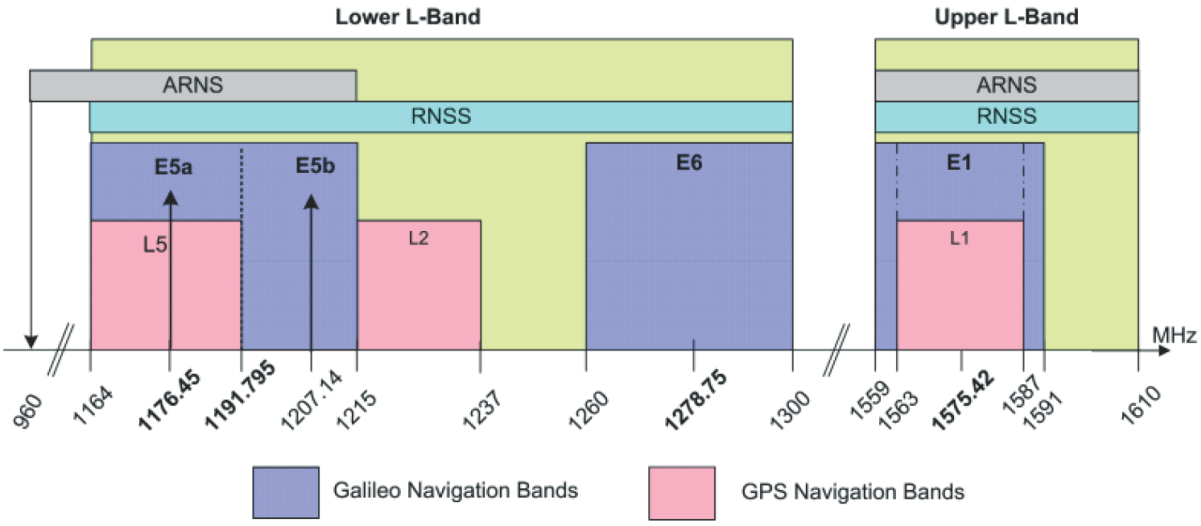

Figure A.2: Galileo frequency plan [Euro 10]

The ground segment is composed by two redundant GCC *(Galileo Control Center)* responsible of orbit management, time and integrity completed by many sensor stations spread all over the world. Those stations are responsible for the integrity of the signals at a regional scale (several countries) or local scale (city) for critical applications.

A.1.2 GPS signal processing

A.1.2.1 The signals

The L1-GPS signal can be spread into the sum of three modulated signals as presented in Eq.A.1 and illustrated in Fig.A.4 where A represents the amplitude of the signal.

$$s_{L1}(t) = \frac{A}{\sqrt{2}} D(t) \left(P(t) \cos(\omega_{L1}\, t) + C(t) \sin(\omega_{L1}\, t) \right) \tag{A.1}$$

- The Carrier L1/L2: carries the transmitted signal
- The navigation message D(t): contains all constellation informations for the positioning processing.
- The spreading codes C(t) and P(t): spreads the navigation message, identify each satellite and synchronise the receiver.

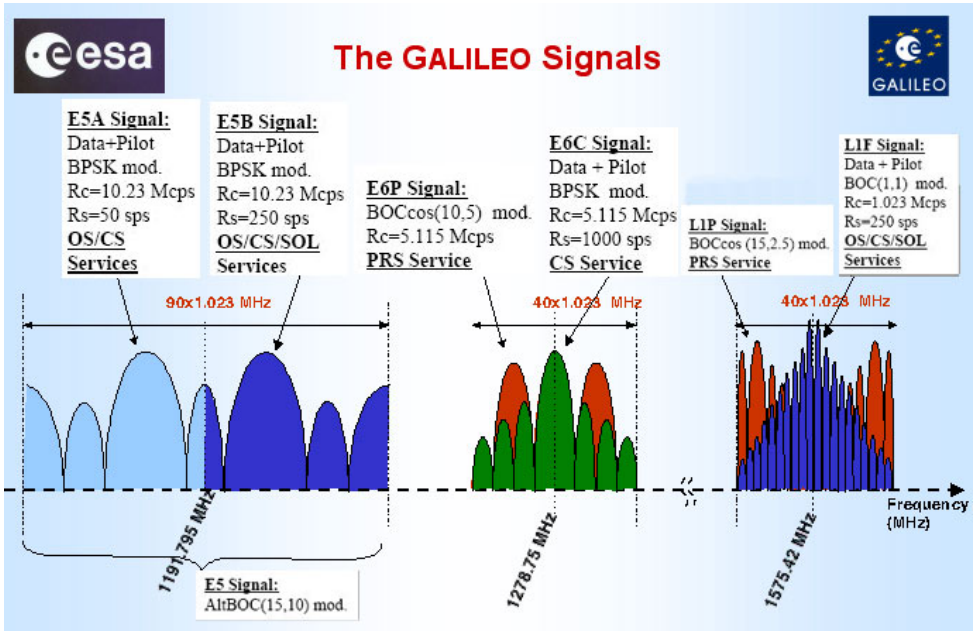

Figure A.3: Galileo spectrum

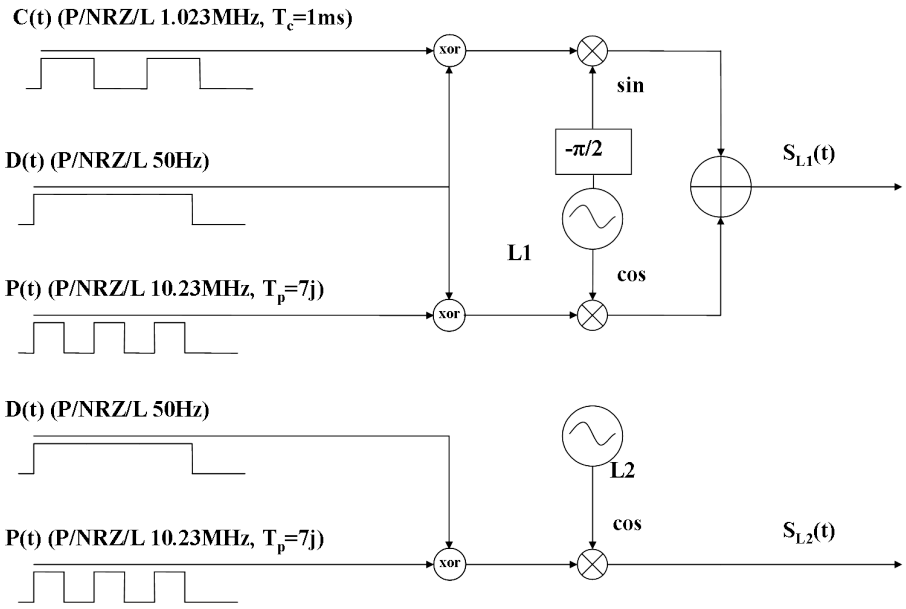

Figure A.4: GPS Modulation scheme

GPS system uses two carrier frequencies L1=1575.42MHz and L2=122760MHz. The L1 carrier frequency is modulated in phase by the P(Y) code and in quadrature by the C/A code. The L2 carrier frequency is modulated only by the P(Y) code. In the following, only L1 carrier frequency will be discussed since supporting the majority of civil applications.

The navigation message, broadcasted by each satellite, contains almanacs, ephemerids, health and correction informations of the transmitting satellite itself and for the rest of the constellation as detailed in Fig.A.5. The data rate is fixed to 50bps.

Using a CDMA approach, each satellite is transmitting its navigation message at the same frequency. To differentiate them, a unique PRN *(Pseudo-Random Noise)* spreading sequence is used by each satellite. Since those sequences are known by the receiver, a correlation process, detailed in the code tracking section, allows the receiver to isolate each satellite from the others

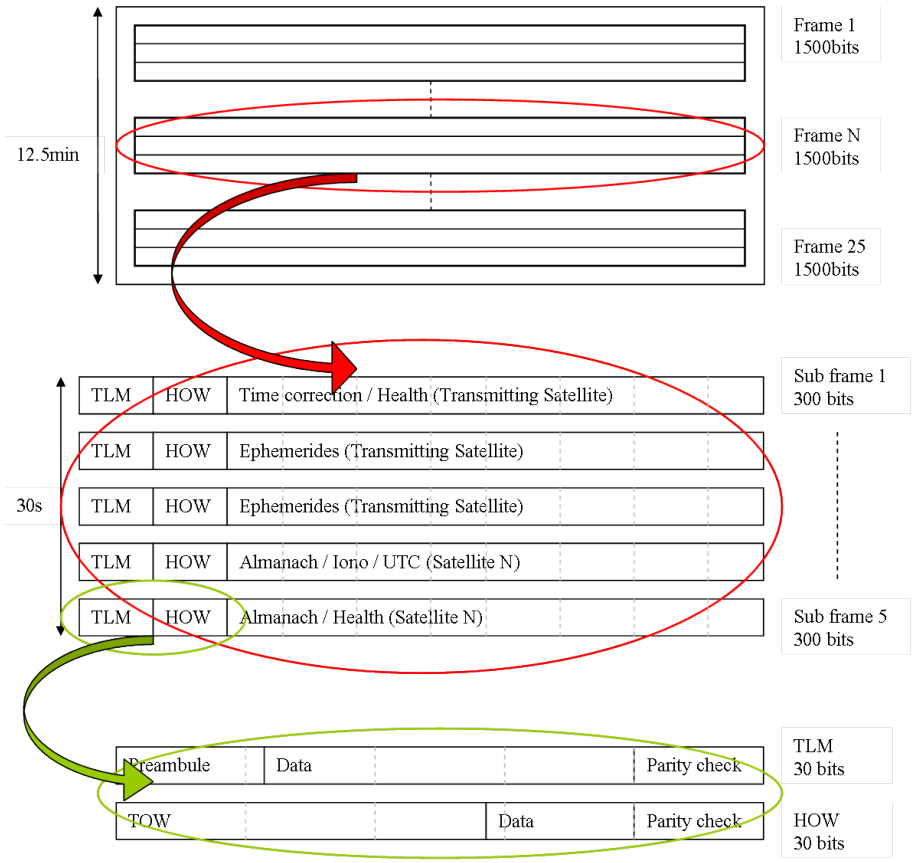

Figure A.5: Decomposition of GPS navigation message

and decode its navigation message. This spreading sequence is also involved in the code tracking process for precise positioning.

Two spreading codes are used by the GPS system: C/A code *(Coarse Acquisition)* and P code encrypted by Y code, also called P(Y) code. The P(Y) code is restricted to military uses and not detailed in the following. The C/A code is a binary sequence of length 1023 chips, belonging to the Gold code family [Misr 10], broadcasted at 1.023Mcps. The time duration of the sequence is 1ms and is unique for each satellite. The specificity of the Gold codes is their almost orthogonality property which allows to achieve almost null inter-correlation between two different codes as visible in Fig.A.6. Note that the C/A code received on Earth surface is about -160dBW, well under the receiver noise. The correlation process permits to compress the transmitted spread signal to remove noise and identify the satellite. In the case of C/A code, the unspreading gain is +43dB.
Due to spectrum allocation restrictions for GNSS systems, signals from different constellations may coexist in the same frequency band such as GPS and Galileo on L1. To minimise the risk of mutual interferences, new modulations have been defined and which spectrums are as far as possible from the pre-existing signals. For this purpose, BOC *(Binary Offset Carrier)* modulations have been created. The principle of BOC(f_s,f_c) modulations is to multiply the original code $C(t)$ of frequency f_c (BPSK modulation) by a square sub-carrier of frequency f_s as presented in Eq.A.2. The main consequence of this modulation is that the power spectral density is split into two parts at $\pm f_s$ with $2\,f_c$ lobe width. This technique permits to use the same frequency bands and allows inter-operability between various systems in the same receiving equipment.

$$C_{BOC(p,q)}(t) = c(t)\, sign\left(\sin\left(2\pi f_s t\right)\right) \tag{A.2}$$

In practice, the BOC modulations are named BOC(p,q) where p and q are multiples of the C/A chip rate (1.023Mcps). For Galileo open services, a hybrid CBOC modulation *(Composite*

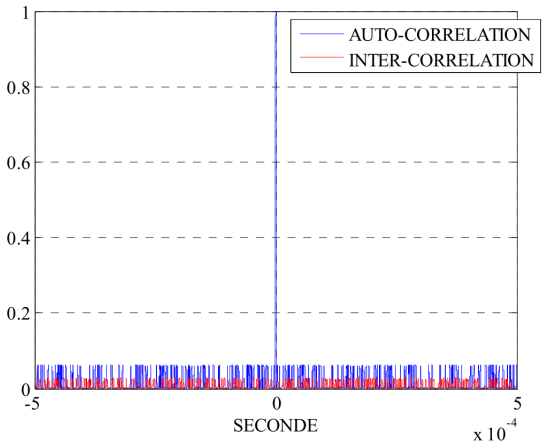

Figure A.6: Auto-correlation and inter-correlation functions between two different C/A codes [Roug 12]

Binary Offset Carrier), combining BOC(1,1) and BOC(6,1), is used as presented in Eq.A.3 where $G_{CBOC(p,q)}(f)$ represents the power spectral density of CBOC signal.

$$G_{CBOC(p,q)}(f) = \frac{10}{11} G_{BOC(1,1)}(f) + \frac{1}{11} G_{BOC(6,1)}(f) \tag{A.3}$$

Note that BPSK or BOC modulations have a direct impact on the autocorrelation function of the sinal as visible in Fig.A.10 where C/A is a BPSK signal and BOC(10,5) and BOC(1,1) are BOC signals. Due to this difference on the autocorrelation function shape, the retained modulation has a strong impact on the code tracking process, since the central peak is narrower, and on pseudo-range error envelopes, BOC signals have secondary peaks.

A.1.2.2 Architecture of a standard GPS receiver

The role of a GNSS receiver is to deliver time, position and speed informations to the user. Note that the reference point is the receiving antenna. To do so, the receiver has to perform several signal processing operations to demodulate the radio signals emitted from the satellites, differentiate them, decode the navigation data and perform the PVT *(Position Velocity Time)* computation. During this process the receiver passes through the following steps :

- Identification of visible satellites
- Acquisition
- Demodulation
- Phase carrier tracking
- Code tracking
- Data extraction
- Navigation message interpretation and PVT

From those collected data, the receiver performs the PVT by using the triangulation principle described hereafter.

A.1.2.3 PVT and triangulation principle

The triangulation process is the last operation made by the receiver. Its principle is common to all GNSS systems where the critical information is the distance separating the satellite from the receiver. This ranging technique lies on the ToA *(Time of Arrival)* principle which consists in

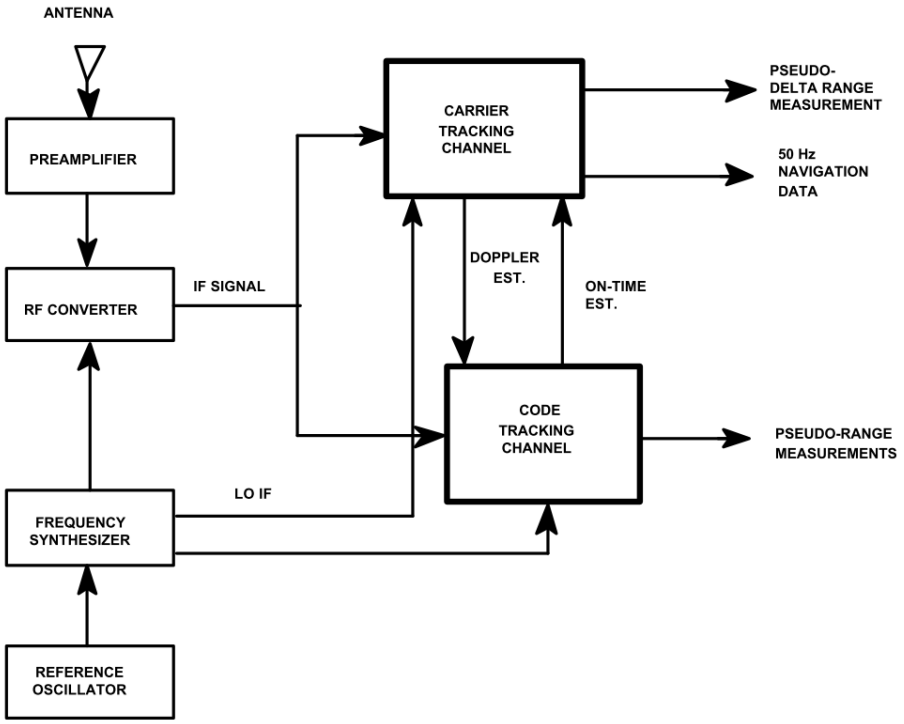

Figure A.7: GPS Signal processing principle [NAVS 96]

measuring the flying time of wave fronts from the transmitter to the receiver. The triangulation principle is the following: by measuring distances and radial speed of some satellites (supposed known trajectories), the receiver can estimate its position and its speed. Note that this distance is called pseudo-range due to synchronisation issues at the receiver discussed in the following. For receiver speed estimation, Doppler estimation techniques are used (PLL).

In the case of a perfect synchronisation between all satellites and the receiver, and for a perfect measure of the pseudo-range ρ_i, the three dimensional position problem can be solved by using three satellites. Then, the mobile will be at the intersection of the three spheres which centers are each satellite and with radius ρ_i. In practice, residual measure errors, ϵ_i, persist and since no atomic clock are embedded into the receiver, the synchronisation is not perfect. Those defaults are presented in Eq.A.4. A time bias Δt is then introduced at the receiver side. Due to this, a fourth satellite has to be considered to solve the three dimensional problem plus the unknown time reference as illustrated in Fig.A.8. Note that a time synchronisation error of 1ns represents 3m in pseudo-range errors.

$$\rho_i = \tau_i \, c = \sqrt{(x - x_i)^2 + (y - yi)^2 + (z - z_i)^2} + c\,\Delta t + \epsilon_i \tag{A.4}$$

The triangulation process leads to PVT computation. Its precision is function of several factors such as ephemerids errors, time errors, atmospheric errors, noise at the receiver or multipaths. The ephemerids errors are corrected by the ground segment which makes precise measurements of satellite position and broadcasts corrections to the space segment. The time error is now very low since four atomic clocks are embedded in the new generation satellites. The ionospheric and tropospheric errors can be corrected by using correction function based on meteorological models or deducted from dual frequency use (L1+L2). The receiver noise can be highly reduced by improving electronic components. At the end, the main sources of errors are multipaths which are caused by the environment close to the receiver and discussed in Section A.1.3.

A.1.2.4 Acquisition step

The acquisition step is the first signal processing operation made by the receiver. It allows to synchronise roughly the receiver to each satellite. The goal is to have a first estimate of the

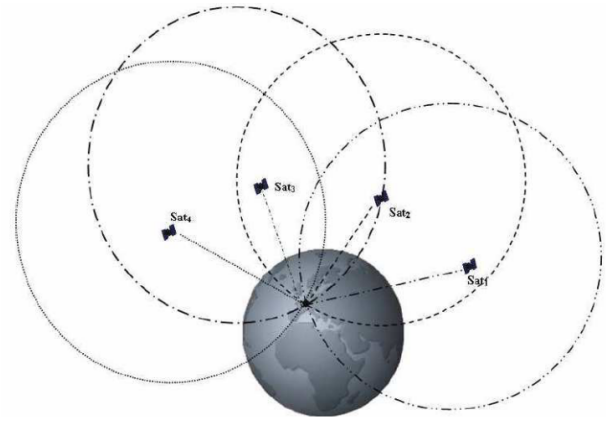

Figure A.8: Triangulation principle [Nahi 09]

Doppler shift due to satellite and receiver motion and of the approximative delay due to the signal propagation from the satellite to the receiver. This approximated delay corresponds to the phase of the C/A code plus the distance ambiguity resolved after extracting the navigation message. During the acquisition operation, th phase of the code is known with one chip precision corresponding to $0.977\mu s$, corresponding to 300m. The distance ambiguity corresponds to the length of the C/A code which have a 1ms period, corresponding to 300km at the speed of light. To increase the precision of the pseudo-range estimation, a code tracking loop has to be used to obtain a precision under the chip resolution. This process is decribed in the following. The reader is reminded that since spreading sequences are used, the received power is lower than the noise as previously mentioned. To reveal the useful signal, a correlation operation has to be performed on the received signal.

In the case of a cold start, the receiver starts to seek every possible satellite without a priori informations in a delay/Doppler space. In the case of a hot start, the receiver has already an a priori information on the state of the constellation which highly reduces the research time *(Time To First Fix or TTFF).*

During the acquisition step, the receiver is going to look into a delay/Doppler grid to find a correlation pic identifying the satellite. One example is given in Fig.A.9 and extracted from Al-Bitar work dealing with fast acquisition techniques. The seeking space is usually sampled every $Tc/2$ in de delay space and every $Tint/2$ in the Doppler space where Tc=1μs represents one C/A chip duration and Tint=20ms represents the integration time also equals to the navigation data rate.

At the end of the acquisition step, the received signal is almost synchronised and phase and code tracking processes can start. Their respective objective is to keep track precisely of the carrier phase and the code phase.

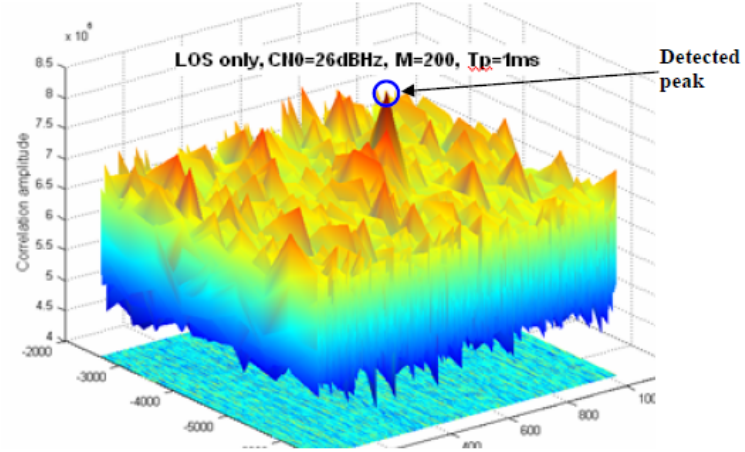

Figure A.9: Estimation of delay and Doppler during acquisition step [Al B 07b]

A.1.2.5 Phase tracking

The PLL *(Phase Lock Loop)* enables to enslave an internal oscillator to an external reference, the received signal. In GPS signal processing, in a lock state, the PLL keeps track of the carrier frequency, plus the Doppler offset. This synchronisation step is necessary before performing the code tracking and the demodulation process of the navigation message. If the PLL unlocks itself, a new acquisition step has to be performed on the lost satellite. The PLL is composed by a phase discriminator, a loop filter and a controlled oscillator. The precision of the PLL depends on the phase discriminator and on the loop filter but is roughly in the order of few Hertz.

A.1.2.6 Code tracking

The code tracking process is based on the correlation technique which quantifies the similarity between two signals. This method is widely used in GNSS processing to identify the satellites and determine the delay of the received code prior to perform the PVT computation. The inter-correlation function between two signals is given by Eq.A.5 where Rc represents the inter-correlation of two codes depending on the time offset τ, T_{int} is the integration time, $c(t)$ the received code and $c'(t)$ the locally generated code replica. Fig.A.10 presents some auto-correlation functions for different signal shapes (C/A and BOCs).

$$R_c(\tau) = \frac{1}{T_{int}} \int_{t_0}^{t_0+T_{int}} c(t)\, c'(t-\tau) d\tau \tag{A.5}$$

The maximum of the auto-correlation is reached when both codes are in phase (relative delay $\tau = 0$). The goal of the code tracking process, also called DLL *(Delay Lock Loop)*, is to keep the two sequences aligned. As for the PLL, the DLL is made of one discriminator, one loop filter and one controlled oscillator. The discriminator function is based on the result of three correlators to estimate the correction to be applied to keep tracking the received code. The three correlators are called *Early*, *Prompt* and *Late* since they are placed slightly before the synchronised maximum, on the synchronised maximum and slightly after the synchronised maximum. The goal of the discriminator is to keep aligned the Early and Late replicas so that the Prompt is always synchronised on the maximum of the inter-correlation function as illustrated in Fig.A.11. For typical value indications, the Early and Late replicas are both 0.5 chip spaced from the Prompt in wide-correlators. In the case of narrow-correlators, Early and Late replicas are spaced by 0.1 chip which reduces the impact of multipath but makes the discriminator more sensitive to noise.

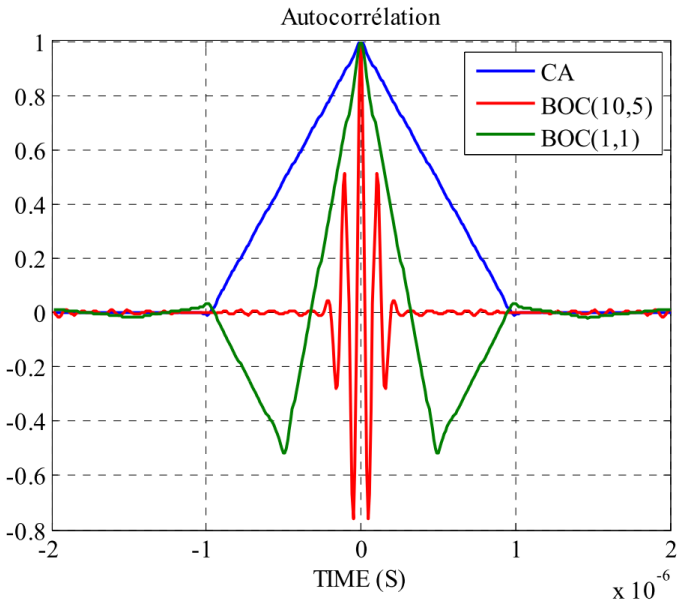

Figure A.10: Example of auto-correlation functions for different signals [Roug 12]

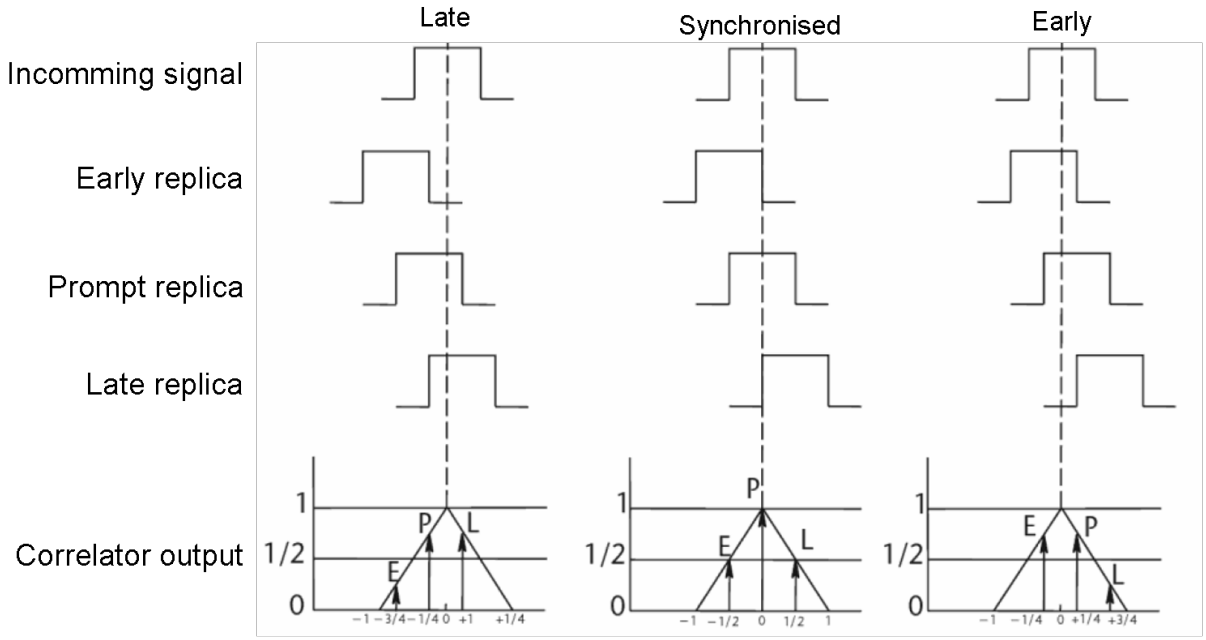

Figure A.11: Synchronisation principle using Early Prompt Late signal replicas [Kapl 05]

Several discriminators are commonly used in the literature as presented in Eq.A.6 to Eq.A.8 [Kapl 05]. Note that each discriminator has his own advantages and their responses to different input errors are different as illustrated in Fig.A.12.

$$D_{Dot\,product\,power} = \sum (I_E - I_L)\, I_P + \sum (Q_E - Q_L)\, Q_P \tag{A.6}$$

$$D_{Early\,minus\,late\,power} = \sum \left(I_E^2 + Q_E^2\right) - \sum \left(I_L^2 + Q_L^2\right) \tag{A.7}$$

$$D_{Early\,minus\,late\,envelope\,normalised} = \frac{\sum \sqrt{I_E^2 + Q_E^2} - \sum \sqrt{I_L^2 + Q_L^2}}{\sum \sqrt{I_E^2 + Q_E^2} + \sum \sqrt{I_L^2 + Q_L^2}} \tag{A.8}$$

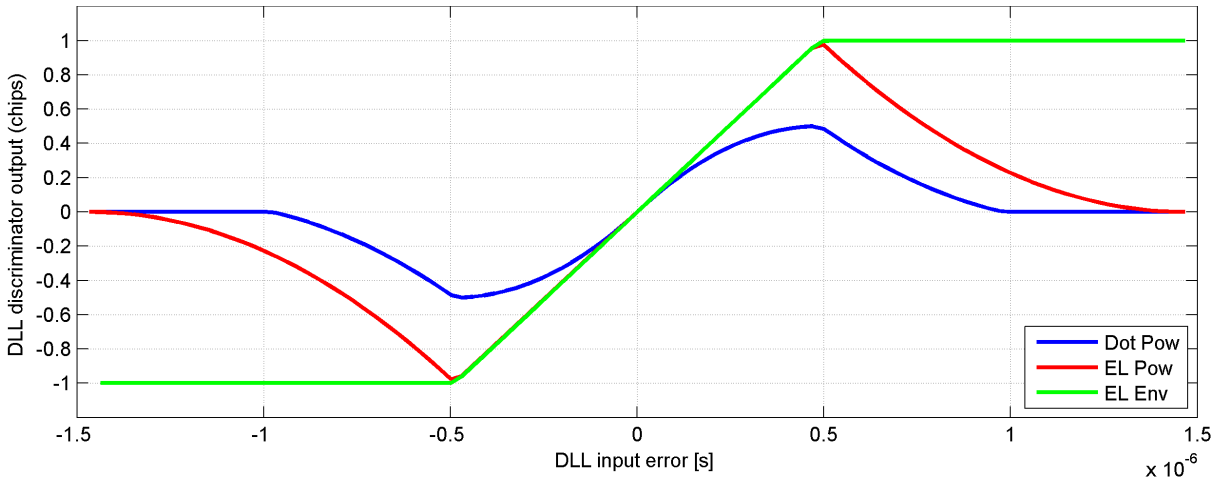

Figure A.12: Discriminator outputs versus of input errors (S curve)

A.1.3 Impact of urban environments on GNSS receivers

Designed for operating in LOS *Line Of Sight* conditions, GNSS receiver performances are highly impacted by the environment close to the mobile receiver. Several types of environments can be met. In rural environments, with sporadic habitations, farmlands and some vegetation, many satellites in sight are usually availables, allowing a precise positioning. In urban environments, the LOS signals are usually blocked by the closest buildings near the receiver which reduce highly the number of available satellites and impact the position precision. Even more, those buildings are also acting like mirrors on which the signal experiences multiple reflections and diffractions before reaching the receiver. Those signal replicas are called multipath (MP) and disrupt highly the tracking processes and the PVT computation as presented in the following. One last environment encountered by GNSS receivers is the indoor environment. Similarly to urban environments, a clear LOS is almost never achieved, multiples interactions are common and the received power is even lower compared to outdoor scenarios since wave fronts have to cross several material layers while entering the buildings. In the following, only outdoor environments will be considered with a particular focus on urban environments since they are the most challenging.

A.1.3.1 Impact of urban building blockage

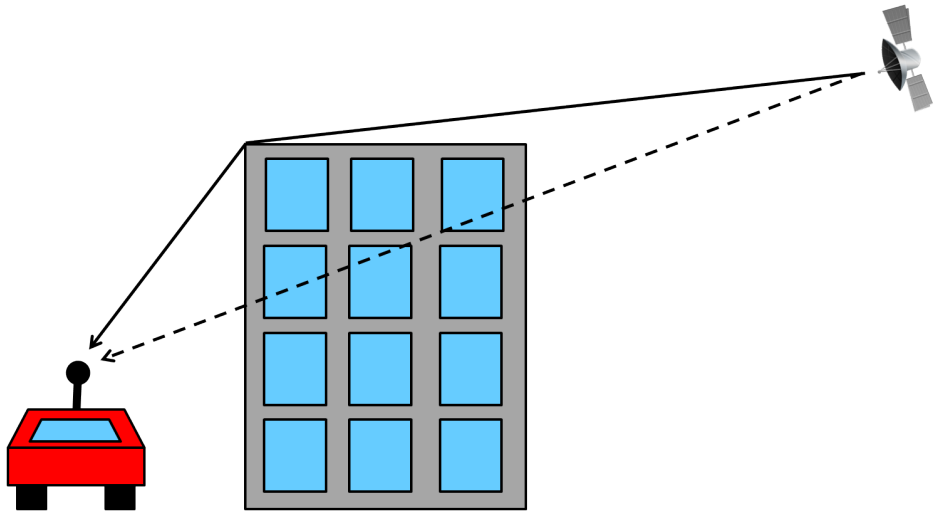

Figure A.13: Principle of building blockage

One of the main issues for satellite navigation systems in urban environments is the lack of satellites in sight, where at least four satellites are required to perform the PVT computation. This lack of availability can be illustrated by the case of dense habitation environments, with high buildings and narrow streets, where the satellite constellation is widely masked by the surrounding facades. Occurring during the acquisition step, this scenario would be the worst and the receiver might never find four satellites to track. In a more common scenario, the receiver is already tracking satellites when momentarily blockage occur which finally unlock the tracking loops and force the receiver to re-acquire the satellite. In a favorable case, the diffraction taking place on top of the surrounding buildings may be sufficient for the receiver to keep track of the satellites. In this case, the received path distance is longer than the LOS signal, thus biasing the pseudo-distance and the PVT computation.

One solution to overcome the satellite availability issue is to optimise the satellite constellation to maintain high elevation satellites available for the receiver. This is the case of the previously presented QZSS system. Note that even if four satellites are visible, their geometrical configuration is not optimum, resulting in high DOP *(Dilution Of Precision)* coefficients and lower positioning accuracy.

A.1.3.2 Impact of urban multipaths

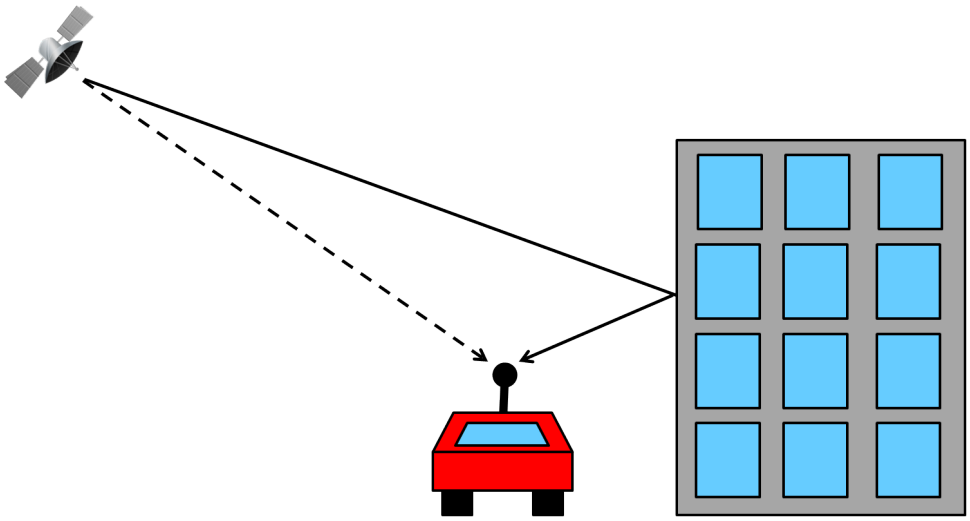

Figure A.14: Principle of urban multipath

One multipath can be described as an attenuated, delayed and phase shifted replica of the original signal. The multipaths are originated from multiple interactions taking place on the environment surrounding the receiver (buildings, trees, cars, ...). Several propagation mechanisms are responsible of multipath, namely diffraction, scattering, reflections and their multiple combination. Multipaths are hard to predict, time varying even at small scale and site related (receiver position, transmitter position, surrounding environment).

Their main impact on GNSS receivers is due to their coherent behaviour. Indeed, multipaths are *real* copies of the original signal and a conventional receiver is not able to differentiate the LOS from the MPs. Lets assume one single constant multipath of 0.7 relative amplitude, 0° phase shift and 0.5 chip delay as presented in Fig.A.15. As visible, the sum of both signals (red) modifies the correlation function shape which is no more a triangular function as for LOS and MP taken separately. This shape modification turns out to modify the synchronisation process as visible on the S curve plot. The result is a synchronisation error also visible as a geometric bias in the pseudo-range estimation conducting to PVT errors.

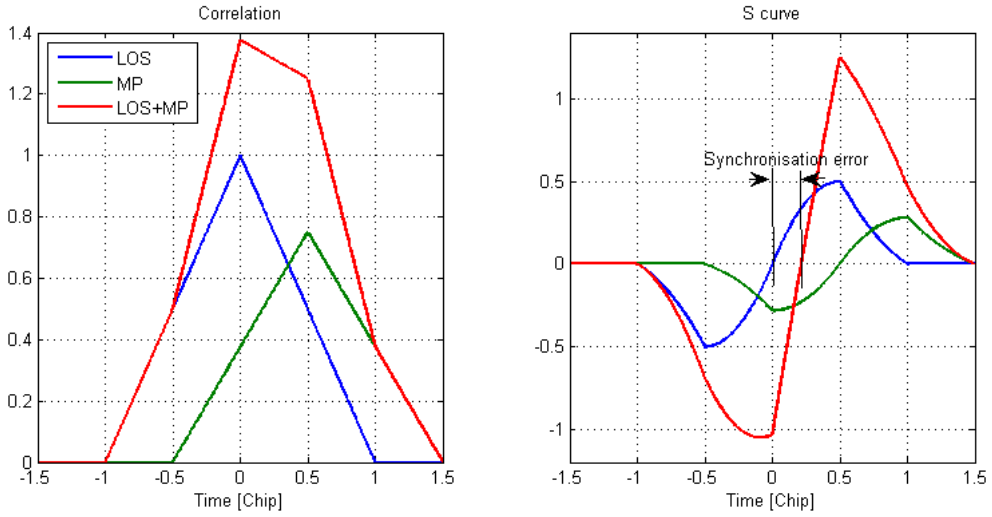

Figure A.15: Impact of the multipath on the correlation function and on synchronisation processing

In the case of one single and constant MP, the synchronisation error is function of the MP power, delay, phase shift and Doppler. Fig.A.16a represents the error envelope made for different powers and delays of one single multipath. Fig.A.16b represents the error envelope made for different phase shifts and delays of one single multipath. Note that in phase and in quadrature cases are the worsts and bound the error envelope.

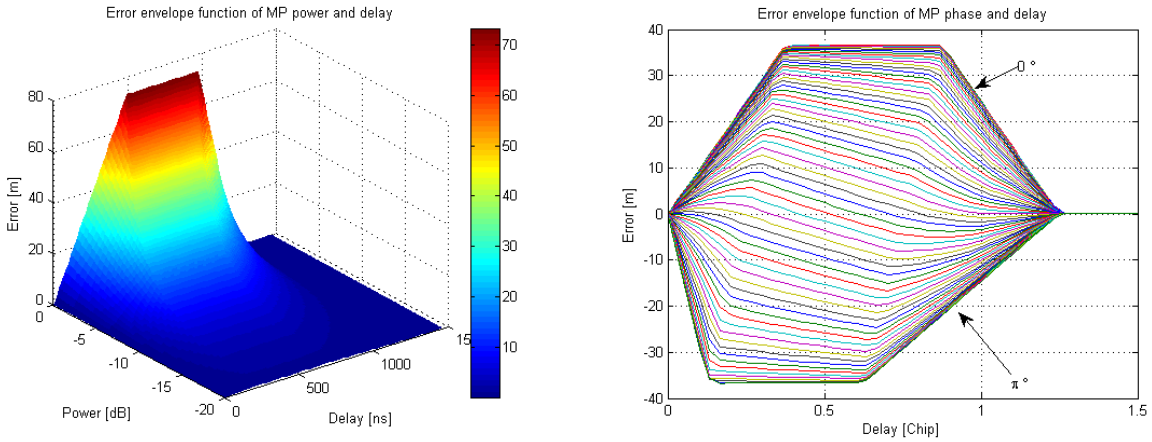

(a) Power/delay space

(b) Phase/delay space

Figure A.16: Influence of power, delay and phase of one constant multipath on the pseudo-range error estimation

A.2 GNSS software receivers

A.2.1 GNSS Macro Rx

The simplified GNSS receiver used in this study was developed by the French Space Agency, CNES. It aims at reproducing the various internal processes of a typical receiver in a simplified way in order to estimate pseudo-range errors. The simplifications are mainly based on the fact that the receiver operates directly on post-correlation synthetic data instead of operating on baseband synthetic data. Hence, the standard C/A GPS code [Park 96] is here modelled as a simple triangular function representing the autocorrelation of the PRN code. Then, in the

presence of multipath, the overall correlation function is constructed by combining the complex delayed correlation functions due to each individual MP. The DLL is implemented as a dot-product discriminator followed by a first-order loop filter [Kapl 05]. Typical values of the input parameters are given next. The *early* and *late* replicas of the local code are separated by 0.25 chips from the *prompt*, and the DLL noise bandwidth is set to 10 Hz. The output of the PLL is emulated assuming noise-free conditions, and then, the phase noise is added to the *prompt* signal using randomly generated samples whose standard deviation corresponds to that of a Costas PLL with 1 Hz noise bandwidth. The tracking time is set to 20 ms.

Two input files are required: the first one contains the receiver parameters and the second one is devoted to the channel characteristics. The channel file contains several parameters such as the time of week, the navigation data, the ionospheric delay or the number of MP. Each path, including the direct signal, is defined considering its power, phase, delay and Doppler. Power and phase parameters are given relative to the direct signal. The output file gathers the pseudo-range error, the tracked phase and the demodulated navigation data. Note that an acquisition step is performed by the receiver but all the simulations presented in the following have been realised assuming that the receiver was in the *locked* state. The thermal noise level was assumed to be -202dB/Hz and the direct signal power -153 dBW.

A.2.2 J-GNSS,[Arta 06]

Software receivers proved to be powerful tools for research and development. They provide access to low level functionalities of GNSS receiver allowing rapid testing of new signal processing algorithms and evaluation of upcoming GNSS signals. Silicom has developed for the CNES a software receiver based on the open source tool Juzzle (www.juzzle.org). The Juzzle software receiver is written in C ANSI and is multi-platform. Its architecture is organized around libraries and functional blocks. They include the basic functionalities that have been identified by exploiting the commonalities between the GNSS signals. The receiver can process simulated signal as well as real IF samples recorded by RF equipment. The different modules of the simulator include the receiver performing signal acquisition and tracking; and signal generation, propagation channel and RF stage emulation in order to simulate signals, and binary file reader for post processing of recorded signals. The Juzzle simulator can be seen as a toolbox providing basic building blocks needed to create a navigation system.

During this study, the GNSS Macro Rx receiver has been used mainly for extensive simulation purposes (statistical analysis made in Chapter 3) while JGNSS has been used during the validation step (Chapter 4) to process digitised measured data.

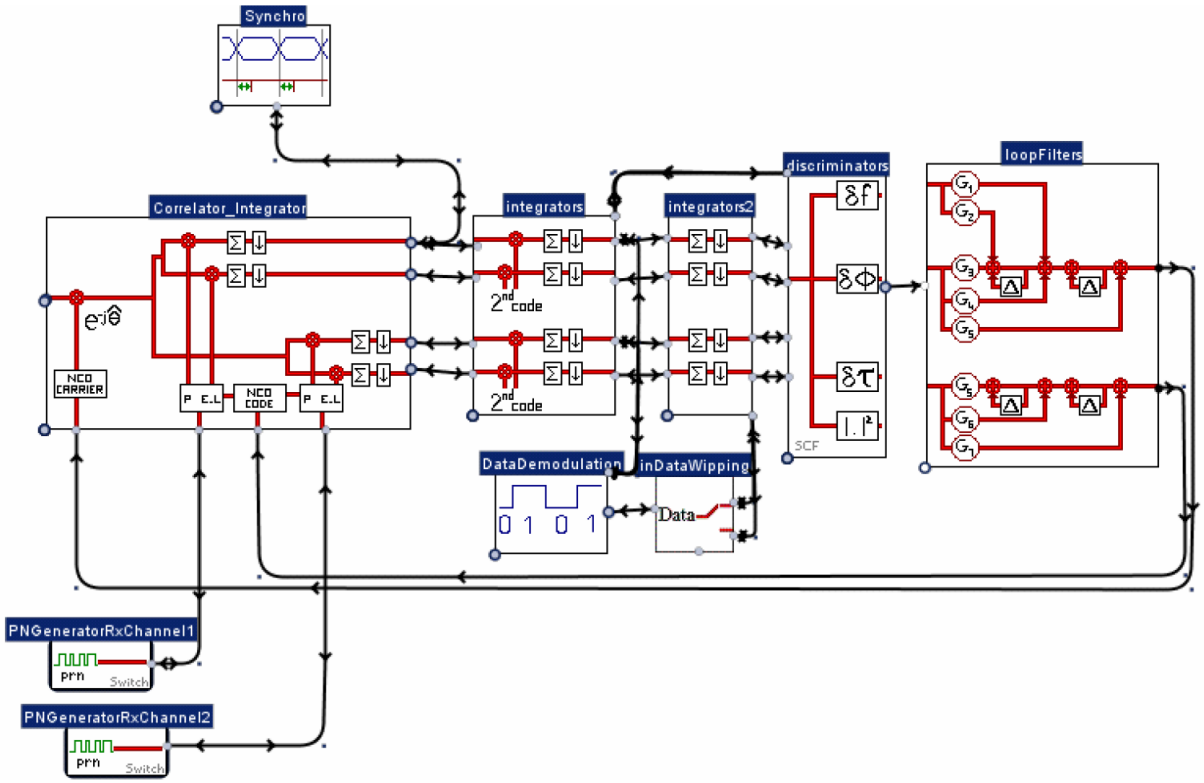

Figure A.17: Tracking architecture of JGNSS software receiver [Arta 07]

Appendix B

Basics of EM numerical methods

Contents

B.1 Current-based asymptotic methods 155

B.1.1 The Physical Optics algorithm 155

B.2 Ray-based asymptotic methods 158

B.2.1 Two ray-based algorithm 158

B.2.2 The Uniform Theory of Diffraction 160

B.3 Electromagnetic reference codes 163

B.3.1 Elsem3D based on MOM 163

B.3.2 SE-WorkBench software suite based on asymptotic methods 163

B.1 Current-based asymptotic methods

B.1.1 The Physical Optics algorithm

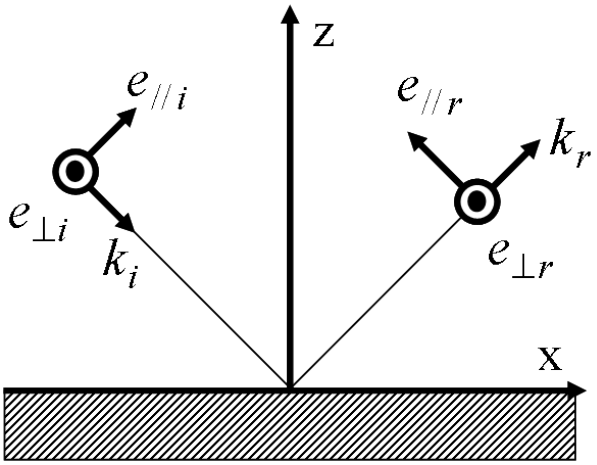

Figure B.1: Chosen convention for incident and reflected bases [Bala 89]

Let $\mathbf{E^{inc}}$ be the incident polarised E field expressed in the global base following θ and ϕ directions. Let $\mathbf{E^{inc'}}$ be the incident polarised E field projected into the plate base. Let $\hat{\mathbf{n}}$ be the normal to the plate following the Z axis. The incidence convention is presented in Fig.B.1 where $\hat{\mathbf{k_i}}$ is in the $-XZ$ plane. The dimension of the plate a and b following Y and X axis respectively. Let

$\mathbf{E^i}$ be the incident polarised E filed projected in the incident polarisation base of the plate.

$$E_0 = \frac{\sqrt{60.EIRP}}{|\mathbf{r_1}|} \tag{B.1}$$

$$\mathbf{E^i} = E_0 \left(\hat{\mathbf{e}_{//}}^i + \hat{\mathbf{e}_{\perp}}^i\right) e^{-\jmath \hat{\mathbf{k_i}} \mathbf{r_1}} \tag{B.2}$$

$$\hat{\mathbf{e}_{\perp}^{\mathbf{i}}} = \frac{\hat{\mathbf{k_i}} \wedge \hat{\mathbf{n}}}{|\hat{\mathbf{k_i}} \wedge \hat{\mathbf{n}}|} \tag{B.3}$$

$$\hat{\mathbf{e}_{//}^{\mathbf{i}}} = \hat{\mathbf{e}_{\perp}^{\mathbf{i}}} \wedge \hat{\mathbf{k_i}} \tag{B.4}$$

Let $\mathbf{E^r}$ be the reflected polarised E filed in the reflected polarisation base of the plate.

$$\mathbf{E^r} = R_{//} \mathbf{E^i}.\hat{\mathbf{e}_{//}}^r + R_{\perp} \mathbf{E^i}.\hat{\mathbf{e}_{\perp}}^r \tag{B.5}$$

In a similar way, H fields $\mathbf{H^i}$ and $\mathbf{H^r}$ are computed

$$H_0 = \frac{E_0}{Z0} \tag{B.6}$$

$$\mathbf{H^i} = H_0 \left(\hat{\mathbf{e}_{//}}^i + \hat{\mathbf{e}_{\perp}}^i\right) e^{-\jmath \hat{\mathbf{k_i}} \mathbf{r_1}} \tag{B.7}$$

$$\mathbf{H^r} = R_{\perp} \mathbf{H^i}.\hat{\mathbf{e}_{//}}^r + R_{//} \mathbf{E^i}.\hat{\mathbf{e}_{\perp}}^r \tag{B.8}$$

The coefficients $R_{//}$ and $R_{\perp}$ represent the Fresnel coefficients. In the case of a perfect electric conductor they are equal to 1 and -1 respectively. In the case of dielectric materials, they are computed as follow:

$$R_{//} = \frac{Z0 \cos(\theta_i) - Z_1 \cos(\theta_t)}{Z0 \cos(\theta_i) + Z_1 \cos(\theta_t)} \tag{B.9}$$

$$R_{\perp} = \frac{Z_1 \cos(\theta_i) - Z0 \cos(\theta_t)}{Z_1 \cos(\theta_i) + Z0 \cos(\theta_t)} \tag{B.10}$$

$$Z0 = 120\pi \tag{B.11}$$

$$Z_1 = \sqrt{\frac{\jmath 2\pi f \mu_r}{\sigma + \jmath 2\pi f \epsilon_r}} \tag{B.12}$$

$$\cos(\theta_t) = \sqrt{1 - (\beta_0/\beta_1) \sin(\theta_i)^2} \tag{B.13}$$

$$\beta_0 = 2\pi f \sqrt{\mu_0 \epsilon_0} \tag{B.14}$$

$$\beta_1 = 2\pi f \sqrt{\epsilon_r \mu_r} \sqrt{\frac{1}{2} \sqrt{1 + \left(\frac{\sigma}{2\pi f \epsilon_r}\right)^2} + 1} \tag{B.15}$$

Let $\mathbf{E^t}$ and $\mathbf{H^t}$ be the tangentials fields over the surface of the plate. They are defined as follow:

$$\mathbf{E^t} = \mathbf{E^i} + \mathbf{E^r} \tag{B.16}$$

$$\mathbf{H^t} = \mathbf{H^i} + \mathbf{H^r} \tag{B.17}$$

$$\tag{B.18}$$

Let $\mathbf{J}$ be the electric surface currents and $\mathbf{M}$ the magnetic surface currents. They are defined as follow:

$$\mathbf{J} = \hat{\mathbf{n}} \wedge \mathbf{H^t} \tag{B.19}$$

$$\mathbf{M} = \mathbf{E^t} \wedge \hat{\mathbf{n}} \tag{B.20}$$

$$\tag{B.21}$$

Those currents are expressed in the plate base.

Let N and L be the radiation integrales which allow to compute the radiated fields.

$$\begin{aligned}
\mathbf{N} &= \iint_S \mathbf{J}\, e^{\jmath\beta r' \cos\psi} ds' && \text{(B.22)}\\
&= \iint_S \left(\hat{\mathbf{a}}_x J_x + \hat{\mathbf{a}}_y J_y + \hat{\mathbf{a}}_z J_z\right) e^{\jmath\beta r' \cos\psi} ds' && \text{(B.23)}\\
\mathbf{L} &= \iint_S \mathbf{M}\, e^{\jmath\beta r' \cos\psi} ds' && \text{(B.24)}\\
&= \iint_S \left(\hat{\mathbf{a}}_x M_x + \hat{\mathbf{a}}_y M_y + \hat{\mathbf{a}}_z M_z\right) e^{\jmath\beta r' \cos\psi} ds' && \text{(B.25)}\\
& && \text{(B.26)}
\end{aligned}$$

Let $\mathbf{E^s}$ and $\mathbf{H^s}$ be the electric and magnetic fields scattered in any direction. Those fields are expressed in the receiver polarisation base:

$$\begin{aligned}
\mathbf{E^s} &= E_\theta \hat{\theta}^s + E_\phi \hat{\phi}^s && \text{(B.27)}\\
\mathbf{H^s} &= H_\theta \hat{\theta}^s + H_\phi \hat{\phi}^s && \text{(B.28)}
\end{aligned}$$

The radiation integrales are then projected into the receiver polarisation base:

$$\begin{aligned}
N_\theta &= \iint \left(\hat{\theta}^s \cdot \mathbf{J}\right) e^{\left(\hat{\mathbf{k_s}} - \hat{\mathbf{k_i}}\right) \wedge \hat{\mathbf{n}}} ds' && \text{(B.29)}\\
N_\phi &= \iint \left(\hat{\phi}^s \cdot \mathbf{J}\right) e^{\left(\hat{\mathbf{k_s}} - \hat{\mathbf{k_i}}\right) \wedge \hat{\mathbf{n}}} ds' && \text{(B.30)}\\
L_\theta &= \iint \left(\hat{\theta}^s \cdot \mathbf{M}\right) e^{\left(\hat{\mathbf{k_s}} - \hat{\mathbf{k_i}}\right) \wedge \hat{\mathbf{n}}} ds' && \text{(B.31)}\\
L_\phi &= \iint \left(\hat{\phi}^s \cdot \mathbf{M}\right) e^{\left(\hat{\mathbf{k_s}} - \hat{\mathbf{k_i}}\right) \wedge \hat{\mathbf{n}}} ds' && \text{(B.32)}
\end{aligned}$$

In the case of a rectangular plate, the surface integral can be analytically converted into the sinc function. The radiation equations become:

$$\begin{aligned}
N_\theta &= a\, b \left(\hat{\theta}^s \cdot \mathbf{J}\right) sinc\left(\xi \cdot \hat{\mathbf{a}}_x\right) sinc\left(\xi \cdot \hat{\mathbf{a}}_y\right) && \text{(B.33)}\\
N_\phi &= a\, b \left(\hat{\phi}^s \cdot \mathbf{J}\right) sinc\left(\xi \cdot \hat{\mathbf{a}}_x\right) sinc\left(\xi \cdot \hat{\mathbf{a}}_y\right) && \text{(B.34)}\\
L_\theta &= a\, b \left(\hat{\theta}^s \cdot \mathbf{M}\right) sinc\left(\xi \cdot \hat{\mathbf{a}}_x\right) sinc\left(\xi \cdot \hat{\mathbf{a}}_y\right) && \text{(B.35)}\\
L_\phi &= a\, b \left(\hat{\phi}^s \cdot \mathbf{M}\right) sinc\left(\xi \cdot \hat{\mathbf{a}}_x\right) sinc\left(\xi \cdot \hat{\mathbf{a}}_y\right) && \text{(B.36)}\\
\xi &= \left(\hat{\mathbf{k_s}} - \hat{\mathbf{k_i}}\right) \wedge \hat{\mathbf{n}} && \text{(B.37)}
\end{aligned}$$

Finally, $\mathbf{E^s}$ and $\mathbf{H^s}$ components are the following:

$$\begin{aligned}
E_r &\simeq 0 && \text{(B.38)}\\
E_\theta &\simeq -\frac{\jmath\beta e^{-\jmath kr}}{4\pi r}\left(L_\phi + Z0 N_\theta\right) && \text{(B.39)}\\
E_\phi &\simeq +\frac{\jmath\beta e^{-\jmath kr}}{4\pi r}\left(L_\theta - Z0 N_\phi\right) && \text{(B.40)}\\
H_r &\simeq 0 && \text{(B.41)}\\
H_\theta &\simeq +\frac{\jmath\beta e^{-\jmath kr}}{4\pi r}\left(N_\phi - \frac{L_\theta}{Z0}\right) && \text{(B.42)}\\
H_\phi &\simeq -\frac{\jmath\beta e^{-\jmath kr}}{4\pi r}\left(N_\theta - \frac{L_\phi}{Z0}\right) && \text{(B.43)}\\
& && \text{(B.44)}
\end{aligned}$$

B.2 Ray-based asymptotic methods

B.2.1 Two ray-based algorithm

B.2.1.1 Shooting and Bouncing Ray algorithm (SBR)

This first ray method is called Shooting and Bouncing Ray method or SBR presented in [COST 02] and [Durg 97]. The principle is to lunch rays from a transmitting point to every directions of the environement following a sampled angular grid. Several propagation mechanisms can be taken into acount such as specular reflexions, PO reflexions or diffractions. A each interaction with the environment, the inpigging ray gives rise to one specular ray in the case of specular reflexion or to multiple rays in the case of PO reflexions or diffractions. This process is repeated until the rays reach the receiver. The pseudo algorithm is given in Fig.B.2. One simple representation is given in Fig.B.3 in the case of specular reflexions. As visible, this algorithm is very sensitive to the initial sampled angular grid for the accuracy of the results (missing specular points compared to Fig.B.5) and the computation time (number of intersection with the environment).

```
{A}    = Discret set of angles to be scan
{S(i)} = Set of sources at i step
Imax   = Maximum number of iterations
{R}    = Set of rays solution
r      = One ray

{S(1)} = {Transmitter}
{R} = {Empty}
i=1
While ({S} non empty and i<Imax)
   For each s in {S(i)}
      For each a in {A}
         r = Lunch ray()
         For each r
            If intersection ray/environment
               {S(i+1)} = {S(i+1)}+{intersection point}
            End If
            If intersection ray/receiver
               {R} = {R}+{r}
            End If
         End For r
      End For a
   End For s
   i=i+1
End While
```

Figure B.2: Ray lunching pseudo algorithm

B.2.1.2 Ray Tracing algorithm (RT)

The second method is called Ray Tracing or RT and is described in [COST 02] and [Ande 93]. This method requieres a priori to know the position of the transmitter, the position of the receiver and the whole environment. This method is based on the theory of images where only specular reflexions can be taken into account. The principle is to build recessively the intermediate images of the sources until rays reach the receiver. This method is described in the following pseudo algorithm which is illustrated by Fig.B.5.

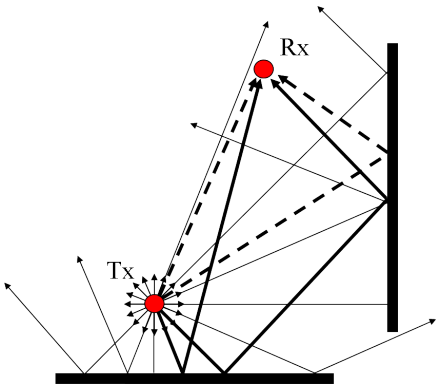

Figure B.3: Principle of the shooting and bouncing ray algorithm

```
{S(i)} = Set of sources at i step
{Rx}   = Receiver
{F}    = Set of facets
{R}    = Set of rays solution
Imax   = Maximum number of iterations
r      = One ray
f      = One facet

Function Recursive_Image(S(i),F)
   For each f in F visible by S(i)
      {F}={F}-{f}
      S(i+1) = image of S(i) by facet f
      If exist r such as direct path from S(i+1) to Rx
         {R}={R}+r
      End if
      i=i+1
      If(i<Imax)
         Recursive_Image(S(i),F)
      End if
      {F}={F}+{f}
   End For f
End Function Recursive_Image

Function Main
   S(1) = {Transmitter}
   R = {Empty}
   i=1
   If exist r such as direct path from S(1) to Rx
      {R}={R}+{r}
   End if
   Recursive_Image(S(i),F)
End Function Main
```

Figure B.4: Ray tracing pseudo algorithm

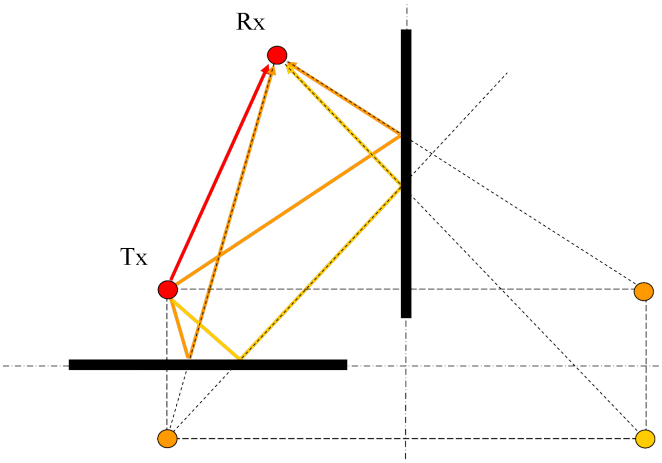

Figure B.5: Principle of the ray tracing algorithm

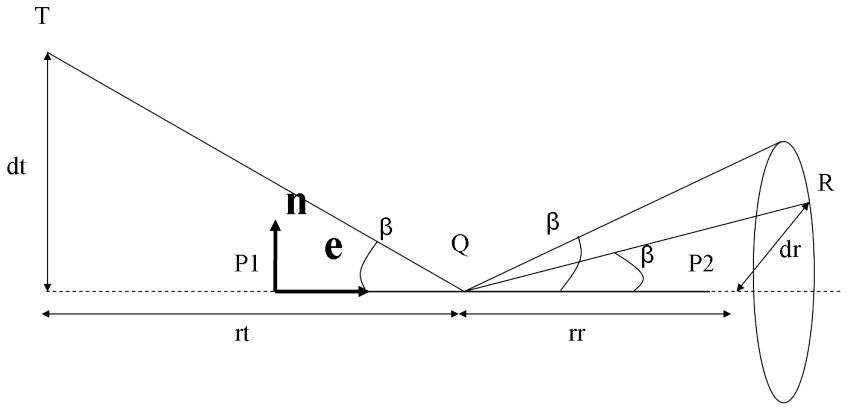

Figure B.6: Geometry of the stationnary diffraction point

B.2.2 The Uniform Theory of Diffraction

B.2.2.1 Computing the stationnary diffraction point

Let P_1 and P_2 be two points defining an edge. Let $\hat{\mathbf{e}}$ be the unit edge vector. Let T and R be the position of the transmitter and the receiver respectively. Let Q be the stationnary diffraction point.

$$Q(t) = P_1 + t\vec{P_1P_2} \tag{B.45}$$

$$\hat{\mathbf{e}} = \frac{(P_2 - P_1)}{|P_2 - P_1|^2} \tag{B.46}$$

$$t = \hat{\mathbf{e}}.\left(\frac{T\,d_r + R\,d_t}{d_r + d_t} - P_1\right) \tag{B.47}$$

$$d_r = |\vec{P_1R} \wedge \hat{\mathbf{e}}| \tag{B.48}$$

$$d_t = |\vec{P_1T} \wedge \hat{\mathbf{e}}| \tag{B.49}$$

The stationnary diffraction exists only if $t \in [0, 1]$. Note that Q also has to be visible from both the transmitter and the receiver and not masked by other objects.

B.2.2.2 The Uniform Theory of Diffraction algorithm

Let $\mathbf{E^{ini}}$ be the incident polarised E field following θ and ϕ components in the global base. This incident field has to be projected into the incident base following $\hat{\beta_0}'$ and $\hat{\phi}'$ unit polarisation

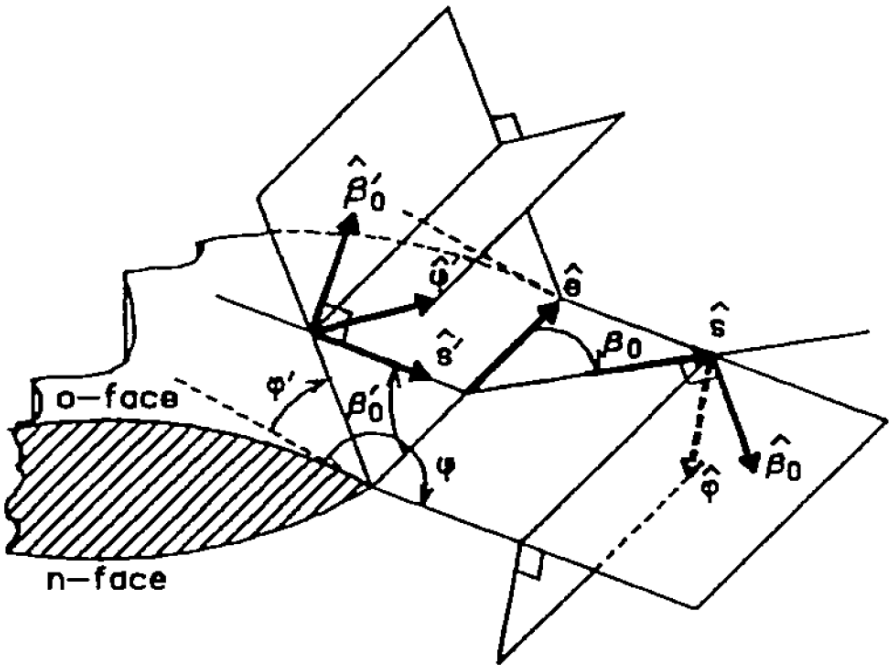

Figure B.7: Definition of the edge fixed coordinate [McNa 90]

vectors. The incident E filed $\mathbf{E^i}$ in the edge fixed coordinate is then defined as follow:

$$\mathbf{E^i} = E^i_{\beta'_0}\hat{\beta_0}' + E^i_{\phi'}\hat{\phi'} \tag{B.50}$$

$$\hat{\phi'} = \frac{-\hat{\mathbf{e}} \wedge \hat{\mathbf{s}'}}{|\hat{\mathbf{e}} \wedge \hat{\mathbf{s}'}|} \tag{B.51}$$

$$\hat{\beta_0}' = \hat{\phi'} \wedge \hat{\mathbf{s}'} \tag{B.52}$$

where $\hat{\mathbf{e}}$ is the unit edge vector and $\hat{\mathbf{s}'}$ the unit incident vector.

The diffracted field is expressed in the diffraction base of the edge fixed coordinate and is defined as follow:

$$\mathbf{E^d} = E^d_{\beta_0}\hat{\beta_0} + E^d_{\phi}\hat{\phi} \tag{B.53}$$

$$\hat{\phi} = \frac{\hat{\mathbf{e}} \wedge \hat{\mathbf{s}}}{|\hat{\mathbf{e}} \wedge \hat{\mathbf{s}}|} \tag{B.54}$$

$$\hat{\beta_0} = \hat{\phi} \wedge \hat{\mathbf{s}} \tag{B.55}$$

where $\hat{\mathbf{s}}$ represent the unit vector in the diffraction direction.

The diffracted field is linked to the incident field by using the following relation:

$$\begin{bmatrix} E^d_{\beta_0} \\ E^d_{\phi} \end{bmatrix} = \begin{bmatrix} -D_s & 0 \\ 0 & -D_h \end{bmatrix} \begin{bmatrix} E^i_{\beta'_0} \\ E^i_{\phi'} \end{bmatrix} \sqrt{\frac{\rho}{s\,(s+\rho)}}\, e^{-\jmath ks} \tag{B.56}$$

where k represents the wave number, s the distance separating the receiver from the diffraction point and ρ the distance separating the transmitter from the diffraction point. The diffracted field is then projected into the polarisation base of the receiver.

The diadic coefficients D_s et D_h are defined as follow:

$$D_s = D_1 + D_2 + R_{s_o}D_3 + R_{s_n}D_4 \tag{B.57}$$

$$D_h = D_1 + D_2 + R_{h_o}D_3 + R_{h_n}D_4 \tag{B.58}$$

with R_s and R_h coefficients being equal to $R_\perp$ and $R_{//}$ from the physical optics algorithm respectively. In the case of a perfect electric conductor, R_s and R_h are equal to -1 and +1 respectively.

The D coefficients are defined as follow:

$$D_1 = \Gamma\, cot\left[\frac{\pi + (\phi - \phi')}{2n}\right] F\left[kL^i a^+\left(\phi - \phi'\right)\right] \tag{B.59}$$

$$D_2 = \Gamma\, cot\left[\frac{\pi - (\phi - \phi')}{2n}\right] F\left[kL^i a^-\left(\phi - \phi'\right)\right] \tag{B.60}$$

$$D_3 = \Gamma\, cot\left[\frac{\pi + (\phi + \phi')}{2n}\right] F\left[kL^{rn} a^+\left(\phi + \phi'\right)\right] \tag{B.61}$$

$$D_4 = \Gamma\, cot\left[\frac{\pi - (\phi + \phi')}{2n}\right] F\left[kL^{ro} a^-\left(\phi + \phi'\right)\right] \tag{B.62}$$

$$\Gamma = \frac{-e^{-\jmath\pi/4}}{2n\sqrt{2\pi k}\sin\beta_0} \tag{B.63}$$

where F is a transition function limitting the divergence effects occuring when passing from one shadow region to another.

The F function is defined over three intervals and equals F_1 is the x argument is inferior to 0.3 and F_2 is the x argument is superior to 5.5. In the intermediate case the F function can be linearly interpolated by using the following values given in Tab.B.1.

$$F_1(x) \approx \left[\sqrt{\pi x} - 2xe^{\jmath\pi/4} - (2/3)x^2 e^{-\jmath pi/4}\right] e^{\jmath\pi/4} e\jmath x \tag{B.64}$$

$$F_2(x) \approx 1 + \frac{\jmath}{2x} - \frac{3}{4x^2} - \frac{15\jmath}{8x^3} + \frac{75}{16x^4} \tag{B.65}$$

x	Real	Imaginary
0.3	0.5729	0.1677
0.5	0.6768	0.2682
0.7	0.7439	0.2549
1.0	0.8095	0.2322
1.5	0.8730	0.1982
2.3	0.9240	0.1577
4.0	0.9658	0.1073
5.5	0.9797	0.0828

Table B.1: Linear interpolation of the F function for argument x between 0.3 and 5.5

The ϕ and ϕ' angles present in the equation of the D coefficient represent the incidence angle taken fro mthe o-face. They are defined as follow:

$$\hat{\mathbf{s_t}}' = \frac{\hat{\mathbf{s}}' - (\hat{\mathbf{s}}' \cdot \hat{\mathbf{e}})\,\hat{\mathbf{e}}}{|\hat{\mathbf{s}}' - (\hat{\mathbf{s}}' \cdot \hat{\mathbf{e}})\,\hat{\mathbf{e}}|} \tag{B.66}$$

$$\hat{\mathbf{s_t}} = \frac{\hat{\mathbf{s}} - (\hat{\mathbf{s}} \cdot \hat{\mathbf{e}})\,\hat{\mathbf{e}}}{|\hat{\mathbf{s}} - (\hat{\mathbf{s}} \cdot \hat{\mathbf{e}})\,\hat{\mathbf{e}}|} \tag{B.67}$$

$$\phi' = \pi - \left[\pi - arccos\left(-\hat{\mathbf{s_t}}' \cdot \hat{\mathbf{t_o}}\right)\right] sign\left(-\hat{\mathbf{s_t}}' \cdot \hat{\mathbf{n_o}}\right) \tag{B.68}$$

$$\phi = \pi - \left[\pi - arccos\left(\hat{\mathbf{s_t}} \cdot \hat{\mathbf{t_o}}\right)\right] sign\left(\hat{\mathbf{s_t}} \cdot \hat{\mathbf{n_o}}\right) \tag{B.69}$$

where $\hat{\mathbf{n_o}}$ represent the normal vector of the o-face and $\hat{\mathbf{t_o}}$ the tangential vector to the surface.

The different parameters which allow to compute the D coefficients are described in the following equations:

$$n = 2 - \frac{\alpha}{\pi} \tag{B.70}$$

$$\beta_0' = \beta_0 = arcsin\left(|\hat{\mathbf{s}} \wedge \hat{\mathbf{e}}|\right) \tag{B.71}$$

$$L^{i,rn,ro} = \frac{ss'}{s+s'} \sin^2 \beta_0 \tag{B.72}$$

$$a^{\pm}\left(\beta^{\pm}\right) = 2\cos^2\left(\frac{2n\pi N^{\pm} - \beta^{\pm}}{2}\right) \tag{B.73}$$

$$\beta^{\pm} = \phi \pm \phi' \tag{B.74}$$

$$N^{\pm} = round\left[\frac{\pm\pi + \beta^{\pm}}{2\pi n}\right] \tag{B.75}$$

where α is the angle between the o-face and the n-face and β_0 the incidence angle taken with respect to the edge.

B.3 Electromagnetic reference codes

B.3.1 Elsem3D based on MOM

Elsem3D is a research code developed by the Electromagnetic and Radar Department (DEMR) of Onera over the past fifteen years [Soud 99] [Bark 00] [Soud 02]. Elsem3D is a living code capitalising Onera know-how in the field of integral equations taking advantage of the most recent improvements from the scientific community. The main targeted applications are EM coupling on structures for EMC issues, RCS of complex objects or antenna radiation pattern computation.

From a technical point of view, Elsem3D is a general tridimensional code based on Integral Equations in Frequency Domain *(IEFD)* solved by MoM techniques. The objects have to be described by segments representing the conducting wires, triangles for the surfaces and tetrahedron for volumes. The common finite element meshing rules, achieved by most general commercial meshers, have to be applied insuring edge continuity between triangles and coincidence of the vertexes. The common mesh size is between $\lambda/5$ to $\lambda/10$. On wired and surfacic parts, the unknowns are the electric J and magnetic M current densities using linear or surfacic integral equation formalism. For volumes, a finite element formalism is applied insuring a natural link with linear and surfacic formalism.

Several types of sources can be used such as planar waves, localised wire generator, TE TM wave guide excitation or user defined field map. The objects can be made of PEC, isotropic and anisotropic dielectrics or surface sheet impedance. The typical outputs are punctual E and H fields, field maps, surface current densities, monostatic and bistatic RCS, antenna impedance or radiation patterns.

The integral methods usually lead to build huge linear system to solve which size is about 1.5 times the number of triangles. The performances of Elsem3D are then tightly linked to the solver qualities. Three solvers are integrated, namely algebraic LU incore, algebraic LU out of core and iterative FMM *(Fast Multilevel Multipole)*. The LU core solver achieves the determination of about few thousands of unknown while LU out of core achieves the determination of about one hundred thousand unknown on parallel machines. The FMM solver, is used for the needs of the present study. Using FMM techniques allows to overtake one million unknowns.

B.3.2 SE-WorkBench software suite based on asymptotic methods

The FERMAT project *(Fonctionnalités pour l'Electromagnétisme et le Radar par les Méthodes Asymptotiques)* [Berg 04] [Mame 06] [Mame 03] associates researchers from Paul Sabatier Uni-

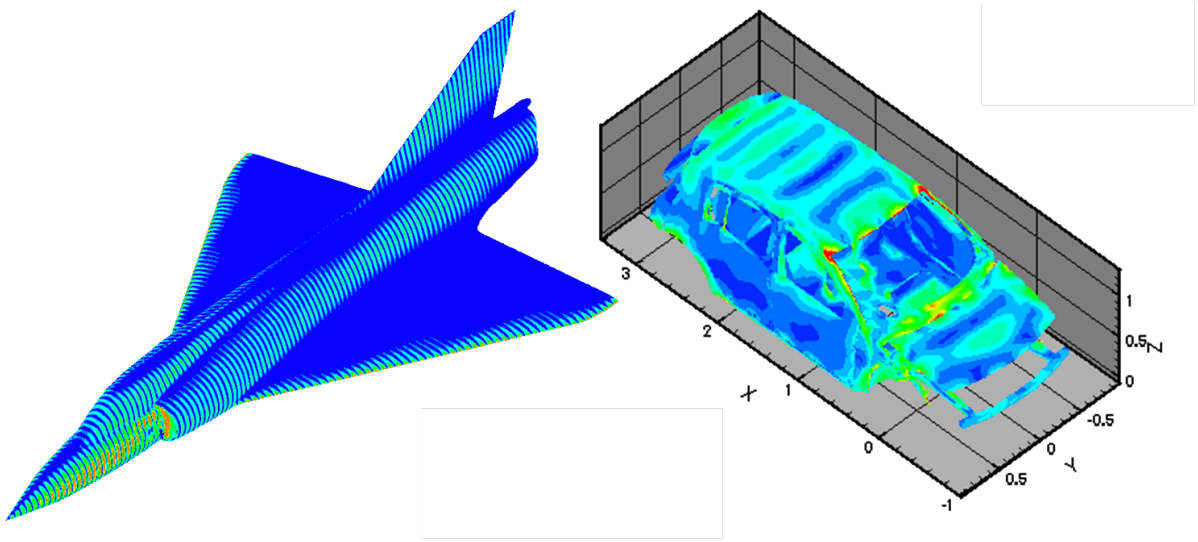

Figure B.8: Elsem3D result examples. (left) Surface currents on MACH generic plane at 1.25GHz (10^6 unknowns). (right) Surface currents on a vehicular for EMC issues

versity in Toulouse, engineers from Onera and developers from Oktal-SE (Oktal Synthetic Environment). This association has lead to the emergence of a complete software suite dedicated to the prediction of electromagnetic fields resulting from EM wave interactions on wide and complex scenes using asymptotic methods and taking advantage of the recent improvements in the field of 3D graphics. The software suite is marketed by Oktal-SE under its international denomination SE-WorkBench. The electromagnetic core of SE-WorkBench is SE-Ray-EM, performing all low-level operations associated to ray launching and electromagnetic modelling which will be discussed farther in this section. SE-WorkBench is the object of regular validations jointly performed by Onera and Oktal-SE which are presented in the international literature.

SE-WorkBench software suite includes various tools for optimizing the EM work flow of the user. The main tools used during this study are briefly described hereafter :

Environment data bases: SE-Physical-Modeller and SE-Agetim tools have been developed to build and manage complex 3D virtual environments made of hundreds of thousands of facets, including physical properties of the materials, to reproduce various elements, e.g. terrain, buildings or vehiculars.

Scenario management: SE-Scenario tool is dedicated to the scenario management for specifying the context of simulation (bistatic RCS, SAR, EM field, antenna pattern,...), add objects into the scene, perform object motion across time or tune the optimisation settings for the ray launching step.

Ray launching techniques: SE-Ray-EM tool is used to perform the EM computation step by launching the rays from the emitter to the environment and back to the receiver. It encompasses the SBR *(Shooting and Bouncing Ray)* method to compute environment intersections with wave fronts and to track the rays into the scene.

Electromagnetic models: Reflection, refraction, diffraction and scattering propagation phenomena are taken into account and reproduced by different EM methods implemented in SE-Ray-EM. Note that the complexity of the virtual scene has a low impact on computation time.

The use of ray launching techniques associated with asymptotic EM formulations, and the efficiency of such coupling in the domain of EM modelling for radar and propagation issues have been proved. However, the limits of such an association are reached when surfaces involved

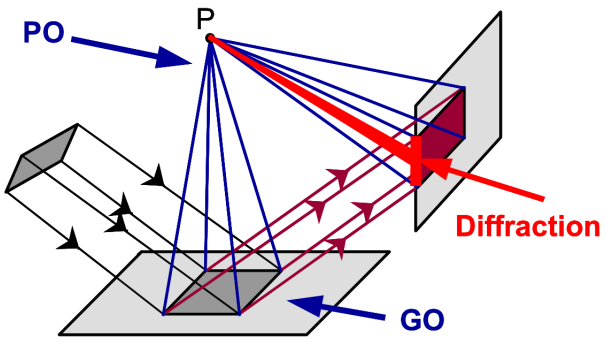

Figure B.9: Multiple interaction principle of SE-Ray-EM [SE 12]

are smaller than a few times the wave length. Nevertheless, multi-domain techniques using full wave methods such as Elsem3D and asymptotic methods such as SE-Ray-EM are possible when estimating embedded antenna patterns on wide and complex vehiculars for example.

Let us focus on the EM core of SE-WorkBench, SE-RAY-EM, performing all electromagnetic computations. This tool is based on asymptotic methods. This approximation is unavoidable as soon as the considered scenes are very wide, with objects much larger compared to the wave length. For such simulation conditions, full wave methods which are based on a direct numerical solving of Maxwell equations are not adapted due to the high number of unknown and asymptotic formulations have to be used instead. A complete set of asymptotic EM techniques is provided in SE-Ray-EM to compute all various phenomena taking place in complex scenes such as propagation, reflection, transmission, scattering and edge diffraction. As presented in Fig.B.9, geometrical optics will be used to model all multiple interactions. The last interaction on the environment is modelled using physical optics techniques. Diffraction is also taken into account at the last interaction by using uniform theory of diffraction, physical theory of diffraction or equivalent current method. Note that each presented EM model has to be used under strict constraints due to the assumptions made.

The commercial delivery of SE-Ray-EM is only suitable for radar concerns and narrow-band EM field computation. To increase the potential of SE-WorkBench software suite, Oktal-SE also provides some dynamic C/C++ libraries to interact with SE-Ray-EM core functions. By using those toolkits, the users can satisfy very specific research needs while conserving the advantage of coupling ray techniques and asymptotic EM methods. Thus, for the specific needs of this thesis, a new tool *"Onera wide-band module"* has been developed. The main advantage compared to SE-Ray-EM is to achieve wide-band representation of channel (delay and direction of arrival) instead of total scattered EM fields.

The Onera wide-band module is interacting with SE-Ray-EM to process the raw EM fields of each ray. Oriented toward wide-band concerns for GNSS propagation issues and channel modelling in mobile context, this tool uses information such as DoA *(Direction of Arrival)*, EM field components or propagation path length of each ray, to compute the complex impulse response of the channel. To reduce the number of rays from millions to thousands, a tapped-delay line approach is used. The principle is to sum coherently all rays incoming in the same tap, commonly representing one delay interval. For the needs of our simulations, this one dimensional approach has been extended to a three dimensional approach considering delay, DoA azimuth and DoA elevation dimensions. Then, one tap is now characterised by the intersection of one delay interval, one DoA azimuth beam and one DoA elevation beam. Due to the specificity of GNSS channel modelling, a specific processing is realised. First, the LOS signal is isolated and processed out of the tapped-delay line, insuring power, phase, delay, DoA coherency over the time. This first step avoids mainly close multipaths to be integrated into the LOS creating fluctuations due to possible interferences. Second, the main multipath contribution, usually

coming from the specular reflection, is isolated. Once isolated, the tapped-delay line is centred on its position. Since GNSS signal processing is very sensitive to delay, this second processing keeps the main multipath contribution at its original delay avoiding high shifts when using wide taps as presented in Fig.B.10 where $\Delta\tau$ represents the tap size and $\delta\tau$ the delay of the main MP contribution.

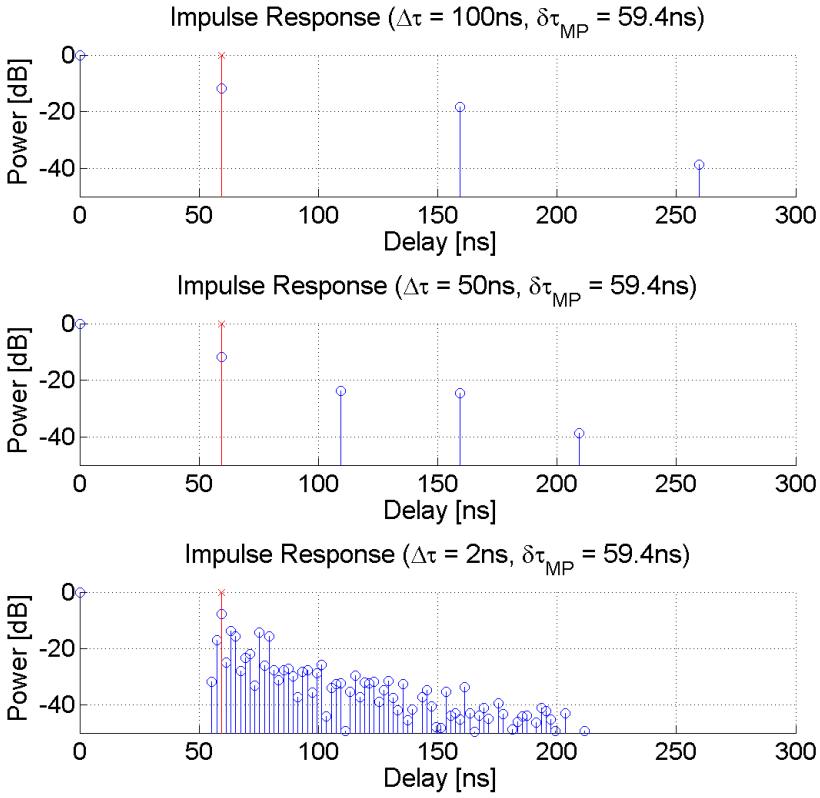

Figure B.10: Principle of the tapped-delay line centering process

Typical simulation outputs are delay relative to the LOS, DoA azimuth, DoA elevation, total power of the tap relative to the LOS, θ and ϕ complex components of E field, and the total number of rays included in the tap. Some examples are given in Fig.B.11 where the simulation scenario, the azimuth power profile and the instantaneous power/delay/Doppler impulse response of the channel are presented.

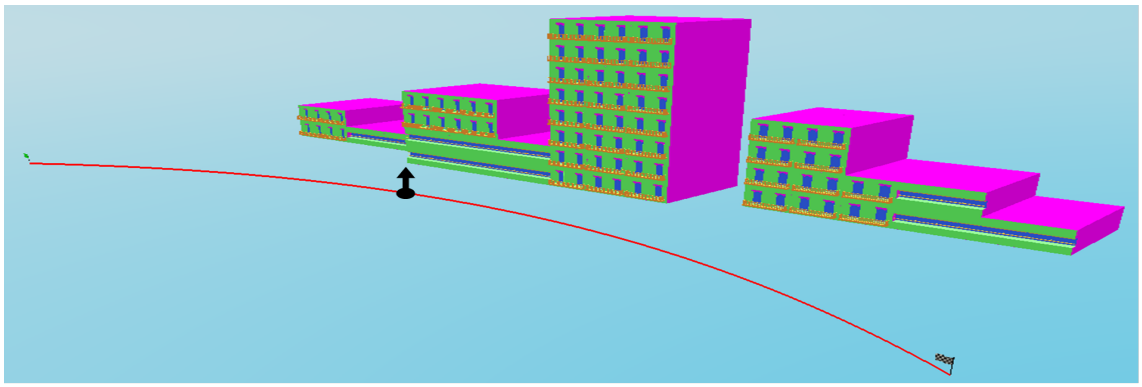

(a) Simulation scenario

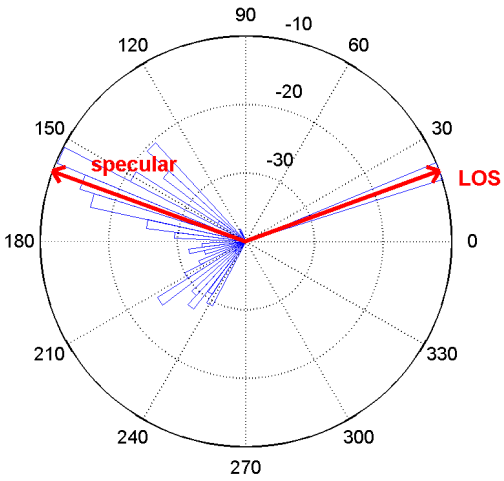

(b) Azimuth power profile

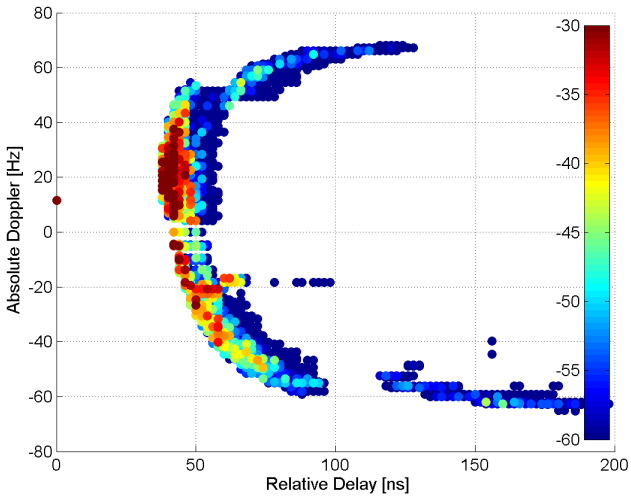

(c) Power/delay/Doppler impulse response

Figure B.11: Example of typical outputs provided by Onera wide-band module

Appendix C

Numerical validation of the three separate EM components of the 3CM

Contents

C.1 Validation of the simplified PO algorithm used for the specular component . . . 169
C.1.1 Bistatic RCS . . . 170
C.1.2 Polarisations . . . 170
C.1.3 Dielectric materials . . . 171
C.1.4 Normal orientation . . . 172
C.1.5 Frequency bands . . . 173
C.1.6 Near field reflection . . . 173
C.1.7 Super-imposition principle . . . 173
C.2 Validation of the double bounce reflection algorithm used for the backscattering component . . . 174
C.2.1 Bistatic RCS . . . 174
C.2.2 Multiple incidences . . . 174
C.2.3 Polarisations . . . 175
C.2.4 Dielectric materials . . . 176
C.3 Validation of the rough surfaces models used for the incoherent component . . . 176
C.3.1 Bistatic RCS . . . 176
C.3.2 Tuning guardrail scattering . . . 177

This appendix presents some validation examples of the implementation of all three EM algorithms namely simplified PO algorithm, double bounce reflection algorithm and rough surfaces models respectively used in the specular component, the backscattering component and the incoherent component of the 3CM.

C.1 Validation of the simplified PO algorithm used for the specular component

This section presents some validation results on canonical configurations of the implementation of the simplified PO algorithm mainly used to reproduce the specular component. This validation exercise has been performed using SE-WorkBench results has the reference.

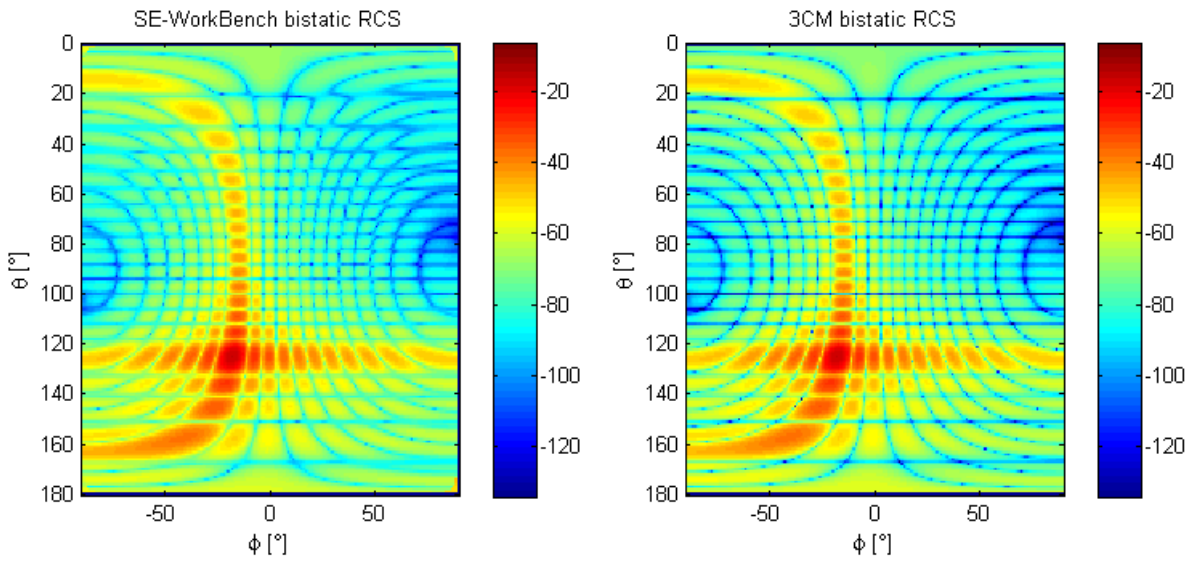

Figure C.1: Validation of the simplified PO algorithm on 3D bistatic RCS of a PEC plate

C.1.1 Bistatic RCS

The first validation example here presented deals with bistatic RCS of a PEC plate. The scenario is the following, the transmitter is place at 20.10^6m with 35° elevation, 18° azimuth and ϕ polarisation. The plate is a square of 2m side with normal X axis. This plate is discretized into square facets of 0.5m side. Note that in the following, ϕ axis represents the azimuth in the horizontal plane oriented from X axis to Y axis where X axis is zeros. θ axis represents the incidence angle taken from the zenith represented by Z axis.

As visible in Fig.C.1, the bistatic RCS pattern is identical. Coming from $\theta = 55°$, $\phi = 18°$, the specular reflection is placed at $\theta = 125°$, $\phi = -18°$. Hardly comparable using this type of representation, RCS absolute values will be validated in the following subsections.

C.1.2 Polarisations

The second validation exercise here performed deals with polarisation effects. Note that the polarisation handling of the 3CM is one of its main assets. For Fig.C.2a, the scenario is the following: the transmitter is placed at 20.10^6m with 40° elevation, 25° azimuth and θ polarisation. The plate is a square of 2m side with normal X axis and made of PEC materials. This plate is discretized into square facets of 0.5m side. The RCS is observed at 20.10^6m, in far field from the plate, in the plane $\theta = 115°$, $\phi \in [-90°, 90°]$. For Fig.C.2b and Fig.C.2c, the simulation parameters are kept constant except the polarisation using respectively ϕ polarisation and $RHCP$ polarisation. Note that the $RHCP$ polarisation is defined following the IEEE convention stating that right handed circular polarisation is rotating counterclockwise for an approaching wave. It can also be defined as $\hat{\theta} + j\hat{\phi}$.

As visible on all three displays, the polarisation implementation in the simplified PO algorithm is in good accordance with SE-WorkBench reference. For all linear polarisations, the sinc motive is clearly visible with -13dB attenuation of the second lobes. As a remark, for θ polarisation, the cross polarisation is very low and not visible on Fig.C.2a. For ϕ polarisation, the cross polarisation level is relatively high but in accordance with SE-WorkBench. Contrary to θ polarisation, the cross polarisation level is high because the RCS is observed in the horizontal plane. Results would be comparable to θ polarisation if the RCS was observed in the vertical plane. For $RHCP$ polarisation, it can be noticed that the polarisation has been inverted as predicted by the theory. Note that SE-WorkBench does not natively handle circular polarisation contrary to 3CM. Post-processing recombination has been made following Eq.C.1 also described

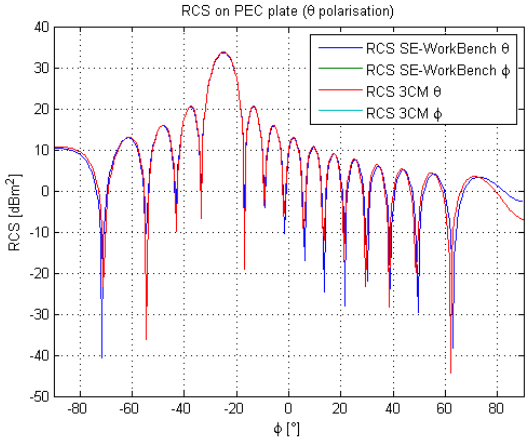

(a) θ polarisation

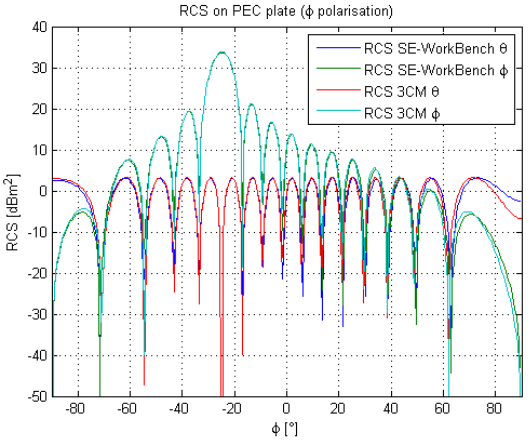

(b) ϕ polarisation

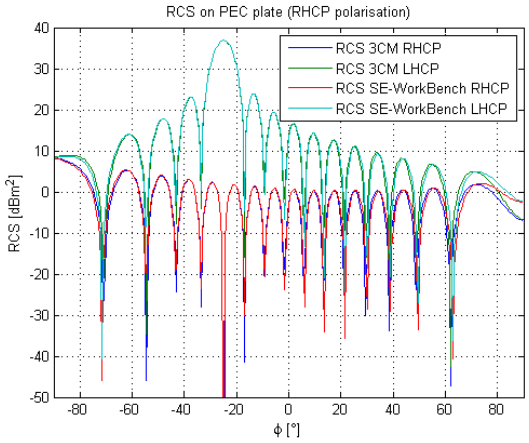

(c) RHCP polarisation

Figure C.2: Validation of the simplified PO algorithm on polarised RCS considering PEC plate

in [Knot 04] to rebuild the circular polarisation. Contrary to [Knot 04], the conjugate of the receiving polarisation matrix is used to reproduce the hermitian transformation.

$$\begin{bmatrix} S_{LL} & S_{LR} \\ S_{RL} & S_{RR} \end{bmatrix} = \frac{1}{2}\begin{bmatrix} 1 & -\jmath \\ 1 & +\jmath \end{bmatrix}\begin{bmatrix} S_{\theta\theta} & S_{\theta\phi} \\ S_{\phi\theta} & S_{\phi\phi} \end{bmatrix}\begin{bmatrix} 1 & 1 \\ -\jmath & +\jmath \end{bmatrix}^{*} \tag{C.1}$$

$$S_{LL} = \frac{1}{2}\left[(+S_{\theta\theta} + S_{\phi\phi}) + \jmath(-S_{\phi\theta} + S_{\theta\phi})\right] \tag{C.2}$$

$$S_{LR} = \frac{1}{2}\left[(+S_{\theta\theta} - S_{\phi\phi}) + \jmath(-S_{\phi\theta} - S_{\theta\phi})\right] \tag{C.3}$$

$$S_{RL} = \frac{1}{2}\left[(+S_{\theta\theta} - S_{\phi\phi}) + \jmath(+S_{\phi\theta} + S_{\theta\phi})\right] \tag{C.4}$$

$$S_{RR} = \frac{1}{2}\left[(+S_{\theta\theta} + S_{\phi\phi}) + \jmath(+S_{\phi\theta} - S_{\theta\phi})\right] \tag{C.5}$$

C.1.3 Dielectric materials

The third validation exercise here performed deals with dielectric materials. Dielectric material is an important parameter since it has an crucial influence on signal polarisation, power and phase. Fig.C.3 represents the RCS of a dielectric plate. The transmitter is place at 20.10^6m with normal incidence and θ polarisation at 1.5GHz. The dielectric plate is a square of 2m side with normal X axis and made of brick with dielectric constant $\epsilon_r = 3.7$, $\mu_r = 1$ and $\sigma = 0$. This plate is discretized into square facets of 0.5m side. The RCS is observed at 100m, in far field

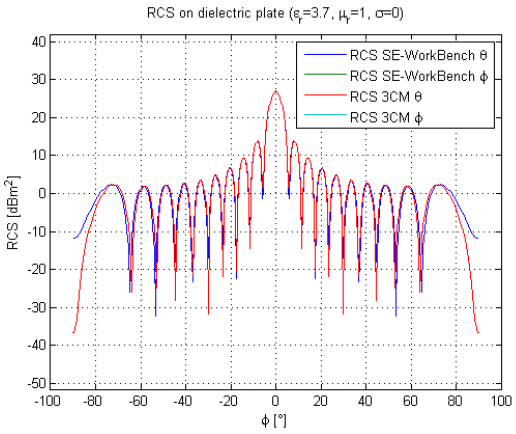

Figure C.3: Validation of the simple PO algorithm considering dielectric materials of a plate

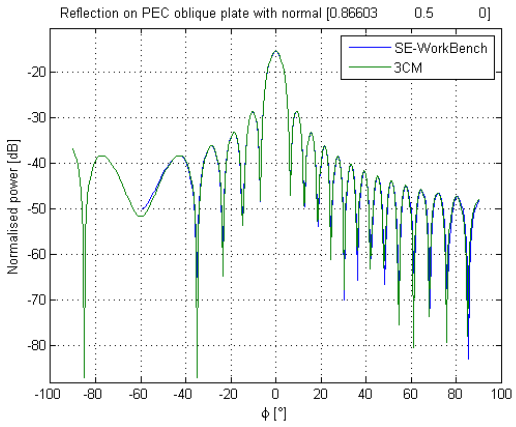

Figure C.4: Validation of the simple PO algorithm considering oblique oriented PEC plate

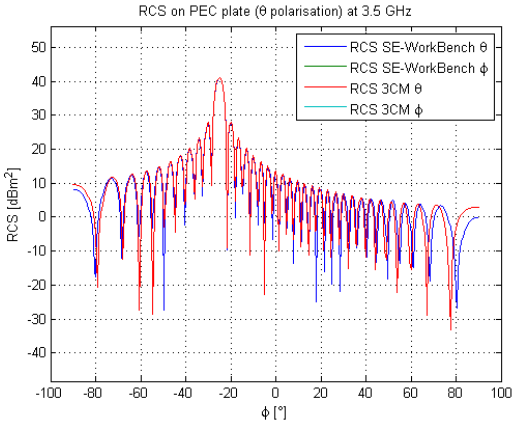

Figure C.5: Validation of the simple PO algorithm considering 3.5GHz center frequency

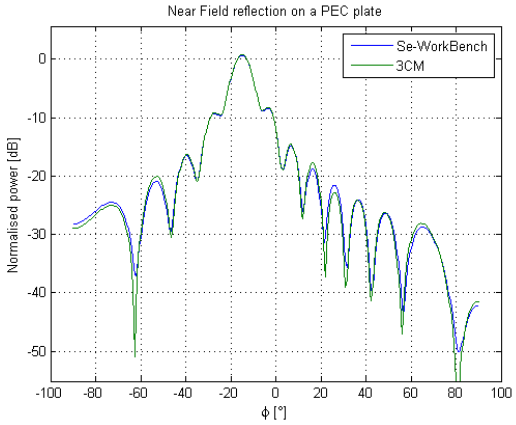

Figure C.6: Validation of the simple PO algorithm in near field conditions of a PEC plate

from the plate, in the plane $\theta = 90°$, $\phi \in [-90°, 90°]$.

As visible in Fig.C.3, the simplified PO algorithm is in very good accordance with the reference made using SE-WorkBench and also w.r.t theoretical results which predict an RCS of $27dBm^2$ in the normal direction using Eq.C.6, where S represents the surface of the plate.

$$RCS = \rho^2 \left(4\pi S^2\right) / \left(\lambda^2\right) \quad \text{(C.6)}$$

$$\rho = \left(\sqrt{\epsilon_r} - 1\right) / \left(\sqrt{\epsilon_r} + 1\right) \quad \text{(C.7)}$$

C.1.4 Normal orientation

The fourth test here performed deals with oblique orientation of the plate. This issue has to be validated since the double bounce reflection algorithm reproducing the backscattering component uses equivalent plates where the normal has been rotated. For Fig.C.4, the scenario is the following: the transmitter is place at 20.10^6m with 10° elevation, 60° azimuth and θ polarisation. The plate is a square of 2m side with normal $[\sqrt{3}/2\ 1/2\ 0]$ equivalent to 30° azimuth and made of PEC materials. This plate is discretized into square facets of 0.5m side. The E field is observed at 100m, in the plane $\theta = 100°$, $\phi \in [-90°, 90°]$. Note that a particular attention has to be paid in the implementation when rotating the plate. The whole plate has to be rotated before discretising it into smaller facets.

As expected the specular component is at 0° azimuth in accordance with results shown in Fig.C.4. Note that the simplified PO algorithm predicts power from -90° to -60° where SE-WorkBench does not. This can be explained by the fact that SE-WorkBench does not calculate E field behind the plate except if EM transmission is possible.

C.1.5 Frequency bands

The fifth test here performed valid the use of higher frequencies for the simplified PO algorithm. The scenario for Fig.C.5 is the same as the one presented for Fig.C.2a except that the frequency is 3.5GHz in this case. As visible, RCS results are still in very good accordance with SE-WorkBench reference.

C.1.6 Near field reflection

Fig.C.6 represents the total power reflected by a PEC plate in near field conditions. The near field is an important issue since the mobile will always be in near field condition considering wide facades. The scenario is the following: the transmitter is place at 20.10^6m with 50° elevation, 15° azimuth and θ polarisation. The plate is a square of 2m side with normal X axis and made of PEC materials. This plate is discretized into square facets of 0.5m side. The E field is observed at 10m, in the plane $\theta = 140°$, $\phi \in [-90°, 90°]$. Note that the far field limit for the whole plate is around 80m while the far field of the small facets is 5m. Since the simplified PO algorithm has been implemented only for far field conditions, each receiving point has to fulfill the far field condition w.r.t the sub-divided facet. Considering higher frequency would implies that either square facets are smaller than 0.5m width or the receiver is farther to the facets. Here also, a good agreement is achieved between SE-WorkBench reference and the simplified PO algorithm.

C.1.7 Super-imposition principle

The principle of this last validation exercise consists in summing the incident EM field with the reflected EM field to achieve constructive and destructive interferences highlighting the specular reflection phenomenon and the blockage phenomenon. The scenario is the following: the transmitter is place at 20.10^6m with 25° elevation, 35° azimuth and θ polarisation. The plate is a 10m width, 7m high with normal X axis and made of PEC materials. This plate is discretized into square facets of 0.5m side. The E field is observed in the horizontal plane from -30m to +30 following X and Y axis.

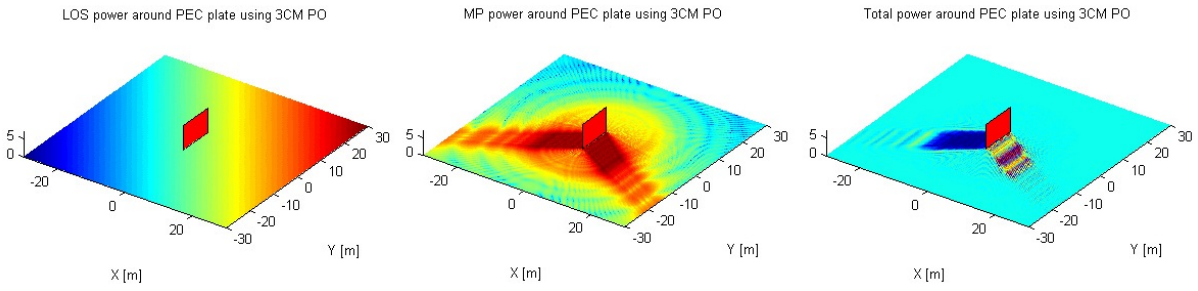

Figure C.7: Validation of the 3CM PO algorithm using the super imposition principle

Left Fig.C.7 present the LOS received power as if the plate is transparent. As visible it slightly decreases w.r.t the incident direction. Note that LOS power is almost constant and only phase shifts are of importance. Center Fig.C.7 present the total power reflected by the plate. As visible, the plate radiates considering both sides. However, when summing LOS contribution and reflected contribution, constructive and destructive interferences are observable in right Fig.C.7. The constructive area represents the specular reflection zone while destructive area represents the blockage zone.

C.2 Validation of the double bounce reflection algorithm used for the backscattering component

This section presents some validation results on canonical configurations of the double bounce reflection algorithm used to model the backscattering component. The reader is reminded that this algorithm is derived from the simplified PO algorithm previously presented. This validation exercise has been performed using SE-WorkBench results has the reference and uses double PO interactions.

C.2.1 Bistatic RCS

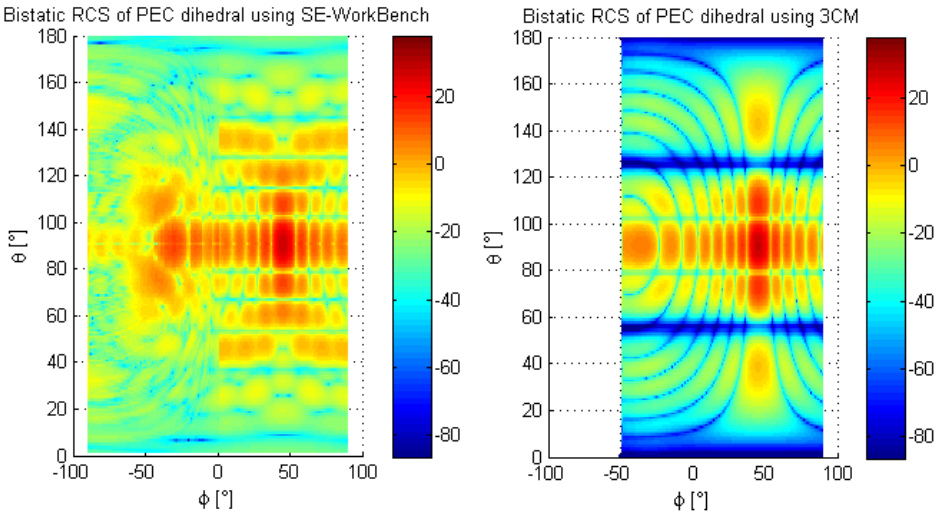

Figure C.8: Validation of the double bounce reflection algorithm considering bistatic RCS on PEC dihedral

The first validation example here presented deals with bistatic RCS of a dihedral. The scenario is the following. The dihedral is made of PEC materials and composed of two plates of 1m per 1m each, oriented toward positive X and positive Y axis. The source is placed at $20.10^6 m$ with 0° elevation, 45° azimuth, θ polarised at 1.5GHz. The RCS is observed at 100m.

As visible in Fig.C.8, the bistatic motive is similar around the main contribution (0° elevation, 45° azimuth) and around the horizontal plane (0° elevation) where the interference motive is well reproduced. However, for angle higher than 35° in elevation a major difference can be observed. Note also that the right plot does not calculate the RCS after -50° in azimuth. This is due to the α correction term which limits the angular power zone to avoid radiation in non physical directions.

C.2.2 Multiple incidences

The second validation here performed deals with RCS considering various incidence angles from 20 to 45° in azimuth and from 0 to 60° in elevation of a PEC dihedral. Simulation parameters are kept constant w.r.t the previously presented case.

As expected, the double bounce reflection model is in very good accordance for the case 0° elevation, 45° azimuth since it has been designed considering this case as a reference. In general, the model is in relatively good accordance considering low elevations (0 and 30°). For higher elevations such as 60° differences are higher but involved power are much lower. Nevertheless, this validation has been performed on canonical isolated dihedrals. In complex cases, when elevation gets high, the backscattering component is low due to masking effects in windows corners which have been highlighted in Section 2.2.

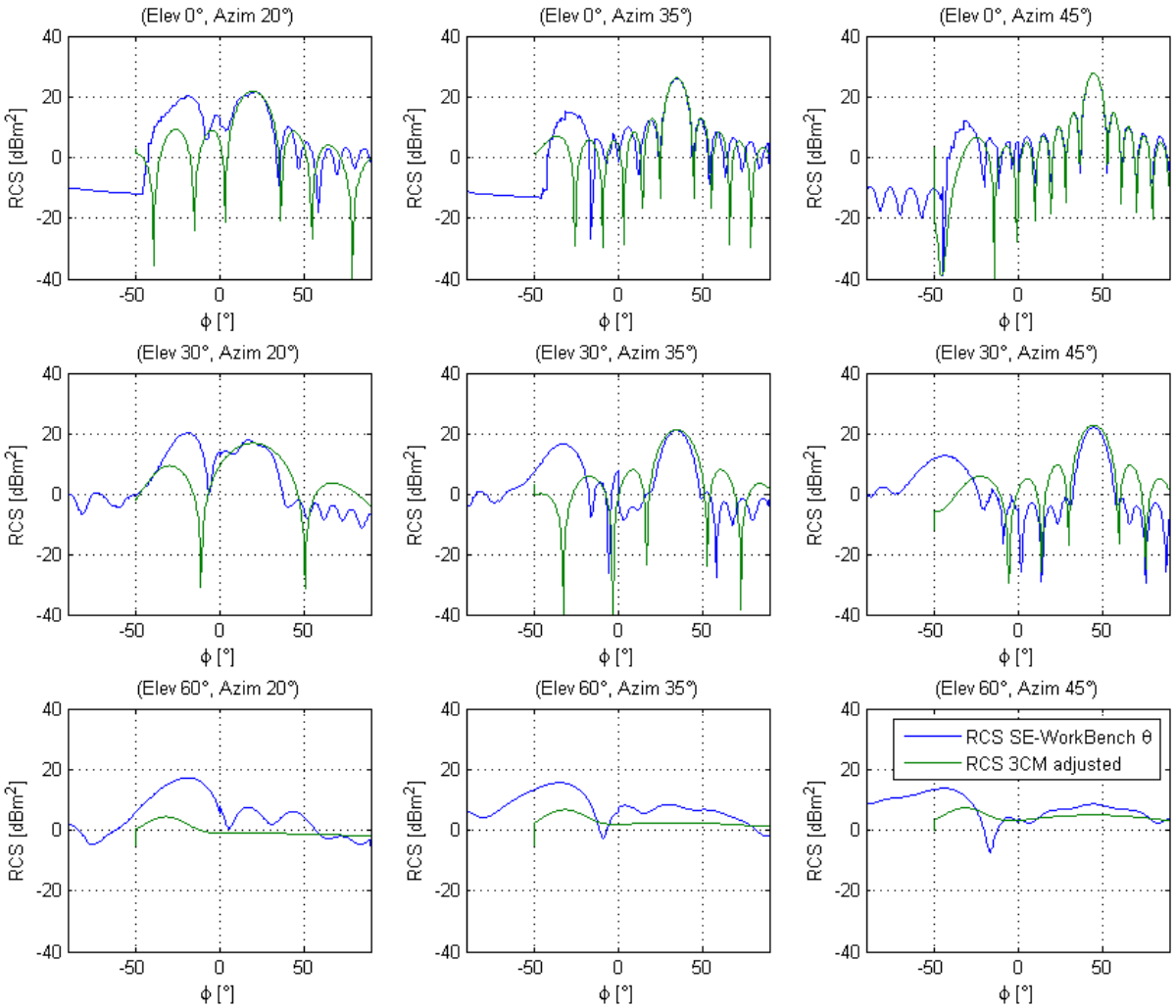

Figure C.9: Validation of the double bounce reflection algorithm considering multiple incidences on PEC dihedral

C.2.3 Polarisations

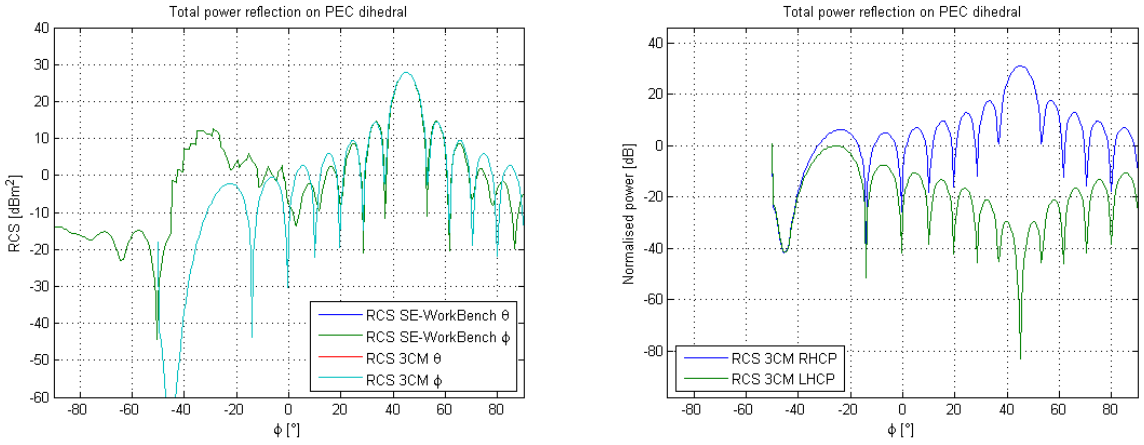

(a) ϕ polarisation

(b) $RHCP$ polarisation

Figure C.10: Validation of the double bounce reflection algorithm on polarised RCS considering PEC dihedral

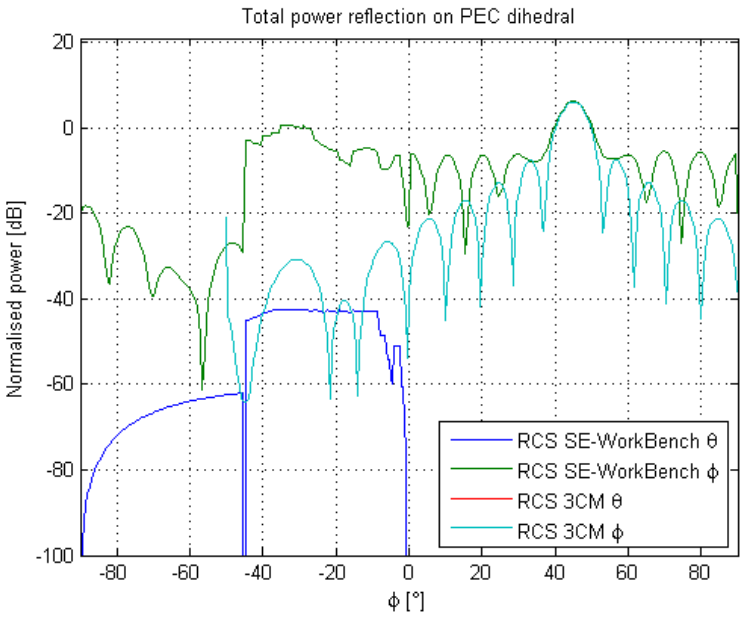

Figure C.11: Validation of the double bounce reflection algorithm considering on dielectric dihedral

The third validation performed deals with polarisation effects. The main issue to validate is the polarisation shift due to the double reflection. As visible in Fig.C.10a for linear polarisation, the polarisation remains unchanged and is in good accordance with SE-WorkBench prediction. For Fig.C.10b, the polarisation is double shifted, meaning unchanged, and $RHCP$ polarisation is reflected as $RHCP$ polarisation. The cross polarisation ($LHCP$) has a minimum in the specular direction in accordance with the theory.

C.2.4 Dielectric materials

The last validation example deals with dielectric materials. As visible in Fig.C.11, the main lobe is in good accordance with SE-WorkBench prediction. However, side lobes are slightly lower using the double bounce reflection algorithm.

C.3 Validation of the rough surfaces models used for the incoherent component

This section presents some examples of the use of the rough surfaces models implemented for the incoherent component. First, the differences between slightly rough and very rough surface models are depicted. Second, a brief example is shown on how the scattering function of the guardrail of the city center facade can be tuned.

C.3.1 Bistatic RCS

The first example deals with bistatic RCS considering a 5m by 5m PEC plate made of rough surfaces and discretized into square facets of 0.5m side. The scenario is the following, the transmitter is place at 20.10^6m with 35° elevation, 18° azimuth and θ polarisation. The RCS is observed at 1000m. Fig.C.12 represents the bistatic RCS of the plate assuming $l = 0.5$ and $h = 0.03$ for the roughness parameters. Fig.C.13 represents the bistatic RCS of the same plate assuming $l = 0.5$ and $h = 0.2$ for the roughness parameters.

As visible for the slightly rough models, small differences are observable. When using the slightly rough model with Gaussian distribution, a specular zone is clearly visible (θ=125°, ϕ=-18°).

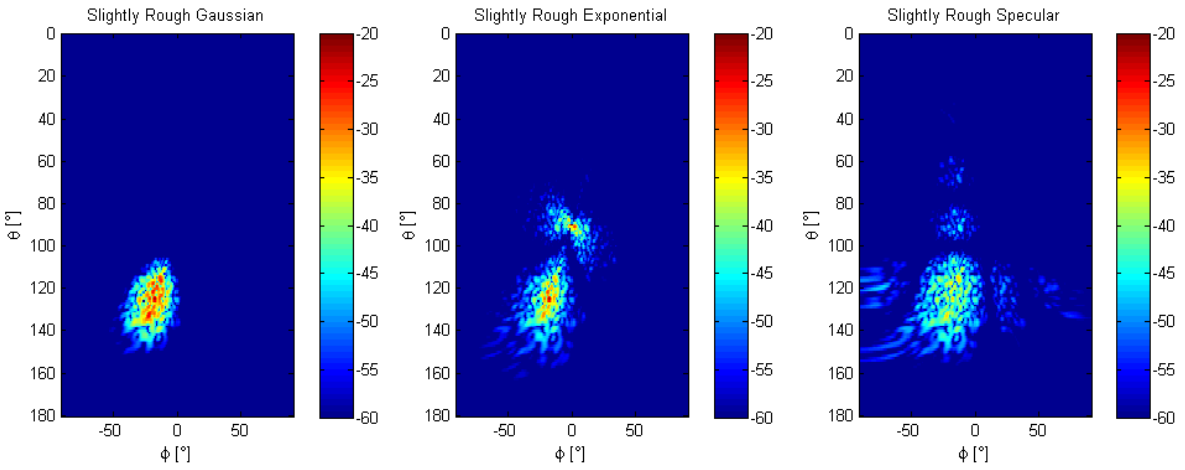

Figure C.12: Example of bistatic RCS using the slightly rough surface models

However, contrary to specular reflection, no interference motive is visible and RCS is highly variable is this region. Using the slightly rough model with exponential distribution is similar to the Gaussian distribution except that a second zone appears around the normal direction (θ=90°, ϕ=0°). The slightly rough specular model is in ad equation with both slightly rough empirical models.

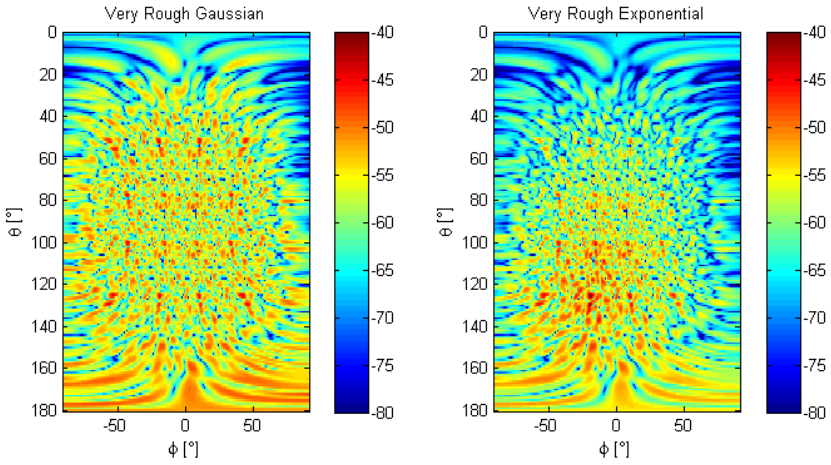

Figure C.13: Example of bistatic RCS using the very rough surface models

Observation of Fig.C.13 reveals that slightly rough and very rough surface models are very different is the way they scatter power. For very rough surface models, the power is spread in all directions with strong variations from one point to its neighbours. The pseudo-specular phenomenon observed with slightly rough surfaces has disappeared.

C.3.2 Tuning guardrail scattering

This last example shows how we proceed to tune the scattering function of the guardrail present on city center facade. To do so, Elsem3D has been used as the reference since bars composing the guardrail are too small and interactions on such objects are not supposed to be calculated using SE-WorkBench. As for Section 2.2.2, the bottom guardrail radiation has been isolated from the rest of the facade. Surface currents are presented in top left of Fig.C.14. An equivalent guardrail is presented in top right of Fig.C.14 using the 3CM formalism. As visible, this simplified guardrail is composed by many small plates randomly thrown in a volume of the size of the guardrail with 0.5m width. The equivalent surface of all small facets is $4m^2$. In the presented case, plates are 0.2m squares made of very rough surface with exponential distribution with

$l = 0.5$ and $h = 0.2$.

Bottom Fig.C.14 represents the radiation of both guardrails (blue Elsem3D, dashed red 3CM) when a mobile is passing at a distance of 10m in front of the guardrail assuming a normal incidence. The plain red curve is the average power scattered by the guardrail assuming a Monte Carlo process over 100 randomly generated similar guardrails.

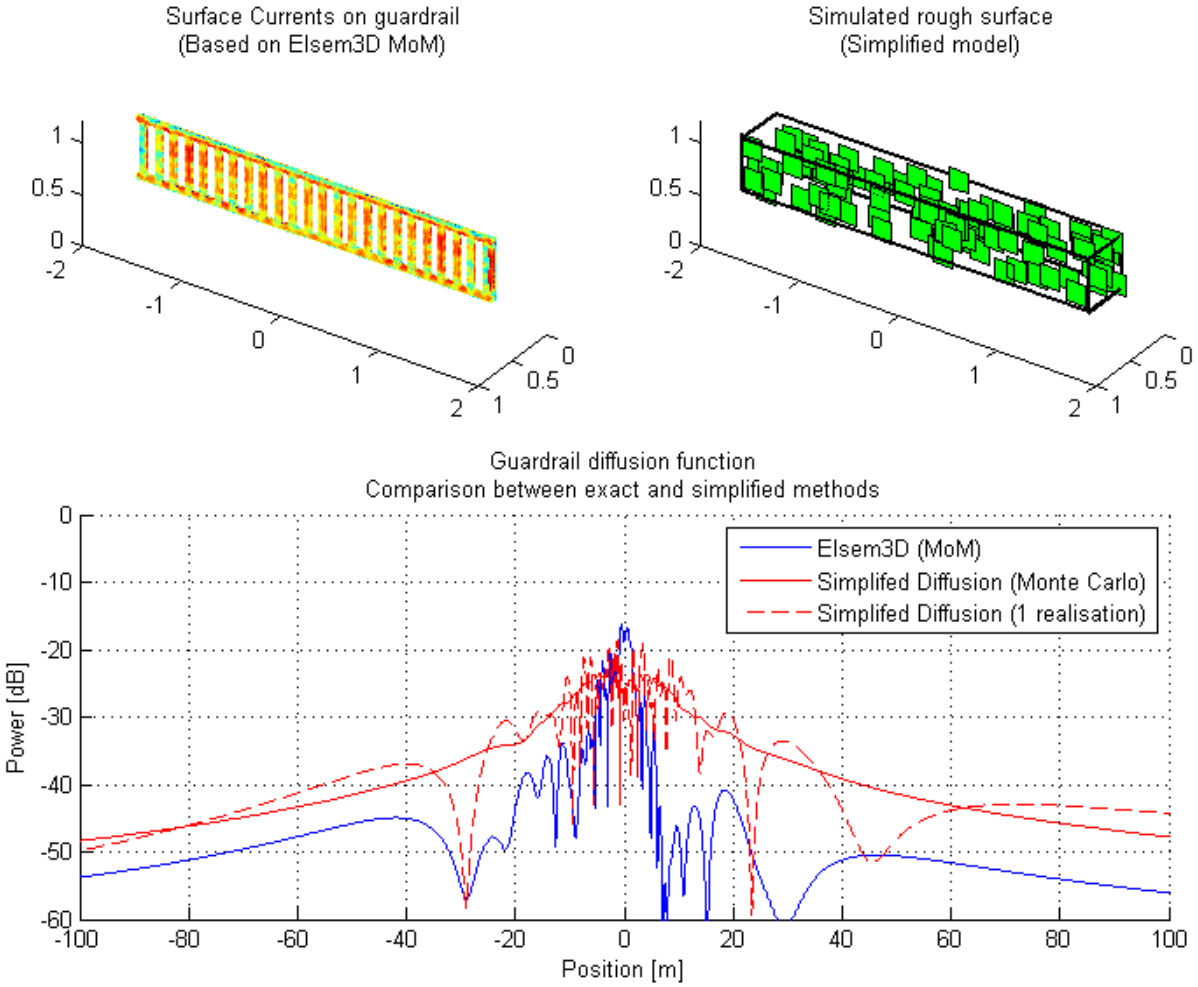

Figure C.14: Example of tuning the very rough surface model to fit the guardrail scattering function

The reader is reminded that this tuning stage is not mandatory for a non site specific simulation using the 3CM.

Appendix D

Résumé étendu

Contents

D.1 Introduction . . . 179
D.2 Etude critique et proposition d'un nouveau simulateur . . . 183
D.2.1 Les différentes approches . . . 183
D.2.2 Les modèles statistiques . . . 183
D.2.3 Les modèles déterministes . . . 185
D.2.4 Les modèles hybrides physico-statistiques . . . 185
D.2.5 Approche retenue et positionnement de la thèse . . . 187
D.3 Etude de l'influence des détails sur des façades complexes . . . 189
D.3.1 Observations préliminaires . . . 189
D.3.2 Analyse faible bande de l'influence des détails . . . 190
D.3.3 Analyse large bande de l'influence des détails . . . 192
D.4 Présentation d'un nouveau modèle d'interaction onde/bâtiments . . . 194
D.4.1 Observations préliminaires . . . 194
D.4.2 Concept du modèle 3CM . . . 194
D.4.3 Validation numérique du modèle 3CM . . . 196
D.5 Implémentation et validation du simulateur de canal SCHUN . . . 198
D.5.1 Implémentation du simulateur de canal SCHUN . . . 199
D.5.2 Validation expérimentale pour les systèmes de communication par satellite (Saint Lary) . . . 201
D.5.3 Validation expérimentale pour les systèmes de navigation par satellite (Toulouse-Capitole) . . . 203
D.6 Conclusion . . . 206

D.1 Introduction

La présente étude est à l'interface entre le domaine de la propagation des ondes EM *(électromagnétique)* et le domaine du traitement de signal appliqué aux systèmes de navigation par satellite.

Bien que la modélisation de la propagation des ondes EM eu été étudiée depuis le début du XIXe siècle avec l'émergence des technologies sans fil [Kenr 30] [Lowe 16] [Stra 30], il faudra attendre la seconde guerre mondiale pour stimuler les applications micro-ondes et la modélisation des phénomènes de propagation EM, notamment pour des applications de radar et de télécommunications. Depuis lors, la modélisation des phénomènes de propagation des ondes EM a connu un réel essor et aujourd'hui encore la demande en systèmes sans-fil ne faiblit pas. De nos jours, les technologies sans fil sont présentes partout. A titre d'exemple, on peut citer les systèmes terrestres de télécommunications mobiles (normes GSM, UMTS ou LTE), les systèmes intra-bâtiment, ou *indoor*, à haut débit (normes Wifi a/b/g/n) ou encore les systèmes de télédiffusion par satellite (normes DVB-S ou SDMB). Cependant, chacun de ces systèmes sans fil est confronté à différentes problématiques liées à la propagation des ondes EM dans leurs milieux respectifs. Contrairement

aux canaux de propagation indoor et terrestre, les canaux de propagation Terre/espace soufrent d'une forte atténuation de la puissance reçue dû a la distance parcourue et à la traversé des couches atmosphériques mais aussi de dépolarisation dû au phénomène de rotation de Faraday en fonction de la fréquence de la liaison.

Au cours des vingt dernières années et grâce à l'étendue de leur zone de couverture associée à de faible coûts d'exploitation, les systèmes satellitaires ont tout d'abord démocratisés la téléphonie par satellite puis la transmission d'information. Aujourd'hui, les systèmes satellitaires sont couramment utilisés pour la diffusion de contenu multimédia et pour les applications de navigation par satellite. Il existe cependant plusieurs différences cruciales entre ces deux types d'applications. La première différence réside dans leurs buts respectifs, débit maximal pour la diffusion multimédia et synchronisation maximale pour les systèmes de navigation. Pour ce faire, la tendance actuelle des systèmes de diffusion multimédia est d'augmenter la fréquence jusqu'aux bandes Ka et Q/V donnant accès à une bande passante plus large. Les systèmes de navigations quant à eux utilisent des codes d'étalement plus importants permettant une synchronisation plus précise. La deuxième différence principale est le segment spatial où les systèmes de diffusion multimédia utilisent principalement des satellites géostationnaires uniques (GEO *(Geostationary Earth Orbit)*) tandis que les systèmes de navigations ont recourt à des constellations de satellites à défilement sur des orbites plus basses (MEO *(Medium Earth Orbit)*). Il en résulte un mouvement du satellite différent, allant de fixe pour un GEO à variable pour un MEO avec des changements d'élévation et d'azimut. Cette différence de mouvement résulte en un décalage Doppler important pour les systèmes utilisant des satellites à défilement. Une dernière différence entre ces deux applications est liée au mouvement du récepteur: fixe ou mobile. Pour les systèmes fixes de diffusion multimédia, la réception s'effectue dans des conditions quasi-optimales. En revanche, pour les systèmes mobiles (radiodiffusion SDMB ou navigation par satellite), le récepteur se déplace dans des environnements complexes où les conditions de propagation optimales sont rarement atteintes. Ces systèmes soufrent alors d'ombrages dus à la végétation, de blocages dus aux bâtiments, d'évanouissements dus aux multitrajets, d'échos retardés, d'étalement Doppler ou de dépolarisation des signaux.

Pour des raisons économiques, les évolutions des systèmes satellitaires sont rares et les marges d'exploitation sont de plus en plus réduites. Ces contraintes impliquent un contrôle strict de nombreux paramètres ayant une incidence sur l'ensemble du système. Afin de concevoir et de maintenir de tels systèmes, des outils spécifiques doivent être créés et intégrés dans des chaînes de simulation systèmes où la propagation des ondes EM ne représente qu'un paramètre parmi tant d'autres influant les performances du système.

Ainsi, la présente étude vise à modéliser le canal de propagation Terre/espace, ou LMS *(Land Mobile Satellite)*, en gardant à l'esprit une approche système liée à l'application finale: les systèmes de navigation par satellite. Ce travail traite plus précisément de la problématique des multitrajets, ou MP *(Multi Path)*, en environnement urbain pour des récepteurs mobiles, où les conditions de propagation des ondes EM sont sévèrement dégradées.

Les enjeux de la présente étude sont d'avoir une meilleure compréhension *a priori* des conditions de propagation des ondes EM dans les milieux urbains complexes afin de garantir la cohérence des évolutions des systèmes de prochaine génération. A titre d'exemple, ce travail pourrait conduire à la conception de nouveaux récepteurs robustes aux MP utilisant des réseaux d'antennes, au design de nouvelles modulations des signaux pour les rendre plus robustes aux MP ou encore à l'ajustement du segment spatial pour une meilleure disponibilité. Ce travail pourrait également contribuer à standardiser les concepts d'intégrité et d'enveloppes d'erreur pour des applications critiques telles que les transports autonomes ou l'aviation civile. Enfin, ce travail représente une alternative aux campagnes de mesures grande échelle généralement très coûteuses.

Au cours de la dernière décennie, plusieurs solutions ont été proposées pour modéliser le canal de propagation LMS pour les télécommunications mobiles par satellite et pour les systèmes de navigation par satellite. Parmi ces modèles, certains d'entre eux sont d'un grand intérêt pour la présente étude.

On retrouve dans la littérature deux approches principales pour la modélisation du canal LMS. La première approche englobe tous les outils déterministes. Ils sont basés sur des techniques de lancer de rayons et l'utilisation de méthodes EM numériques plus ou moins rigoureuses reproduisant les interactions entre les ondes et l'environnement. Particulièrement adaptées à la modélisation du canal de propagation LMS, les approches déterministes offrent une vaste gamme de sorties dans le cas d'environnements synthétiques maitrisés, et notamment, la puissance, la phase, la polarisation, le retard, les directions d'arrivées, ou DoA *(Direction of Arrival)*, ou l'étalement Doppler lié à chaque rayon. Toutefois, ces approches présentent plusieurs inconvénients. Tout d'abord, elles ont besoin d'une description précise des environnements synthétiques tels que les matériaux, la géométrie de la scène ou la présence de détails sur les bâtiments. Deuxièmement, elles sont difficiles à mettre en oeuvre car elles utilisent des méthodes numériques complexes permettant des simulations précises, mais généralement prohibitives en temps de calcul.

La seconde approche englobe tous les modèles hybrides physico-statistiques. Les approches hybrides sont un compromis entre temps de calcul et précision de la solution. Cependant, comme ce compromis est spécifique à chaque application et dépend des paramètres finaux étudiés tel que le *level crossing rate* pour les systèmes de communication ou l'erreur de pseudo-distance pour les systèmes de navigation par satellite, un très grand nombre d'approches hybrides ont été proposées. L'une d'elles a été introduite par Oestges [Oest 00] en 2000. Présentant des temps de calculs raisonnables, ce modèle présente en plus l'avantage d'être basé sur des méthodes numériques permettant de calculer les interactions EM sur un environnement simplifié. Conçu pour des systèmes de télécommunications bande étroite, ce modèle souffre cependant d'un manque de réalisme en termes de réponse large bande du canal de propagation. Des travaux plus récents ont été proposés par Lehner [Lehn 07b] en 2007. Sur la base de campagnes de mesures, ce modèle large bande conçu pour les systèmes de navigation par satellite présente l'avantage d'être standardisé par l'UIT sous la recommandation UIT-R P.681-7 [ITU 09]. Cependant, ce modèle présente plusieurs inconvénients: il est essentiellement empirique, ne repose sur aucune méthode EM numérique, n'est pertinent que pour des environnements très similaires à ceux où les mesures ont été réalisées, reste inadapté à la problématique de diversité de satellite et est limité à la bande L.

En définitive, les approches hybrides physico-statistiques semblent être un bon compris pour modéliser le canal de propagation LMS. Suffisamment précises avec des temps de calcul raisonnable, ces approches présentent un meilleur compromis comparé aux approches déterministes. Toutefois, les modèles existants sont soit inadaptés aux questions large bande et à la problématique de la navigation par satellite soit incomplets en termes de modélisation EM les rendant peu polyvalents.

En conclusion, cette étude est motivée par la nécessité de comprendre et de modéliser finement les phénomènes de propagation des ondes EM affectant les systèmes de navigation par satellite pour améliorer la précision de représentation du canal de propagation sans pour autant négliger l'efficacité en temps de calcul. Cette étude consiste donc à élaborer un simulateur de canal de propagation basé sur une approche physico-statistique et adapté à la modélisation des multitrajets pour les systèmes de navigation par satellite.

Le raisonnement qui a été suivi au cours de cette étude peut être divisé en quatre parties.

Le chapitre 1 présente une synthèse critique des modèles de canal LMS existants et détaille l'approche de modélisation proposée. La première section passe en revue les principales approches qui peuvent être trouvées dans la littérature pour modéliser le canal de propagation LMS. Trois approches sont décrites dans les premières sous-sections, à savoir statistiques, déterministes et hybride physico-statistiques. Un focus particulier est fait sur approches hybrides physico-statistiques. Le concept de ville virtuelle est également abordé. La deuxième section détaille l'approche suivie conduisant à la conception d'un nouveau simulateur de canal LMS large bande temps réel: SCHUN *(Simplified CHannel for Urban Navigation)*. La première partie expose les principaux objectifs ainsi que les contraintes qui doivent être remplies par le simulateur. De l'examen critique des modèles LMS existants, une approche hybride physico-statistique a été choisie et sont présentés le positionnement de l'approche retenue par rapport aux modèles existants, la macro architecture du simulateur ainsi que les sorties typiques attendues.

Le chapitre 2 est centré sur la question de la modélisation des environnements urbains complexes et plus particulièrement sur la simplification de la représentation des façades. L'interrogation principale est la façon dont les petits détails présents sur les façades complexes interagissent avec des fronts d'ondes et comment les supprimer pour simplifier la représentation des environnements urbains complexes sans dégrader la modélisation du canal de propagation. La première section détaille le protocole expérimental qui a été utilisé, où les petits éléments présents sur les façades ont été étudiés à l'aide de la méthode des moments, ou MoM *(Method of Moments)*. La deuxième section présente quelques observations préliminaires sur les courants de surface induits, les surfaces équivalentes radar ou encore les motifs de diffusion calculés sur des façades canoniques isolées. La troisième section présente les résultats de l'impact de petits éléments sur des séries temporelles de puissance bande étroite tandis que la quatrième section s'attache à l'aspect large bande du canal à travers l'émulation logicielle d'un récepteur de navigation. Enfin, dans la cinquième section, l'approximation de façades 2.5D est présentée et des recommandations sont faites quant au niveau de simplification acceptable lors de la représentation d'environnement urbains complexes pour des études faible bande et large bande.

Le Chapitre 3 traite de la modélisation simplifiée des interactions EM sur les bâtiments. Ce chapitre introduit un nouveau modèle physique simplifié reproduisant la fonction de macro-diffusion par des façades complexes selon l'approximation de façade 2.5D. Le modèle 3CM *(3 Component Model]* est basé sur une approche physique où l'interaction d'un front d'onde avec une façade complexe produit une fonction de macro-diffusion qui peut être divisée en la contribution de trois mécanismes de propagation différents, à savoir la réflexion spéculaire, la rétrodiffusion et la diffusion incohérente. La première section présente quelques observations préliminaires faites sur des résultats de simulations et des mesures expérimentales ayant conduit à l'isolation des différents mécanismes de propagation. La deuxième section présente l'approche choisie et détaille chacun des trois mécanismes de propagation. La troisième section présente des validations EM et système du modèle 3CM considérant des configurations canoniques et des scénarios urbains simples. Un outil logiciel commercial basé sur les méthodes asymptotiques a été utilisé comme référence durant cette validation.

Le chapitre 4 présente l'intégration des résultats des chapitres précédents en un simulateur de canal de propagation basé sur une approche physico-statistique et adapté à la modélisation des multitrajets pour les systèmes de navigation par satellite: SCHUN. La première section est consacrée à la présentation globale et à la mise en oeuvre du simulateur SCHUN avec un rappel des principaux choix de conception qui ont été faits, des capacités du simulateur et une présentation du scénario de référence utilisé par le simulateur. Sont ensuite présentés l'algorithme de synthèse des environnements virtuels ainsi que le modèle obstruction du trajet direct pour reproduire les effets de blocage dû aux bâtiments. Dans un dernier temps une nouvelle méthode pour réduire le nombre de multitrajets est présentée. Les deuxième et troisième sections présentent deux validations expérimentales du simulateur SCHUN basée sur deux campagnes de mesures différentes.

La validation expérimentale faite dans la seconde section est orientée vers les systèmes de communication MIMO par satellite avec diversité de polarisation. Pour cette validation, différents paramètres du système ont été analysés sur les séries temporelle bande étroite comme, les canaux co et cross polarisés, l'étalement Doppler du spectre, les distributions d'atténuation, l'estimation du facteur de Rice, le *level crossing rate* ou encore la durée des évanouissements. L'autre campagne expérimentale présentée dans la troisième section consiste en une validation indirecte large bande, où le canal de propagation est observé à travers l'émulation logicielle d'un récepteur de navigation par satellite. Plusieurs paramètres internes au récepteur sont analysés comme le C/N0 et l'erreur de pseudo-distance à l'aide des canaux mesurés et des canaux synthétisés en utilisant le simulateur SCHUN. Enfin, une brève discussion est menée sur les capacités et les limites actuelles du simulateur SCHUN suivie d'une conclusion venant clore ce résumé étendu en français.

D.2 Etude critique et proposition d'un nouveau simulateur

D.2.1 Les différentes approches

On retrouve généralement dans la littérature trois grands types d'approches pour modéliser le canal de propagation LMS, à savoir statistique, déterministe et hybride physico-statistique. L'approche retenue par l'utilisateur est le reflet d'un compromis entre temps de calcul et précision de la solution finale. Intuitivement, l'utilisation de statistiques dans un modèle réduit le temps de calcul au détriment de la précision du résultat en opérant des simplifications. A l'inverse, l'introduction de déterminisme dans un modèle augmente le temps de calcul au bénéfice de la précision grâce à l'utilisation de modèles EM complexes.

Bien que très différentes dans leurs conceptions respectives, toutes les approches de modélisation peuvent être regroupées compte tenu de la modélisation des deux entités essentielles: l'environnement de propagation et les interactions EM sur l'environnement. D'après la littérature, tous les modèles présentés ci-après ont été regroupés dans la Figure.D.1 en fonction de la modélisation de chacune des deux entités essentielles. Les approches statistiques sont basées sur une représentation très simplifiée de l'environnement de propagation avec absence de modélisation des interactions EM avec l'environnement. Les approches déterministes sont quant à elles basées sur la modélisation d'environnements déterministes réalistes sur lesquels des interactions EM physiques sont calculées. Les modèles hybrides physico-statistiques sont eux basées soit sur des environnements statistiques avec des interactions EM physiques soit sur des environnements déterministes avec des interactions statistiques ou simplifiées.

D.2.2 Les modèles statistiques

On recense essentiellement trois types d'approches statistiques, les modèles de distribution d'atténuation bande étroite, les modèles faible bande à état discrets et enfin les modèles large bande à états discrets. Les modèles de distribution d'atténuation bande étroite permettent de reproduire la puissance totale reçue en combinant les masquages à moyenne échelle dû aux bâtiments avec les évanouissements à petite échelle dû aux multitrajets. Ces modèles présentent l'avantage d'être simples et efficaces en termes de temps de calcul. En revanche, ces modèles sont extrêmement dépendants des environnements où ont été effectués les mesures. En pratique, ces modèles ne sont utilisés que pour le dimensionnement des marges opérationnelles des systèmes de communication par satellite et montrent des limites critiques dans le cas d'une forte variation des conditions de masquage. Une approche plus précise est définitivement requise pour les applications mobiles. Ainsi, les distributions d'atténuation faible bande sont écartées de la présente étude critique.

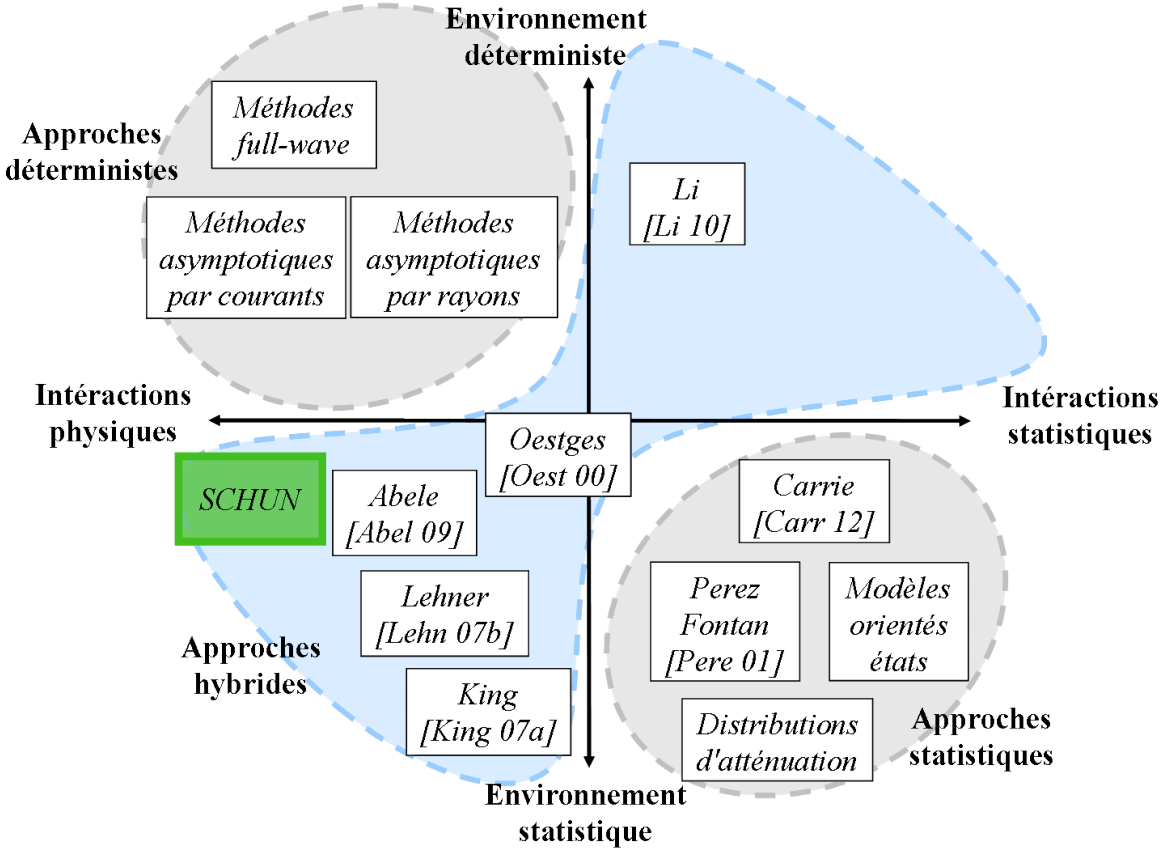

Figure D.1: Classification des différentes approches et positionnement de l'approche retenue

Une alternative aux modèles de distributions d'atténuation bande étroite est de les combiner avec des chaînes de Markov pour construire des modèles statistiques faible bande à états discrets. Le principe est d'associer une distribution d'atténuation bande étroite à chaque état discret de la chaine de Markov, chaque état étant représentatif de la condition de masquage du trajet direct. Cette technique permet de générer des séries temporelles plus réalistes avec des temps de calcul réduits. La complexité de ces modèles est raisonnable et la mémoire allouée aux paramètres d'entrée est réduite (W et matrices P). Le principal inconvénient de cette méthode est sa dépendance à l'égard de campagnes de mesure permettant d'ajuster la machine d'état ainsi que les distributions d'atténuation bande étroite. Ce réglage dépend principalement du type d'environnement et de la configuration elevation/azimut de la source.

Les deux types de modélisation précédemment présentées sont cependant orientées vers des problématiques faible bande, représentant un inconvénient critique pour nos applications. Des modèles plus avancés et orientés large bande ont été proposés plus récemment en intégrant la dimension de retard des échos. On peut citer parmi eux le modèle Perez-Fontan [Pere 01] reposant sur l'hypothèse WSSUS ou le modèle Carrié [Carr 12] portant sur la modélisation des canaux LMS MIMO corrélés. Cependant, ces modèles souffrent soit de limitations pour des applications de diversité de satellites soit d'un manque de réalisme lors de la synthèse des multitrajets. D'une manière générale, la principale limite des modèles statistiques est leur dépendance aux campagnes de mesures permettant de les ajustés.

D.2.3 Les modèles déterministes

Full-wave	Méthode intégrale dans le domaine fréquentiel (IEFD, MoM) Méthode des éléments finis dans le domaine fréquentiel (FEFM) Méthode des différences finies dans le domaine temporel (FDTD)	
Asymptotiques	**Méthodes par rayons**	**Méthodes par courants**
	Optique géométrique (GO, SBR, RT) Théorie uniforme de la diffraction (UTD)	Optique physique (PO) Théorie physique de la diffraction (PTD)

Table D.1: Synthèse des différentes méthodes numériques présentent dans les approches déterministes

Deux types d'approches déterministes sont couramment utilisées, les méthodes *full-wave* et les méthodes asymptotiques. Bien que polyvalentes et ne reposant sur aucune hypothèse limitante, les méthodes full-wave sont restreintes à des problèmes de quelques longueur d'ondes à cause de leur consommation en ressources informatiques (CPU et mémoire) ce qui les rend inadaptées pour de grand environnement urbains à haute fréquence. Ces méthodes ne sont donc pas considérées dans la suite de notre étude critique.

A l'heure actuelle, les méthodes asymptotiques restent la meilleure solution compte tenu de leur précision globale et du nombre de sorties possibles permettant de réaliser des études paramétriques. DoA, puissance, retard ou Doppler sont des informations facilement accessibles grâce aux méthodes par rayons et par courants. Proche de la réalité, les méthodes asymptotiques sont cependant tributaires de la modélisation des environnements. Pour des résultats précis, l'environnement doit être fidèlement représenté en termes de géométrie (complexe en général) et de matériaux (nombreux types de matériaux). Cette étape de modélisation devient rapidement limitée aux environnements de moyenne taille (à l'échelle d'une rue). A noter également que les simulations sont souvent orientées vers des scénarios spécifiques, ou *site specific*, ce qui signifie que pour chaque scène, un nouvel environnement doit être produit. En termes de temps de calcul, les méthodes asymptotiques sont encore prohibitives, même si les méthodes par rayon sont quelque peu plus rapides comparées aux méthodes par courant. Néanmoins, les méthodes asymptotiques par rayons, telles que l'optique géométrique ou GO *(Geometrical Optics)*, restent insuffisantes pour reproduire les nombreuses contributions du canal dans les milieux urbains complexes et de récentes mesures [Arta 08] ont montrées que les récepteurs GNSS logiciel perdent régulièrement la poursuite des satellites. Les méthodes par courant et notamment l'optique physique ou PO *(Physical Optics)* sont plus adaptées à cette problématique de représentation fidèle des multitrajets, mais sont aussi plus consommatrices en ressources et en temps de calcul.

En définitive, les méthodes asymptotiques sont particulièrement adaptées à la problématique de la modélisation du canal LMS. Leur principal inconvénient reste le temps de calcul. Néanmoins, les méthodes asymptotiques par courant sont une bonne référence, pour des environnements à échelle d'une rue, et ces méthodes seront utilisées dans le présent document comme méthodes de référence au travers de la suite logicielle SE-WorkBench présenté en Annexe B.3.

D.2.4 Les modèles hybrides physico-statistiques

Il existe beaucoup de modèles hybrides physico-statistiques où chacun est basé sur un équilibre spécifique entre modélisation statistique et déterministe. Cet équilibre est généralement représentatif d'un compromis particulier fait pour chaque type d'application. Pour chacun des modèles hybrides ci-après décrits, l'application ciblée est rappelée ainsi que les principaux avantages et inconvénients concernant la modélisation de l'environnement et des interactions EM.

Le premier modèle a été introduit par Oestges [Oest 00] en 2000 et traite de la modélisation du canal de propagation LMS pour les systèmes de communication par satellite LEO *(Low Earth*

Orbit). A noter qu'il est particulièrement axé sur l'évaluation de performances système. Le principal avantage de l'approche retenue réside dans l'utilisation de techniques de tracer de rayons. L'utilisation du concept de ville virtuelle est aussi l'un de ses points forts permettant de gérer nativement les questions de diversité de satellite. Principalement utilisé pour la synthèse de séries temporelles bande étroite, ce modèle est partiellement adapté à la problématique large bande. Cependant, l'aspect large bande présente des limitations concernant la modélisation de la composante multitrajet et plus particulièrement l'étalement de retard en raison de l'utilisation de méthodes asymptotiques par rayon telles que l'OG.

Le second modèle a été introduit par King [King 07a] en 2007 et traite de la modélisation MIMO du canal de propagation LMS. Parmi les trois différents modèles proposés, le modèle large bande souffre d'un recours intensif aux statistiques extraits de campagnes de mesures permettant d'ajuster les chaînes de Markov ainsi que les distributions d'atténuation et les coefficients de corrélation MIMO. Cette approche basée exclusivement sur des mesures expérimentales présente l'inconvénient d'être rigide et peu polyvalente.

Le troisième modèle a été introduit par Lehner [Lehn 07b] en 2007 et traite de la modélisation du canal LMS pour la navigation par satellite dans différents environnements ciblant les applications véhiculaire et piéton. Ce modèle est standardisé par l'UIT. Cependant, le modèle LMMC souffre d'un recours omniprésent aux statistiques, dérivées de mesures en bande L, permettant de modéliser la composante multitrajet (puissance, nombre et position des éléments de diffusion, profil de retard ...). L'approche, consistant à jeter des diffuseurs ponctuels dans l'environnement en fonction de la position du satellite, affecte significativement les résultats de diversité de satellites puisque différentes réalisations décorrélées du même environnement sont utilisées pour modéliser la composante multitrajet. L'utilisation de distributions statistiques ajustées aux environnements mesurés rend d'autant plus inappropriées les simulations pour des environnements très différents de ceux mesurés. A noter aussi que les interactions EM entre le trajet direct et l'environnement sont calculées en utilisant des modèles EM scalaires simples tels que la diffraction de Kirchhoff-Fresnel, ou le modèle empirique MED *(Modified Exponential Decay)* représentant l'atténuation à travers les arbres.

Le quatrième modèle a été introduit par Abele [Abel 09] en 2009 et traite de la problématique générale de la modélisation du canal LMS pour les systèmes de télécommunication par satellite en bande L, S et C. Le simulateur est basé sur une approche modulaire qui permet à l'utilisateur de choisir le niveau de précision en utilisant des modèles empiriques simples ou physiques plus rigoureux. Ce simulateur reste cependant axé sur une modélisation bande étroite. Néanmoins, un modèle original a été proposé dans le cadre de ce travail permettant de synthétiser simplement la puissance totale multitrajet provenant d'environnements urbains complexes.

Un dernier modèle a été introduit par Li [Li 10] en 2010 et traite de la modélisation temps réel faible bande du canal LMS pour les systèmes de télécommunication par satellite. Ce modèle a l'avantage d'être basé sur des environnements 3D réalistes gérant nativement la question de la diversité de satellite. Toutefois, ce modèle souffre d'une procédure d'ajustement basée exclusivement sur des simulations numériques, contrairement au recours conventionnel aux campagnes de mesures.

A l'heure actuelle, bien que conçus pour des applications aux besoins spécifiques, les modèles hybrides physico-statistiques présentent un bon compromis permettant d'optimiser les temps de calcul grâce à une composante statistique tout en conservant des résultats réalistes en utilisant des modèles physiques EM ou des ajustement par rapport à des données expérimentales. Ainsi, pour chaque segment d'application, les approches hybrides sont suffisamment précises avec des temps de calcul réduits par rapport aux méthodes déterministes passe partout mais coûteuses en ressources.

D.2.5 Approche retenue et positionnement de la thèse

Les principales contraintes de design permettant de répondre à nos objectifs sont les suivantes:

- Représentation large bande du canal de propagation LMS avec une attention particulière sur la modélisation des multitrajets en termes d'amplitude, phase, polarisation, retard et Doppler.
- Calcul pseudo-temps-réel.
- Conception indépendante de campagnes de mesures.
- Gestion native de la diversité de satellite, de la diversité spatiale de reception, de la diversité de fréquence et de la diversité de polarisation.
- Adaptable en fréquence aux bandes L, S et C.
- Gestion de grands environnements.
- Diversité des sorties possibles (DoA, spectre Doppler ...).

A partir des contraintes énoncées, les modèles LMS existants précédemment décrits ont été comparés dans le Tableau.D.2. Il en ressort qu'aucuns de ces modèles ne satisfait pleinement nos objectifs et un nouveau simulateur de canal devra par conséquent être développé.

		Large bande	Temps réel	Indépendant de mesures	Orienté MIMO	Ajustable en fréquence	Grande scènes	Polyvalence des sorties
Statistique	Markov	✗	✓	✗	✗	✗	✓	✗
	[Pere 01]	✓	✓	✗	✗	✗	✓	✗
	[Carr 12]	✗	✓	✗	✓	~	✓	✗
Déterministe	Asymp. Cur.	✓	✗	✓	✓	✓	~	✓
	Asymp. Rays	✓	~	✓	✓	✓	~	✓
Hybride physico-statistique	[Oest 00]	~	~	✓	✓	✓	✓	~
	[King 07a]	✓	~	✗	✓	✗	✓	✗
	[Lehn 07b]	✓	✓	~	~	~	✓	✓
	[Abel 09]	✗	~	✓	✗	✓	✓	✗
	[Li 10]	✗	✓	✓	✓	~	~	✗

Table D.2: Comparaison critique des modèles de canal existant en fonction de nos objectifs

L'approche finale retenue est basée sur une approche hybride physico-statistique, présentant le meilleur compromis en termes de précision et de temps de calcul. L'architecture globale du simulateur SCHUN *(Simplified CHannel for Urban Navigation)* proposé est présentée Fig.D.2. Comparé aux autres modèles hybrides, ce simulateur de canal n'intègre que peu de statistiques, leur usage étant restreint à la synthèse d'environnements virtuels. La synthèse de ces environnements est d'ailleurs indépendante des paramètres de simulation tels que la position des satellites, le type de configuration MIMO ou encore le type de sorties contrairement à certains modèles existants. Sur le plan des interactions EM, le simulateur SCHUN intègre autant que possible de modèles physiques basés sur la théorie EM assurant une certaine polyvalence (fréquence, polarisation ...), sans pour autant négliger les temps de calcul.

Les modèles d'interaction EM simplifiés, sur la végétation et sur les bâtiments, sont basés sur des modèles physiques EM tels que GO et PO. Le modèle reproduisant le masquage par les bâtiments est quant à lui basé sur l'UTD. A noter que le modèle d'interaction avec la végétation ne sera pas traité dans le cadre de ce document. Cet aspect pourra cependant être traité dans les évolutions futures du simulateur SCHUN en adaptant la littérature existante [Chef 10] [Abel 09].

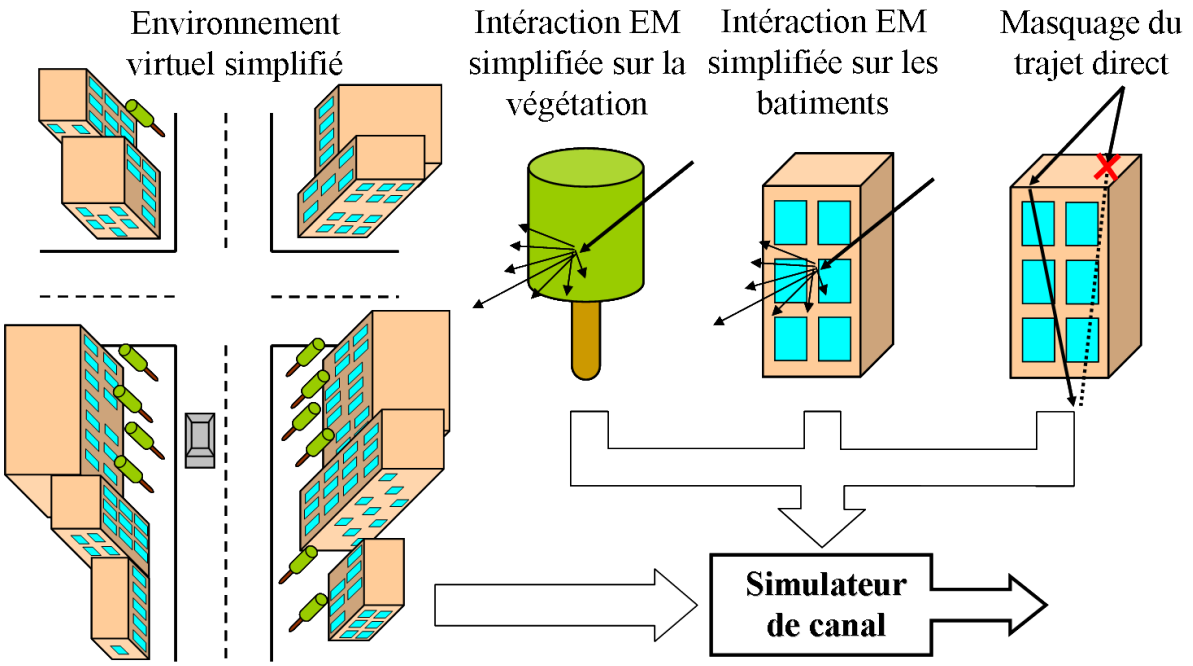

Figure D.2: Architecture hybride proposée pour le simulateur SCHUN

Le point de départ de notre réflexion porte sur la modélisation d'environnements urbains complexes. L'accent a été mis sur la façon de représenter l'environnement et son impact sur le canal de propagation LMS. Comme mentionné précédemment, l'utilisation d'outils déterministes nécessite une représentation précise de l'environnement. Ainsi, un nombre infini de paramètres peuvent être pris en compte dans une telle modélisation: le géo-référencement des objets, les matériaux diélectriques, l'architecture, les espèces d'arbres ou de mobilier urbain.

Dans une première approximation, et d'après les modèles de canal LMS existants, seuls les macro-objets tels que les bâtiments et les arbres semblent avoir un impact majeur sur le comportement du canal. Dans cette première approximation, le mobilier urbain a été négligé. Cela peut se justifier par le fait que la modélisation des lampadaires et autres panneaux de signalisation ne nécessitent pas de nouveaux développements puisqu'ils sont déjà intégrés dans certains modèles existants. Ils pourront ainsi être ajoutés dans un dernier temps. En seconde approximation, l'effet de la végétation a été exclu de la présente étude, mais est déjà considéré comme requis pour les futures évolutions du simulateur.

D.3 Etude de l'influence des détails sur des façades complexes

Dans le cadre de la présente étude, les environnements urbains ont été ciblés et l'accent a été mis sur la modélisation des interactions EM entre les ondes et les bâtiments. Deux approches sont habituellement retenues lors de la modélisation des bâtiments. D'un coté les maillages 3D complexes des façades: ils sont précis mais restent inadaptés à la modélisation d'environnements urbains à l'échelle d'une ville et requièrent de très longs temps de calcul. De l'autre coté, les modélisations utilisant une représentation plane des façades: simples, ces modélisations restent cependant limitées en termes de réalisme de la scène. Le Chapitre 2 traite de la problématique de la synthèse d'environnements simplifiés satisfaisant le compromis entre réalisme et temps de calcul. L'objectif du Chapitre 2 est de quantifier l'influence des petits diffuseurs présents sur les façades complexes dans le but d'identifier quel est le niveau de détail suffisant, permettant de représenter les phénomènes de propagation, sans avoir recours aux modélisations 3D complexes. Cette étude a été réalisée à l'aide d'outils adaptés basés sur la MoM (Elsem3D, Annexe B.3.1) permettant de modéliser les interactions EM avec des objets de petite taille. L'approche est simple: deux façades sont représentées avec quatre niveaux de détail. En faisant évoluer ce niveau de détail, avec plus ou moins de petits objets sur la façade, et en observant certains paramètres tels que les courants de surface, la diffusion en champ proche, la puissance MP totale ou l'erreur de pseudo-distance d'un récepteur de navigation, la contribution de chaque type de diffuseurs peut être isolée et éliminée. La solution finale proposée est donc un modèle intermédiaire, basé sur l'approximation de façade 2.5D, permettant de représenter les bâtiments sans utiliser de maillage 3D complexe, tout en restant plus riche qu'une modélisation 2D avec des surfaces planes. L'accent est mis sur la façon de représenter l'architecture d'une façade, ainsi que sur l'impact des petits détails réels, sur le comportement global du canal. Les conclusions et recommandations de ce chapitre conduisent à des gains de temps de calcul importants, compte tenu d'une représentation plus simple des façades.

D.3.1 Observations préliminaires

Cette section présente plusieurs observations préliminaires sur l'influence des petits éléments et sur les phénomènes de propagations se déroulant à proximité de façades complexes. Cette analyse est réalisée sur des façades canoniques isolées. La figure Fig.D.3 illustre les quatre niveaux de détails utilisés pour représenter une façade de type centre ville de Toulouse. La figure Fig.D.4 illustre l'influence des détails sur la fonction de diffusion à proximité de la façade centre ville de Toulouse pour chacune des quatre résolutions. D'une manière générale, les principales observations faites sur les courants de surfaces, les surfaces équivalentes radar ainsi que sur les fonctions de diffusion sont les suivantes:

- Les courants de surface sont sensibles à l'incidence de la source et présentent un motif en stries en cas d'incidence normale. Pour les incidences quasi-rasantes il en ressort que les bords saillants présentent des concentrations de courant élevées. L'analyse des courants de surface révèle également un masquage quasi-optique entre les différents éléments d'une même façade (balcon et rambardes sur les murs).

- L'étude montre que les SER *(Surface Equivalente Radar)* en champ lointain et en champ proche sont différentes. A noter que les petits objets réduisent le phénomène spéculaire tout en augmentant le phénomène de diffusion ainsi que la contribution en polarisation croisée.

- La réflexion spéculaire reste la plus forte contribution. Elle provient des grandes surfaces lisses et possède un profil angulaire limité. La contribution des petits éléments est inférieure à celle de la réflexion spéculaire et n'est visible qu'en dehors de la zone spéculaire.

- Les effets dièdres et trièdres qui ont lieu dans les coins les fenêtres ont été mis en évidence sur les courants de surface, les SER et les fonctions de diffusion. Ce phénomène sera décrit

comme *rétrodiffusion* dans le Chapitre 3.

- L'architecture de la façade a un fort impact sur tous les paramètres observés. L'étape de classification des façades réelles en façades synthétiques est donc à ne pas négliger.

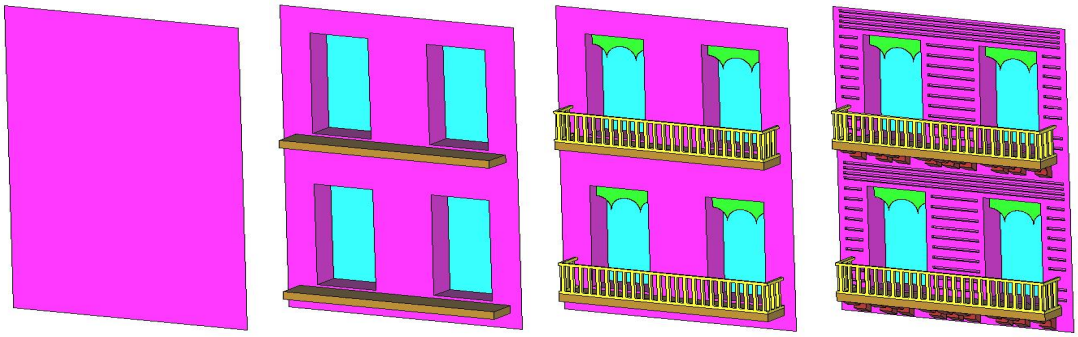

(a) Résolution nulle (b) Résolution faible (c) Résolution moyenne (d) Résolution élevée

Figure D.3: Représentation des quatre niveaux de détail d'une façade type centre ville de Toulouse

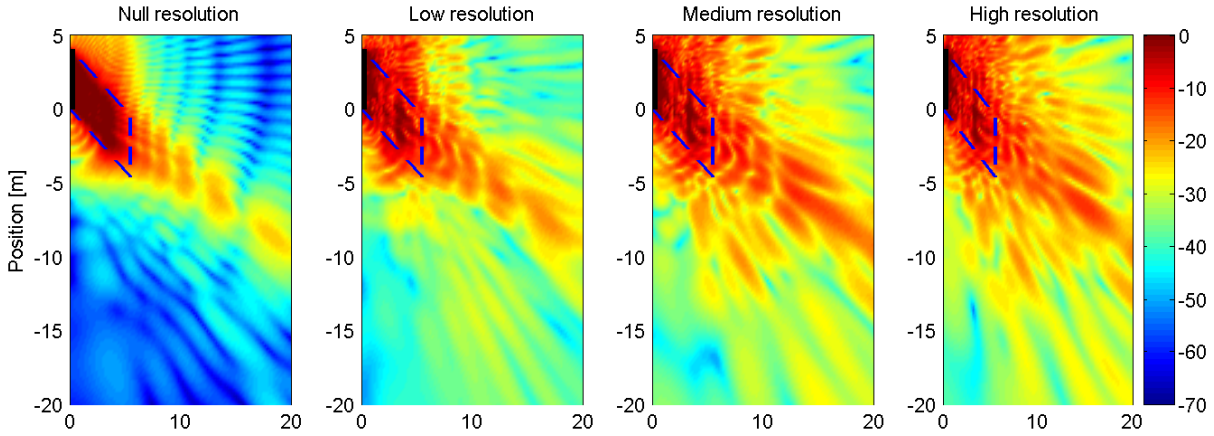

Figure D.4: Motif de diffusion en champ proche dans le plan horizontal d'une façade complexe de type centre ville dans une configuration polarisation ϕ, 40° d'élévation, 40° d'azimut

D.3.2 Analyse faible bande de l'influence des détails

Cette seconde partie de l'analyse traite du cas de canyon urbains simples construits en associant de plusieurs façades canoniques isolées. La principale donnée de comparaison est la série temporelle de puissance faible bande générée en fonction de la résolution du canyon urbain comme illustré Fig.D.5. A noter que la résolution élevée est considérée comme étant la simulation de référence pour l'illustration en bas de la figure Fig.D.5. En considérant une étude statistique paramétrique jouant sur différents paramètres de simulation (canyon urbains, positions de l'émetteur, polarisation de l'émetteur, vitesse du récepteur), leurs influence à pu être mise en évidence. A titre d'exemple car les résultats sont significatifs, la figure Fig.D.6 représente l'influence de la résolution de l'environnement tandis que la figure Fig.D.7 illustre l'influence de la vitesse du mobile. Les principales conclusions sont les suivantes:

- Les détails de l'ordre de la longueur d'onde, ou inférieurs, contribuent fortement au phénomène de diffusion et sont particulièrement visibles hors la zone de réflexion spéculaire. Les négliger en utilisant une résolution nulle déséquilibrerait les phénomènes spéculaires et diffus favorisant de fortes réflexions.

- La résolution nulle montre des limites évidentes puisqu'elle ne reproduit pas le phénomène de diffusion. Il en résulte une puissance MP surestimée dans les cas d'incidence typique pour les systèmes LMS et sous-estimée dans les cas d'incidences extrêmes. La résolution nulle est comparable à un modèle de réflexion on/off avec des effets de transition marqués.
- En utilisant la résolution faible où les détails modélisés sont grands devant la longueur d'onde, la réflexion spéculaire est bien reproduite mais le phénomène de diffusion manque encore de réalisme par rapport à la résolution moyenne. La résolution faible semble acceptable si elle est toutefois légèrement corrigée par un coefficient empirique d'environ +2dB sur la puissance MP moyenne diffusée et filtrée afin de réduire la dynamique du signal.
- Le cas des faibles vitesses de déplacement (5 km/h) semble plus contraignant puisque le processus d'intégration ayant lieu au sein des récepteurs de navigation ne compense pas les évanouissements profonds comme c'est le cas pour des vitesses de déplacement plus importantes (50 et 90 km/h).
- La résolution moyenne semble être le meilleur compromis puisque la résolution élevée n'est de toute façon pas applicable à l'échelle d'une ville.

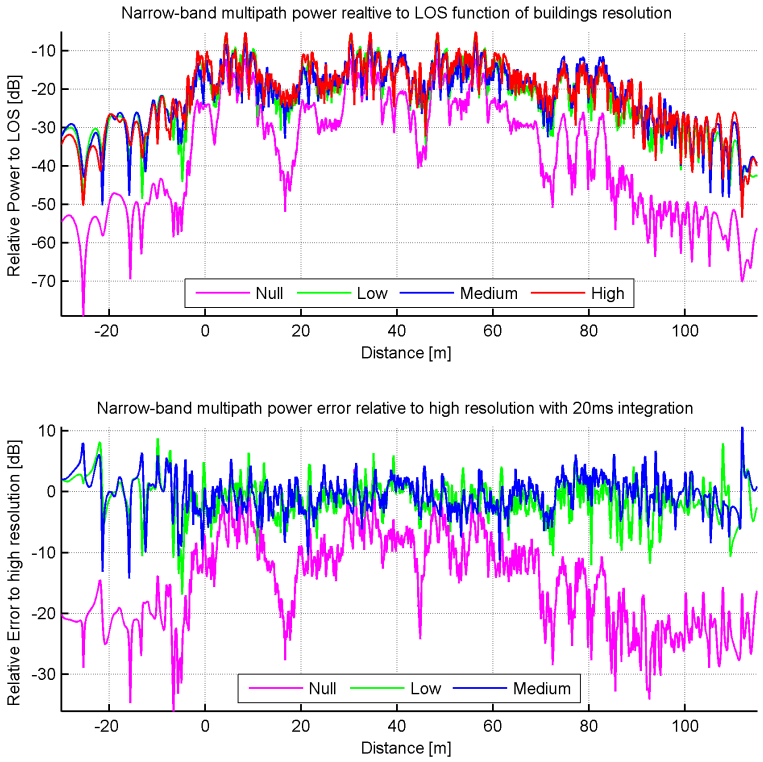

Figure D.5: Exemple de série temporelle de puissance faible bande fonction de la résolution du canal. Paramètres de simulation: canyon urbain 1, azimut 40°, élévation 80°, Tx polarisation ϕ, vitesse 50 km/h

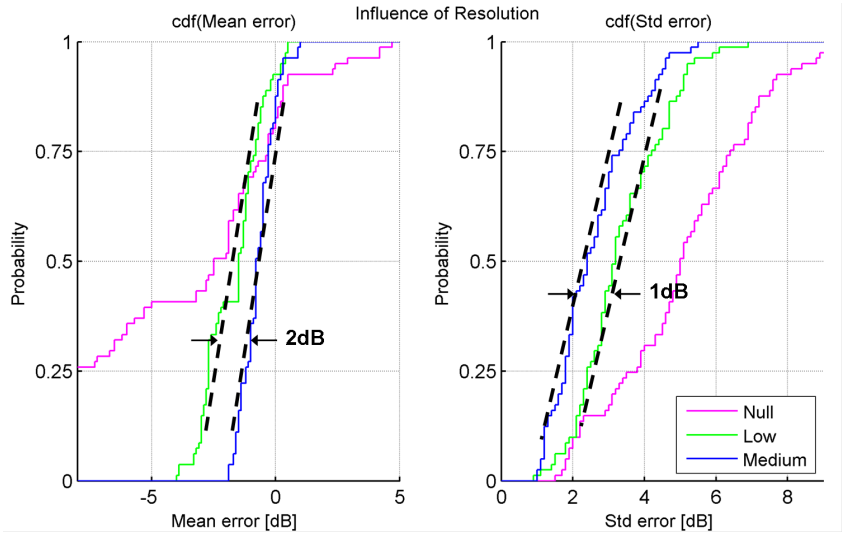

Figure D.6: Influence de la résolution de l'environnement sur la puissance totale diffusée par rapport à la résolution élevée

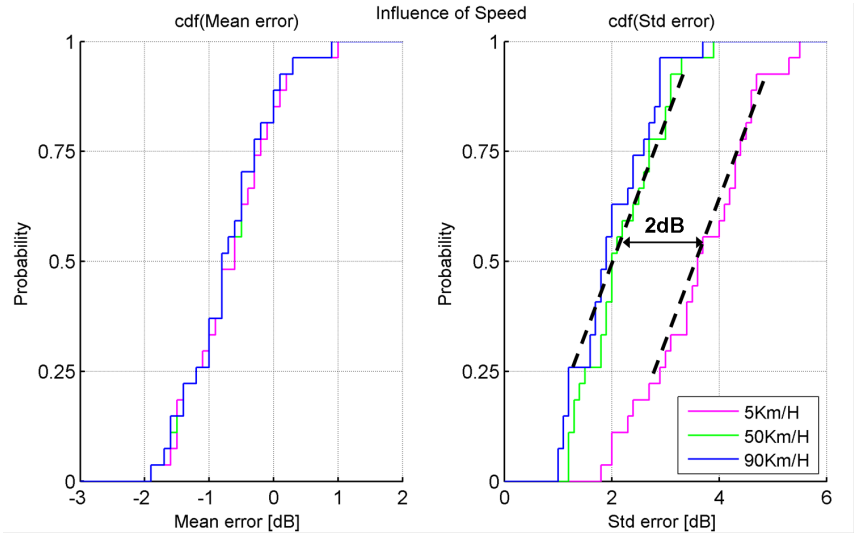

Figure D.7: Influence de la vitesse sur la puissance totale diffusée par rapport à la résolution élevée

D.3.3 Analyse large bande de l'influence des détails

La troisième partie de l'analyse porte sur des aspects large bande orientés vers les systèmes de navigation par satellite. La figure Fig.D.8 représente l'évolution des paramètres large bande du canal en fonction du déplacement du mobile. La figure Fig.D.9 est la synthèse de l'étude paramétrique sur l'influence de la résolution et de la vitesse sur l'erreur de pseudo distance. Dans cette représentation, il est admis qu'une erreur relative de pseudo-distance par rapport au cas de résolution élevée inférieure à 1m (carré en pointillés noirs) peut être considérée comme non significative. Les principales conclusions de cette analyse large bande sont les suivantes:

- Comme observé, le récepteur semble être influencé par les MP dès -15 dB par rapport au LOS. Dans des conditions LOS, les résolutions faibles et moyennes présentent des résultats similaires. Pour les configurations d'incidences extrêmes en conditions LOS, la résolution nulle est même acceptable, puisque la puissance MP est de toute façon très faible. En revanche, lorsque le signal direct est très fortement atténué, les contributions MP deviennent prédominantes et la résolution de l'environnement a un impact plus fort sur les récepteurs de navigation. Le phénomène de diffusion devient donc critique à modéliser.

- En dehors du cas d'incidences extrêmes, la résolution nulle n'est pas adaptée car elle surestime l'erreur de pseudo-distance due à de forts échos.
- Le cas de déplacements lents est lui aussi contraignant puisque les MP restent stable dans un laps de temps plus long et ne sont pas moyennés, ce qui induit de forts biais dans l'estimation de la pseudo-distance.

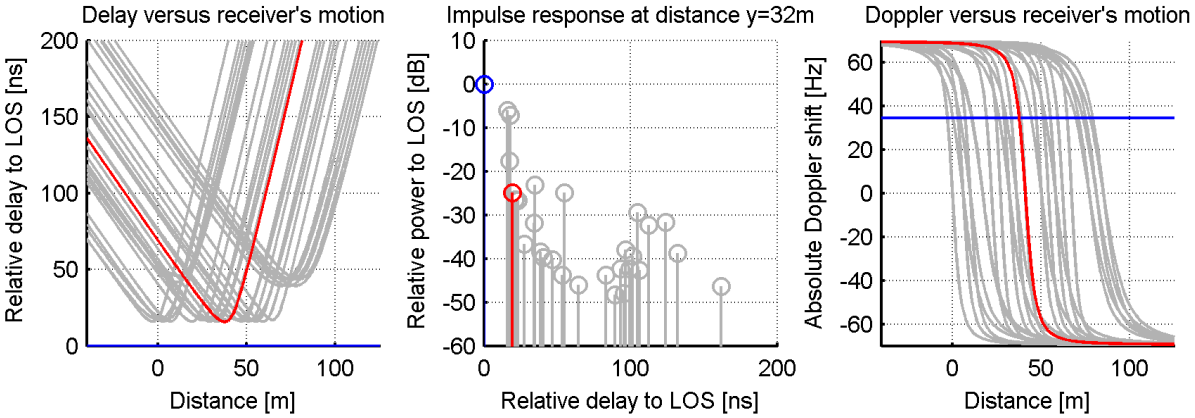

Figure D.8: Evolution des paramètres large bande en fonction du déplacement du mobile dans le canyon urbain (Délais, réponse impulsionnelle instantanée, Doppler)

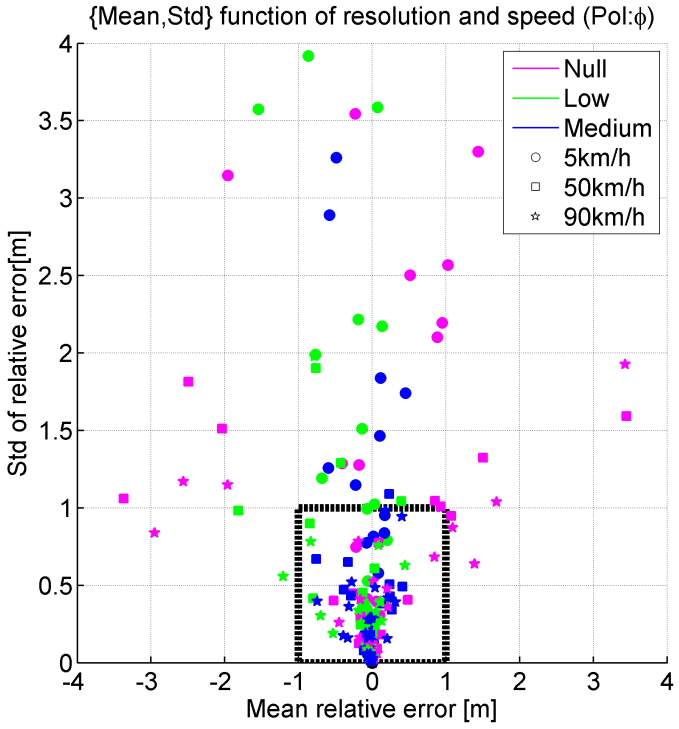

Figure D.9: Etude paramétrique de l'influence de la résolution de l'environnement et de la vitesse du mobile sur le couple d'erreur {Mean,Std}

D'après les recommandations présentées ci-dessus, la modélisation des environnements urbains complexes peut être simplifiée, en termes de détails présents sur les façades, sans changements importants dans le comportement du canal. Cette étude sur la simplification de l'environnement a conduit à une résolution intermédiaire où une modélisation 2.5D des façades est recommandée. Finalement, l'utilisation de l'approximation de façade 2.5D permet une synthèse plus rapide que les modèles 3D et plus réaliste que les modèles 2D sur de grandes zones urbaines. Les simplifications opérées permettent également l'utilisation de méthodes asymptotiques telles que

PO, puisque les petits objets ont été retirés et que les hypothèses asymptotiques sont alors remplies. Cependant, la méthode asymptotique PO reste contraignante en temps de calcul et une nouvelle méthode simplifiée représentant les interactions onde/bâtiments doit être proposée, en accord avec l'approximation de façade 2.5D, pour réduire les temps de calcul.

D.4 Présentation d'un nouveau modèle d'interaction onde/bâtiments

D.4.1 Observations préliminaires

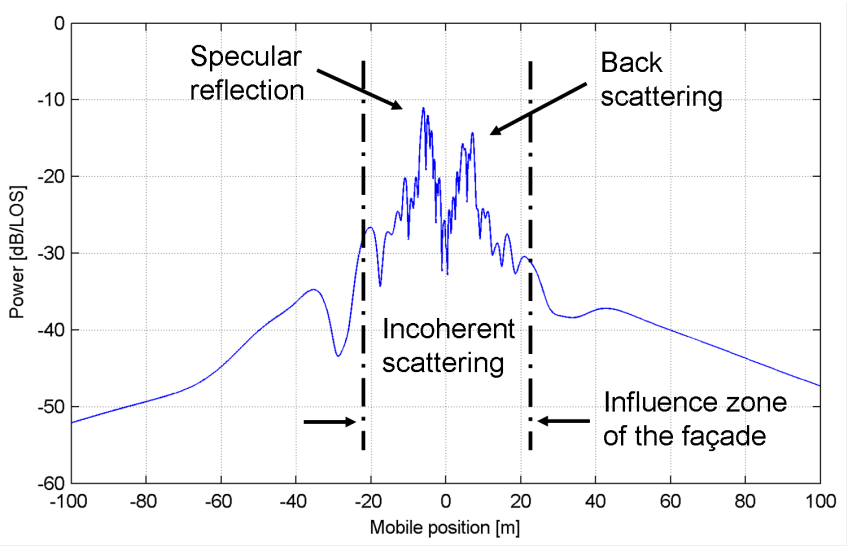

Figure D.10: Puissance totale faible bande reçue lorsqu'un mobile passe à proximité d'une façade complexe (Simulation Elsem3D - MoM)

La première étape de design du nouveau modèle d'interaction EM entre ondes et bâtiments est passée par l'observation. Plusieurs observations ont été faites en utilisant aussi bien des outils numériques, Elsem3D basé sur la MoM (Fig.D.10) ou SE-WorkBench basé sur les méthodes asymptotiques, et des résultats expérimentaux publiés par le DLR. Cette phase d'observation a permis de mettre en évidence plusieurs mécanismes de propagation distincts:

- Un phénomène de réflexion spéculaire, de puissance élevée, provenant de l'avant du mobile. Ce mécanisme est couramment identifié dans la littérature scientifique.
- Un mécanisme de propagation vers l'arrière, également appelé rétrodiffusion ou backscattering, de puissance moyenne, venant de l'arrière du mobile. Ce mécanisme n'est pas identifié dans la littérature scientifique et est généralement intégré à la composante diffuse incohérente bien que le mécanisme de propagation soit très différent.
- Une zone d'influence de la façade, limitée dans l'espace, liée au mécanisme de diffusion à cause de petits éléments présents sur les façades complexes.

D.4.2 Concept du modèle 3CM

La problématique de la diffusion par les surfaces rugueuses a déjà été étudiée notamment dans [Degl 07] et [Pong 04]. D'autres approches visant à homogénéiser les matériaux diélectriques constituant une façade dans un matériau équivalent ont été présentées dans [Most 11]. Des travaux récents discutant quant à eux de la question de la polarisation ont conduits à un modèle empirique basé sur des campagnes de mesures et présenté dans [Vitu 12]. Notre objectif dans cette étude est de concevoir un nouveau modèle de diffusion par les bâtiments basé sur les modèles EM avec un recours minimal aux approches empiriques et aux campagnes de mesure

tout en satisfaisant le compromis entre temps de calcul et polyvalence.

D'après les observations faites précédemment, il en ressort que le phénomène de diffusion par les bâtiments peut être divisé en trois composantes, chacune étant lié à un mécanisme de propagation particulier. Les trois composantes identifiées lors de l'élaboration du modèle 3CM *(Component Model)* sont présentées dans la figure Fig.D.11 et décrites ci-après. A noter que ce principe de décomposition de la fonction de diffusion par les bâtiments a l'avantage d'être potentiellement applicable aux outils de ray-tracing existants sans modifications majeures.

Le modèle 3CM repose sur trois mécanismes de propagation:

- *La réflexion spéculaire:* reproduit un mécanisme de réflexion sur les grandes surfaces lisses telles que les fenêtres et les murs des façades. Cette composante est la plus puissante. Dans son implémentation, la composante spéculaire est basée sur une version simplifiée de l'algorithme PO.

- *La rétrodiffusion ou backscattering:* reproduit une double réflexion au niveau des changements de plan dans l'architecture de la façade tels que le renfoncement des fenêtres ou la protubérance de certains balcons, donnant lieu à des effets dièdres. La composante de backscattering est moins puissante que la réflexion spéculaire mais reste responsable d'importantes contributions venant du côté opposé du signal direct. D'après les modèles existants, cette composante est généralement intégrée à la composante de diffusion incohérente bien que le mécanisme EM soit cohérent. Dans son implémentation, la composante de backscattering est basée sur le même algorithme PO simplifié que le modèle de réflexion spéculaire.

- *La diffusion incohérente:* reproduit le phénomène de diffusion dû aux petits éléments présents sur les façades complexes. Cette composante permet une transition plus douce entre la zone spéculaire et la zone de rétrodiffusion. La diffusion incohérente est aussi caractéristique de la zone d'influence de la façade. Coté implémentation, puisque les petits détails ne devraient pas être considérés par les méthodes asymptotiques telles que PO, l'implémentation de cette composante empirique est basée sur des modèles analytiques extraits de [Ruck 70].

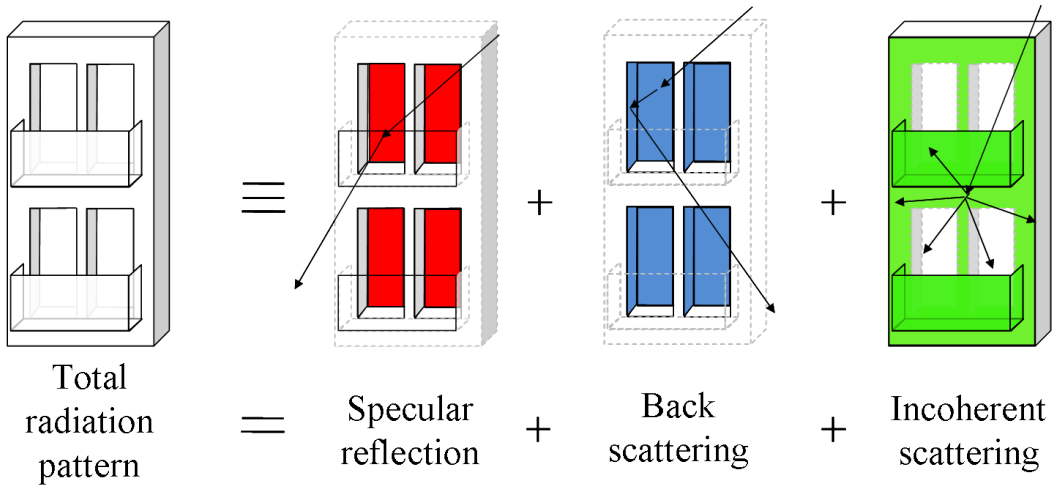

Figure D.11: Principe de décomposition du modèle 3CM

Le principal avantage de l'approche retenue pour le 3CM est son faible cout calculatoire: la fonction de diffusion d'une façade complexe peut ainsi être divisée en trois composantes, chacune étant facile et rapide à modéliser. Cette réduction de l'effort de calcul permet des temps de calcul relativement faibles comparés aux méthodes full-PO. Un autre avantage du 3CM est sa base

EM physique qui lui donne plus de réalisme et de polyvalence comparé aux modèles empiriques. De plus, le 3CM est capable de générer un profil large bande réaliste tout en conservant les informations de Doppler instantané et de DoA.

D.4.3 Validation numérique du modèle 3CM

La première étape de validation a consisté à valider numériquement chacune des trois composantes EM du modèle 3CM. Ces trois composantes ont ensuite été intégrées dans un nouveau modèle, le 3CM, lui-même validé par rapport à des outils numériques dans des configurations canoniques plus complexes. A titre d'exemple, la figure Fig.D.12 présente la puissance totale diffusée par une façade canonique isolée de type centre ville de Toulouse pour différents couples élévation/azimut du satellite où sont comparés les résultats issus d'Elsem3D, de SE-WorkBench et du 3CM. La figure Fig.D.13 présente le cas d'un canyon urbain simple associant plusieurs façades canoniques. La simulation de ce canal par le modèle 3CM a permis d'extraire notamment le spectrogramme (Fig.D.14) à partir de la réponse complexe faible bande du canal le long de la trajectoire du mobile ainsi que la réponse impulsionnelle large bande instantanée du canal (Fig.D.15)

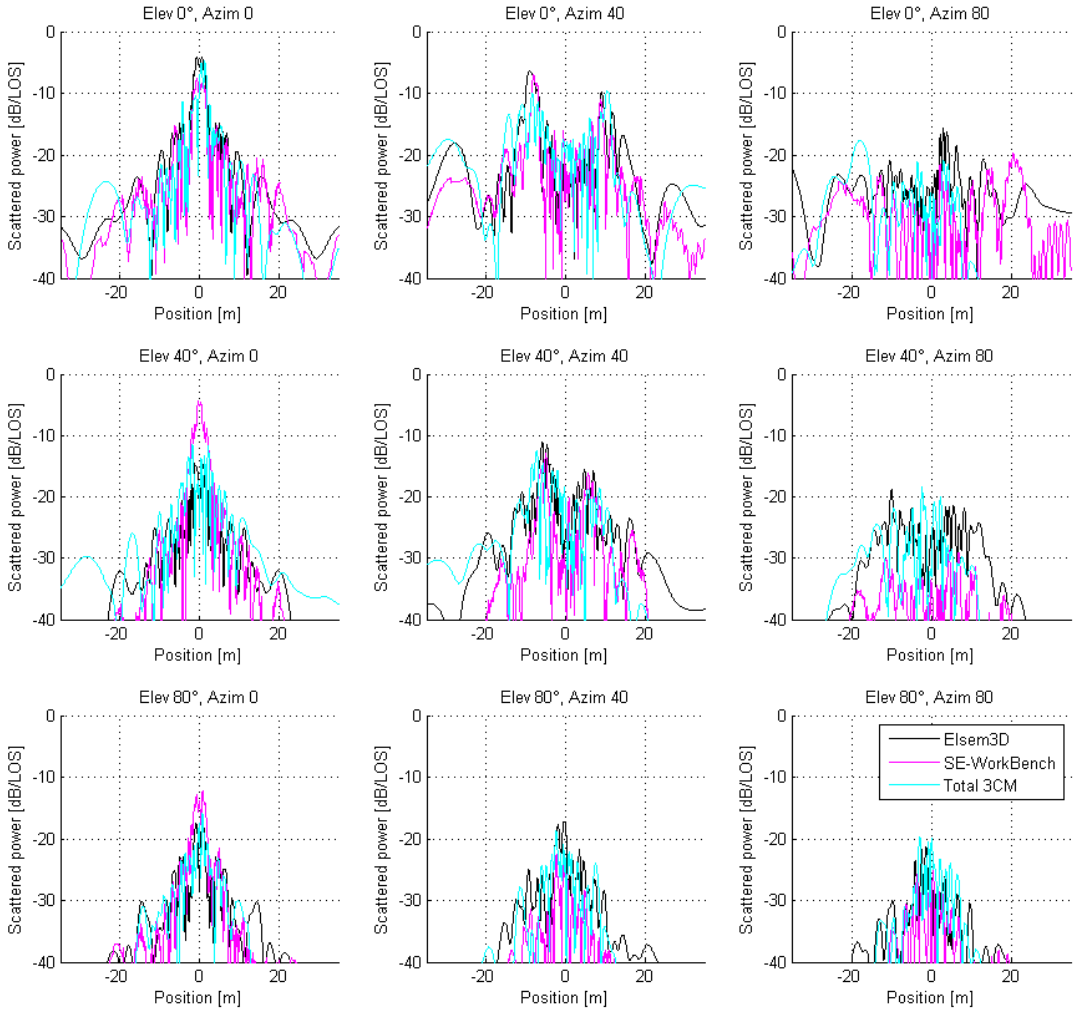

Figure D.12: Puissance totale diffusée par une façade canonique isolée de type centre ville de Toulouse pour différents couples élévation/azimut du satellite

En conclusion, le modèle 3CM est orienté vers la modélisation large bande du canal et des MP avec une attention particulière à la réduction des temps de calcul. Basé sur un algorithme PO simplifié, le 3CM permet d'atteindre un facteur 100 de gain en temps de calcul comparé à SE-WorkBench et aux outils déterministes conventionnels. Puisqu'il est basé sur des modèles

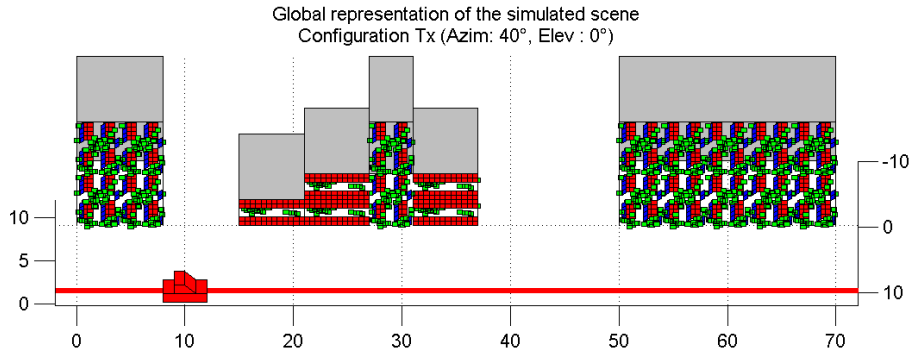

Figure D.13: Représentation 3CM simplifiée du canyon concidéré

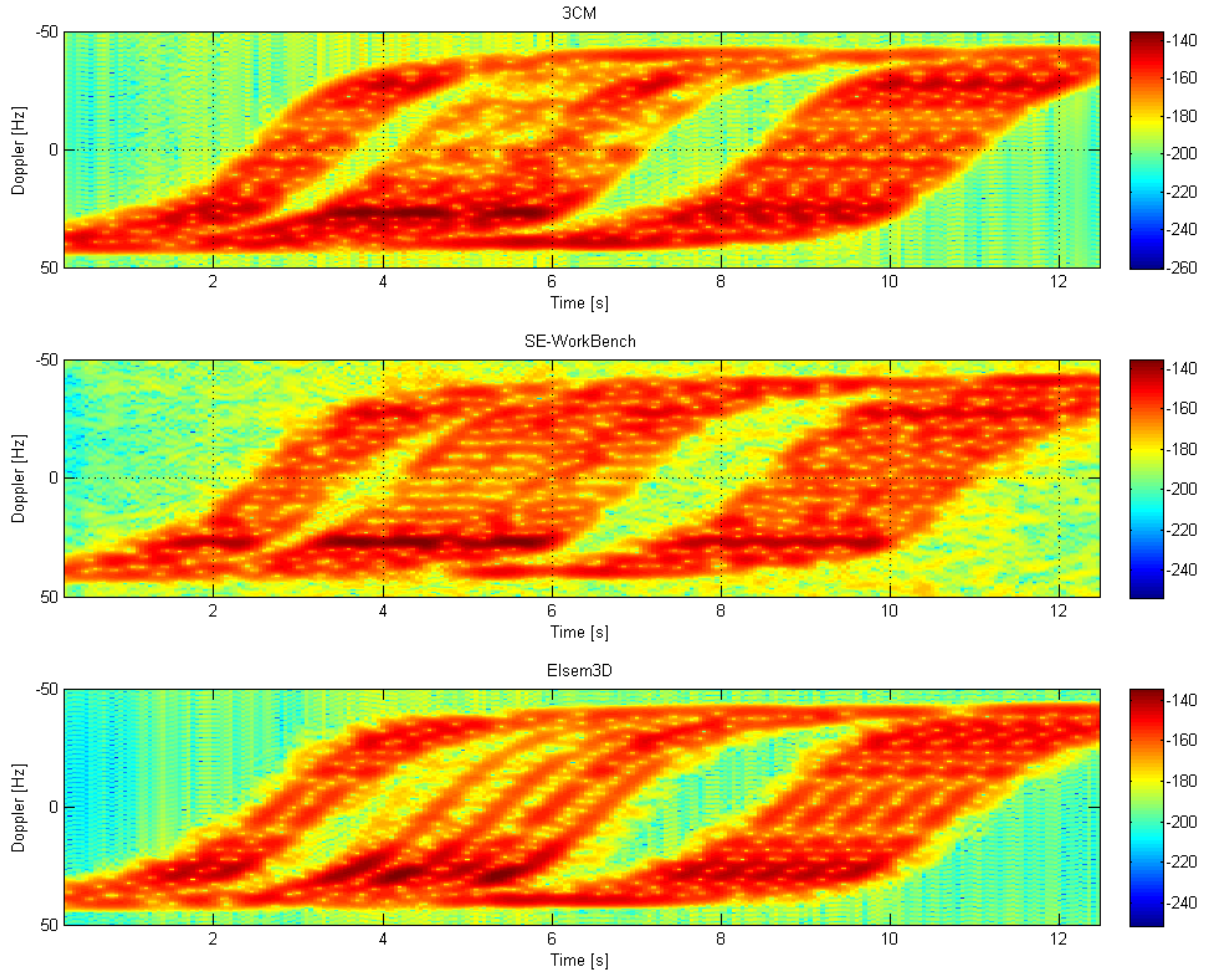

Figure D.14: Spectrogramme le long de la trajectoire du mobile

EM asymptotiques, le 3CM gère parfaitement les matériaux diélectriques et les polarisations elliptiques. Il est également adaptable en fréquence et conçu pour les bandes L, S et C, a priori sans restrictions pour des fréquences plus élevées, bien que cette éventualité n'ait pas encore été étudiée. Les sorties typiques du 3CM sont les retards, Doppler, DoA ainsi que l'amplitude complexe polarisée de chaque rayon. Enfin, le 3CM est adapté aux études MIMO avec diversité d'émission, diversité de polarisation, diversité de fréquence et optimisé pour des diversités spatiales en réception. Le modèle 3CM, est maintenant prêt à être intégré dans un nouveau modèle de canal plus complet reproduisant notamment les masquages du LOS permettant de simuler avec plus de réalisme des environnements plus complexes.

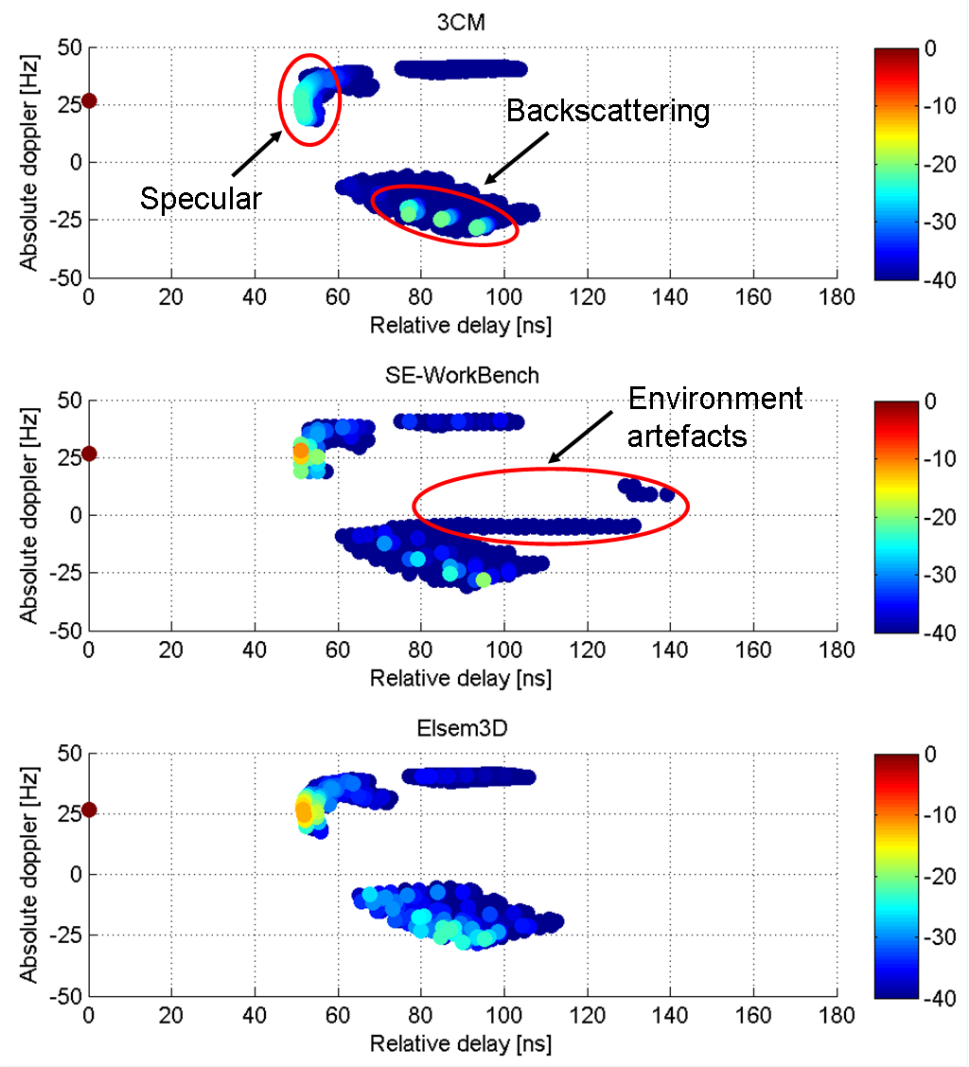

Figure D.15: Réponse impulsionnelle instantanée du canal représentée dans l'espace Puissance/Délais/Doppler

D.5 Implémentation et validation du simulateur de canal SCHUN

Les objectifs du Chapitre 4 consistent à présenter l'implémentation et la validation expérimentale d'un nouveau simulateur de canal de propagation basé sur une approche hybride physico-statistique et adapté à la modélisation des multitrajets pour les systèmes de navigation par satellite.

Le Chapitre 4 est le point focal des travaux menés lors de cette thèse. Pour rappel, grâce à l'examen critique des modèles existants, le Chapitre 1 a présenté une nouvelle philosophie de conception conduisant au design d'un simulateur de canal LMS répondant à nos objectifs. L'étude menée dans le Chapitre 2 a permis de simplifier la modélisation d'environnements complexes en proposant une approximation 2.5D des façades afin de prendre en compte l'architecture spécifique de chaque façade. Basé sur l'approximation de façade 2.5D, le Chapitre 3 a introduit un nouveau modèle large bande d'interaction EM ente ondes et bâtiments basé sur les méthodes numériques EM et en particulier sur l'algorithme PO. Ce modèle permet de prendre en compte la macro rugosité des façades liée à leur architecture ainsi que la micro rugosité liée à l'aspect non lisse des surfaces. Ce dernier chapitre fusionne les observations, conclusions et recommandations formulées précédemment conduisant à la conception d'un nouveau simulateur de canal LMS: SCHUN *(Simplified CHannel for Urban Navigation)*.

D.5.1 Implémentation du simulateur de canal SCHUN

Cette première partie présente l'implémentation finale du simulateur SCHUN comme étant un outil de simulation complet et indépendant permettant d'effectuer la synthèse d'environnements génériques et de reproduire la réponse impulsionnelle complexe du canal de propagation variant dans le temps pour des applications mobiles. A titre d'exemple, la figure Fig.D.16 illustre la synthèse d'environnements urbains virtuels à partir de statistiques d'entrée connues. Deux modèles de masquage du trajet direct ont aussi été proposés: l'un simple, basé sur les méthodes d'intersection de rayons, l'autre plus complexe, basé sur l'algorithme UTD (Fig.D.17). Contrairement au premier modèle, plus adapté à la synthèse de séries temporelles on/off corrélées, le second modèle permet de reproduire des transitions plus douces entre les états LOS et NLOS pour un plus grand réalisme des séries temporelles générées. Enfin, une nouvelle méthode de réduction du nombre de multitrajet basée sur la modélisation de l'environnement est introduite. Cette nouvelle méthode n'a pas encore été entièrement validée, mais présente déjà des perspectives intéressantes pour le post-traitement des réponses impulsionnelles du canal. L'un des principaux domaines d'application ciblé par cette technique est la simulation de systèmes complexes où la propagation EM intervient.

Les deux sections suivantes sont consacrées aux validations expérimentales du simulateur SCHUN. Pour ce faire, deux campagnes de mesures expérimentales ont été utilisées.

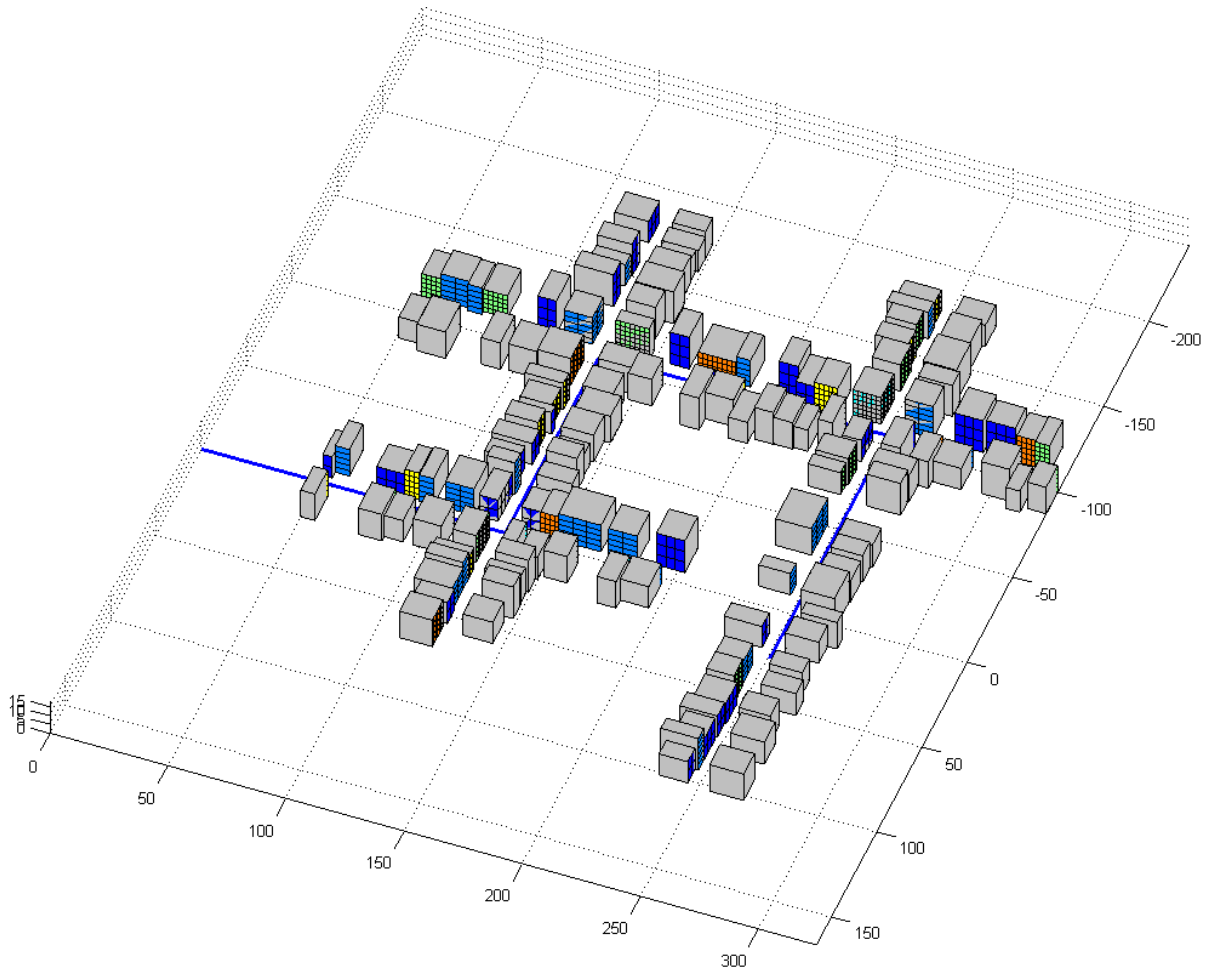

Figure D.16: Exemple d'environnement générique généré statistiquement à partir du concept de ville virtuelle

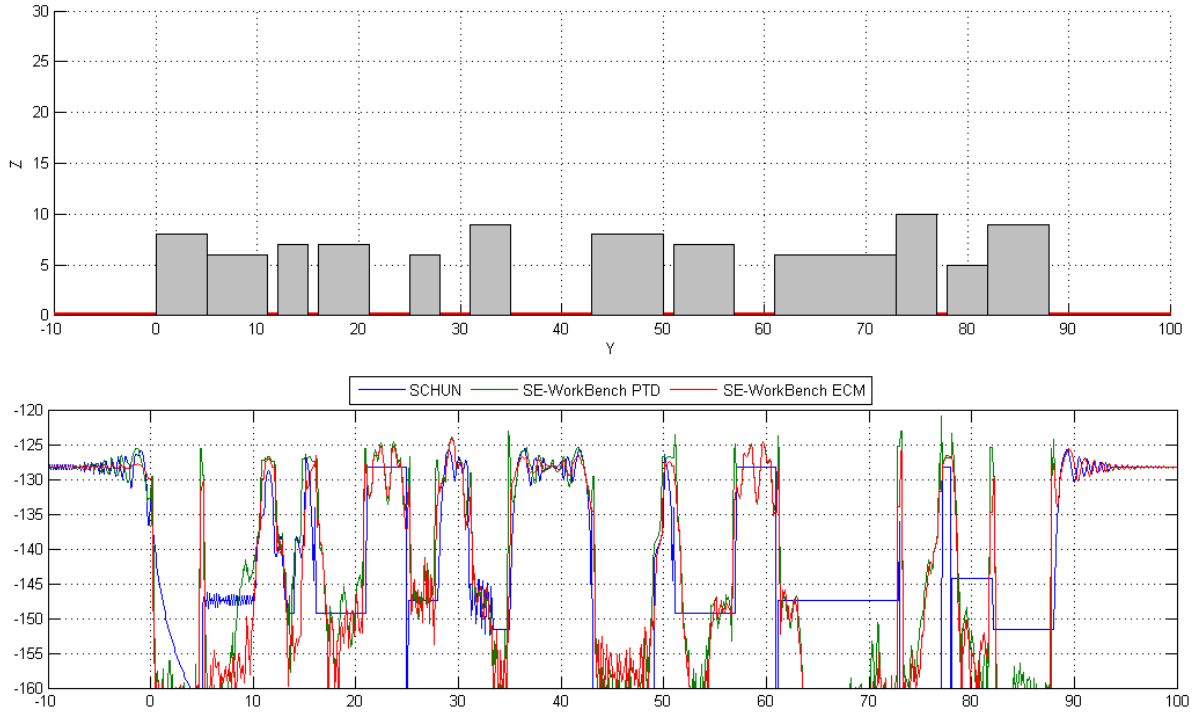

Figure D.17: Validation du modèle de diffraction par les bâtiments en comparant la méthode UTD utilisée dans SCHUN aux méthodes PTD et ECM utilisées dans SE-WorkBench

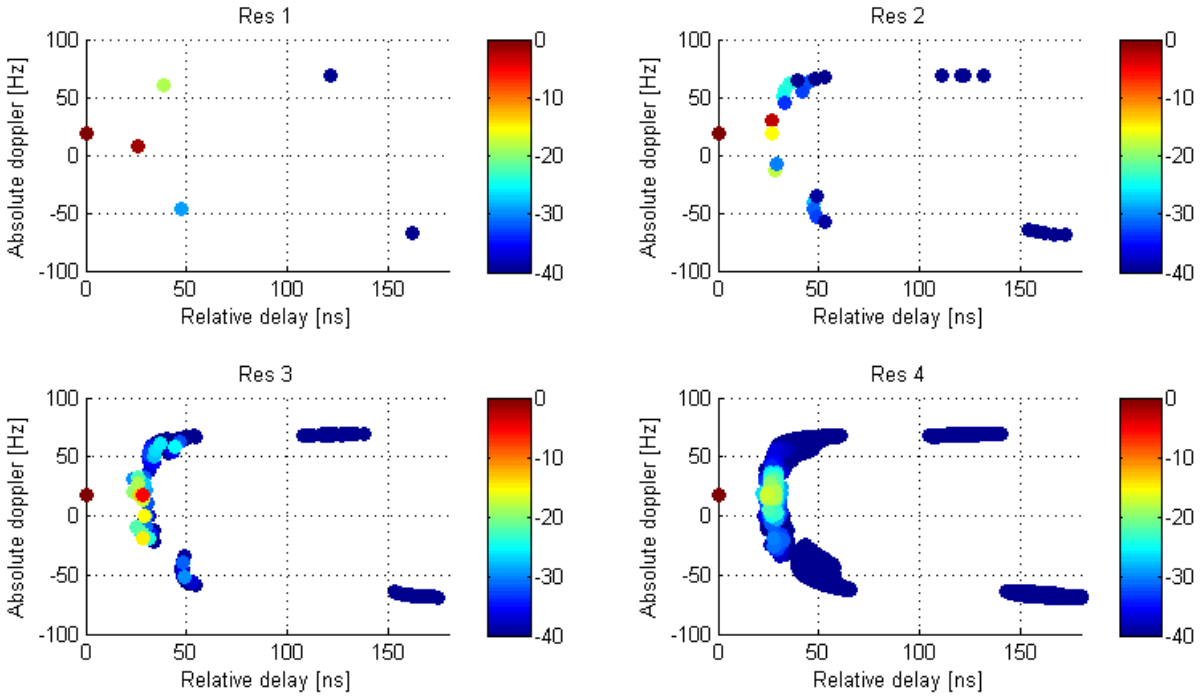

Figure D.18: Exemple de réduction du nombre de multitrajets dans la réponse impulsionnelle instantannée

D.5.2 Validation expérimentale pour les systèmes de communication par satellite (Saint Lary)

La première expérience a été coréalisée par le CNES et l'Onera dans le village de Saint Lary, France, entre 2011 et 2012. Cette campagne de mesure porte sur les problématiques MIMO pour des applications mobiles de télécommunication par satellite à l'aide des liens GEO. Cette première validation expérimentale a été réalisée en analysant diverses paramètres issus des séries temporelles complexes faible bande du canal de propagation suivant les composantes circulaires co et contra polarisées. Plusieurs paramètres ont été analysés tels que la puissance bande étroite, la distribution des atténuations (Fig.D.20) le spectre Doppler (Fig.D.20), l'estimation du facteur de Rice (Fig.D.22), le *level crossing rate* ou encore la durée des évanouissements.

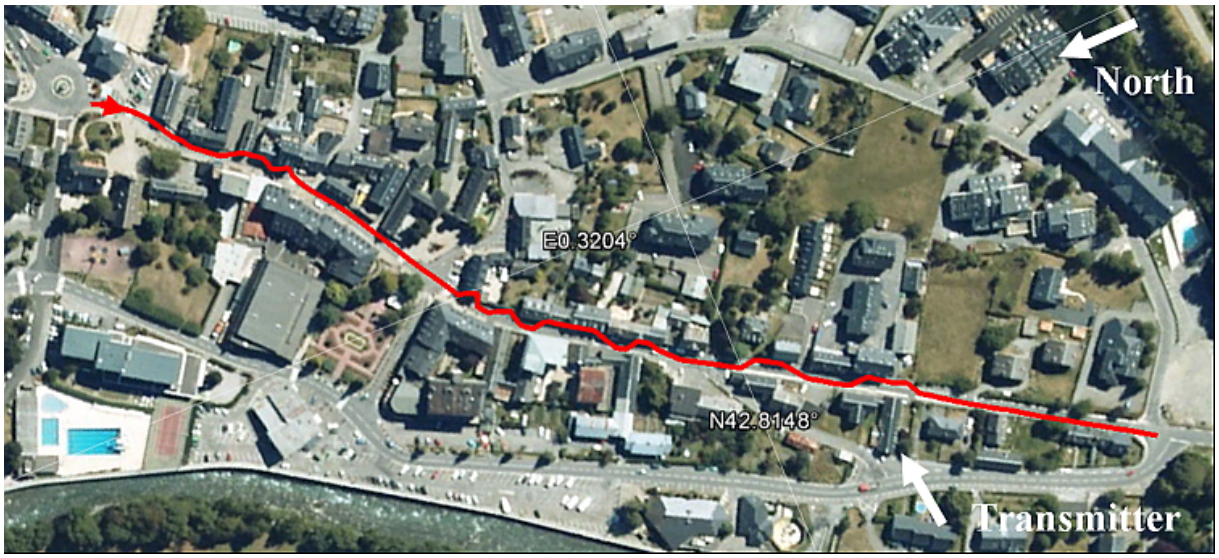

Figure D.19: Trajectoire de référence dans le village de Saint Lary

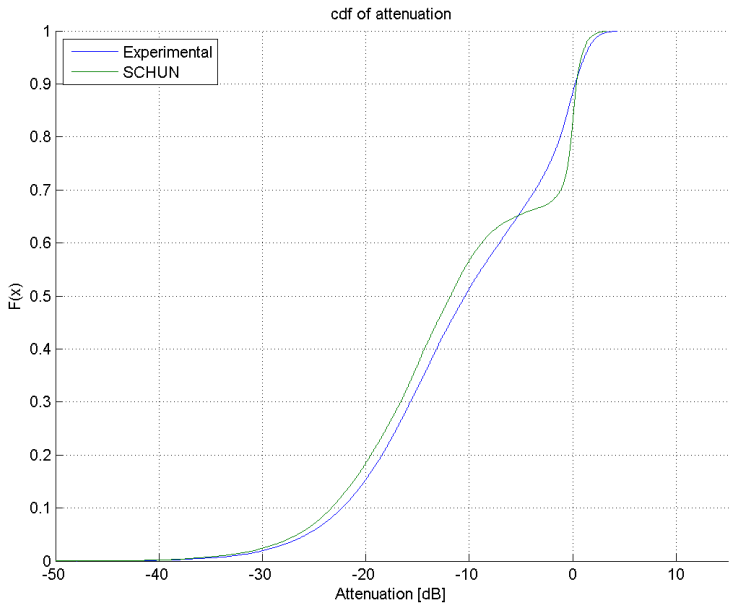

Figure D.20: Distribution de l'atténuation sur le canal co-polarisé

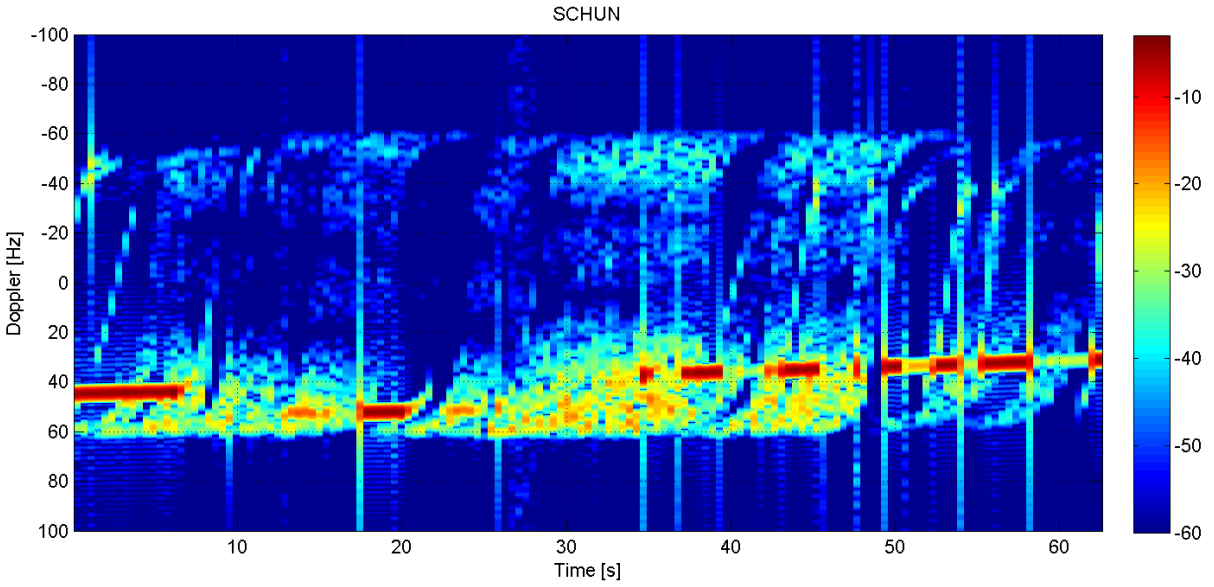

Figure D.21: Spectrogramme le long de la trajectoire du mobile

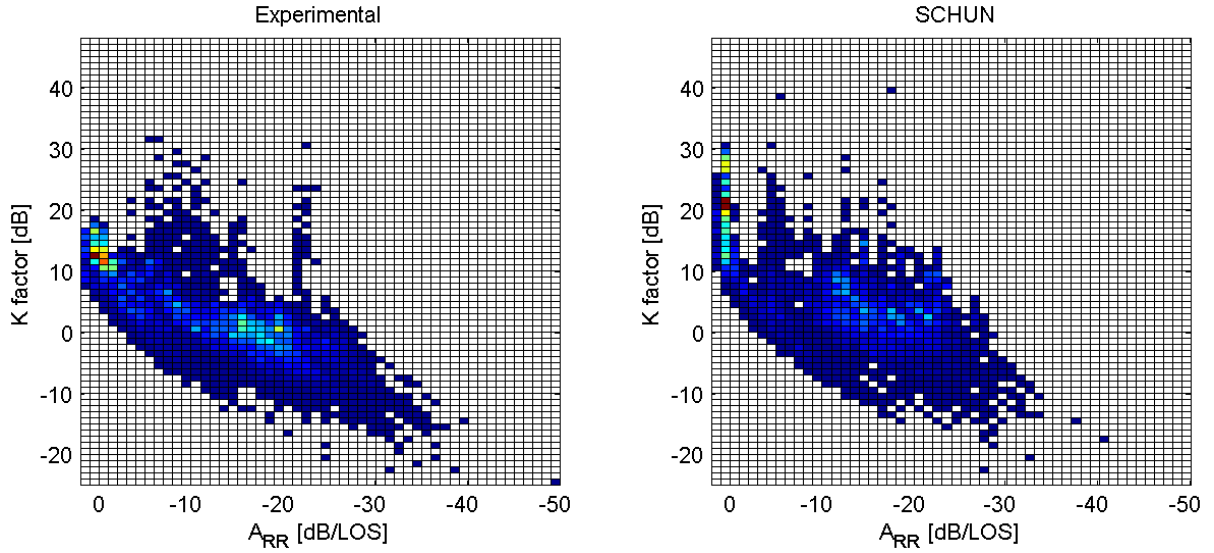

Figure D.22: Estimation du facteur de Rice en fonction de la puissance cohérente sur le canal co-polarisé

Les principales observations et conclusions sont les suivantes:

- La première difficulté a été de modéliser l'environnement réel en utilisant le formalisme du simulateur SCHUN. Cet environnement virtuel utilise les empreintes des constructions provenant du cadastre pour reproduire les bâtiments. Une inspection visuelle des façades a ensuite permis d'ajuster l'architecture et la hauteur des bâtiments. En raison des limites actuelles du simulateur SCHUN, la végétation n'a pas été incluse dans la scène virtuelle. L'absence de végétation dans la scène est une limitation forte déjà identifiée du simulateur. De plus, l'hypothèse de cuboïde pour représenter les bâtiments peut également être limitante lorsque la géométrie complexe de certains toits doit être reproduite.

- En général, les macro-effets dus à l'obstruction du trajet direct par les bâtiments sont bien reproduits par le simulateur SCHUN. La Puissance moyenne des MP est également cohérente avec les mesures en termes de série temporelle co et contra polarisées et sur les cdf d'atténuations.

- Concernant les fluctuations rapides du canal, les résultats révèlent un manque de dy-

namique sur les séries temporelles générées avec SCHUN. En effet, les évanouissements ne sont ni assez nombreux ni assez profonds comparés aux résultats expérimentaux. Cette observation a un impact direct sur les statistiques du second ordre qui affecte le *level crossing rate* et la durée des évanouissements. Ce problème mérite d'être réexaminé et corrigé.

- L'analyse Doppler n'a pas inclus de résultats expérimentaux dus à des dérives d'horloge lors des mesures rendant leur exploitation peu fiable. Cependant, les résultats présentés à partir de la synthèse de séries temporelles basées sur SCHUN sont conformes aux résultats théoriques attendus.

- L'analyse du facteur K a révélé une tendance du simulateur SCHUN à générer des états LOS très clairs avec peu multitrajets. Cette observation est cependant peut être biaisée par la fin de la trajectoire étudiée où la végétation, absente dans la simulation SCHUN et présente dans la réalité, peut avoir un fort impact sur la puissance totale multitrajet reçue. De plus, les toits simples tels que ceux utilisés dans l'environnement virtuel SCHUN peuvent également avoir un impact sur ce phénomène où les sous-états de masquage du trajet direct ne sont pas reproduits.

D.5.3 Validation expérimentale pour les systèmes de navigation par satellite (Toulouse-Capitole)

La deuxième expérience a été coréalisée par le CNES et l'ISAE dans le centre de Toulouse, France, en 2011 et aborde la question des systèmes de navigation par satellite dans les environnements urbains denses. Cette campagne de mesures a mis l'accent sur l'influence globale du canal de propagation sur la chaîne de traitement des récepteurs de navigation et aucune mesure directe du canal n'a été effectuée. Cette deuxième validation expérimentale est par conséquent orientée vers l'utilisation du simulateur SCHUN pour des simulations systèmes visant une validation indirecte en comparant l'influence du canal de propagation sur un récepteur de navigation par satellite logiciel. Plusieurs paramètres internes au récepteur ont été comparés et analysés, à savoir le C/N0 et l'erreur de pseudo-distance.

		PRN02	PRN04	PRN07	PRN08	PRN10	PRN13
In-situ	Rx 4T (Experimental)	✓	✗	✓	✓	✓	✓
	Rx 6H (Experimental)	✓	✓	✓	✓	✓	✓
Post-processed	BGM (Experimental)	✓	✓	✓	✗	✓	✗
	SCHUN (Simulation)	✓	✓	✓	✓	✗	✓

Table D.3: Résumé des comparaisons des séries temporelles de C/N0 utilisant des récepteurs embarqués durant les mesures (Rx 4T et Rx 6H) ainsi que les données post-traitées en utilisant JGNSS à partir des données BGM et du simulateur SCHUN pour les PRN02, PRN04, PRN07, PRN08, PRN10 et PRN13

Figure D.23: Trajectoire de référence dans le centre ville de Toulouse

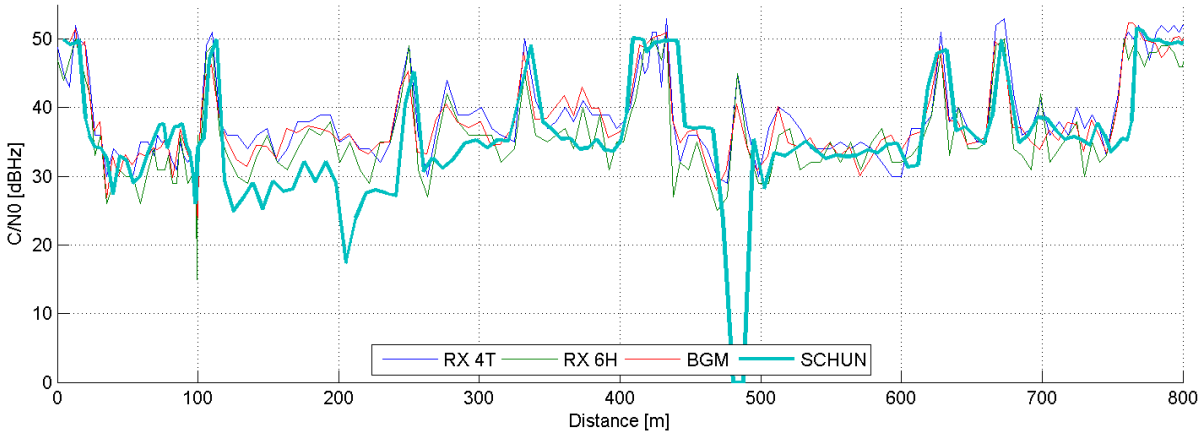

Figure D.24: Comparaison des séries temporelles de C/N0 estimées pour le PRN07

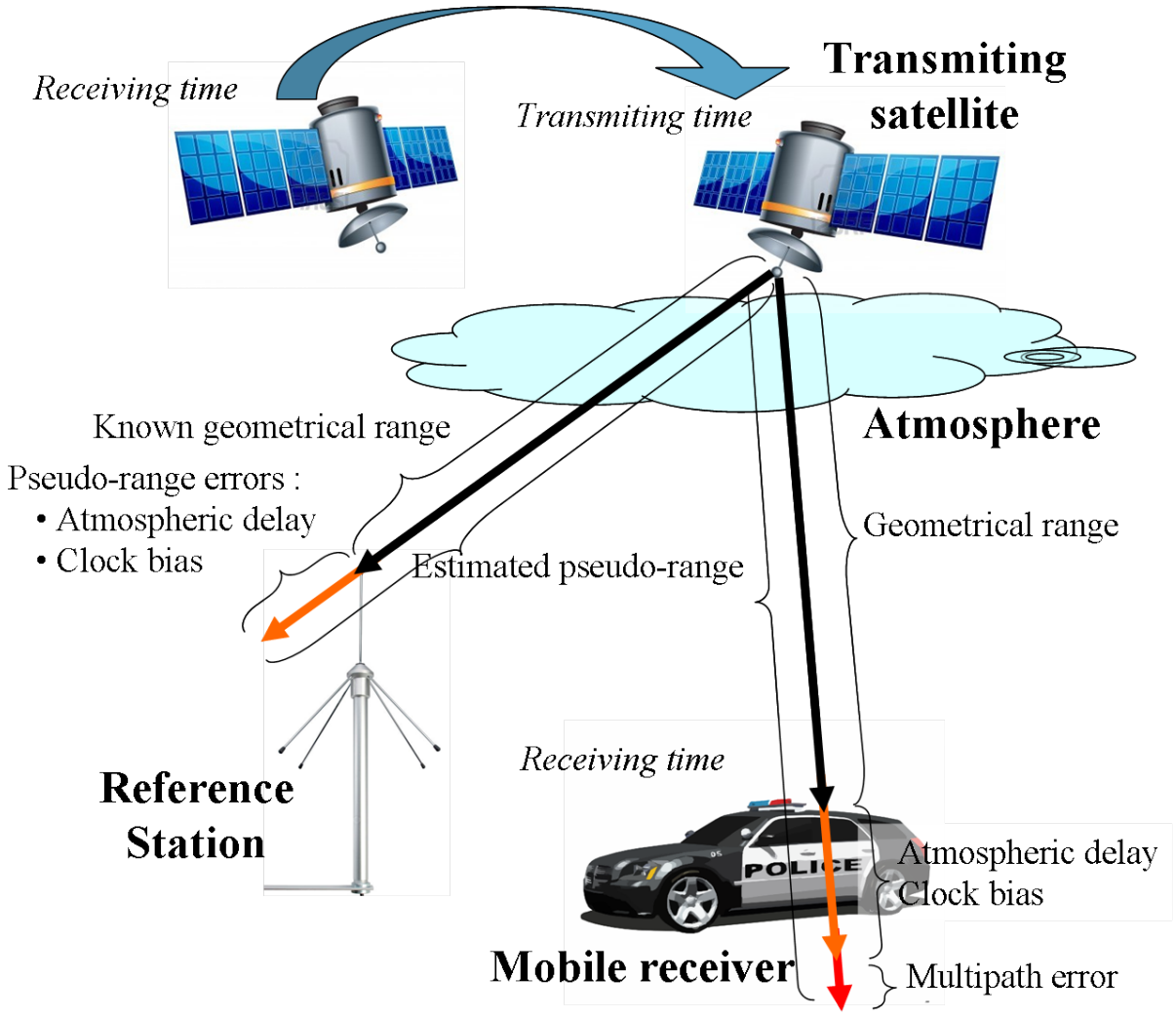

Figure D.25: Principe d'estimation de l'erreur de pseudo-distance commise par le récepteur et dû aux multitrajets en conditions expérimentales

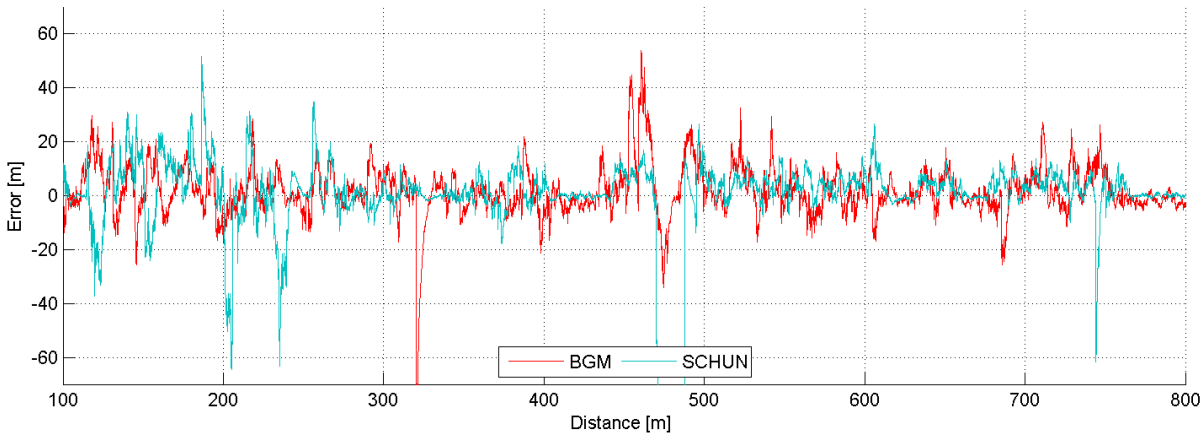

Figure D.26: Série temporelle d'erreur de pseudo-distance pour le PRN07

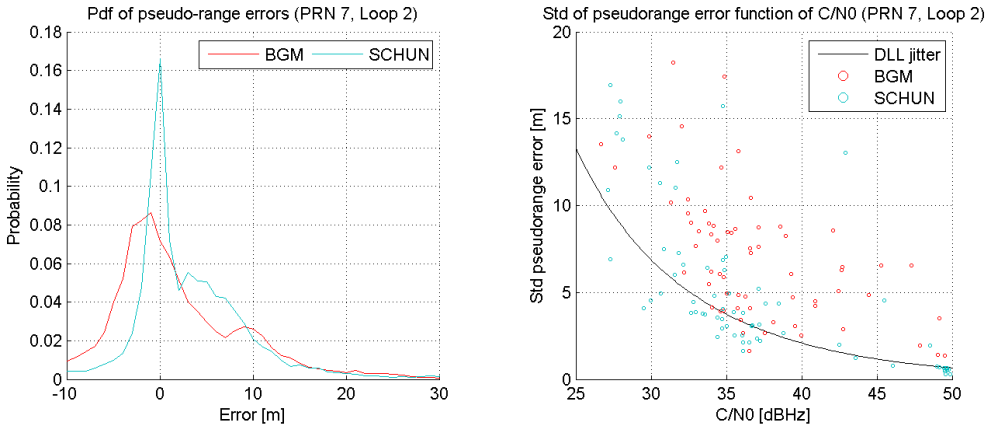

(a) (b)

Figure D.27: Distribution de l'erreur de pseudo-distance et variance de la boucle DLL en fonction du C/N0 estimé pour le PRN07

Les principales observations et conclusions sont les suivantes:

- Pour les besoins de cette validation, un environnement urbain très complexe (Fig.D.23) a été créé et intégré dans le simulateur SCHUN. La trajectoire complexe du mobile avec des changements de rue et des vitesses variables a été reproduite. La constellation des satellites GPS a également été reproduite et la validation du canal propagation a été effectuée simultanément sur six satellites.

- Au cours du processus de validation, l'importance de reproduire fidèlement l'environnement et en particulier la hauteur des bâtiments dans les canyons urbains a été présentée comme critique. En raison de sa construction et de l'incertitude sur la hauteur des bâtiments dans la base de données SE-WorkBench, la suite logicielle SE-WorkBench n'a pas été intégrée au processus du validation.

- L'utilisation du simulateur de canal SCHUN pour générer différents canaux de propagation s'est avérée être un succès et les séries temporelles de C/N0 (Fig.D.24, Tab.D.3) présentent une très bonne cohérence avec les données mesurées. Comme pour Saint-Lary, le simulateur SCHUN tend cependant à sous-estimer les sous-états du trajet direct, produisant des états LOS trop idéaux.

- D'après l'analyse des erreurs de pseudo-distance, le traitement des mesures réelles s'est révélé être très difficile et des erreurs résiduelles étaient encore présentes dans les résultats préliminaires justifiant un ajustement empirique à l'aide d'un satellite en condition LOS (PRN04). De plus, les séries temporelles d'erreurs de pseudo-distance se comportant comme du bruit thermique (Fig.D.26) elles sont d'autant plus difficiles à comparer. Une brève analyse statistique basée sur la distribution de l'erreur de pseudo-distance ainsi que sur la variance de la DLL (Fig.D.27) ont permis de comparer les résultats entre simulations et mesures expérimentales avec un accord raisonnable.

D.6 Conclusion

Au cours de ce travail de thèse un simulateur de canal de propagation basé sur une approche physico-statistique et adapté à la modélisation des multitrajets pour les systèmes de navigation par satellite a été présenté. Tout au long de ce document, plusieurs résultats innovants ont été présentés.

Le premier résultat innovant réside dans l'approximation de façades 2.5D et dans les recommandations qui en ont découlées. D'après notre étude rigoureuse utilisant une méthode full-wave, il

a été démontré que les murs texturés, représentatifs de l'architecture de la façade, se comportent différemment des murs lisses. En effet, les murs lisses tendent à surestimer le phénomène spéculaire au détriment du phénomène de diffusion. Comme présenté dans ce document, ce déséquilibre a un fort impact sur les systèmes de navigation par satellite justifiant l'utilisation de représentation 2.5D des façades.

Une autre des originalités de ce travail provient du modèle 3CM où la fonction de diffusion d'une façade complexe a été décomposée en trois mécanismes de propagation différents, en accord avec diverses simulations numériques et mesures expérimentales. Selon l'approximation de façade 2.5D, chaque macro-élément de la façade peut ainsi être relié à un mécanisme de propagation spécifique où les parties lisses donnent lieu à des réflexions spéculaires, les éléments protubérants donnent lieu à des rétrodiffusions et les surfaces rugueuses donnent lieu à une diffusion incohérente. En résumé, l'approximation de façade 2.5D a introduit une nouvelle façon de représenter les environnements urbains complexes tandis que le modèle 3CM a introduit une nouvelle façon de calculer simplement et efficacement les interactions EM entre les ondes et les bâtiments.

Néanmoins, la principale contribution de ce travail reste le simulateur de canal SCHUN fusionnant les observations, recommandations et conclusions partielles réalisées tout au long de ce document. Ce nouveau simulateur est basé sur une approche hybride physico-statistique, bénéficiant de faibles temps de calcul liés à l'intégration d'approches statistiques mais aussi de polyvalence liée à l'utilisation de méthodes déterministes. La composante statistique est essentiellement utilisée au cours de l'étape de synthèse de l'environnement permettant de générer rapidement de grands scénarios réalistes en utilisant le concept de ville virtuelle. Contrairement aux générateurs de villes virtuelles existants, le générateur d'environnement du simulateur SCHUN utilise une représentation 3D des bâtiments et intègre les macro-détails architecturaux des façades dans la modélisation d'environnements urbains complexes. Bien que minoritaires, les statistiques sont aussi utilisés dans le modèle 3CM permettant de générer aléatoirement les facettes responsables de la composante diffuse incohérente. Le reste de la modélisation est basée sur des modèles EM déterministes simplifiés (PO dans le modèle 3CM et UTD dans le modèle de diffraction du trajet direct) et les algorithmes classiques de rayons (propagation des rayons, intersection des rayons, calcul du point de diffraction stationnaire). La conception globale du simulateur SCHUN nous a permis de répondre à nos attentes en termes de modélisation large bande du canal de propagation LMS, de réduction du temps de calcul, d'indépendance envers des campagnes de mesure, de prise en compte des problématiques MIMO avec diversité de satellite, diversité spatiale en réception, diversité de fréquence et diversité de polarisation, de prise en compte des fréquence de la bande L à la bande C, de gestion de grands scénarios ou encore de polyvalence des sorties.

Enfin, ce travail est novateur au regard du processus de validation fusionnant des outils numériques et des campagnes expérimentales et s'appuyant sur les paramètres du canal de propagation ou encore son impact sur les systèmes de navigation par satellite. Au cours de ce travail, le choix a été fait d'utiliser les méthodes EM les plus rigoureuses (Elsem3D basé sur la méthode des moments) afin de mieux comprendre les mécanismes de propagation sous-jacents avant de simplifier le calcul EM en utilisant des outils asymptotiques (suite logicielle SE-WorkBench) en enfin proposer un modèle simplifié basé sur l'algorithme PO réduit au strict nécessaire. Au cours de ce processus, une attention permanente a été accordée aux applications de navigation par satellite, où chaque nouvelle étape de modélisation faisait l'objet de validations partielles en utilisant des récepteurs GNSS logiciels. Une fois construit, le simulateur SCHUN a été consolidé grâce à l'utilisation de deux campagnes de mesures basées soit sur les paramètres du canal de propagation soit par l'intermédiaire d'un récepteur de navigation par satellite. Tout au long de ces deux validations, le simulateur SCHUN a présenté un accord raisonnable avec les mesures, même si certains points spécifiques nécessitent d'être approfondis dans le futur.

Concernant les perspectives de développements ultérieurs du simulateur SCHUN, un accent particulier et primordial doit être mis sur les effets de la végétation puisque ceux-ci restent la principale limite actuelle du simulateur SCHUN. D'autres éléments urbains comme les lampadaires ou les abris bus pourraient également être intégrés dans un dernier temps. L'ajout de tels modèles permettrait au simulateur SCHUN de pouvoir être utilisé dans une plus large gamme d'environnements allant de l'urbain au rural. Cette mise à jour pourrait également conduire à de nouvelles validations expérimentales pour consolider ce nouveau simulateur SCHUN, notamment sur certains aspects qui n'ont pas fait l'objet de validations expérimentales directes pour le moment. Sont donc visés par ces nouvelles validations les configurations MIMO diversité de fréquence bien que des simulations ait été effectuées en bande L (Capitole) et en bande S (Saint Lary), configuration MIMO diversité de satellite pour télécommunications bien que la validation Capitole est été effectuée pour six satellites simultanément ou encore gain MIMO en diversité de polarisation bien que les canaux co contra polarisés aient été étudiés dans la validation Saint Lary. Un dernier exercice de validation pourrait aussi consister à valider le modèle SCHUN pour des fréquences plus élevées, typiquement dans les bande Ku et Ka.

Une autre piste à investiguer dans de nouveaux travaux de recherche pourrait consister à caractériser l'algorithme de réduction des multitrajets brièvement présenté dans le dernier chapitre. En consolidant l'approche déjà imaginée, le simulateur SCHUN pourrait ainsi être intégré dans les chaînes de simulation de systèmes complexes ou dans des émulateurs hardware de canal. Ce travail pourrait en outre permettre de standardiser les prototypes de nouveaux récepteurs GNSS ou encore de designer une troisième génération de modulation pour les signaux de navigation par satellite.

Personnal Bibliography

International workshops:

- M. Ait-Ighil, S. Rougerie, J. Lemorton, G. Carrié, G. Artaud, C. Bourga, and M. Bousquet, "Channel Modelling in Complex Urban Environments for Testing Multipath Mitigation Methods Enhanced by Antenna Array," presented at *ESA Workshop on Radiowave Propagation 2011*, ESA/ESTEC, Noordwijk, The Netherlands, December 2011, pp. 1-9.

- M. Ait-Ighil, F. Perez-Fontan, J. Lemorton, F. Lacoste, G. Artaud, C. Bourga, and M. Bousquet, "Simplified Model for Building Scattering in Urban Environment for GNSS Propagation Channels," presented at *ESA Workshop on Radiowave Propagation 2011*, ESA/ESTEC, Noordwijk, The Netherlands, December 2011, pp. 1-13.

- M. Ait-Ighil, F. Perez-Fontan, J. Lemorton, F. Lacoste, G. Artaud, C. Bourga, and M. Bousquet, "Simplified Model for Building Scattering in Urban Environment for GNSS Propagation Channels," presented at the *7th COST IC0802 Meeting*, *"Propagation tools and data for integrated telecommunication, navigation and earth observation systems"*, Portsmouth, England, April 2012.

- M. Ait-Ighil, F. Perez-Fontan, J. Lemorton, F. Lacoste, C. Bourga, and M. Bousquet, "Simple Model for Complex Building Scattering in Urban Environment Based on a Three Macro Propagation Phenomena Approach," presented at the *4Th COST IC1004 Meeting*, *"Cooperative Radio Communications for Green Smart Environments"*, Lyon, France, May 2012, pp. 1-6.

International conferences:

- M. Ait-Ighil, J. Lemorton, F. Perez-Fontan, F. Lacoste, V. Gobin, G. Artaud, C. Bourga, and M. Bousquet, "Numerical analysis of the impact of building face features on LMS channel modelling," in *Antennas and Propagation (EUCAP), Proceedings of the 5th European Conference on,* Rome, Italy, 2011, pp. 3566 -3570.

- M. Ait-Ighil, F. Perez-Fontan, J. Lemorton, F. Lacoste, G. Artaud, C. Bourga, and M. Bousquet, "A three components model for simplified building scattering in urban environment," in *Antennas and Propagation (EUCAP), 2012 6th European Conference on,*, Prague, Czech Republic, 2012, pp. 2449 -2453.

- "SCHUN - an Hybrid Land Mobile Satellite Channel Simulator Enhanced for Multipath Modelling Applied to Satellite Navigation Systems", abstract accepted for Eucap2013.

International journals:

- M. Ait-Ighil, J. Lemorton, F. Perez-Fontan, F. Lacoste, G. Artaud, C. Bourga, and M. Bousquet, "Simplifying the Propagation Environment Representation for LMS Channel Modelling," in *EURASIP Journal on Wireless Communications and Networking 2012*, Mar. 2012, **published**

- M. Ait-Ighil, S. Rougerie, J. Lemorton, G. Carrié, G. Artaud, C. Bourga, and M. Bousquet, "Channel Modelling in Complex Urban Environments for Testing Multipath Mitigation Methods Enhanced by Antenna Array," in *Special issue of Space Communications Journal*, **accepted in principle**

- M. Ait-Ighil, F. Perez-Fontan, J. Lemorton, F. Lacoste, G. Artaud, C. Bourga, and M. Bousquet, "Simple model for complex building scattering - A three component model based on macro propagation phenomena approach," in *IEEE Trans. on Antennas and Propagation*, **submitted under 2nd review**

Short Term Scientific Missions:

- Short Term Scientific Mission with Prof. PEREZ-FONTAN, funded by COST IC0802 *"Propagation tools and data for integrated telecommunication, navigation and earth observation systems"*, 5 weeks stay at the University of Vigo, Spain, October 2010.
- Short Term Scientific Mission with Prof. PEREZ-FONTAN, funded by COST IC0802 *"Propagation tools and data for integrated telecommunication, navigation and earth observation systems"*, 4 weeks stay at the University of Vigo, Spain, November 2011.

Bibliography

[Abel 08] A. Abele, F. Perez Fontan, M. Bousquet, P. Valtr, J. Lemorton, L. Castanet, F. Lacoste, and E. Corbel. "A physical/statistical model of the propagation channel for land mobile satellite systems". In: *ESA workshop on propagation*, Noordwijk, The Netherlands, Dec. 2008.

[Abel 09] A. Abele. *Modelisation du Canal de Propagation par Satellite dans les Bandes L, S et C.* PhD thesis, Institut superieur de l'aeronautique et de l'espace, Dec. 2009. PDF.

[Ait 11] M. Ait-Ighil, S. Rougerie, J. Lemorton, G. Carrié, G. Artaud, C. Bourga, and M. Bousquet. "Channel Modelling in Complex Urban Environments for Testing Multipath Mitigation Methods Enhanced by Antenna Array". pp. 1–9, ESA/ESTEC, Noordwijk, The Netherlands, Dec. 2011.

[Ait 12] M. Ait-Ighil, J. Lemorton, F. Perez-Fontan, F. Lacoste, G. Artaud, C. Bourga, and M. Bousquet. "Simplifying the Propagation Environment Representation for LMS Channel Modelling". *EURASIP Journal on Wireless Communications and Networking 2012*, March 2012.

[Al B 07a] H. Al Bitar. "DLR model simplification - Alyotech group/Cril technology". Dec. 2007.

[Al B 07b] H. Al Bitar. *Techniques avancees de traitement du signal GPS pour les services LBS.* PhD thesis, Institut National Polytechnique de Toulouse, July 2007.

[Ande 93] H. Anderson. "A ray-tracing propagation model for digital broadcast systems in urban areas". *IEEE Transactions on Broadcasting*, Vol. 39, No. 3, pp. 309 –317, Sep. 1993.

[Arta 06] G. Artaud. "Juzzle software receiver". ESTEC, Noordwijk, the Netherlands, 2006.

[Arta 07] G. Artaud, L. Ries, J. Dantepal, J. L. Issler, T. Grelier, A. Delatour, O. Julien, and C. Macabiau. "CBOC Performances Using Software Receiver". Noordwijk, The Netherlands, Apr. 2007.

[Arta 08] G. Artaud, L. Ries, Y. Gregoire, M. Jeannot, J. Dantepal, and D. Zobler. "GNSS receiver test bench". In: *ENC GNSS, Toulouse Space Show 2008*, Toulouse, France, Apr. 2008.

[Bala 89] C. A. Balanis. *Advanced Engineering Electromagnetics.* John Wiley and Sons (WIE), July 1989.

[Bark 00] A. Barka, P. Soudais, and D. Volpert. "Scattering from 3-D cavities with a plug and play numerical scheme combining IE, PDE, and modal techniques". *Antennas and Propagation, IEEE Transactions on*, Vol. 48, No. 5, pp. 704 –712, 2000.

[Bart 92] R. M. Barts and W. L. Stutzman. "Modeling and Simulation of Mobile Satellite Propagation". *IEEE TRANSACTIONS ON ANTENNAS AND PROPAGATION*, Vol. 40, No. 4, 1992.

[Bell 63] P. Bello. "Characterization of Randomly Time-Variant Linear Channels". *IEEE Transactions on Communications Systems*, Vol. 11, No. 4, pp. 360–393, Dec. 1963.

[Berg 04] A. Berges, J. Latger, and H. J. Mametsa. "FERMAT : a new radar simulation approach". UK, 2004.

[Carr 12] G. Carrie, F. Perez-Fontan, F. Lacoste, and J. Lemorton. "A generative MIMO channel model: Encompassing single satellite and satellite diversity cases". In: *2012 6th European Conference on Antennas and Propagation (EUCAP)*, pp. 2454 –2458, March 2012.

[Chef 10] M. Cheffena and F. Perez-Fontan. "Land Mobile Satellite Channel Simulator Along Roadside Trees". *IEEE Antennas and Wireless Propagation Letters*, Vol. 9, pp. 748 –751, 2010.

[COST 02] COST255. *Cost Action 255 - Radiowave Propagation Modelling for SatCom Services at Ku-Band and Above*. R.A. Harris, final report Ed., March 2002.

[Degl 07] V. Degli-Esposti, F. Fuschini, E. M. Vitucci, and G. Falciasecca. "Measurement and Modelling of Scattering From Buildings". *Antennas and Propagation, IEEE Transactions on*, Vol. 55, No. 1, pp. 143–153, 2007.

[Diaz 96] L. Diaz and T. Milligan. *Antenna Engineering Using Physical Optics: Practical CAD Techniques and Software*. Artech House Publishers, Har/Dskt Ed., Sep. 1996.

[Dida 00] D. Didascalou, M. Younis, and W. Wiesbeck. "Millimeter-wave scattering and penetration in isolated vegetation structures". *Geoscience and Remote Sensing, IEEE Transactions on*, Vol. 38, No. 5, pp. 2106–2113, 2000.

[Durg 97] G. Durgin, N. Patwari, and T. Rappaport. "Improved 3D ray launching method for wireless propagation prediction". *Electronics Letters*, Vol. 33, No. 16, pp. 1412 –1413, 1997.

[Euro 10] "European GNSS (Galileo) Open Service - Signal In Space Interface Control Document". Tech. Rep. OS SIS ICD Issue 1.1, European Union, Sep. 2010.

[Fail 89] M. Failli. *Cost 207 Digital Land Mobile Radio Communications: Final Report*. Directorate General, Telecommunications, Information Industries and Innovation, 1989.

[Garc 10] J. Garcia-Molina, F. Zanier, M. Crisci, R. Prieto-Cerdeira, P. Giordano, A. Steingass, and A. Hornbostel. "Land mobile multipath channel reduction effects on a real GNSS receiver". In: *2010 5th ESA Workshop on Satellite Navigation Technologies and European Workshop on GNSS Signals and Signal Processing (NAVITEC)*, pp. 1 –7, Dec. 2010.

[Gunt 10] C. Gunther and P. Henkel. "Reduced-Noise Ionosphere-Free Carrier Smoothed Code". *IEEE Transactions on Aerospace and Electronic Systems*, Vol. 46, No. 1, pp. 323 –334, Jan. 2010.

[Huss 02] L. Husson, J. C. Dany, K. Berradi, S. Chambon, and A. Beffani. "Scalable multistate markovian modeling of time series of received power from measurements of mobile satellite transmissions in the L-Band". In: *20 th AIAA International Communications Satellite Systems Conference and Exhibit, Montreal, Canada*, 2002.

[Ishi 91] A. Ishimaru. "Wave propagation and scattering in random media and rough surfaces". *Proceedings of the IEEE*, Vol. 79, No. 10, pp. 1359–1366, 1991.

[ITU 07] ITU. "ITU-R P.833-6 Attenuation in vegetation". Attenuation in vegetation ITU-R P.833-6, ITU, Jan. 2007.

[ITU 09] ITU. "ITU-R P.681-7 Propagation data required for the design of Earth-space land mobile telecommunication systems". Propagation data required for the design of Earth-space land mobile telecommunication systems ITU-R P.681-7, ITU, Oct. 2009.

[ITU 86] ITU. "ITU-R P.236-6 Influence of terrain irregularities and vegetation on tropospheric propagation". Influence of terrain irregularities and vegetation on tropospheric propagation ITU-R P.236-6, CCIR XVth Plenary Assembly, Dubrovnik, 1986.

[Jahn 01] A. Jahn. "Propagation considerations and fading countermeasures for mobile multimedia services". *International Journal of Satellite Communications*, Vol. 19, No. 3, pp. 223–250, 2001.

[Jahn 96] A. Jahn, H. Bischl, and G. Heiss. "Channel characterisation for spread spectrum satellite communications". In: *Spread Spectrum Techniques and Applications Proceedings, 1996., IEEE 4th International Symposium on*, pp. 1221–1226 vol.3, 1996.

[Jake 94] W. C. Jakes and D. C. Cox, Eds. *Microwave Mobile Communications*. Wiley-IEEE Press, 1994.

[Jong 04] Y. de Jong and M. Herben. "A tree-scattering model for improved propagation prediction in urban microcells". *Vehicular Technology, IEEE Transactions on*, Vol. 53, No. 2, pp. 503–513, 2004.

[Kapl 05] E. Kaplan and C. Hegarty. *Understanding GPS: Principles And Applications*. Artech House, 2nd revised edition Ed., Dec. 2005.

[Kara 94] Y. Karasawa, K. Minamisono, and T. Matsudo. "A propagation channel model for personal mobile satellite services". In: *PIERS'94*, Noordwijk, The Netherlands, July 1994.

[Kenr 30] G. Kenrick and G. Pickard. "Summary of Progress in the Study of Radio Wave Propagation Phenomena". *Proceedings of the Institute of Radio Engineers*, Vol. 18, No. 4, pp. 649 – 668, Apr. 1930.

[King 05] P. R. King, B. G. Evans, and S. Stavrou. "Physical-statistical model for the land mobile-satellite channel applied to satellite/HAP-MIMO". *Wireless Conference 2005 - Next Generation Wireless and Mobile Communications and Services (European Wireless), 11th European*, pp. 1 –5, Apr. 2005.

[King 07a] P. King. *Modelling and Measurement of the land mobile satellite MIMO radio propagation channel.pdf*. PhD thesis, University of Surrey, Apr. 2007.

[King 07b] P. King and S. Stavrou. "Low Elevation Wideband Land Mobile Satellite MIMO Channel Characteristics". *IEEE Transactions on Wireless Communications*, Vol. 6, No. 7, pp. 2712 –2720, July 2007.

[Knot 04] E. F. Knott, J. F. Shaeffer, and M. T. Tuley. *Radar cross section*. SciTech Publishing, Jan. 2004.

[Krac 07] B. Krach, A. Lehner, and A. Steingass. "Technical Note on the Implementation of the Land Mobile Satellite Channel Model - Software Usage". Technical note DLR-KN-FS-02-07, DLR, Germany, July 2007.

[Laco 10] F. Lacoste, F. Carvalho, F. P. Fontan, A. N. Fernandez, V. Fabbro, and G. Scot. "MISO and SIMO measurements of the Land Mobile Satellite propagation channel at S-band". In: *2010 Proceedings of the Fourth European Conference on Antennas and Propagation (EuCAP)*, pp. 1 –5, Apr. 2010.

[Laco 12] F. Lacoste, J. Lemorton, L. Casadebaig, and F. Rousseau. "Measurements of the land mobile and nomadic satellite channels at 2.2 GHz and 3.8 GHz". In: *2012 6th European Conference on Antennas and Propagation (EUCAP)*, pp. 2422 –2426, March 2012.

[Lehn 07a] A. Lehner and A. Steingass. "Time Series Multipath Modeling of Suburban Environments in Landmobile Satellite Navigation". In: *Antennas and Propagation, 2007. EuCAP 2007. The Second European Conference on*, pp. 1–7, 2007.

[Lehn 07b] A. Lehner. *Multipath channel modelling for satellite navigation systems.* PhD thesis, Erlangen, Allemagne, 2007.

[Lehn 08] A. Lehner and A. Steingass. "Differences in Multipath propagation between urban and suburban environments". In: *4th ESA Workshop on Satellite Navigation User Equipment Technologies NAVITEC 2008*, Noordwijk, The Netherlands,, Dec. 2008.

[Li 10] X. Li. *Un modele hybride statistique-deterministe du canal LMS en environnements complexes.* PhD thesis, University of Poitiers, Poitiers, France, Dec. 2010.

[Lowe 16] F. Lowenstein. "The Mechanism of Radiation and Propagation in Radio Communication". *Proceedings of the Institute of Radio Engineers*, Vol. 4, No. 3, pp. 271 – 280, June 1916.

[Lutz 96] E. Lutz. "A markov model for correlated land mobile satellite channels". *International Journal of Satellite Communications*, Vol. 14, No. 4, pp. 333–339, 1996.

[Mame 03] J. Mametsa, S. Laybros, and A. Berges. "Asymptotic Formulations and Shooting Ray Coupling for Fast 3D Scattering Field Evaluation from Complex Objects and Environment - Applications". Turin, Italy, 2003.

[Mame 06] H. Mametsa, S. Laybros, A. Berges, P. Combes, P. N'Guyen, and P. Pitot. "FERMAT: A high frequency em scattering code from complex scenes including objects and environment". In: *Antennas and Propagation, 2006. EuCAP 2006. First European Conference on*, pp. 1–4, 2006.

[McNa 90] D. A. McNamara and C. W. I. Pistotius. *Introduction to the Uniform Geometrical Theory of Diffraction.* Artech Print on Demand, Jan. 1990.

[Milo 09] M. Milojevic, M. Haardt, E. Eberlein, and A. Heuberger. "Channel Modeling for Multiple Satellite Broadcasting Systems". *Broadcasting, IEEE Transactions on*, Vol. 55, No. 4, pp. 705–718, 2009.

[Misr 10] P. Misra and P. Enge. *Global Positioning System: Signals, Measurements, and Performance.* Ganga-Jamuna Press, Dec. 2010.

[Moli 04] A. Molisch. "A generic model for MIMO wireless propagation channels in macro- and microcells". *IEEE Transactions on Signal Processing*, Vol. 52, No. 1, pp. 61 – 71, Jan. 2004.

[Most 11] S. Mostarshedi, E. Richalot, J. Wiart, and O. Picon. "An assessment of complex scattered electric field through building facade homogenization". In: *Antennas and Propagation (EUCAP), Proceedings of the 5th European Conference on*, pp. 3293 –3296, Apr. 2011.

[Nahi 09] D. F. Nahimana. *Impact des multitrajets sur les performances des systemes de navigation par satellite : Contribution a l'amelioration de la precision de localisation par modelisation bayesienne.* PhD thesis, Ecole centrale de Lille, Lille, France, Feb. 2009.

[NAVS 96] "NAVSTAR GPS User equipment introduction". Tech. Rep. public release version, Navigation Center, United States Coast Guard, Sep. 1996.

[Oest 00] C. Oestges. *Propagation Modelling of Low Earth-Orbit Satellite Personal Communication Systems.* PhD thesis, Universite Louvain la Neuve, Louvain la Neuve, Belgium, Dec. 2000.

[Oest 99a] C. Oestges, S. Saunders, and D. Vanhoenacker-Janvier. "Physical statistical modelling of the land mobile satellite channel based on ray tracing". *Microwaves, Antennas and Propagation, IEE Proceedings* -, Vol. 146, No. 1, pp. 45–49, 1999.

[Oest 99b] C. Oestges and D. Vanhoenacker-Janvier. "Physical-statistical prediction of performance for land mobile satellite communication systems". *Microwaves, Antennas and Propagation, IEE Proceedings* -, Vol. 146, No. 5, pp. 362–368, 1999.

[Offi 12] "Official U.S. Government information about the Global Positioning System (GPS) and related topics". http://www.gps.gov/systems/gps/control/, 2012.

[Ouat 11] B. Ouattara. *Développement d'une approche radar pour l'étude des réflexions sur les batiments et l'analyse des irrégularités de façade.* PhD thesis, Université Paris Est, Paris, France, June 2011.

[Park 96] B. W. Parkinson and J. J. Spilker. *Global Positioning System: Theory & Applications (Volume One).* AIAA (American Institute of Aeronautics & Ast, 1st Ed., Jan. 1996.

[Pars 00] J. Parsons. *The mobile radio propagation channel.* John Wiley, Chichester, 2nd ed. Ed., 2000.

[Pere 01] F. Perez Fontan, M. Vazquez-Castro, C. Cabado, J. Garcia, and E. Kubista. "Statistical modeling of the LMS channel". *Vehicular Technology, IEEE Transactions on*, Vol. 50, No. 6, pp. 1549–1567, 2001.

[Pere 05] F. Perez Fontan, S. Martinez, B. Sanmartin, C. Enjamio, P. Marino, and F. Machado. "An enhanced Markov chain based model for the narrowband LMS channel in built-up areas". *International Journal of Satellite Communications and Networking*, Vol. 23, No. 2, pp. 111–128, 2005.

[Pere 07] F. Perez Fontan, A. Abele, B. Montenegro, F. Lacoste, V. Fabbro, L. Castanet, B. Sanmartin, and P. Valtr. "Modelling of the Land Mobile Satellite Channel using a Virtual City Approach". In: *Antennas and Propagation, 2007. EuCAP 2007. The Second European Conference on*, pp. 1–7, 2007.

[Pere 09] C. Pereira, Y. Pousset, V. Vauzelle, and P. Combeau. "Sensitivity of the MIMO Channel Characterization to the Modeling of the Environment". *Antennas and Propagation, IEEE Transactions on*, Vol. 57, No. 4, pp. 1218–1227, 2009.

[Pere 97] F. Perez Fontan, J. P. Gonzalez, M. J. S. Ferreiro, M. A. V. Castro, S. Buonomo, and J. P. Baptista. "Complexe enveloppe three-state markov model based simulator for the narrowband LMS channel". *International Journal of Satellite Communications*, Vol. 15, No. 1, pp. 1–15, 1997.

[Pong 04] P. Pongsilamanee and H. Bertoni. "Specular and nonspecular scattering from building facades". *Antennas and Propagation, IEEE Transactions on*, Vol. 52, No. 7, pp. 1879 – 1889, July 2004.

[Rokh 90] V. Rokhlin. "Rapid solution of integral equations of scattering theory in two dimensions". *J. Comput. Phys.*, Vol. 86, No. 2, pp. 414–439, 1990.

[Roug 12] S. Rougerie. *Algorithme de diversite d'antennes applique a la reception des signaux GNSS en environnement urbain et sur terminal mobile.* PhD thesis, University of Toulouse, Toulouse, France, Jan. 2012.

[Ruck 70] G. T. Ruck, D. E. Barrick, W. D. Stuart, and C. K. Krichbaum. *Radar Cross Section Handbook. Volumes 1 & 2.* Plenum, 1 Ed., Jan. 1970.

[Sale 87] A. Saleh and R. Valenzuela. "A Statistical Model for Indoor Multipath Propagation". *Selected Areas in Communications, IEEE Journal on*, Vol. 5, No. 2, pp. 128–137, 1987.

[Satn 08] Satnex. *Influence of the Variability of the Propagation Channel on Mobile, Fixed Multimedia and Optical Satellite Communications.* Laurent Castanet, ONERA, France, Jan. 2008.

[Saun 07] S. Saunders and A. Aragon-Zavala. *Antennas And Propagation for Wireless Communication Systems.* John Wiley & Sons Ltd, 2nd revised edition Ed., March 2007.

[Saun 91] S. Saunders. *Diffraction modelling of mobile radio wave propagation in built-up areas.* PhD thesis, Brunel University, 1991.

[Saun 96] S. Saunders and B. Evans. "Physical model of shadowing probability for land mobile satellite propagation". *Electronics Letters*, Vol. 32, No. 17, Aug. 1996.

[Sche 03] M. Schenewerk. "A brief review of basic GPS orbit interpolation strategies". *GPS Solutions*, Vol. 6, No. 4, pp. 265–267, March 2003.

[Schu 10] F. M. Schubert, B. H. Fleury, P. Robertson, R. Prieto-Cerdeirai, A. Steingass, and A. Lehner. "Modeling of multipath propagation components caused by trees and forests". In: *2010 Proceedings of the Fourth European Conference on Antennas and Propagation (EuCAP)*, pp. 1 –5, Apr. 2010.

[Schw 88] F. Schwering, E. Violette, and R. Espeland. "Millimeter-wave propagation in vegetation: experiments and theory". *Geoscience and Remote Sensing, IEEE Transactions on*, Vol. 26, No. 3, pp. 355–367, 1988.

[SE 12] O. SE. "SE-Ray-EM commercial presentation". http://www.oktal-se.fr/se-workbench/website/software/pdf/SE-RAY-EM.pdf, 2012.

[Soud 02] P. Soudais, P. Leca, J. Simon, and T. Volpert. "Computation of the scattering from inhomogeneous objects with a discrete rotational symmetry and a nonsymmetric part". *IEEE Transactions on Antennas and Propagation*, Vol. 50, No. 2, pp. 168 –174, Feb. 2002.

[Soud 99] P. Soudais, H. Steve, and F. Dubois. "Scattering from several test-objects computed by 3-D hybrid IE/PDE methods". *Antennas and Propagation, IEEE Transactions on*, Vol. 47, No. 4, pp. 646 –653, 1999.

[Stei 01] A. Steingass, A. Lehner, and F. Schubert. "A Location and Movement Dependent GNSS Multipath Error Model for Pedestrian Applications". pp. 2284–2296, Sep. 2001.

[Stra 30] J. Stratton. "The Effect of Rain and Fog on the Propagation of Very Short Radio Waves". *Proceedings of the Institute of Radio Engineers*, Vol. 18, No. 6, pp. 1064 – 1074, June 1930.

[Tepe 03] C. Tepedelenlioglu, A. Abdi, and G. Giannakis. "The Ricean K factor: estimation and performance analysis". *Wireless Communications, IEEE Transactions on*, Vol. 2, No. 4, pp. 799–810, 2003.

[Torr 98] S. Torrico, H. Bertoni, and R. Lang. "Modeling tree effects on path loss in a residential environment". *Antennas and Propagation, IEEE Transactions on*, Vol. 46, No. 6, pp. 872 –880, 1998.

[Valt 09] P. Valtr, F. Perez Fontan, and A. Abele. "Propagation modelling in virtual environments, characterization of mobile propagation channel". In: *Antennas and Propagation, 2009. EuCAP 2009. 3rd European Conference on*, pp. 3678–3681, 2009.

[Vitu 12] E. Vitucci, F. Mani, V. Degli-Esposti, and C. Oestges. "Polarimetric Properties of Diffuse Scattering From Building Walls: Experimental Parameterization of a Ray-Tracing Model". *Antennas and Propagation, IEEE Transactions on*, Vol. 60, No. 6, pp. 2961 –2969, June 2012.

[Welc 67] P. Welch. "The use of fast Fourier transform for the estimation of power spectra: A method based on time averaging over short, modified periodograms". *Audio and Electroacoustics, IEEE Transactions on*, Vol. 15, No. 2, pp. 70 – 73, 1967.

Résumé

Ce travail de thèse porte sur la modélisation des phénomènes de propagation affectant les signaux de navigation par satellite en environnement urbain dense avec une focalisation particulière sur les multitrajets et l'aspect large bande du canal de propagation espace/Terre. Le simulateur de canal pseudo temps-réel développé, SCHUN (Simplified CHannel for Urban Navigation), repose sur une approche hybride physico-statistique. La composante statistique de la modélisation permet essentiellement de générer une ville virtuelle à partir de distributions de bâtiments connues. Le reste de la modélisation s'appuie sur une approche physique simplifiée où les interactions ondes électromagnétiques/ville virtuelle reposent d'une part sur un modèle de macro-diffusion à l'échelle des façades, (3CM (Three Component Model)), et d'autre part sur un modèle physique de masquage du trajet direct par les bâtiments. Les principales méthodes numériques sous-jacentes sont l'optique physique et la théorie uniforme de la diffraction. Le simulateur de canal SCHUN ouvre aujourd'hui des perspectives intéressantes pour la modélisation large bande du canal de propagation espace/Terre. Optimisé pour des temps de calcul raisonnables, alliant une composante statistique à une composante physique simplifiée, ce simulateur a été conçu et validé par des mesures expérimentales pour répondre à des besoins de simulation des systèmes à diversité de satellite, diversité de réception, diversité de polarisation ou encore diversité de fréquence pour des applications de navigation par satellite.

Mots-clés : Canal de propagation - Navigation par satellite - Multitrajets

Abstract

This PhD work deals with land mobile satellite channel modelling and addresses the specific issue of satellite navigation systems in urban environments with a particular focus on multipath modelling and wide-band representation of the channel. The developed land mobile satellite channel simulator, SCHUN (Simplified CHannel for Urban Navigation), is based on a hybrid physical-statistical approach satisfying fast computation requirements. The statistical component of the modelling is mainly used during the virtual city synthesis step based on known statistical distributions of building height and street width. The rest of the modelling comes from deterministic methods using simplified electromagnetic interaction models reproducing building macro-scattering (3CM model (Three Component Model)) and building blockage of the direct path. The main underlying electromagnetic methods are the physical optics and the uniform theory of diffraction. The SCHUN simulator now opens interesting perspectives for the modelling of wide-band land mobile satellite propagation channel in dense urban environments. Optimised for pseudo real-time constraints, it uses both physical and statistical approaches. Furthermore, the SCHUN simulator has been designed and validated against measurements to answer specific needs of satellite diversity, receiving diversity, polarisation diversity or frequency diversity for satellite navigation applications.

Keywords : LMS channel propagation - Satellite navigation - Multipath